AFIT/DS/ENP/98-01

OPTIMAL ATMOSPHERIC COMPENSATION FOR ANISOPLANATISM IN ADAPTIVE-OPTICAL SYSTEMS

DISSERTATION

Matthew Raymond Whiteley
Captain, USAF

AFIT/DS/ENP/98-01

The views expressed in this dissertation are those of the author and do not reflect the official policy or position of the Department of Defense or the U. S. Government.

AFIT/DS/ENP/98-01

OPTIMAL ATMOSPHERIC COMPENSATION FOR ANISOPLANATISM IN ADAPTIVE-OPTICAL SYSTEMS

DISSERTATION

Presented to the Faculty of the Graduate School of Engineering

of the Air Force Institute of Technology

Air University

In Partial Fulfillment of the

Requirements for the Degree of

Doctor of Philosophy

Matthew Raymond Whiteley, B.S., M.S.

Captain, USAF

September, 1998

AFIT/DS/ENP/98-01

OPTIMAL ATMOSPHERIC COMPENSATION FOR ANISOPLANATISM IN ADAPTIVE-OPTICAL SYSTEMS

Matthew R. Whiteley, B.S., M.S.

Captain, USAF

Approved:

Byron M Welsh — 8-17-98

Dr. Byron M. Welsh — Date
Chairman, Advisory Committee

Michael C. Roggemann — 8/14/98

Dr. Michael C. Roggemann — Date
Member, Advisory Committee

M. Pachter — 8.14.98

Dr. Meir Pachter — Date
Member, Advisory Committee

Won S. Roh — Aug 17, 98

Dr. Won Roh — Date
Member, Advisory Committee

Richard F Deckro — 14 Aug 98

Dr. Richard F. Deckro — Date
Dean's Representative

Accepted:

Robert A Calico Jr

Robert A. Calico, Jr.
Dean, Graduate School of Engineering

Acknowledgements

In the concluding paragraphs of his treatise on optics, Isaac Newton wrote the following words [53]:

> *And if natural Philosophy in all its Parts, by pursuing this Method, shall at length be perfected, the Bounds of Moral Philosophy will also be enlarged. For as we can know by natural Philosophy what is the first Cause, what Power he has over us, and what Benefits we receive from him, so far our Duty towards him, as well as that towards one another, will appear to us by the Light of Nature.*

And so it seems that Newton understood then what scientists often overlook today–that their research has merit far beyond the confines of its stated results. Research is challenging, inspiring, humbling, and in the end, rewarding.

The most rewarding part of my research at AFIT has been working with the people who have helped to shape that experience. Special thanks to Dr. Byron Welsh, my research advisor, whose unique insights and sound advice are reflected in the character of this work. Thanks also to Dr. Michael Roggemann, who served as my advisor while on faculty at AFIT, and provided the original motivation for this work. Special thanks to those who have served on my research committee: Dr. Meir Pachter, Dr. Won Roh, and Dr. Ted Luke. Thanks to Major Pat Gardner, Ph.D., a friend and colleague, whose laboratory data contributed greatly to this work. Thanks also to Major Todd Steiner, Ph.D. and Major Rich Bagnell, Ph.D. of the Air Force Research Laboratory who sponsored this research effort.

On a personal level, I would like to thank the chaplains and congregation of Our Lady Queen of Peace parish at Wright-Patterson for their support throughout my extended stay here. You are a model of the Christian community. Finally, I should thank my family members– immediate, extended, and departed who have encouraged me throughout my years of formal education. My success is yours also.

Matthew Raymond Whiteley

Table of Contents

List of Figures

List of Tables

List of Symbols

Symbol Page

List of Abbreviations

Abstract

Anisoplanatism in adaptive optics (AO) systems is a performance-degrading effect that arises whenever light from the wave-front sensor beacon and light from the object of interest sample different volumes of optical turbulence. This effect occurs if there is either a spatial separation between the object and the beacon, or a spatial separation between the wave-front sensor and phase-compensation aperture, or if both types of separation are present in the AO system. Anisoplanatism results in an increased value of the aperture-averaged residual phase variance after AO compensation, which causes an exponential decrease in system performance. This dissertation offers a theoretical framework in which the most-general form of anisoplanatism can be analyzed. In this framework, anisoplanatism is characterized by the correlation of Zernike coefficients of object and beacon turbulence-induced phase. It is shown through theoretical calculations validated with experimental data, that while most Zernike coefficients are uncorrelated in the absence of anisoplanatism, moderate amounts of anisoplanatism result in an enhanced cross-correlation of the Zernike coefficients. This fact, along with a theoretical description of the performance-degradation process motivates the application of optimal estimation theory to AO compensation. Using the general anisoplanatism analysis framework, the optimal compensation theory is applied to imaging, beam-projection, and interferometric systems. In imaging systems, optimal compensation reduces the effect of anisoplanatism, increasing beacon separation limits by up to three times, and enabling estimation of wave-front tilt from a laser beacon, which cannot be measured conventionally. For beam-projection systems such as Airborne Laser, optimal compensation can decrease the AO update rate by over 70%. In interferometric systems, a fringe visibility increase of 25% is realized by applying optimal compensation, resulting in enhanced image reconstruction at large baseline separations.

OPTIMAL ATMOSPHERIC COMPENSATION FOR ANISOPLANATISM IN ADAPTIVE-OPTICAL SYSTEMS

I. Introduction

1.1 Overview

A fundamental result in the study of optics is that all optical systems are limited in resolution by the effects of diffraction. For a system unaffected by fixed aberrations, the limiting angular resolution due to diffraction, designated θ_d is often expressed as [35]:

$$\theta_d \propto \frac{\lambda}{D}, \tag{1}$$

where λ is the propagation wavelength of the electromagnetic radiation, and D is the aperture diameter of the optical system. Thus, the limiting angular resolution of an optical system is decreased by imaging at shorter wavelengths, or by increasing the aperture size. For imaging at visible wavelengths ($\lambda = 500$ nm), the diffraction limit is approximately 5 μrad or 1 arcsec for a 10 cm aperture, 0.1 arcsec for a 1 m aperture, 0.01 arcsec for a 10 m aperture, and so on.

The diffraction limit in Eq. 1 applies strictly to an optical system operating in free-space or vacuum, which is a reasonable description of most laboratory systems. When imaging through extended atmospheric paths, however, the assumption of vacuum propagation is no longer valid. In this case, atmospheric effects must be considered. Even when imaging through clear air so that atmospheric scattering and absorption effects are negligible, phase aberration effects caused by atmospheric turbulence degrade the resolution of an imaging system. It has been found, both theoretically and experimentally, that the resolution of an optical system is limited to approximately 1 arcsec no matter how large the aperture diameter [20]. Increasing the size of a telescope's aperture will increase the irradiance incident on the system's focal plane, but will not provide higher-resolution imagery for reasonable light levels. Therefore, any optical system operating at visible wave-

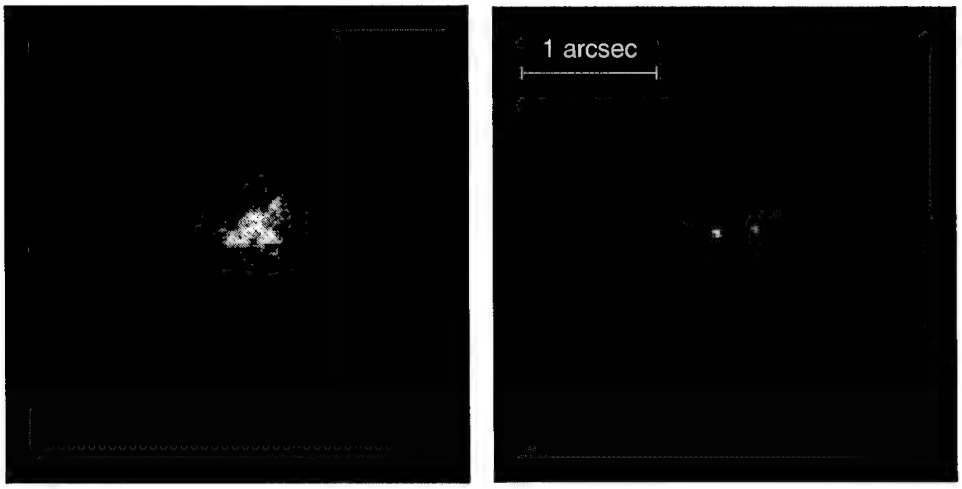

Figure 1. Example of adaptive optics compensation in astronomical imaging. These images show the binary star k-Peg as seen through the 3.5 m telescope at the Starfire Optical Range without atmospheric compensation (left) and with adaptive-optical correction applied (right). Actual binary star separation is 0.3 arcsec. (Photo courtesy Air Force Research Laboratory)

lengths with an aperture larger than approximately 10 cm is *turbulence-limited* when used for imaging over extended atmospheric paths, since the limiting resolution angle imposed by turbulence is larger than that imposed by diffraction.

To improve the resolution of turbulence-limited optical systems, adaptive optics (AO) compensation technology has been developed [69]. In an ideal AO system, the turbulence-induced phase incident from the object being observed is measured using a wave-front sensing device, and the conjugate phase is formed on the surface of a compensation device. Reflection from this surface removes phase aberrations from the incident wave-front, and system performance is restored to its diffraction limit. An example of AO compensation applied to astronomical imaging is shown in Figure 1. These long-exposure images show a close binary star pair as seen through the 3.5 m telescope operated at the Air Force Research Laboratory's Starfire Optical Range. Without AO compensation, the binary pair cannot be resolved, since the separation is 0.3 arcsec. The star pair is imaged as a bright spot approximately 1 arcsec in diameter. When AO compensation is applied, each of the stars is clearly resolved, and the actual separation is apparent. The image of each

star represents a system point spread function (PSF) which is nearly diffraction-limited (approximately 0.03 arcsec for this system).

The performance of a practical adaptive-optical compensation system can be degraded by a number of factors related to system design. Inaccuracies in wave-front measurement due to finite light levels, inadequate wave-front spatial sampling, or poor phase reconstruction techniques lead to reduced AO system performance [65]. Phase conjugation errors caused by deformable mirror physical constraints and control defects also limit the benefits of using adaptive-optics [64]. Even when wave-front sensor and phase conjugation effects are negligible, adaptive optics compensation may still be degraded due to the nature of atmospheric turbulence, and the manner in which turbulence measurements are obtained in an AO system. This effect is classified broadly as turbulence-induced *anisoplanatism* [21, 22, 68]

The term "anisoplanatism" as it applies to adaptive optics is borrowed from terminology associated with fixed optics. An isoplanatic region A is any region in which the imaging PSF, designated here as K, is invariant with respect to a spatial translation [9]:

$$K(\vec{r}, \vec{r}\,') = K_A(\vec{r}\,' - \vec{r}), \tag{2}$$

where K_A represents the diffraction-limited PSF centered at the position $\vec{r}$. The term "anisoplanatic" is therefore used to imply that the isoplanatic condition of Eq. 2 does not hold.

In the context of adaptive optics, anisoplanatism typically refers to a performance degradation that results when the optical source used as a beacon for wave-front sensing is separated from the object being observed. To understand the physical origin of turbulence-induced anisoplanatism, consider the diagrams shown in Figure 2(a)-(b). For the ideal AO system of Figure 2(a), the object of interest is bright enough to be used as the AO beacon for wave-front sensing. Thus, neglecting wave-front sensing errors, the measured phase aberration in the system aperture is the same as the object phase aberration, and ideal phase conjugation removes all wave-front errors induced by propagation through optical turbulence. When the object of interest is too dim to provide for wave-front sensing, a

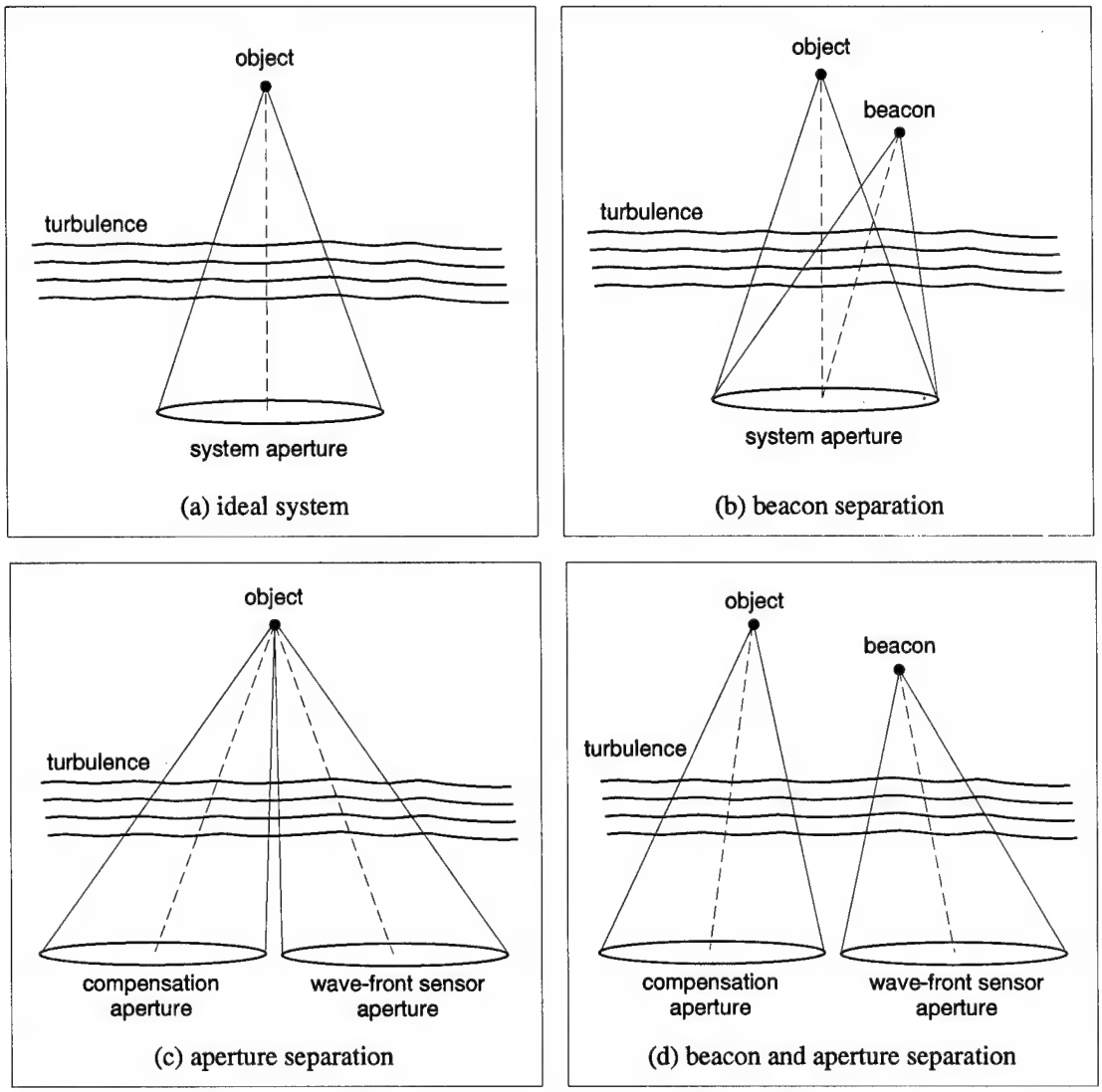

Figure 2. Physical origin of turbulence-induced anisoplanatism in adaptive-optical systems. (a) An ideal system, where the object of interest is also used as the AO beacon. (b) Anisoplanatism introduced by separation between object and beacon. (c) Anisoplanatism introduced by separation between wave-front-sensing aperture and wave-front-compensation aperture. (d) Generalized anisoplanatism in an AO system, with both object/beacon source and sensing/compensation aperture separation.

separate bright source or beacon must be used to obtain the phase aberration information, as depicted in Figure 2(b). Light propagating from the object and the beacon sample different volumes of turbulence. As a result, the turbulence-induced phase incident in the aperture from the object and the source will not be equal, but instead, only partially correlated.

The degree of correlation between the object and beacon phase depends upon the difference in the turbulence volumes sampled by the light as it propagates from each source to the system aperture. According to conventional theory [44, 78], turbulence is stochastic in nature, and must be characterized by its statistical properties. Stochastic models for turbulence specify second-order statistics such as the spatial correlation of the index of refraction fluctuation, which depends upon the spatial separation between turbulence sampling points. It therefore follows that the statistical nature of turbulence-induced phase can also be characterized by spatial correlation properties, which are determined by the spatial separation of field points along the propagation path from each source. The degradation in AO compensation performance associated with the conventional anisoplanatism geometry shown in Figure 2(b) results directly from the partial correlation of object and beacon phase.

This understanding of the physical origin of anisoplanatism leads naturally to an understanding of this phenomenon encompassing a more-diverse class of AO system configurations. Figure 2(c) illustrates the turbulence-sample volume differences resulting from a separation of the wave-front-sensing aperture and wave-front-compensation aperture when the object is bright enough to be used as the AO beacon. In this configuration, the sensed wave-front will again be only partially correlated with the conjugate phase required for proper compensation. The most general form of this decorrelation process occurs when both the object and beacon as well as the sensing aperture and compensation aperture are separated, as depicted in Figure 2(d). The system configurations shown in Figure 2(b)-(d) are affected by anisoplanatism in a general sense; that is, *the object and beacon phase are only partially correlated.* This generalized view of anisoplanatism naturally gives rise to a unified approach to the analysis of diverse AO system configurations. In this unified approach, the aperture and source geometry is generalized, and the phase correlation is

quantified as a function of the spatial position of the object, beacon, wave-front-sensing aperture and wave-front-compensation aperture. The object and beacon phase correlation quantifies the manifestation of anisoplanatism in the given system configuration.

The generalized view of anisoplanatism espoused in this research is enlightening, as it exposes the mechanism of anisoplanatic degradation in AO compensation performance. The ability to quantify the spatial correlation of the turbulence-induced phase leads directly to the application of optimal estimation techniques [43] in AO compensation. When applied to AO compensation for anisoplanatic systems, the wealth of knowledge represented by optimal estimation theory produces immediate dividends. The result is an optimal atmospheric compensation analysis technique which indicates how the performance of systems affected by anisoplanatism may be improved. Thus, the limits on optical performance imposed by the nature of turbulence are expanded, and diffraction-limited performance over extended turbulence paths is made more accessible.

1.2 Historical background and research motivation

The effects of the atmosphere on optical propagation are rooted in everyday experience with natural phenomena. Negative temperature gradients resulting from solar loading on the earth's surface give rise to "mirages" in the distance, commonly observed by desert travelers or highway drivers looking over an asphalt surface. These mirages are actually images of the sky and surrounding landscape produced by the refractive qualities of heated air. At night, positive temperature gradients produce a "looming" effect, which enables us to see objects below the horizon. Indeed, we are all familiar with the "twinkling" of stars or distant city lights which is caused by refractive effects of optical turbulence.

Atmospheric effects were considered in the earliest of modern treatises on optics. Christiaan Huygens (1629-1695) noted the steady variations in the optical properties of the atmosphere [41]:

> *If then you look through [a telescope] at different hours of the day, leaving it always fixed in the same way, you will see that the same spots will not always appear at the middle of the aperture of the telescope, but that generally in the morning and in the evening, when there are more vapours near the earth, these objects seem to rise higher, so that the half or more of them will no longer be*

visible; and so that they seem lower toward mid-day when these vapours are dissipated.

Although Isaac Newton (1642-1727) attributed a different fundamental nature to light than Huygens, he seemed to understand the limits that atmospheric effects place on optical systems [53]:

> *If the Theory of making Telescopes could at length be fully brought into Practice, yet there would be certain Bounds beyond which Telescopes could not perform. For the Air through which we look upon the Stars, is in a perpetual Tremor; as may be seen by the tremulous Motion of Shadows cast from high Towers, and by the twinkling of the fix'd Stars.*

After the time of Huygens and Newton, research in optics, electricity, and magnetism developed almost independently, until James Clerk Maxwell (1831-1879) was able to describe all known electromagnetic phenomena in terms of a system of field equations, leading to the conjecture that light waves are electromagnetic waves. This insight, and the experiments that followed to test the theory has lead directly to our current understanding of optical phenomena, including optical propagation through turbulent media.

Maxwell's field theory also advanced the development of electronic components, enabling a practical design theory for electronic circuits to be developed. By the early 1950s, Babcock [3, 4] understood that an electronically-controlled system could be constructed to correct for phase aberrations introduced by propagation through turbulence, resulting in improved optical performance when the corrected light was focused by a lens. Babcock also pointed out that the reference star must be of adequate brightness to provide for wave-front sensing, and that good compensation performance is limited to a small angular extent around the reference star. Thus, anisoplanatism was understood to be a performance-limiting factor from the earliest days of adaptive optics technology.

The science of atmospheric optics was advanced in the early 1960s by Tatarski [78], who drew upon the turbulence-characterization work of Kolmogorov [44] to develop a stochastic model for the effects of turbulence in optical systems. Tatarski's work was used by Hufnagel and Stanley [40] and Fried [20] as a basis for understanding the degradation of optical resolution caused by atmospheric turbulence. Specifically, Fried introduced the concept of an atmospheric coherence diameter r_0, demonstrating that the resolution of

optical systems with aperture diameter less than r_0 is limited by diffraction, whereas turbulence effects limit the resolution of systems with aperture diameter larger than r_0. Fried's work illustrates theoretically that optical systems reach a limiting performance determined by the statistical properties of the turbulence, not by the physical extent of the aperture. Fried also introduced modal analysis techniques in the analysis of turbulence-induced phase [19].

With continued growth in a theoretical understanding of atmospheric turbulence [37, 47,54,92] and technology advances in the late 1960s and 1970s [34], adaptive optics became a viable technology for imaging applications, especially in astronomy. With practical AO systems being tested, effects of anisoplanatism began to be investigated theoretically [21, 45]. Following Fried's convention [22], anisoplanatism effects were characterized by an isoplanatic angle, designated θ_0. Fried argued that optical performance is degraded by a factor $\exp[-(\theta/\theta_0)^{5/3}]$, where θ represents the angular separation between the object of interest and a natural guide star (NGS) used as the AO beacon. Thus, the extent of "angular anisoplanatism" scales according to the isoplanatic angle. This fact has also been exploited in theoretical works regarding the temporal analysis of AO systems [84]. Others [74] have questioned the appropriateness of this measure for angular anisoplanatism. Alternative methods of establishing performance limits imposed by angular anisoplanatism have been addressed by Troxel et al. [82,83].

The period of the mid-1980s through the mid-1990s was marked by significant advances in adaptive optics technology. In 1985, Foy and Labeyrie first introduced the concept of laser guide star (LGS) adaptive optics in the open literature [18] to provide increased sky coverage for atmospheric compensation. The first experimental results were reported by Thompson et al. in 1987 [80]. Atmospheric composition using the laser guide star was first reported by Primmerman et al. [56] and Fugate et al. [25]. The finite altitude of the LGS for adaptive optics introduces a form of performance degradation referred to as "focal anisoplanatism." This effect has been investigated in detail in works by Gardner et al [27], Welsh and Gardner [93], Tyler [87], Fried and Belsher [23], Esposito et al. [17], and Molodij and Rousset [51].

Concurrent with many of the recent advances in adaptive optics technology, theoretical modeling of compensation performance has lead to the application of optimal control in AO systems. The use of optimal estimation techniques in atmospheric compensation dates back to the work of Valley and Wandzura [88], who pointed out that an optimal compensation could be achieved in a system whose performance is degraded by anisoplanatism by estimating the object phase given beacon phase measurements and knowledge of turbulence statistics. Optimal phase reconstruction from wave-front sensor slope measurements has also been explored in the spatial domain [16,86,91] and in the time domain [15,90,97]. Optimal modal compensation for NGS and LGS adaptive optics has recently been developed by Whiteley et al. [96] to partially-recover performance degradation in astronomical imaging systems degraded by both angular and focal anisoplanatism.

Throughout the history of adaptive optics research, the concept of anisoplanatism has been expanded due to changes in adaptive optics technology. For instance, consideration of the focal anisoplanatic effect with a laser guide star represented an expansion in the original concept of anisoplanatism as introduced by Babcock and Fried. Performance degradation was no longer related to an angular field separation, but rather to an altitude difference between the object and LGS beacon. Prior to the advent of laser-guide star adaptive optics, focal anisoplanatism had not been addressed in system analysis efforts. Focal anisoplanatism became relevant only after LGS beacon technology was developed.

Today, adaptive optics is being applied to new problems, including dynamic beam projection systems like the Airborne Laser [26], multiple beacon compensation [42, 72], and optical interferometric systems [75]. Ground-based and spaced-based variants of the Airborne Laser are being considered for weapons, propulsion, and laser communication applications. Interferometric imaging applications with adaptive optics are promising technologies for advanced surveillance of space assets and astronomy. While conventional analysis of anisoplanatism has a rich history dating back to the earliest days of adaptive optics technology, current analysis methods are inadequate to treat the diverse nature of emerging AO applications. The concept of anisoplanatism and the associated analysis methods must be expanded to treat these new systems so their performance capabilities and limitations may be properly assessed.

1.3 Problem statement and research scope

Although adaptive optics has its origin in astronomical applications, and much of the current research applies directly to those applications, AO technology is now being incorporated into advanced weapon and surveillance systems. The current analysis methods for anisoplanatism are inadequate to treat the broadened scope of adaptive optics technologies. The desire to establish the performance capabilities and limits of this expanded class of AO systems is the key motivation for the problem addressed in this dissertation:

> Establish a unified framework for the analysis of anisoplanatism in a broad class of adaptive-optical ground-based imaging systems, dynamic beam-projection systems, and interferometric imaging systems; and quantify performance improvement obtained through optimal atmospheric compensation techniques applied to each system type.

To this end, it is assumed that the most-general form of anisoplanatism is manifested in an interferometric system, where both the object source and beacon source as well as the wave-front-sensing aperture and wave-front-compensation aperture may be separated spatially. This assumption serves as the primary method of unifying the analysis of imaging, beam-projection, and interferometric systems. Performance degradation due to turbulence-induced anisoplanatism and the associated optimal compensation theory are developed for the case of an interferometric system, with imaging and beam-projection systems being a special case of this more-general analysis. The results obtained in this research are for multi-layer, wide-sense stationary, isotropic turbulence with finite outer scale. For ground-based AO imaging, NGS and LGS compensation methods are explored, demonstrating the performance improvement obtained with optimal compensation. Tilt compensation performance is investigated in the case of the Airborne Laser system both with and without optimal compensation. For an adaptive-optical interferometer, the effect of angular anisoplanatism on system performance is investigated, and optimal compensation theory is applied to provide enhanced visibility measurements with AO compensation.

1.4 Key results

The theory and analysis conducted in this research and presented in this document have lead to the following key results:

- The adaptive optics compensation performance of imaging, beam-projection, and interferometric systems may be analyzed in a unified context, where imaging and beam-projection applications are viewed as a limiting case of an adaptive-optical interferometer. An optimal modal compensation theory for anisoplanatism in adaptive optics is developed, where the generalized effect of anisoplanatism is characterized by the cross-correlation of Zernike phase coefficients.
- A theoretical and experimental analysis of the cross-correlation of Zernike phase coefficients with finite turbulence outer scale demonstrates that while most Zernike coefficients are uncorrelated when no anisoplanatism is present in an AO system, the cross-correlation of many Zernike modes is enhanced when moderate levels of anisoplanatism exist.
- In ground-based AO imaging systems, application of the optimal compensation theory results in increased Strehl ratio performance when angular and focal anisoplanatism are present in the system. For NGS compensation, equivalent performance can be obtained at larger angular beacon offsets. For LGS compensation, equivalent performance can be obtained at lower LGS altitudes. The optimal compensation theory leads to a new class of LGS tilt-sensing methods, where tilt components are estimated from higher-order, off-axis LGS measurements.
- When time-delays are present in a dynamic beam-projection system like the Airborne Laser, application of optimal modal compensation results in increased Strehl ratio performance at longer time delays. Using the optimal estimator for tilt components, higher-order modal measurements can be used to enhance beam-steering performance. Consequently, the AO bandwidth for the Airborne Laser system can be reduced by over 70%, while maintaining a constant performance level.
- The theoretical generalized anisoplanatism framework permits the analysis of angular anisoplanatism in adaptive-optics for interferometry. Angular anisoplanatism is shown to impose more severe limitations in an adaptive-optical interferometer than in an imaging AO system. Application of the optimal compensation theory in adaptive-optical interferometry leads to a simplified system design, as the optimal conjugate phase can be formed on a single deformable mirror, based on wave-front measure-

ments in each baseline aperture. Optimal compensation also results in increased fringe visibility for larger AO beacon angular offsets, leading to a greater capability to reconstruct object irradiance information from interferometric measurements.

1.5 Dissertation organization

The remainder of this dissertation is organized into six chapters. Chapter II presents the background and analysis required to understand the effects of turbulence and anisoplanatism on the performance of optical systems. Turbulence statistics and modeling are discussed, and wave propagation in turbulent media is explored. On the basis of this standard theory, optical system performance is analyzed in imaging, beam-projection, and interferometric applications. Adaptive optics technology and modal analysis of compensation performance are introduced, leading to a quantification of the performance degradation that results from both angular and focal anisoplanatism.

Optimal compensation for anisoplanatic systems is discussed in Chapter III. In this analysis, the compensation performance of an adaptive-optical interferometer is considered using modal analysis techniques. Compensation is shown to be suboptimal when beacon measurements are used directly. Optimal compensation requires that the conjugate phase be estimated from modal beacon measurements, given knowledge of the spatial cross-correlation of the Zernike modes. The form of the optimal estimator is specified and its performance is quantified, indicating the need to evaluate the Zernike coefficient cross-correlation for a generalized analysis geometry. The cross-correlation calculation is detailed, and the resulting expression is validated by comparison with theoretical and experimental results. The results of Chapter III are also applicable to imaging and beam-projection systems, by considering limiting cases of the more-general results for the adaptive-optical interferometer.

Chapter IV, Chapter V, and Chapter VI deal with the application of the optimal compensation theory to adaptive optics for ground-based imaging systems, a beam-projection system (Airborne Laser), and an optical interferometer, respectively. For each application, the general theory is specialized, refining notation, and considering the peculiar features of each system type. Optimal compensation is shown to yield enhanced performance and to

expand the limitations placed on system operation by turbulence-induced anisoplanatism. Conclusions from this research and recommendations for future research are summarized in Chapter VII.

1.6 Summary

In this chapter, atmospheric compensation through adaptive optics has been briefly introduced, and the concept of anisoplanatism was discussed as a factor which degrades compensation performance. Since AO technology has its roots in instrumentation for astronomical imaging, the analysis of anisoplanatism has conventionally focused on the system geometries experienced in those applications. Directed-energy weapon systems like the Airborne Laser and interferometric systems for high-resolution surveillance also experience performance degradation with the same physical origin as conventional anisoplanatism, but these effects are not easily explained by conventional analysis methods. In order to analyze these systems, the concept of anisoplanatism must be generalized to include any physical configuration which results in a partial correlation of the sensed wavefront aberration and the required conjugate phase. To achieve this goal, a unified approach to understanding turbulence degradation and anisoplanatic effects will be taken for a broad class of optical systems in Chapter II. This unified analysis leads to the development of an optimal compensation theory for adaptive optics in Chapter III which requires the generalized form of anisoplanatism be quantified for a modal phase decomposition. Application of the optical compensation theory for anisoplanatism in adaptive optics will be discussed in Chapters IV, V, and VI for ground-based imaging, beam-projection (Airborne Laser), and interferometric imaging systems.

II. Atmospheric and Adaptive Optics

2.1 Introduction

The purpose of this chapter is to review the fundamental concepts associated with atmospheric and adaptive optics, and to provide a theoretical framework in which the effects of turbulence on conventional and interferometric optical systems can be understood. Modal compensation of atmospheric aberrations is discussed, and the concept of turbulence-induced anisoplanatism in adaptive optics is introduced. Notation used throughout the remaining chapters is established here, and quantities important to later analyses are derived.

Section 2.2 of this chapter explores the effects of turbulence-induced phase aberrations on optical systems. The section begins with a discussion of the statistics of index of refraction fluctuations in the atmosphere, leading to the subject of wave propagation in turbulent media and turbulence modeling. A theoretical development is then presented which can be used to quantify turbulence effects on conventional imaging, beam-projection, and interferometric systems.

Adaptive optics technology is overviewed in Section 2.3. A typical adaptive optics system is considered, and the function of each system component is described. The unique characteristics of natural and laser-guide-star adaptive optics are discussed, and the concept of modal atmospheric compensation is introduced as a means of quantifying the performance of an adaptive optics system.

Section 2.4 discusses turbulence-induced anisoplanatism in adaptive optics. Anisoplanatism is studied using modal analysis techniques, and its effects on adaptive-optical system performance is explored. This development sets the stage for the analysis presented in Chapter III, when optimal methods for modal compensation of atmospheric aberrations are considered. A brief summary of the chapter is presented in Section 2.5.

2.2 Turbulence effects on optical systems

The effects of turbulence in optical systems arise from variations in the index of refraction along the propagation path. Large-scale variations of n at the spatial posi-

tion $\vec{\xi}$ can be related to slowly-varying atmospheric characteristics such as pressure and temperature by the following steady-state deterministic relationship [71]:

$$n\left(\vec{\xi}\right) - 1 = 77.6 \times 10^{-6} \left(1 + \frac{7.52 \times 10^{-3}}{\lambda^2}\right) \frac{P\left(\vec{\xi}\right)}{T\left(\vec{\xi}\right)}, \tag{3}$$

where λ is the propagation wavelength measured in μm, $P\left(\vec{\xi}\right)$ is the atmospheric pressure in millibars, and $T\left(\vec{\xi}\right)$ is the atmospheric temperature in degrees Kelvin. Smaller-scale variations in the index of refraction must be regarded as stochastic, depending upon random changes in local atmospheric parameters, most notably temperature and velocity. Thus, the analysis of turbulence effects on optical systems is inherently stochastic in nature, requiring a statistical characterization of the index of refraction fluctuations.

2.2.1 Statistics of atmospheric index of refraction fluctuations. Our understanding of the phenomenology of atmospheric optical turbulence has its origin in the work of Kolmogorov [44] and Obukov. Kolmogorov argued that when eddies are formed in a turbulent flow, those of larger scale size break up into smaller eddies, and that the eddy scale distribution follows a universal law based upon energy conservation. In the standard theory, statistics of the air speed field $v\left(\vec{\xi}\right)$ are characterized by the structure function $D_v\left(\vec{\xi}, \vec{s}\right)$, which is defined as:

$$D_v\left(\vec{\xi}, \vec{s}\right) \equiv \left\langle \left[v\left(\vec{\xi}\right) - v\left(\vec{\xi} + \vec{s}\right)\right]^2 \right\rangle, \tag{4}$$

where $\vec{\xi}$ and $\vec{\xi} + \vec{s}$ are spatial locations within the field, and $\langle \cdot \rangle$ represents averaging with respect to an ensemble of turbulence realizations. In their development, Kolmogorov and Obukov made two key assumptions. First, they assumed that the air speed field in the turbulent flow is wide-sense stationary [32] or homogeneous, such that the structure function depends only upon the separation of points at which it is sampled, i.e., $D_v\left(\vec{\xi}, \vec{s}\right) = D_v(\vec{s})$. Furthermore, they assumed that the field was also isotropic; that is D_v depends only upon $s = |\vec{s}|$. For the range of separations $L_i \leq s \leq L_0$ known as the inertial subrange, where L_i is the turbulence inner scale and L_0 is the turbulence outer scale, the

Kolmogorov-Obukov law says that:

$$D_v(s) \propto s^{2/3}. \tag{5}$$

Index of refraction fluctuations $n'\left(\vec{\xi}\right)$ associated with a turbulent flow are analyzed in a manner similar to the air speed field. The structure function of the index of refraction fluctuations is designated $D_{n'}(\vec{s})$, and is defined by:

$$D_{n'}(\vec{s}) \equiv \left\langle \left[n'\left(\vec{\xi}\right) - n'(\vec{\xi}+\vec{s}) \right]^2 \right\rangle. \tag{6}$$

By employing the concept of conservative passive additives, Tatarski [78, 79] showed that for homogeneous and isotropic turbulence, $D_{n'}$ varies with separation in the same manner as D_v in the inertial subrange. Specifically, $D_{n'}(s,z)$ is given by:

$$D_{n'}(s,z) = C_n^2(z) s^{2/3}, \tag{7}$$

where $C_n^2(z)$ is the index of refraction structure constant, which specifies the steady variation of the turbulence strength with altitude z. The units of $C_n^2(z)$ are meters$^{-2/3}$.

For the purpose of analysis, it is often useful to express turbulence statistics in the spatial-frequency domain instead of the spatial domain. The spectral equivalent of $D_{n'}(s,z)$ is the power spectral density (PSD) of the index of refraction fluctuations, designated $W_{n'}(k,z)$. If k represents a spatial frequency (in units of inverse meters), then $W_{n'}(k,z)$ is related to $D_{n'}(s,z)$ as follows [71]:

$$W_{n'}(k,z) = (\sqrt{2\pi}k)^{-2} \int_0^\infty \mathrm{d}s \left[\frac{\sin(2\pi k s)}{2\pi k s}\right] \frac{\partial}{\partial s}\left[s^2 \frac{\partial D_{n'}(s,z)}{\partial s}\right]. \tag{8}$$

Using the form of $D_{n'}(s,z)$ given in Eq. (7), the integral over s in Eq. (8) may evaluated to yield the following expression for $W_{n'}(k,z)$:

$$W_{n'}(k,z) = \frac{\sqrt{3}\,\Gamma(8/3)}{2(2\pi)^{8/3}} C_n^2(z) k^{-11/3}. \tag{9}$$

The form of $W_{n'}(k,z)$ specified in Eq. (9) is commonly referred to as the Kolmogorov spectrum, since the corresponding structure function scales with distance according to Kolomogorov's law.

While the mathematical form of Eq. (9) is simple (a power law), and has been used widely in the analysis of atmospheric optics, its application is limited. When used in propagation calculations, Eq. (9) results in non-physical theoretical predictions, such as an infinite variance for the turbulence-induced phase, and a non-zero phase correlation at large spatial separations. Note that as it is defined in Eq. (9), $W_{n'}(k,z) \rightarrow \infty$ as $k \rightarrow 0$. To provide a finite limit on $W_{n'}(k,z)$ as $k \rightarrow 0$, the effect of the turbulence outer scale is incorporated into $W_{n'}(k,z)$. A common way to include the outer scale effect is as follows [89]:

$$W_{n'}(k,z) = \frac{\sqrt{3}\,\Gamma(8/3)}{2(2\pi)^{8/3}} C_n^2(z)(k^2 + k_0^2)^{-11/6}, \tag{10}$$

where $k_0 = L_0^{-1}$. This form of $W_{n'}(k,z)$ is referred to as the von Kármán spectrum. The functional dependence of $W_{n'}$ on k is shown in Figure 3. Throughout this research, the von Kármán spectrum will be employed as an appropriate statistical model for atmospheric optical turbulence. Use of the von Kármán spectrum places this research in concert with the majority of other research efforts employing finite outer scale models [68, 71, 76, 98].

2.2.2 Wave propagation in turbulent media. Under reasonable physical assumptions, Maxwell's equations in the presence of a dielectric media (such as the atmosphere) imply a scalar wave equation for each component of the vector electromagnetic field given by [71]:

$$\nabla^2 \underline{u}\left(\vec{\xi}\right) + \left(\frac{2\pi}{\lambda}\right)^2 n^2\left(\vec{\xi}\right)\, \underline{u}\left(\vec{\xi}\right) = 0, \tag{11}$$

where the notation $\underline{u}$ is used to indicate that the scalar field is a complex quantity. To solve this wave equation, the Rytov method [78] may be employed, where $\underline{u}\left(\vec{\xi}\right)$ is expressed as:

$$\underline{u}\left(\vec{\xi}\right) = \exp\left[\Psi\left(\vec{\xi}\right)\right], \tag{12}$$

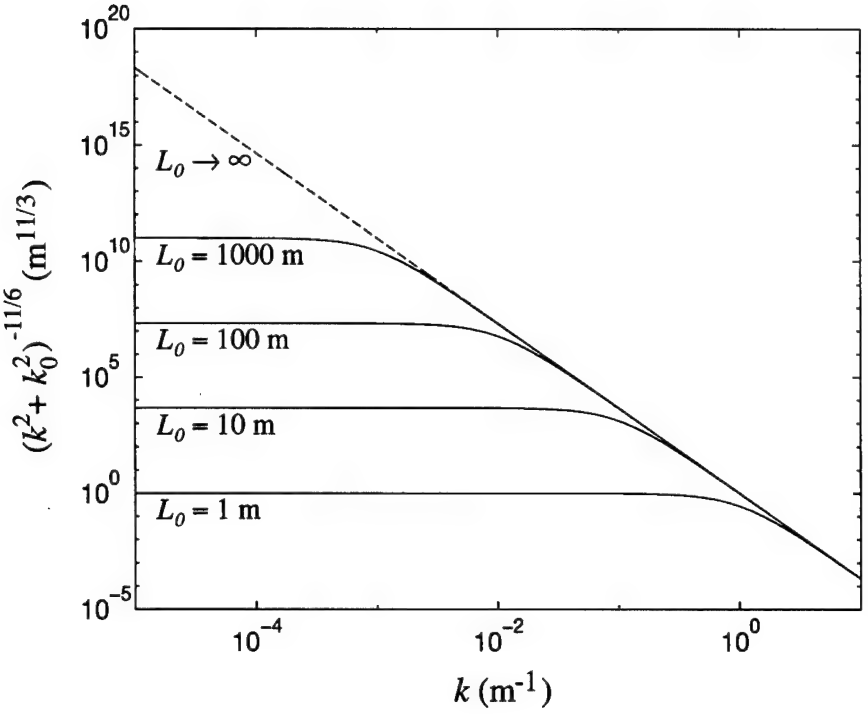

Figure 3. Effect of outer scale L_0 on the von Kármán spectrum. For $L_0 \to \infty$, the Kolmogorov spectrum is recovered (dashed line).

and Eq. (11) is transformed into the nonlinear Riccati equation [71]:

$$\nabla^2 \Psi\left(\vec{\xi}\right) + \left[\nabla \Psi\left(\vec{\xi}\right)\right]^2 = -\left(\frac{2\pi}{\lambda}\right)^2 n^2\left(\vec{\xi}\right). \tag{13}$$

Now, if the index of refraction fluctuations are assumed to be small, then we may say that $n\left(\vec{\xi}\right) = 1 + \epsilon\, n'\left(\vec{\xi}\right)$, where ϵ is some small number. A solution to Eq. (13) is obtained by a perturbation method where it is assumed that $\Psi\left(\vec{\xi}\right)$ can be written as a power series in ϵ:

$$\Psi\left(\vec{\xi}\right) = \Psi_0\left(\vec{\xi}\right) + \epsilon \Psi_1\left(\vec{\xi}\right) + \epsilon^2 \Psi_2\left(\vec{\xi}\right) + \cdots. \tag{14}$$

Retaining only the first two terms results in the second order solution for the scalar field:

$$\underline{u}\left(\vec{\xi}\right) = \hat{\underline{u}}\left(\vec{\xi}\right) \exp\left[\Psi_1\left(\vec{\xi}\right)\right], \tag{15}$$

where $\hat{\underline{u}}\left(\vec{\xi}\right)$ represents the solution to the wave equation in free space [Eq. (11) with $n\left(\vec{\xi}\right) = 1$]; that is, the wave that is undisturbed by turbulence.

The perturbed field $\Psi_1\left(\vec{\xi}\right)$ is obtained with the Green's function for free-space propagation as [71]:

$$\Psi_1\left(\vec{\xi}\right) = \frac{1}{2\pi\hat{\underline{u}}\left(\vec{\xi}\right)}\left(\frac{2\pi}{\lambda}\right)^2 \int d\vec{\xi}\,'\,\hat{\underline{u}}\left(\vec{\xi}\,'\right) n'\left(\vec{\xi}\,'\right) \frac{\exp\left(j\frac{2\pi}{\lambda}\left|\vec{\xi}-\vec{\xi}\,'\right|\right)}{\left|\vec{\xi}-\vec{\xi}\,'\right|}, \tag{16}$$

where the integration is over the source volume denoted by the primed coordinate. The real and imaginary components of $\Psi_1\left(\vec{\xi}\right)$ are identified as $\chi\left(\vec{\xi}\right)$, the log-amplitude fluctuation and $\phi\left(\vec{\xi}\right)$, the turbulence-induced phase, respectively, and Ψ_1 may be expressed as:

$$\Psi_1\left(\vec{\xi}\right) \equiv \chi\left(\vec{\xi}\right) + j\phi\left(\vec{\xi}\right). \tag{17}$$

Thus, $\chi\left(\vec{\xi}\right)$ and $\phi\left(\vec{\xi}\right)$ are computed as follows:

$$\chi\left(\vec{\xi}\right) = \frac{1}{2}\left[\Psi_1\left(\vec{\xi}\right) + \Psi_1^*\left(\vec{\xi}\right)\right], \tag{18}$$

$$\phi\left(\vec{\xi}\right) = \frac{1}{2j}\left[\Psi_1\left(\vec{\xi}\right) - \Psi_1^*\left(\vec{\xi}\right)\right]. \tag{19}$$

In this research, weak turbulence is assumed, and therefore log-amplitude fluctuations are assumed to be negligible ($\chi\left(\vec{\xi}\right) = 0$). Thus, according to Eq. (15), the turbulence-induced phase-aberrated field is written as:

$$\underline{u}\left(\vec{\xi}\right) = \hat{\underline{u}}\left(\vec{\xi}\right)\exp\left[j\phi\left(\vec{\xi}\right)\right]. \tag{20}$$

If diffraction effects are also assumed to be negligible, then the turbulence-induced phase at position $\vec{r}$ transverse to the propagation direction represents the integrated effect of index of refraction fluctuations along the path:

$$\phi(\vec{r}) = \int_0^L dz\left(\frac{2\pi}{\lambda}\right) n'(\vec{r}, z), \tag{21}$$

where $n'(\vec{r}, z)$ is the index of refraction fluctuation at a point specified by the transverse vector $\vec{r}$ at position z along the propagation path of length L.

From Eq. (21), the statistical properties of the turbulence-induced phase may be derived. First, since $\phi(\vec{r})$ can be viewed as the sum of a large number of random variables, all of which are zero-mean, then by the central limit theorem [36], $\phi(\vec{r})$ will be zero-mean Gaussian. Furthermore, by employing the Fourier-transform relation between the PSD and the autocorrelation, the PSD of the turbulence-induced phase $W_\phi(k)$ associated with plane-wave propagation may be computed as:

$$\begin{aligned} W_\phi(k) &= \mathcal{FT}\left\{\langle\phi(\vec{r})\phi(\vec{r}+\vec{s})\rangle\right\} \\ &= \int_0^L \mathrm{d}z \left(\frac{2\pi}{\lambda}\right) \int_0^L \mathrm{d}z' \left(\frac{2\pi}{\lambda}\right) \mathcal{FT}\left\{\langle n'(\vec{r}, z) n'[(\vec{r}, z') + \vec{s}]\rangle\right\} \\ &= \int_0^L \mathrm{d}z \left(\frac{2\pi}{\lambda}\right)^2 W_{n'}(k, z), \end{aligned} \tag{22}$$

where $\mathcal{FT}\{\cdot\}$ denotes the two-dimensional Fourier transform operation, and the index of refraction fluctuations have been assumed to be uncorrelated in altitude. Using the Kolmogorov PSD given in Eq. (9), $W_\phi(k)$ is computed as:

$$W_\phi(k) = \frac{\sqrt{3}\,\Gamma(8/3)}{2(2\pi)^{8/3}} \left[\left(\frac{2\pi}{\lambda}\right)^2 \int_0^L \mathrm{d}z\, C_n^2(z)\right] k^{-11/3}. \tag{23}$$

For isotropic phase, the phase structure function D_ϕ is computed directly from $W_\phi(k)$ as [71]:

$$D_\phi(s) = 4\pi \int_0^\infty \mathrm{d}k\, k\, W_\phi(k)[1 - J_0(2\pi k s)], \tag{24}$$

where J_0 is the Bessel function of the first kind of order zero. Substituting Eq. (23) into Eq. (24), and performing the integration with respect to k yields the following:

$$D_\phi(s) = 2.91 \left[\left(\frac{2\pi}{\lambda}\right)^2 \int_0^L \mathrm{d}z\, C_n^2(z)\right] s^{5/3}. \tag{25}$$

Thus, if the atmospheric coherence diameter r_0 is defined as:

$$r_0 \equiv \left[\frac{2.91}{6.88} \left(\frac{2\pi}{\lambda}\right)^2 \int_0^L \mathrm{d}z\, C_n^2(z)\right]^{-3/5}, \tag{26}$$

following the convention of Fried [20], then $D_\phi(s)$ is expressed as:

$$D_\phi(s) = 6.88 \left(\frac{s}{r_0}\right)^{5/3}. \tag{27}$$

This expression for the phase structure function has been widely used to describe the effects of turbulence-induced phase on the performance of optical systems [68]. While Eq. (27) strictly applies only to turbulence with infinite outer scale, the atmospheric coherence diameter r_0 defined in Eq. (26) is useful in characterizing the optical properties of the atmosphere even when finite turbulence outer scale effects are considered. Since r_0 depends explicitly upon the value of C_n^2 integrated over the propagation path, it can be used to parameterize the turbulence profile in propagation calculations.

2.2.3 Turbulence modeling. To simplify calculations associated with propagation through turbulent media, a layered atmospheric model is often assumed [61, 68, 81]. In a layered atmospheric model, C_n^2 is regarded as being approximately constant within the layer, and index of refraction fluctuations are assumed to be uncorrelated from layer to layer. For a layered atmospheric model, the expression for the turbulence-induced phase equivalent to Eq. (21) is given by:

$$\phi(\vec{r}) = \frac{2\pi}{\lambda} \sum_l \Delta z_l \, n'(\vec{r}, z_l), \tag{28}$$

where each layer is indexed by the subscript l, is located at an altitude z_l, and is of thickness Δz_l. With a layered model, $W_\phi(k)$ is computed similarly to Eq. (22):

$$\begin{aligned} W_\phi(k) &= \mathcal{FT}\left\{\langle \phi(\vec{r})\phi(\vec{r}+\vec{s})\rangle\right\} \\ &= \sum_l \Delta z_l \left(\frac{2\pi}{\lambda}\right) \sum_{l'} \Delta z_{l'} \left(\frac{2\pi}{\lambda}\right) \mathcal{FT}\left\{\langle n'(\vec{r}, z_l) n'[(\vec{r}, z_{l'}) + \vec{s}]\rangle\right\} \\ &= \sum_l \Delta z_l \left(\frac{2\pi}{\lambda}\right)^2 W_{n'}(k, z_l). \end{aligned} \tag{29}$$

The quantity within the summation is regarded as the PSD of the phase in the lth layer, designated $W_\phi(k, z_l)$. Thus, for a layered turbulence model, it may be said that:

$$W_\phi(k) = \sum_l W_\phi(k, z_l). \tag{30}$$

For finite turbulence outer scale, Eq. (10) is substituted into Eq. (29) to yield the von Kármán spectrum for phase in the lth layer:

$$W_\phi(k, z_l) = \frac{\sqrt{3}\,\Gamma(8/3)}{2(2\pi)^{8/3}} \left(\frac{2\pi}{\lambda}\right)^2 \Delta z_l\, C_n^2(z_l)\, (k^2 + k_0^2)^{-11/6}. \tag{31}$$

Troxel et al. [82] have shown that a four-layer turbulence model is adequate for many imaging and propagation calculations. For the four-layer model, the layer altitude and thickness are chosen such that the moments of C_n^2 for continuous turbulence match the moments of C_n^2 for a layered model through seventh order ($0 \leq m \leq 7$):

$$\int_0^L \mathrm{d}z\, z^m C_n^2(z) = \sum_{l=1}^{4} \Delta z_l\, z_l^m\, C_n^2(z_l). \tag{32}$$

For $m = 0$, Eq. (32) implies that:

$$\sum_{l=1}^{4} \frac{\Delta z_l\, C_n^2(z_l)}{\int_0^L \mathrm{d}z\, C_n^2(z)} = 1. \tag{33}$$

The term inside the summation of Eq. (33) is identified as a turbulence-dependent layer weight w_l:

$$w_l = \frac{\Delta z_l\, C_n^2(z_l)}{\int_0^L \mathrm{d}z\, C_n^2(z)}. \tag{34}$$

Using Eq. (34) along with the definition of r_0 in Eq. (26), it may be said that:

$$\Delta z_l\, C_n^2(z_l) = w_l\, \frac{6.88}{2.91} \left(\frac{2\pi}{\lambda}\right)^{-2} r_0^{-5/3}. \tag{35}$$

Thus, substituting Eq. (35) into Eq. (31) yields the following parametric form for $W_\phi(k, z_l)$:

$$W_\phi(k, z_l) = \frac{\sqrt{3}\,\Gamma(8/3)}{2(2\pi)^{8/3}}\, \frac{6.88}{2.91}\, w_l\, r_0^{-5/3} (k^2 + k_0^2)^{-11/6}. \tag{36}$$

C_n^2 model	w_1	w_2	w_3	w_4	r_0 (m)
HV-21	0.8902	0.0443	0.0591	0.0064	0.050
HV-54	0.6877	0.0204	0.2554	0.0365	0.042
SLC-N	0.4965	0.4623	0.0299	0.0113	0.103
SLC-D	0.7397	0.2513	0.0048	0.0042	0.051
GRNWD	0.8615	0.0980	0.0394	0.0011	0.077

Table 1. Layer weights and associated atmospheric coherence diameter r_0 for 4-layer atmospheric turbulence models. For each model, layers are located at altitude $z_1 = 200$ m, $z_2 = 2$ km, $z_3 = 10$ km, and $z_4 = 18$ km.

Troxel et al. [82] calculated the weights corresponding to a four-layer model with $z_1 = 200$ m, $z_2 = 2$ km, $z_3 = 10$ km, and $z_4 = 18$ km. The layer weights and corresponding r_0 for various C_n^2 models have been calculated [82], and are presented in Table 1. The models designated HV-21 and HV-54 are the Hufnagel-Valley model [39] with 21 and 54 mph upper atmospheric winds, respectively. The models designated SLC-N and SLC-D are based on data collected at the Air Force Maui Optical Site (AMOS), and modified to simulate nighttime (N) and daytime (D) conditions [68]. The model designated GRNWD is Greenwood's "good-seeing" model [33]. As is indicated in Table 1, r_0 ranges from 4 cm to over 10 cm depending upon which model is used for C_n^2.

2.2.4 Temporal turbulence statistics. The discussion of the statistics of turbulence-induced phase up to this point has dealt specifically with the spatial evolution of turbulence, assuming that any temporal evolution occurs on time scales that are large compared to the period of the phase measurement. This analysis may be easily extended to account for the first-order temporal effects introduced by turbulence motion. To accomplish this result, Taylor's frozen-flow hypothesis is assumed [32, 68]. This hypothesis states that over short intervals of time τ, the temporal evolution of the index of refraction fluctuation $n'[(\vec{r}, z_l), t]$ is accurately described as a uniform bulk motion due to atmospheric winds with velocity $\vec{v}_l$ for the lth atmospheric layer. Mathematically, this hypothesis is expressed as:

$$n'[(\vec{r}, z_l), t + \tau] = n'[(\vec{r}, z_l) - \vec{v}_l \tau, t]. \tag{37}$$

Thus, temporal delays correspond to an equivalent spatial separation $\vec{v}_l\tau$. The temporal autocorrelation of the turbulence-induced phase, designated $R_\phi(\tau)$, is therefore calculated as follows:

$$\begin{aligned} R_\phi(\tau) &= \langle \phi(\vec{r},t)\phi(\vec{r},t+\tau)\rangle \\ &= \sum_l \Delta z_l \left(\frac{2\pi}{\lambda}\right) \sum_{l'} \Delta z_{l'} \left(\frac{2\pi}{\lambda}\right) \langle n'[(\vec{r},z_l),t]n'[(\vec{r},z_{l'}),t+\tau]\rangle \\ &= \sum_l \Delta z_l \left(\frac{2\pi}{\lambda}\right) \sum_{l'} \Delta z_{l'} \left(\frac{2\pi}{\lambda}\right) \langle n'[(\vec{r},z_l),t]n'[(\vec{r},z_{l'}) - \vec{v}_{l'}\tau,t]\rangle \\ &= \sum_l \Delta z_l \left(\frac{2\pi}{\lambda}\right)^2 B_{n'}(-\vec{v}_l\tau), \end{aligned} \tag{38}$$

where $B_{n'}$ is the spatial autocorrelation of the index of refraction fluctuations, and the turbulence has been assumed to be uncorrelated layer to layer. Thus, using the frozen-flow hypothesis, the temporal autocorrelation of the turbulence-induced phase is related directly to the spatial autocorrelation of the index of refraction fluctuations. Therefore, temporal turbulence statistics may be understood in the same context as spatial turbulence statistics with proper accounting for the time-equivalent spatial separation $\vec{v}_l\tau$.

2.2.5 Optical system performance. The turbulence-induced phase acquired upon propagation from an optical source to the aperture of an optical system affects the performance of that system. For a given realization of the turbulence, the atmospheric phase will act as a fixed aberration, thereby degrading the performance of the optical system from its diffraction limit [9]. Often, the irradiance from a low-light level source on the focal plane of an optical system must be integrated temporally to the enhance signal-to-noise ratio. If this is the case, then an ensemble of turbulence realizations are averaged by the system, resulting in a further degradation of system performance [32].

In order to quantify the performance degradation associated with averaging over an ensemble of atmospheric phase realizations, consider the representative multi-aperture optical system shown in Figure 4. As shown here, this diagram is a schematic representation of a spatial optical interferometer, which would be used for interferometric imaging applications. This system collects light with two baseline apertures of radius R and vector

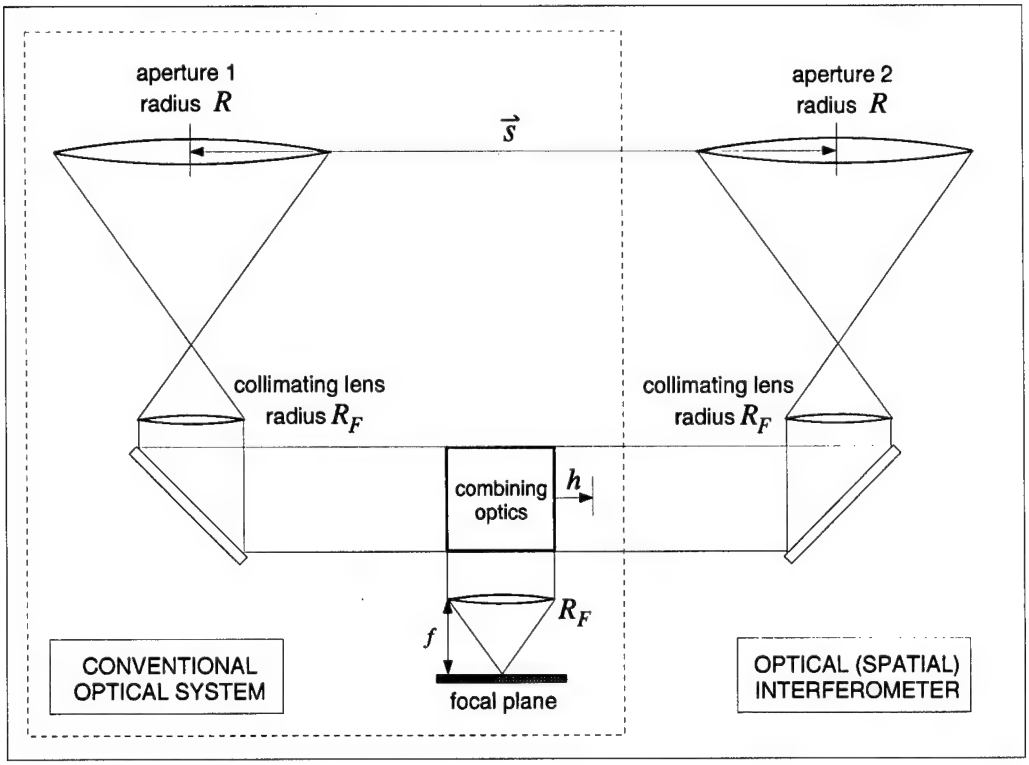

Figure 4. Representative multi-aperture system used for analyzing the effect of turbulence-induced phase aberrations on optical system performance. As shown here, the entire system is an optical spatial interferometer, as would be used for interferometric imaging applications. If aperture 2 is removed, the remaining system (within the dashed line) is a conventional optical system, as would be used for imaging or beam-projection applications.

separation $\vec{s}$, collimates the light through lenses of radius R_F, and combines the collimated light using suitable optics with a variable path difference h. The combined irradiance is then focused onto a detector located on the focal plane of a lens also of radius R_F. The analysis which follows is conducted for this general system. It is recognized, however, that the results of the general analysis will also be applicable to a conventional optical system, if only those quantities associated with aperture 1 are considered. As indicated in Figure 4, the system contained within the dashed line represents a conventional optical system, such as would be used for imaging or beam-projection applications.

The quantity of interest to assess optical system performance is the long-exposure irradiance on the focal plane, designated $\langle i_F(\vec{x})\rangle$, and calculated as:

$$\langle i_F(\vec{x})\rangle = \langle \underline{u}_F(\vec{x})\underline{u}_F^*(\vec{x})\rangle\,, \tag{39}$$

where $\underline{u}_F(\vec{x})$ is the instantaneous field at a point on the focal plane located by $\vec{x}$. From the Fresnel diffraction formula, $\underline{u}_F(\vec{x})$ is proportional to the Fourier transform of the field incident on the lens [31]:

$$\underline{u}_F(\vec{x}) = \frac{\exp\left[j\frac{\pi}{\lambda f}|\vec{x}|^2\right]}{j\lambda f}\int \mathrm{d}\vec{\eta}\,\underline{U}(\vec{\eta})\,P(\vec{\eta})\,\exp\left[-j\frac{2\pi}{\lambda}\vec{\eta}\cdot\vec{x}\right], \tag{40}$$

where f is the focal length of the lens, $U(\vec{\eta})$ is the field incident on the lens at a point located by $\vec{\eta}$, $P(\vec{\eta})$ is the lens pupil function defined by:

$$P(\vec{\eta}) = \begin{cases} 1 & \text{if } |\vec{\eta}| \le R_F \\ 0 & \text{otherwise} \end{cases}, \tag{41}$$

and the integration is taken to be over all space. Thus, $\langle i_F(\vec{x})\rangle$ is calculated as:

$$\langle i_F(\vec{x})\rangle = \frac{1}{(\lambda f)^2}\int \mathrm{d}\vec{\eta}\int \mathrm{d}\vec{\eta}\,'\,\langle \underline{U}(\vec{\eta})\underline{U}^*(\vec{\eta}\,')\rangle\,P(\vec{\eta})P^*(\vec{\eta}\,')\exp\left[-j\frac{2\pi}{\lambda}(\vec{\eta}-\vec{\eta}\,')\cdot\vec{x}\right]. \tag{42}$$

Due to the construction of the interferometer, $\underline{U}(\vec{\eta})$ is the superposition of fields from aperture 1 and aperture 2, $\underline{U}_1(\vec{\eta})$ and $\underline{U}_2(\vec{\eta})$, respectively:

$$\underline{U}(\vec{\eta}) = \underline{U}_1(\vec{\eta}) + \underline{U}_2(\vec{\eta})\exp\left(j\frac{2\pi}{\lambda}h\right), \tag{43}$$

where the exponential term accounts for the optical phase resulting from the path difference h. Suppose there is a turbulence-induced phase associated with each aperture, designated ϕ_{o1} for propagation from a source object o to aperture 1, and ϕ_{o2}, for propagation from source object o to aperture 2. In this case, according to Eq. (20), the expression for $\underline{U}(\vec{\eta})$

in Eq. (43) may be expanded as:

$$\underline{U}(\vec{\eta}) = \hat{\underline{U}}_{o1}(\vec{\eta}) \exp[j\phi_{o1}(\vec{\eta})] + \hat{\underline{U}}_{o2}(\vec{\eta}) \exp[j\phi_{o2}(\vec{\eta})] \exp\left(j\frac{2\pi}{\lambda}h\right), \tag{44}$$

where $\hat{\underline{U}}_{o1}(\vec{\eta})$ and $\hat{\underline{U}}_{o2}(\vec{\eta})$ are the fields associated with free-space propagation from the source object to aperture 1 and aperture 2, respectively. Substituting Eq. (44) into Eq. (42) and assuming that the unaberrated field is independent of the turbulence-induced phase results in the following expression for $\langle i_F(\vec{x})\rangle$:

$$\begin{aligned}
\langle i_F(\vec{x})\rangle \;=\; & \frac{1}{(\lambda f)^2}\int \mathrm{d}\vec{\eta}\int \mathrm{d}\vec{\eta}\,' P(\vec{\eta})P^*(\vec{\eta}\,') \exp\left[-j\frac{2\pi}{\lambda}(\vec{\eta}-\vec{\eta}\,')\cdot\vec{x}\right] \\
& \times \left\{ \begin{array}{l}
\left\langle \hat{\underline{U}}_{o1}(\vec{\eta})\hat{\underline{U}}^*_{o1}(\vec{\eta}\,')\right\rangle \exp\left\{-\frac{1}{2}\left\langle[\phi_{o1}(\vec{\eta})-\phi_{o1}(\vec{\eta}\,')]^2\right\rangle\right\} \\
+\left\langle \hat{\underline{U}}_{o2}(\vec{\eta})\hat{\underline{U}}^*_{o2}(\vec{\eta}\,')\right\rangle \exp\left\{-\frac{1}{2}\left\langle[\phi_{o2}(\vec{\eta})-\phi_{o2}(\vec{\eta}\,')]^2\right\rangle\right\} \\
+\left\langle \hat{\underline{U}}_{o1}(\vec{\eta})\hat{\underline{U}}^*_{o2}(\vec{\eta}\,')\right\rangle \exp\left\{-\frac{1}{2}\left\langle[\phi_{o1}(\vec{\eta})-\phi_{o2}(\vec{\eta}\,')]^2\right\rangle\right\} \exp\left(-j\frac{2\pi}{\lambda}h\right) \\
+\left\langle \hat{\underline{U}}_{o2}(\vec{\eta})\hat{\underline{U}}^*_{o1}(\vec{\eta}\,')\right\rangle \exp\left\{-\frac{1}{2}\left\langle[\phi_{o2}(\vec{\eta})-\phi_{o1}(\vec{\eta}\,')]^2\right\rangle\right\} \exp\left(j\frac{2\pi}{\lambda}h\right),
\end{array} \right.
\end{aligned} \tag{45}$$

where the zero-mean Gaussian nature of the turbulence-induced phase has been used to simplify the expected value of the exponential terms [20]; that is, for example:

$$\langle \exp\{j[\phi_{o1}(\vec{\eta})-\phi_{o1}(\vec{\eta}\,')]\}\rangle = \exp\left\{-\frac{1}{2}\left\langle[\phi_{o1}(\vec{\eta})-\phi_{o1}(\vec{\eta}\,')]^2\right\rangle\right\}. \tag{46}$$

The expression in Eq. (45) can be simplified if the aperture-specific field and phase quantities are expressed as field and phase quantities in the plane of the baseline apertures, with the vector arguments scaled by the ratio R/R_F to account for the effect of the collimating lens, and referencing all vector arguments to the center of aperture 1:

$$\hat{\underline{U}}_o\left(\frac{R}{R_F}\vec{\eta}\right) = \hat{\underline{U}}_{o1}(\vec{\eta}) \quad \text{and} \quad \phi_o\left(\frac{R}{R_F}\vec{\eta}\right) = \phi_{o1}(\vec{\eta}), \tag{47}$$

$$\hat{\underline{U}}_o\left(\frac{R}{R_F}\vec{\eta}+\vec{s}\right) = \hat{\underline{U}}_{o2}(\vec{\eta}) \quad \text{and} \quad \phi_o\left(\frac{R}{R_F}\vec{\eta}+\vec{s}\right) = \phi_{o2}(\vec{\eta}). \tag{48}$$

Employing the definition of the mutual intensity [32] of the unaberrated fields, designated $\hat{\underline{J}}_o$, and definition of the structure function of turbulence-induced phase D_{ϕ_o} for wide-sense

stationary statistics:

$$\hat{\underline{J}}_o(\vec{r}_1 - \vec{r}_2) \equiv \left\langle \hat{\underline{U}}_o(\vec{r}_1)\hat{\underline{U}}_o^*(\vec{r}_2)\right\rangle, \tag{49}$$

$$D_{\phi_o}(\vec{r}_1 - \vec{r}_2) \equiv \langle[\phi_o(\vec{r}_1) - \phi_o(\vec{r}_2)]^2\rangle, \tag{50}$$

then Eq. (45) can be rewritten as:

$$\begin{aligned}\langle i_F(\vec{x})\rangle = \frac{1}{(\lambda f)^2}\int \mathrm{d}\vec{\eta}\int \mathrm{d}\vec{\eta}\,' P(\vec{\eta})P^*(\vec{\eta}\,')\exp\left[-j\frac{2\pi}{\lambda}(\vec{\eta}-\vec{\eta}\,')\cdot\vec{x}\right] \\ \times\left\{\begin{array}{l} 2\hat{\underline{J}}_o\left[\frac{R}{R_F}(\vec{\eta}-\vec{\eta}\,')\right]\exp\left\{-\frac{1}{2}D_{\phi_o}\left[\frac{R}{R_F}(\vec{\eta}-\vec{\eta}\,')\right]\right\} \\ +\hat{\underline{J}}_o\left[\frac{R}{R_F}(\vec{\eta}-\vec{\eta}\,')-\vec{s}\right]\exp\left\{-\frac{1}{2}D_{\phi_o}\left[\frac{R}{R_F}(\vec{\eta}-\vec{\eta}\,')-\vec{s}\right]\right\}\exp\left(-j\frac{2\pi}{\lambda}h\right) \\ +\hat{\underline{J}}_o\left[\frac{R}{R_F}(\vec{\eta}-\vec{\eta}\,')+\vec{s}\right]\exp\left\{-\frac{1}{2}D_{\phi_o}\left[\frac{R}{R_F}(\vec{\eta}-\vec{\eta}\,')+\vec{s}\right]\right\}\exp\left(j\frac{2\pi}{\lambda}h\right). \end{array}\right.\end{aligned} \tag{51}$$

At this point, using the variable transformation $\Delta\vec{\eta} = \vec{\eta} - \vec{\eta}'$ and $\Sigma\vec{\eta} = (\vec{\eta}+\vec{\eta}')/2$, Eq. (51) is rewritten as:

$$\begin{aligned}\langle i_F(\vec{x})\rangle = \frac{1}{(\lambda f)^2}\int \mathrm{d}\Delta\vec{\eta}\;\mathcal{P}(\Delta\vec{\eta})\;\exp\left[-j\frac{2\pi}{\lambda}\Delta\vec{\eta}\cdot\vec{x}\right] \\ \times\left\{\begin{array}{l} 2\hat{\underline{J}}_o\left[\frac{R}{R_F}\Delta\vec{\eta}\right]\exp\left\{-\frac{1}{2}D_{\phi_o}\left[\frac{R}{R_F}\Delta\vec{\eta}\right]\right\} \\ +\hat{\underline{J}}_o\left[\frac{R}{R_F}\Delta\vec{\eta}-\vec{s}\right]\exp\left\{-\frac{1}{2}D_{\phi_o}\left[\frac{R}{R_F}\Delta\vec{\eta}-\vec{s}\right]\right\}\exp\left(-j\frac{2\pi}{\lambda}h\right) \\ +\hat{\underline{J}}_o\left[\frac{R}{R_F}\Delta\vec{\eta}+\vec{s}\right]\exp\left\{-\frac{1}{2}D_{\phi_o}\left[\frac{R}{R_F}\Delta\vec{\eta}+\vec{s}\right]\right\}\exp\left(j\frac{2\pi}{\lambda}h\right), \end{array}\right.\end{aligned} \tag{52}$$

where $\mathcal{P}(\Delta\vec{\eta})$ is the autocorrelation of the pupil function, defined as:

$$\mathcal{P}(\Delta\vec{\eta}) \equiv \int \mathrm{d}\Sigma\vec{\eta}\;P(\Sigma\vec{\eta}+\Delta\vec{\eta}/2)P^*(\Sigma\vec{\eta}-\Delta\vec{\eta}/2). \tag{53}$$

By the definition of $\hat{\underline{J}}_o$ for wide-sense stationary fields [Eq. (49)], the following conjugate symmetry relationship holds:

$$\hat{\underline{J}}_o\left[\frac{R}{R_F}\Delta\vec{\eta}-\vec{s}\right] = \hat{\underline{J}}_o^*\left[-\frac{R}{R_F}\Delta\vec{\eta}+\vec{s}\right]. \tag{54}$$

Assuming isotropic phase statistics, the phase structure function is independent of the direction of field-point separation:

$$D_{\phi_o}\left[\frac{R}{R_F}\Delta\vec{\eta}-\vec{s}\right]=D_{\phi_o}\left[-\frac{R}{R_F}\Delta\vec{\eta}+\vec{s}\right]. \tag{55}$$

Thus, recognizing that the limits on $\Delta\vec{\eta}$ are symmetric with respect to $\Delta\vec{\eta}=0$, the expression for $\langle i_F(\vec{x})\rangle$ in Eq. (52) can be rewritten as:

$$\begin{aligned}\langle i_F(\vec{x})\rangle \;=\; & \frac{2}{(\lambda f)^2}\int \mathrm{d}\Delta\vec{\eta}\;\mathcal{P}(\Delta\vec{\eta})\;\exp\left[-j\frac{2\pi}{\lambda}\Delta\vec{\eta}\cdot\vec{x}\right] \\ & \times\left\{\begin{array}{l}\hat{\underline{\mathrm{J}}}_o\left[\frac{R}{R_F}\Delta\vec{\eta}\right]\exp\left\{-\frac{1}{2}D_{\phi_o}\left[\frac{R}{R_F}\Delta\vec{\eta}\right]\right\} \\ +\left|\hat{\underline{\mathrm{J}}}_o\left[\frac{R}{R_F}\Delta\vec{\eta}+\vec{s}\right]\right|\cos\left(\frac{2\pi}{\lambda}h+\psi'\right)\exp\left\{-\frac{1}{2}D_{\phi_o}\left[\frac{R}{R_F}\Delta\vec{\eta}+\vec{s}\right]\right\},\end{array}\right.\end{aligned} \tag{56}$$

where ψ' is defined as:

$$\psi' \equiv \arg\left\{\hat{\underline{\mathrm{J}}}_o\left[\frac{R}{R_F}\Delta\vec{\eta}+\vec{s}\right]\right\}. \tag{57}$$

In the considerations which follow, Eq. (56) will serve as a basis for quantifying turbulence degradation in optical systems.

2.2.5.1 Imaging systems. The performance of a conventional imaging system is obtained from Eq. (56), given three important considerations. First, an imaging system is unaffected by any phase aberration which is uniform over the extent of the aperture, since the only effect of this phase is to introduce a time delay in the image formation process. Thus, the turbulence-induced phase relevant to imaging analysis is obtained by subtracting a uniform phase shift from the actual phase. This phase is referred to as the piston-removed phase [68]. Secondly, the quantity $\left|\hat{\underline{\mathrm{J}}}_o\left[\frac{R}{R_F}\Delta\vec{\eta}+\vec{s}\right]\right|$ must be set to zero in Eq. (56), since the field is not sampled beyond the physical extent of the aperture in a single-aperture system. Finally, due to conservation of energy, the irradiance in a single-aperture system is half of $\langle i_F(\vec{x})\rangle$ for two apertures. Hence, the long exposure irradiance on the focal plane of an imaging system, $I(\vec{x})$ is given by:

$$I(\vec{x}) = \frac{1}{(\lambda f)^2} \int \mathrm{d}\Delta\vec{\eta}\ \mathcal{P}(\Delta\vec{\eta})\ \exp\left[-j\frac{2\pi}{\lambda}\Delta\vec{\eta}\cdot\vec{x}\right] \hat{\underline{\mathrm{J}}}_o\left[\frac{R}{R_F}\Delta\vec{\eta}\right] \times \exp\left\{-\frac{1}{2}D_{\phi_o}\left[\frac{R}{R_F}\Delta\vec{\eta}\right]\right\}, \tag{58}$$

where D_{ϕ_o} is implicitly the structure function of the piston-removed phase (for a single-aperture system this is identical to the structure function of the piston-included phase).

Imaging performance is quantified by the Strehl ratio (SR), defined as the ratio of the irradiance with aberrations present divided by the diffraction-limited irradiance on the optical axis [9]:

$$\mathrm{SR} \equiv \frac{I(\vec{x}=0)}{\hat{I}(\vec{x}=0)}, \tag{59}$$

where $\hat{I}(\vec{x}=0)$ is obtained from Eq. (58) by setting $D_{\phi_o}=0$. For a distant point source, $\hat{\underline{\mathrm{J}}}_o$ is a constant [32], and SR is given by:

$$\mathrm{SR} = \frac{\int \mathrm{d}\Delta\vec{\eta}\ \mathcal{P}(\Delta\vec{\eta})\ \exp\left\{-\frac{1}{2}D_{\phi_o}\left[\frac{R}{R_F}\Delta\vec{\eta}\right]\right\}}{\int \mathrm{d}\Delta\vec{\eta}\ \mathcal{P}(\Delta\vec{\eta})}. \tag{60}$$

Since the phase variance is a stationary quantity, the phase structure function is given explicitly as:

$$D_{\phi_o}\left[\frac{R}{R_F}\Delta\vec{\eta}\right] = 2\left\langle\phi_o^2(\vec{r})\right\rangle - 2\left\langle\phi_o(\vec{r})\phi_o\left(\vec{r}+\frac{R}{R_F}\Delta\vec{\eta}\right)\right\rangle, \tag{61}$$

and SR can be written as:

$$\mathrm{SR} = \exp\left[-\left\langle\phi_o^2(\vec{r})\right\rangle\right] \frac{\int \mathrm{d}\Delta\vec{\eta}\ \mathcal{P}(\Delta\vec{\eta})\ \exp\left[\left\langle\phi_o(\vec{r})\phi_o\left(\vec{r}+\frac{R}{R_F}\Delta\vec{\eta}\right)\right\rangle\right]}{\int \mathrm{d}\Delta\vec{\eta}\ \mathcal{P}(\Delta\vec{\eta})}. \tag{62}$$

A lower bound on SR is obtained from Eq. (62) by setting $\left\langle\phi_o(\vec{r})\phi_o\left(\vec{r}+\frac{R}{R_F}\Delta\vec{\eta}\right)\right\rangle$ to zero [70, 71] so that:

$$\mathrm{SR} \geq \exp\left[-\left\langle\phi_o^2(\vec{r})\right\rangle\right]. \tag{63}$$

It is convenient to express Eq. (63) in terms of the aperture-averaged phase variance, ε^2, defined as:

$$\varepsilon^2 = \int \mathrm{d}\vec{\rho}\, W(\vec{\rho}) \left\langle \phi_o^2(R\vec{\rho}) \right\rangle , \tag{64}$$

where $\vec{\rho}$ represents a normalized aperture vector whose magnitude is 1 along the circumference of aperture 1, $W(\vec{\rho})$ is the uniform aperture weighting function given by:

$$W(\vec{\rho}) = \begin{cases} \frac{1}{\pi} & \text{if } |\vec{\rho}| \leq 1 \\ 0 & \text{otherwise} \end{cases} , \tag{65}$$

and the integration is over all space. Since $\langle \phi_o^2(\vec{r}) \rangle$ is constant over the extent of the aperture, and $\int \mathrm{d}\vec{\rho}\, W(\vec{\rho}) = 1$, then without loss of generality, it may be said that $\varepsilon^2 = \langle \phi_o^2(\vec{r}) \rangle$, and the lower bound on the Strehl ratio is expressed as:

$$\mathrm{SR} \geq \exp(-\varepsilon^2). \tag{66}$$

Thus, as $\varepsilon^2 \to 0$, $\mathrm{SR} \to 1$, and the long-exposure irradiance on the optical axis approaches the diffraction-limited irradiance.

2.2.5.2 Beam-projection systems. As discussed previously, beam-projection applications employ the same optical system as imaging applications. In fact, a beam-projection system may be thought of as an imaging system run backwards, as indicated in Figure 5. In the case of an imaging system, light propagates from a distant source and is focused onto a detector. In a beam-projection system, light propagates from a laser source, and is focused onto a distant target. The key difference between these applications lies in where the turbulence-induced phase is acquired along the optical path. In the imaging application, the phase is induced before entering the optical system. In a beam-projection application, the phase is induced after exiting the optical system. Thus, the analysis presented previously for imaging system performance may not be applied directly to a beam-projection system.

Quantification of the effects of turbulence on system performance, however, is related for both imaging and beam projection systems. Lukin has rigorously shown [49] that at

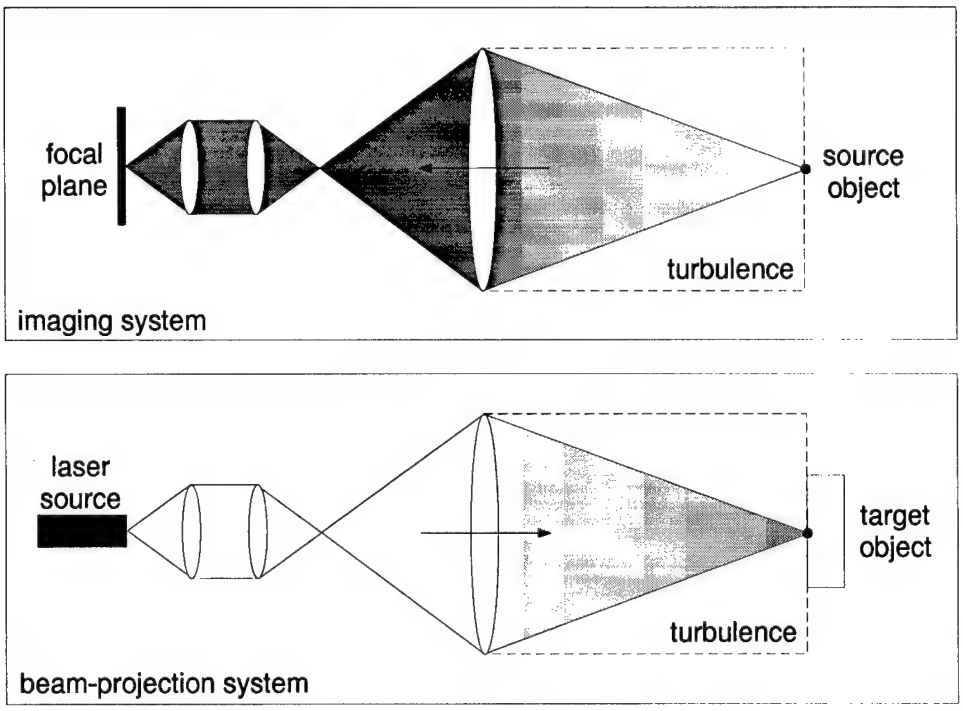

Figure 5. Conventional optical systems for imaging (top) and beam-projection applications (bottom). Arrows indicate the direction of light propagation. Shading notionally shows the relative amount of phase induced by propagation through turbulence.

a given time, the phase induced by propagation from an aperture to a target object is conjugate to the phase induced by propagation from a source to the aperture. In the notation used here, this implies that $\phi_{1o} = -\phi_{o1}$. If it is assumed that most of the phase is induced near the aperture, then the long-exposure irradiance at the target object will be given by Eq. (58), with f replaced by the range of the target object. Even if the turbulence is concentrated a considerable distance along the propagation path, a Fourier-transform relationship exits between the field at that point and the field at the focal point which is similar to Eq. (40), but with scaled arguments [31]. Thus, the analysis of the long-exposure irradiance at the target object can be carried out as for the imaging system, and will yield the same lower bound for the Strehl ratio. Hence, Eq. 66 can also be used to quantify the effect of turbulence-induced phase in a beam-projection system.

2.2.5.3 Interferometric systems. The performance of an interferometric system can be derived directly from Eq. (56), considering that for interferometric applications, it is not necessary to spatially resolve the irradiance on the focal plane. Instead, the long-exposure irradiance is integrated over the extent of a single-element detector, yielding the integrated irradiance I given by:

$$I = \int \mathrm{d}\vec{x}\ \langle i_F(\vec{x}) \rangle \tag{67}$$

Substituting Eq. (56) into Eq. (67) and exchanging the order of integration yields the following expression for I:

$$\begin{aligned} I \;=\; & \frac{2}{(\lambda f)^2} \int \mathrm{d}\Delta\vec{\eta}\ \mathcal{P}(\Delta\vec{\eta}) \left\{ \int \mathrm{d}\vec{x}\ \exp\left[-j\frac{2\pi}{\lambda} \Delta\vec{\eta} \cdot \vec{x} \right] \right\} \\ & \times \left\{ \begin{array}{l} \hat{\underline{\mathrm{J}}}_o \left[\frac{R}{R_F} \Delta\vec{\eta} \right] \exp\left\{ -\frac{1}{2} D_{\phi_o} \left[\frac{R}{R_F} \Delta\vec{\eta} \right] \right\} \\ + \left| \hat{\underline{\mathrm{J}}}_o \left[\frac{R}{R_F} \Delta\vec{\eta} + \vec{s} \right] \right| \cos\left(\frac{2\pi}{\lambda} h + \psi' \right) \exp\left\{ -\frac{1}{2} D_{\phi_o} \left[\frac{R}{R_F} \Delta\vec{\eta} + \vec{s} \right] \right\}, \end{array} \right. \end{aligned} \tag{68}$$

Performing the integration over $\vec{x}$ yields a Dirac delta function, which makes the integration over $\Delta\vec{\eta}$ trivial, resulting in the following expression for I:

$$I = I_0 \left\{ 1 + |\hat{\mu}_o(\vec{s})| \cos\left(\frac{2\pi}{\lambda} h + \psi \right) \exp\left[-\frac{1}{2} D_{\phi_o}(\vec{s}) \right] \right\}, \tag{69}$$

where $I_0 \equiv 2(\lambda f)^{-1} \mathcal{P}(0) \hat{\underline{\mathrm{J}}}_o(0)$, the magnitude of the normalized mutual intensity $|\hat{\mu}_o(\vec{s})| \equiv |\hat{\underline{\mathrm{J}}}_o(\vec{s})| / \hat{\underline{\mathrm{J}}}_o(0)$, and $\psi = \arg[\hat{\underline{\mathrm{J}}}_o(\vec{s})]$. Hence, at a fixed baseline $\vec{s}$, I is modulated sinusoidally as the path difference h is varied. This intensity modulation is commonly referred to as the *fringe*. Using measurements of the irradiance modulation, the fringe visibility V is calculated as [32]:

$$V \equiv \frac{\max(I) - \min(I)}{\max(I) + \min(I)}. \tag{70}$$

Using Eq. (69), Eq. (70) implies that V is given by:

$$V = |\hat{\mu}_o(\vec{s})| \exp\left[-\frac{1}{2} D_{\phi_o}(\vec{s}) \right], \tag{71}$$

which says that the fringe visibility for long-exposure irradiance measurements in an interferometer is determined by the magnitude of the normalized mutual intensity and by the value of the phase structure function, both evaluated at the baseline separation $\vec{s}$. If turbulence effects are negligible, then $D_{\phi_o} \rightarrow 0$, and the fringe visibility for free-space propagation is given by $\hat{V} = |\hat{\mu}_o(\vec{s})|$. In analogy with the Strehl ratio definition of Eq. (59), the fringe Strehl ratio (FSR) may be defined as:

$$\text{FSR} \equiv \frac{V}{\hat{V}} = \exp\left[-\frac{1}{2} D_{\phi_o}(\vec{s})\right]. \tag{72}$$

As indicated in Eq. (72), the effect of turbulence-induced phase aberrations in an interferometric system is to reduce fringe visibility beyond what would be expected if aberrations were not present in the system.

Since the apertures are separated by $\vec{s}$, then $D_{\phi_o}(\vec{s})$ can be calculated by measuring the phase in each aperture at corresponding (but otherwise arbitrary) locations:

$$D_{\phi_o}(\vec{s}) = \left\langle [\phi_{o1}(\vec{r}) - \phi_{o2}(\vec{r})]^2 \right\rangle. \tag{73}$$

Consider the aperture-averaged differential-phase variance δ^2 defined as:

$$\delta^2 \equiv \int \mathrm{d}\vec{\rho}\, W(\vec{\rho}) \left\langle [\phi_{o1}(R\vec{\rho}) - \phi_{o2}(R\vec{\rho})]^2 \right\rangle. \tag{74}$$

Since $\langle [\phi_{o1}(R\vec{\rho}) - \phi_{o2}(R\vec{\rho})]^2 \rangle$ is a spatially-stationary quantity, then:

$$\begin{aligned} \delta^2 &= \left\langle [\phi_{o1}(R\vec{\rho}) - \phi_{o2}(R\vec{\rho})]^2 \right\rangle \int \mathrm{d}\vec{\rho}\, W(\vec{\rho}) \\ &= \left\langle [\phi_{o1}(R\vec{\rho}) - \phi_{o2}(R\vec{\rho})]^2 \right\rangle \\ &= D_{\phi_o}(\vec{s}). \end{aligned} \tag{75}$$

Hence, the fringe Strehl ratio may be written as:

$$\text{FSR} = \exp\left(-\frac{1}{2}\,\delta^2\right). \tag{76}$$

Thus, as $\delta^2 \rightarrow 0$, then FSR $\rightarrow 1$, and the performance of an interferometric system approaches that which is expected for free-space propagation.

2.3 Adaptive-optical systems

In Section 2.2, it was shown that the effect of turbulence-induced phase is to degrade optical system performance. The performance degradation is dependent upon the aperture-averaged phase variance (differential phase variance for interferometric systems). Reducing the phase variance will enhance the performance of the system. To reduce the phase variance, the turbulence-induced phase must be compensated. An adaptive optics system removes phase aberrations through reflection from a surface which is phase-conjugate to the incident wave-front. The resulting wave-front is (ideally) planar, and the performance of the optical system is restored to its diffraction limit [69].

2.3.1 System components and description. Adaptive-optical compensation requires that the turbulence-induced phase can be sensed, and that the sensed phase can be removed by a suitable device. The schematic diagram in Figure 6 depicts a typical AO system. In this configuration, the compensating device is a deformable mirror (DM). Upon reflection from the mirror, light passes through a beam splitter. Part of the light is focused onto the focal plane of the system, while the other part is passed onto the wave-front sensor (WFS), which measures the turbulence-induced phase. Reconstructed phase from the WFS is used to drive the mechanical actuators of the DM. As depicted in Figure 6, the system is closed-loop, with the WFS measuring the residual phase after partial conjugation by the DM.

There are two main types of wave-front sensors used in AO systems. These two types are referred to as Hartmann wave-front sensors and shearing interferometers [68]. While the instrumentation used for these two WFS types is different, both are sensitive to the local gradient of the turbulence-induced phase. Thus, measurements from either type of instrument can be employed in a similar manner.

There are also two main types of deformable mirrors. Deformable mirrors are generally classified as being either segmented or continuous. A segmented mirror is made up

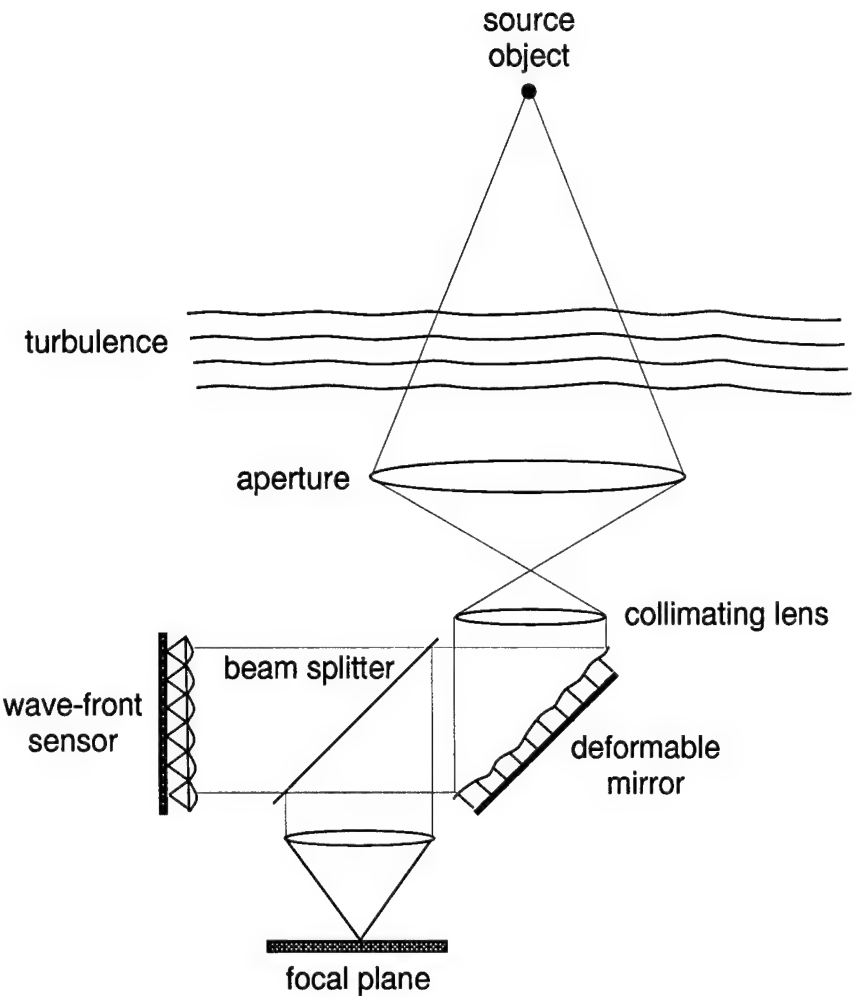

Figure 6. Typical adaptive optics system. The turbulence-induced phase is measured by the wave-front sensor, and the conjugate phase is placed on the deformable mirror. When the deformable mirror is placed before the wave-front sensor as shown here, the system is closed-loop, and the wave-front sensor detects the residual phase after partial conjugation by the deformable mirror.

of an array of closely-spaced, individually controlled mirror segments that are driven by mechanical actuators. Continuous deformable mirrors have a continuous reflective surface called a face plate that can be pushed or pulled from behind by mechanical actuators to form a surface which is phase-conjugate to the incident wave-front.

2.3.2 Natural-guide-star adaptive optics. Ideally, the object of interest will be bright enough so that an accurate phase measurement can be obtained by the AO system. If this is not the case, then another source must be employed. Often, a naturally-occurring nearby star is used, and is referred to as a natural guide star or natural beacon. Because the maximum permissible angular separation between the object of interest and the NGS at visible wavelengths is a few arc-seconds, the probability of acquiring a NGS of sufficient brightness at a particular region in the sky is small [27]. Therefore, NGS adaptive optics may only be used when imaging bright objects or when the object of interest is near a sufficiently bright source. Nonetheless, a NGS is often used for wave-front tilt compensation, since the maximum angular separation is larger for wave-front tilt than for higher-order phase components [71].

2.3.3 Laser-guide-star adaptive optics. To overcome the sky coverage limitations imposed on NGS adaptive optics, an artificial beacon or laser guide star is used for adaptive-optical imaging. The use of a LGS in adaptive optics was first suggested in the open literature by Foy and Labeyrie in 1985 [18]. The LGS is formed by projecting a focused laser beam into the atmosphere [25, 56, 80], where a beacon is formed by scattering or resonance processes in certain atmospheric layers. The optical system used to transmit the beam into the atmosphere is usually the same as the system used to receive the beacon light. Since the transmitting and receiving apertures are the same, the LGS application is referred to as *monostatic*. If different apertures are used for transmitting and receiving, then the LGS application is referred to as *bistatic*. The design of AO systems employing laser guide stars has been studied in detail [27].

Laser guide star applications are classified by the processes involved in beacon formation. Rayleigh beacons are formed by Rayleigh scattering from air molecules at altitudes from 10 km to 30 km. Sodium (Na) beacons are formed by the resonance fluorescence of

sodium atoms in the mesosphere [27] at an altitude of approximately 90 km. The performance of AO systems employing either Rayleigh or Na beacons depends upon many factors, most notably laser power requirements and anisoplanatism [93].

As was originally pointed out by Pilkington [55], the LGS cannot directly provide for tilt compensation. When the LGS beacon is formed, the angular deflection of the beam due to turbulence results in a spatial displacement of the beacon which preserves the tilt induced on the upward path. All higher-order aberrations are not preserved in this process. Since the beacon light propagates back to the system aperture along the same path as the upward propagation, the preserved wave-front tilt is naturally conjugated. The result is a null tilt measurement with only higher-order aberrations present in the LGS signal. This effect has been referred to in the literature as *beam reciprocity* [5–7]. Due to the lack of tilt information, the LGS signal is conventionally used only for higher-order wave-front compensation [23] with a nearby NGS providing the tilt correction [24].

2.3.4 Zernike modal compensation of phase aberrations. The turbulence-induced phase that has been discussed in the preceding sections varies randomly in space and time. In order to characterize the spatial variation of the phase at a given time, it is useful to decompose the phase with respect to a set of basis functions. Since the relevant quantity is the phase within a circular aperture, Zernike polynomials are an appropriate basis set [9]. Zernike polynomials, designated $Z_i(\vec{\rho})$, are defined on a circle of unit radius, with the normalized polar vector $\vec{\rho}$ specifying a location in the plane of the circle. The subscript i designates a particular Zernike mode. In this research, we follow the ordering convention of Noll [54], where each subscript i designates an ordered pair (n_i, m_i), specifying the radial and azimuthal order of the polynomial. With this ordering scheme, the orthonormality of the basis set can be written as:

$$\int \mathrm{d}\vec{\rho}\, W(\vec{\rho}) Z_i(\vec{\rho}) Z_j(\vec{\rho}) = \delta_{ij}, \tag{77}$$

where δ_{ij} is the Kronecker delta and $W(\vec{\rho})$ is the aperture weighting function given in Eq. (65).

Using Noll's ordering method, the Zernike polynomials are defined as:

$$Z_i(\rho,\theta) = \sqrt{n_i+1}\, R_{n_i}^{m_i}(\rho)\sqrt{2}\cos m_i\theta,\ i \text{ even},\ m_i \neq 0 \tag{78}$$

$$Z_i(\rho,\theta) = \sqrt{n_i+1}\, R_{n_i}^{m_i}(\rho)\sqrt{2}\sin m_i\theta,\ i \text{ odd},\ m_i \neq 0 \tag{79}$$

$$Z_i(\rho,\theta) = \sqrt{n_i+1}\, R_{n_i}^{0}(\rho),\ m_i = 0, \tag{80}$$

where the radial function $R_{n_i}^{m_i}(\rho)$ is given by:

$$R_{n_i}^{m_i}(\rho) = \sum_{q=0}^{(n_i-m_i)/2} \frac{(-1)^q (n_i-q)!}{q![(n_i+m_i)/2-q]![(n_i-m_i)/2-q]!}\rho^{n_i-2q}. \tag{81}$$

The values of n_i and m_i are always integers and satisfy $m_i \leq n_i$, $n_i - |m_i| =$ even. The Zernike polynomials through Noll's order $i = 21$ along with the corresponding values of n_i and m_i are listed in Table 2.

With the Zernike polynomials as a basis set, the turbulence-induced phase from the object of interest in an aperture of radius R may be expanded as follows:

$$\phi_o(R\vec{\rho}) = \sum_i a_{oi} Z_i(\vec{\rho}), \tag{82}$$

where a_{oi} is the coefficient obtained by projection of the phase onto the ith Zernike polynomial:

$$a_{oi} = \int \mathrm{d}\vec{\rho}\, W(\vec{\rho})\phi_o(R\vec{\rho})Z_i(\vec{\rho}). \tag{83}$$

In addition to being a complete set on the unit circle, the low-order Zernike polynomials correspond to classic fixed aberrations in optical systems. For instance, $Z_1(\vec{\rho})$ represents a piston aberration. The orthogonal components of tilt (x-tilt and y-tilt respectively), are represented by $Z_2(\vec{\rho})$ and $Z_3(\vec{\rho})$. Of the higher-order polynomials, $Z_4(\vec{\rho})$ represents defocus, $Z_5(\vec{\rho})$ and $Z_6(\vec{\rho})$ represent orthogonal components of astigmatism, $Z_7(\vec{\rho})$ and $Z_8(\vec{\rho})$ represent orthogonal components of coma, and $Z_{11}(\vec{\rho})$ represents spherical aberration. The corresponding coefficients a_{oi} indicate the amount of each type of aberration present in the turbulence-induced phase. Graphical representations of several low-order Zernike polynomials are shown in Figure 7. From the definition of a_{oi} in Eq. (83), it is clear that since

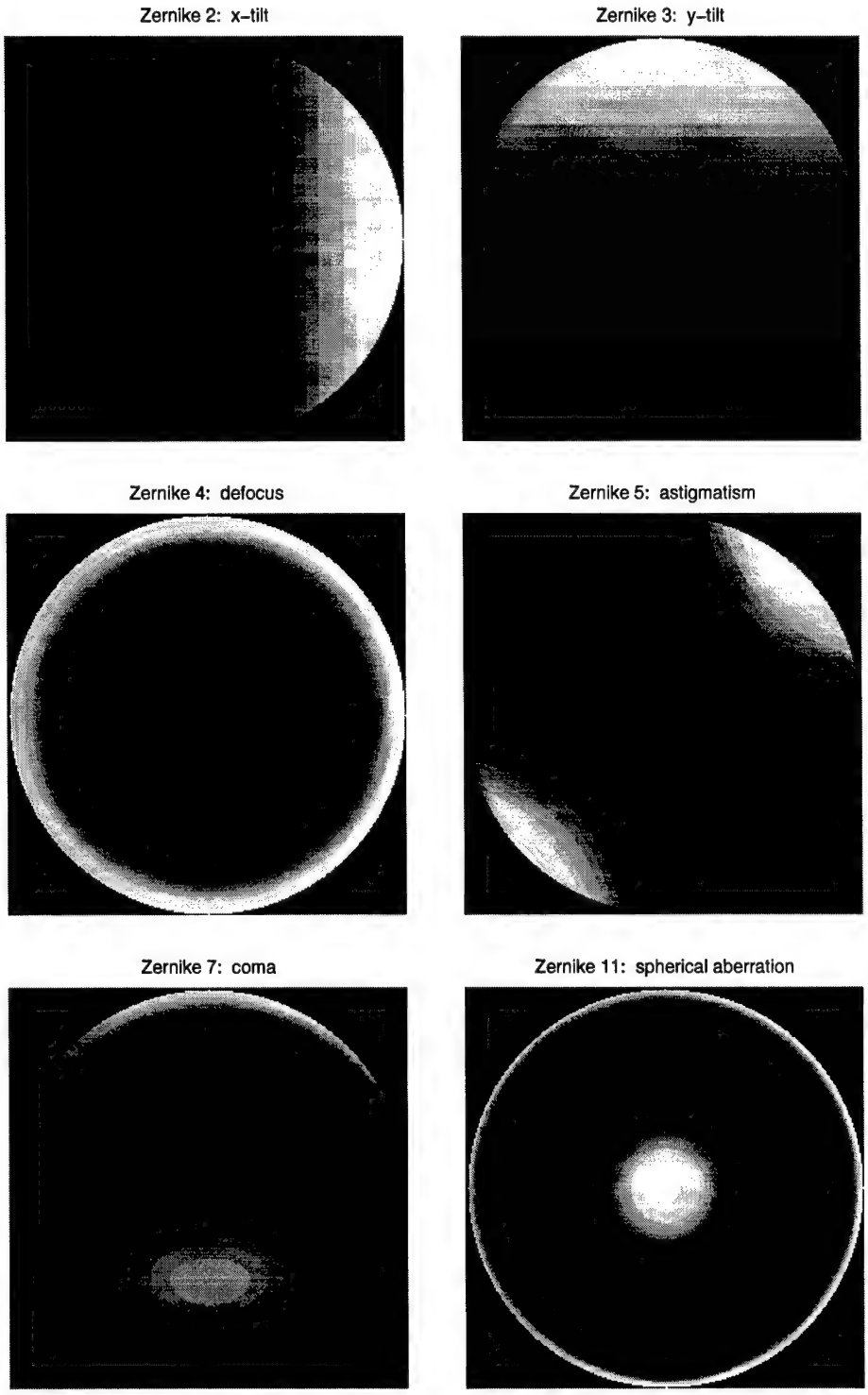

Figure 7. Graphical representations of low-order Zernike polynomials. Light areas correspond to the highest values of $Z_i(\vec{\rho})$, dark areas correspond to the lowest.

Noll's order i	radial order n_i	azimuthal order m_i	Zernike polynomial $Z_i(\rho,\theta)$
1	0	0	1
2	1	1	$2\rho\cos\theta$
3	1	1	$2\rho\sin\theta$
4	2	0	$3.464\rho^2 - 1.732$
5	2	2	$2.449\rho^2\sin 2\theta$
6	2	2	$2.449\rho^2\cos 2\theta$
7	3	1	$(8.485\rho^3 - 5.657\rho)\sin\theta$
8	3	1	$(8.485\rho^3 - 5.657\rho)\cos\theta$
9	3	3	$2.828\rho^3\sin 3\theta$
10	3	3	$2.828\rho^3\cos 3\theta$
11	4	0	$3.416\rho^4 - 13.416\rho^2 + 2.236$
12	4	2	$(12.649\rho^4 - 9.487\rho^2)\cos 2\theta$
13	4	2	$(12.649\rho^4 - 9.487\rho^2)\sin 2\theta$
14	4	4	$3.162\rho^4\cos 4\theta$
15	4	4	$3.162\rho^4\sin 4\theta$
16	5	1	$(34.641\rho^5 - 41.569\rho^3 + 10.392\rho)\cos\theta$
17	5	1	$(34.641\rho^5 - 41.569\rho^3 + 10.392\rho)\sin\theta$
18	5	3	$(17.321\rho^5 - 13.856\rho^3)\cos 3\theta$
19	5	3	$(17.321\rho^5 - 13.856\rho^3)\sin 3\theta$
20	5	5	$3.464\rho^5\cos 5\theta$
21	5	5	$3.464\rho^5\sin 5\theta$

Table 2. Zernike polynomials through Noll's order $i = 21$. The radial and azimuthal orders of the ith polynomial are specified by the ordered pair (n_i, m_i).

ϕ_o is zero-mean Gaussian, a_{oi} must also be zero-mean Gaussian.

The Zernike phase expansion technique has been used extensively in the analysis of atmospheric turbulence [38, 54, 63], and is often referred to as *modal analysis*. Modal analysis has been applied to wave-front correction in adaptive-optical systems, since the effects of modal compensation are related directly to the statistical properties of the Zernike expansion coefficients [14,92]. To see this, consider the effect of applying a conjugate phase $\tilde{\phi}_o$ to the deformable mirror in an AO system, for $\tilde{\phi}_o$ represented by a finite series of modal components through order N:

$$\tilde{\phi}_o(R\vec{\rho}) = \sum_{i=2}^{N} \tilde{a}_{oi} Z_i(\vec{\rho}), \tag{84}$$

where $\tilde{a}_{oi}$ is the ith Zernike coefficient of the conjugate phase. Thus, the Nth order aperture-averaged residual phase variance ε_N^2 is calculated according to the definition of ε^2 given in Eq. (64), with ϕ_o replaced by $\phi_o - \tilde{\phi}_o$:

$$\begin{aligned}\varepsilon_N^2 &= \int \mathrm{d}\vec{\rho}\, W(\vec{\rho}) \left\langle \left[\phi_o(R\vec{\rho}) - \tilde{\phi}_o(R\vec{\rho})\right]^2 \right\rangle \\ &= \int \mathrm{d}\vec{\rho}\, W(\vec{\rho}) \left\langle \left[\phi_o(R\vec{\rho}) - \sum_{i=2}^{N} \tilde{a}_{oi} Z_i(\vec{\rho})\right]^2 \right\rangle . \end{aligned} \tag{85}$$

By employing the orthonormality property of the Zernike polynomials on the unit circle [Eq. (77)], ε_N^2 may be expressed as:

$$\varepsilon_N^2 = \int \mathrm{d}\vec{\rho}\, W(\vec{\rho}) \left\langle \phi_o^2(R\vec{\rho}) \right\rangle - \sum_{i=2}^{N} \left\langle a_{oi}^2 \right\rangle + \sum_{i=2}^{N} \left\langle (a_{oi} - \tilde{a}_{oi})^2 \right\rangle . \tag{86}$$

In an ideal AO system, $\tilde{a}_{oi} = a_{oi}$, and the third term of Eq. (86) is zero, such that:

$$\varepsilon_N^2 = \int \mathrm{d}\vec{\rho}\, W(\vec{\rho}) \left\langle \phi_o^2(R\vec{\rho}) \right\rangle - \sum_{i=2}^{N} \left\langle a_{oi}^2 \right\rangle . \tag{87}$$

Thus, the aperture-averaged phase variance is reduced by the sum of the modal phase coefficient variances $\langle a_{oi}^2 \rangle$ through Nth order. Since $\langle a_{oi}^2 \rangle$ is a positive quantity for all i, then ε_N^2 always decreases with increasing N.

For Kolmogorov turbulence, the aperture-averaged piston-removed phase variance for an astronomical source object is given by [54]:

$$\int \mathrm{d}\vec{\rho}\, W(\vec{\rho}) \left\langle \phi_o^2(R\vec{\rho}) \right\rangle = 1.0299 \left(\frac{D}{r_0}\right)^{5/3} . \tag{88}$$

The Kolmogorov modal covariance of a_{oi} and a_{oj}, designated $\langle a_{oi} a_{oj} \rangle$, is zero for $(i-j)$ odd, and for $(i-j)$ even is given by [54, 92]:

$$\begin{aligned}\langle a_{oi} a_{oj} \rangle &= 0.0072 \left(\frac{D}{r_0}\right)^{5/3} (-1)^{(n_i+n_j-2m_i)/2} [(n_i+1)(n_j+1)]^{1/2} \pi^{8/3} \delta_{m_i m_j} \\ &\quad \times \frac{\Gamma(14/3)\Gamma[(n_i+n_j-5/3)/2]}{\Gamma[(n_i-n_j+17/3)/2]\Gamma[(n_j-n_i+17/3)/2]\Gamma[(n_i+n_j+23/3)/2]} . \end{aligned} \tag{89}$$

Table 3 shows the value of $\langle a_{oi} a_{oj} \rangle (D/r_0)^{-5/3}$ for $i, j = 2-10$. Using Eq. (88) and Eq. (89),

	2	3	4	5	6	7	8	9	10
2	0.448	0	0	0	0	0	-0.014	0	0
3	0	0.448	0	0	0	-0.014	0	0	0
4	0	0	0.023	0	0	0	0	0	0
5	0	0	0	0.023	0	0	0	0	0
6	0	0	0	0	0.023	0	0	0	0
7	0	-0.014	0	0	0	0.006	0	0	0
8	-0.014	0	0	0	0	0	0.006	0	0
9	0	0	0	0	0	0	0	0.006	0
10	0	0	0	0	0	0	0	0	0.006

Table 3. Covariance matrix of low-order Zernike coefficients. Table shows the value of $\langle a_{oi} a_{oj} \rangle (D/r_0)^{-5/3}$ for $i, j = 2 - 10$, with rows representing i, columns representing j.

ε_N^2 for an ideal AO system can be computed from Eq. (87). For an imaging system, Strehl performance is determined by replacing ε^2 with ε_N^2 in Eq. (66). Thus, for Nth-order compensation, SR is determined by:

$$\text{SR} \geq \exp(-\varepsilon_N^2). \tag{90}$$

Since ε_N^2 is proportional to $(D/r_0)^{5/3}$ for all N, the value of the relative aperture diameter D/r_0 will determine the Strehl performance of an imaging system for a given order of modal compensation. Figure 8 shows the Strehl ratio improvement as a function of compensation order N for $D/r_0 = 5, 10, 15, 20, 25, 30$, beginning with $N = 2$, and continuing through $N = 105$ (all modes with $n_i \leq 13$). As is shown in Figure 8, without AO compensation, SR is near zero for all values of D/r_0 considered. For $D/r_0 = 5$, nearly diffraction-limited performance can be achieved by an ideal AO system with modal compensation through $N = 15$. For $D/r_0 = 30$, however, SR is appreciably greater than zero only for $N \geq 25$. Thus, the order of modal compensation required in an ideal AO system for nearly diffraction-limited performance depends upon the size of the system aperture, relative to the atmospheric coherence diameter.

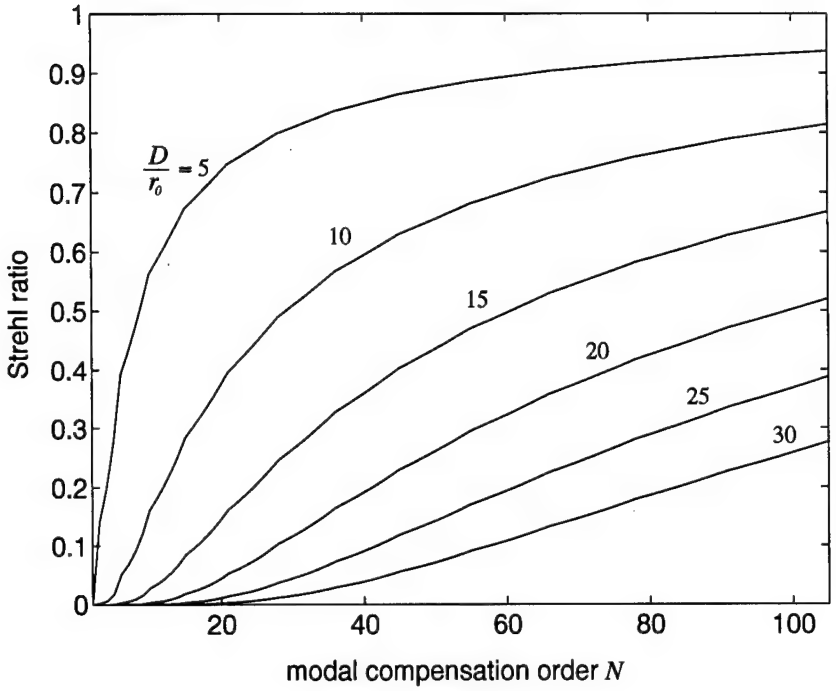

Figure 8. Effect of modal compensation order N on Strehl ratio for the relative aperture diameter D/r_0.

2.4 Anisoplanatism in adaptive optics

As was mentioned in Section 2.3, an ideal adaptive optics system uses light from the object under observation for wave-front sensing, and compensation performance is given by the results shown in Figure 8. When a source other than the object being observed is employed in wave-front sensing, however, compensation performance is degraded. This effect is referred to as *anisoplanatism.* As it applies to adaptive optics, the term "anisoplanatism" is borrowed from the terminology for fixed optical systems, where the isoplanatic region is defined as that region in which the imaging system point spread function can be considered translation invariant [9]. Anisoplanatism in adaptive-optical systems implies that the point spread function of the fixed optical system plus the atmosphere is not translation invariant [45]. As pointed out by Fried [21], the term "anisoplanatism" refers to a variety of effects brought on by the stochastic nature of atmospheric turbulence.

In an AO system, anisoplanatism occurs when the turbulence-induced phase measured by the WFS does not match the turbulence-induced phase incident in the compensation aperture from the object of interest. This occurs whenever light from the WFS beacon and the object sample different volumes of turbulence. Anisoplanatic effects are present if there is a spatial separation between the object and beacon, a spatial separation between the wave-front-sensing aperture and the wave-front-compensation aperture, or when time delays in the system cause the beacon phase and the object phase to be only partially correlated due to atmospheric winds or motion of the system components. Therefore, in adaptive optics, anisoplanatism is a spatial and temporal effect present in every system to some degree.

Conventionally, anisoplanatic effects are classified into two types: angular and focal anisoplanatism. Angular anisoplanatism arises when the beacon has an angular displacement θ_b in the field of view from the object being imaged, as is depicted in Figure 9. One of the principle advantages of the LGS over the NGS is that it can be positioned anywhere in the field of view. Thus, the angular separation between the beacon and object may be taken to zero. In this case, an AO system may still suffer from focal anisoplanatism, as the beacon is located at a lower altitude than the object. Hence, light from the object passes through more turbulent atmosphere than the light coming from the beacon. An example of focal anisoplanatism in an AO system is shown in Figure 9.

Fried quantified the general effects of angular anisoplanatism on fixed imaging and beam-projection systems and characterized the magnitude of the angular anisoplanatic effect by the parameter θ_0, which is referred to as the isoplanatic patch [22] or isoplanatic angle, and is calculated as:

$$\theta_0 \equiv \left[2.905 \left(\frac{2\pi}{\lambda} \right)^2 \int_0^L dz \, C_n^2(z) \, z^{5/3} \right]^{-3/5}, \tag{91}$$

For the HV-21 profile in Table 1, $\theta_0 \simeq 7$ μrad (1.4 arcsec). Since the HV-21 profile yields $r_0 = 5$ cm and $\theta_0 = 7$ μrad, the HV-21 profile is often referred to as $\mathrm{HV}_{5/7}$. Fried defined the isoplanatic angle such that for $\theta_b = \theta_0$, the aperture-averaged residual phase variance is 1 rad^2, which implies that SR $\simeq 0.4$. Fried's definition of θ_0 has been shown to be a

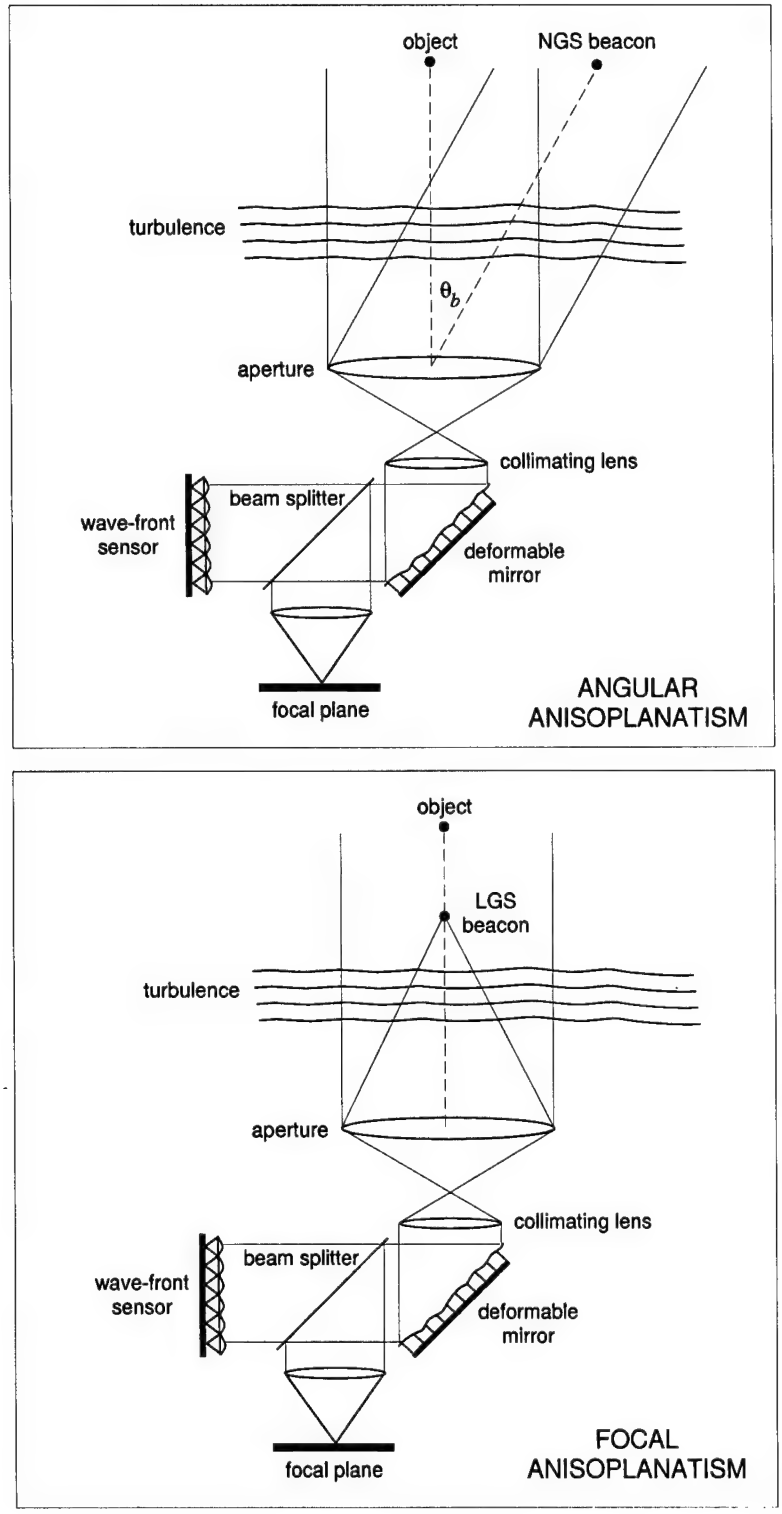

Figure 9. Examples of angular and focal anisoplanatism in an adaptive optics system.

pessimistic indicator of AO system performance, as it includes the effect of the piston phase component in quantifying the isoplanatic angle [74]. Since imaging system performance is insensitive to piston phase, actual angular anisoplanatic degradation is less severe than predicted by Fried's analysis. Further analysis efforts have explored the degrading effects of various forms of spatial and temporal anisoplanatism on wave-front compensation in adaptive-optical systems [23, 82–84, 87, 93].

Anisoplanatic effects can also be quantified using modal analysis techniques. Over the past several years, many works have been published in which the correlative properties of modal coefficients for various forms of anisoplanatism have been quantified [17, 51, 62, 74, 76, 94]. When examining wave-front compensation, the authors of these studies have used modal correlation calculations in order to compute the aperture-averaged residual phase variance, thus establishing limits for effective compensation when system performance is degraded by turbulence-induced anisoplanatism.

To quantify anisoplanatism in modal compensation, consider the aperture-averaged residual phase variance when the phase from the beacon, designated ϕ_b is used as the conjugate phase. In this case, Eq. (86) is written as:

$$\varepsilon_N^2 = \int \mathrm{d}\vec{\rho}\, W(\vec{\rho}) \left\langle \phi_o^2(R\vec{\rho}) \right\rangle - \sum_{i=2}^{N} \left\langle a_{oi}^2 \right\rangle + \sum_{i=2}^{N} \left\langle (a_{oi} - a_{bi})^2 \right\rangle, \tag{92}$$

where a_{bi} is the ith Zernike coefficient of the beacon phase:

$$a_{bi} \equiv \int \mathrm{d}\vec{\rho}\, W(\vec{\rho}) \phi_b(R\vec{\rho}) Z_i(\vec{\rho}). \tag{93}$$

Since ϕ_b is only partially correlated with ϕ_o, then $a_{bi} \neq a_{oi}$, and $\langle (a_{oi} - a_{bi})^2 \rangle > 0$ for all i. It follows that:

$$\sum_{i=2}^{N} \left\langle (a_{oi} - a_{bi})^2 \right\rangle > 0, \tag{94}$$

and since this term is additive in Eq. (92), ε_N^2 is always increased when anisoplanatism is present in the system, leading to a decreased value for the Strehl ratio.

The expression for ε_N^2 in Eq. 92 may be simplified by expanding the third term to yield:

$$\varepsilon_N^2 = \int \mathrm{d}\vec{\rho}\, W(\vec{\rho}) \left\langle \phi_o^2(R\vec{\rho}) \right\rangle - \sum_{i=2}^{N} \left[2 \left\langle a_{oi} a_{bi} \right\rangle - \left\langle a_{bi}^2 \right\rangle \right]. \tag{95}$$

From Eq. (95), it is apparent that the value of $\langle a_{oi} a_{bi} \rangle$ (the correlation of the object and beacon phase coefficients) determines the magnitude of the anisoplanatic effect. From the analysis methods of Stone et al [74] and Molodij and Rousset [51], ε_N^2 may be quantified according to Eq. 95. The corresponding Strehl ratio is shown in Figure 10 for modal compensation through $N = 6, 10, 15, 21$, with $D/r_0 = 5$ and the HV-21 C_n^2 profile. Figure 10(a) shows the degradation of SR with increasing NGS beacon offset angle, which has been normalized to Fried's isoplanatic angle given in Eq. (91). These results demonstrate that for piston-removed phase, the Strehl ratio may be significantly larger than 0.4 at $\theta_b/\theta_0 = 1$. For modal compensation at a particular NGS offset, anisoplanatism may be partially overcome by increasing the order of correction, N. Figure 10(b) shows the degradation of SR with decreasing LGS altitude due to focal anisoplanatism. As the LGS altitude increases, system performance approaches that of an NGS adaptive optics system with $\theta_b = 0$. Although the Strehl ratio calculation has been performed over the entire range of LGS altitude from 10 km to 100 km, LGS beacons may only be formed over a limited subset of these ranges. Rayleigh beacons can be formed from 10 km to 30 km, whereas sodium beacons are formed near 90 km altitude. The results shown in Figure 10(b) illustrate the advantage of the sodium LGS over the Rayleigh LGS due to decreased focal anisoplanatism.

Although anisoplanatism takes many forms, its effect is universal; that is, turbulence-induced anisoplanatism degrades the performance of an adaptive optics system. While the forms of anisoplanatism are diverse, all forms are quantified by the correlative properties of the turbulence-induced phase. Any AO system in which the phase incident upon the system aperture is only partially correlated with the conjugate phase placed on the deformable mirror will suffer anisoplanatic effects. Therefore, instead of investigating a particular form of anisoplanatism (angular, focal, temporal, etc.) as it applies to a given system, this work concentrates instead on the manifestation of anisoplanatism (broadly defined) in that system, and its effect on system performance.

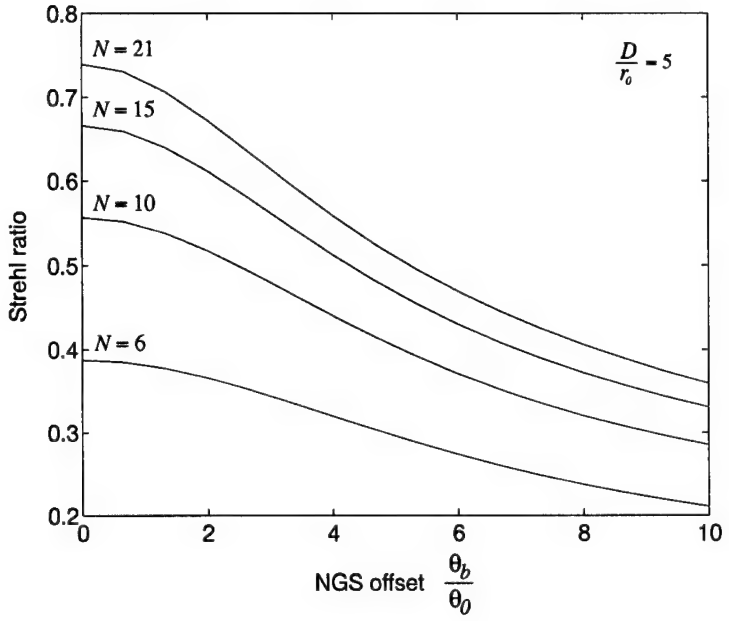

(a)

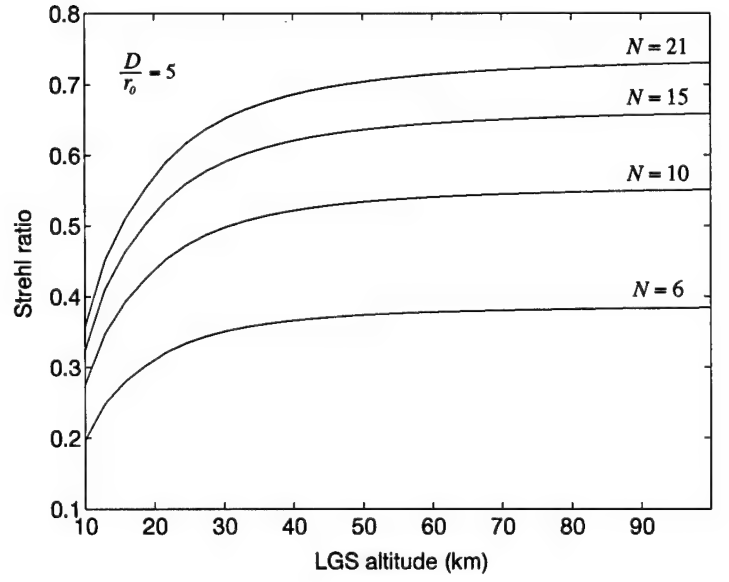

(b)

Figure 10. Degradation of Strehl ratio due to anisoplanatism. (a) Angular anisoplanatism effect on Strehl ratio for normalized NGS beacon offset θ_b/θ_0. (b) Focal anisoplanatism effect on Strehl ratio as LGS beacon altitude increases. Results shown are for modal compensation through $N = 6, 10, 15, 21$, with $D/r_0 = 5$ using the HV-21 C_n^2 profile.

2.5 *Summary*

This chapter provides the background knowledge in atmospheric and adaptive optics necessary to understand the analysis and application chapters which follow. The effects of turbulence in optical systems were discussed, beginning with fundamental considerations regarding the stochastic nature of index of refraction fluctuations in the atmosphere, which is characterized by the spatial PSD $W_{n'}(\vec{k})$. By considering the effect of small perturbations in the index of refraction on wave propagation, it is was shown that a random phase is induced by turbulence as an electromagnetic wave travels through the atmosphere. The stochastic nature of the turbulence-induced phase is also specified by its spatial PSD $W_{\phi}(\vec{k})$, which is calculated directly from $W_{n'}(\vec{k})$. Equivalently, the statistical properties of turbulence-induced phase may be quantified by the phase structure function $D_{\phi}(s)$, which indicates the mean-square difference in phase for points separated by a distance s. It was shown that $D_{\phi}(s)$ scales with the atmospheric coherence diameter r_0, which is used to quantify the magnitude of turbulence effects in optical systems according to the relative aperture diameter D/r_0.

From the basic results of frequency analysis of optical systems, a framework was developed in which turbulence effects in imaging, beam-projection, and interferometric systems can be understood. It was shown that the performance of imaging and beam-projection systems may be quantified by a Strehl ratio (SR), and that SR $\geq \exp(-\varepsilon^2)$, where ε^2 is the aperture-averaged phase variance. For interferometric systems, a fringe Strehl ratio (FSR) was defined, which is given by FSR $\equiv \exp(-\delta^2/2)$, where δ^2 is the aperture-averaged differential phase variance between the baseline apertures.

Adaptive-optical systems were discussed, and the components common to most AO systems were described, reviewing issues related to the use of natural and laser guide stars. The concept of modal compensation in AO systems was presented, illustrating that as D/r_0 increases, higher-order modal compensation is required to maintain system performance. The performance of an AO system is also degraded by turbulence-induced anisoplanatism. For NGS adaptive optics, angular anisoplanatism reduces the Strehl ratio with increasing angular separation between the beacon and the object of interest. For LGS adaptive optics, focal anisoplanatism reduces the Strehl ratio as the beacon altitude is decreased.

In modal compensation applications, anisoplanatism requires higher-order correction in order to maintain performance. Anisoplanatism affects all non-ideal AO systems to some degree, since it arises whenever the phase from the object of interest and the conjugate phase placed on the deformable mirror are only partially correlated. In the context of modal analysis, anisoplanatic effects are quantified by the correlation of beacon and object phase coefficients.

III. Optimal Compensation for Anisoplanatic Systems

3.1 Introduction

This chapter builds upon the background in atmospheric and adaptive optics presented in Chapter II through an in-depth analysis of atmospheric compensation in AO systems degraded by turbulence-induced anisoplanatism. This analysis begins in Section 3.2 by considering the compensation performance of an adaptive-optical interferometric system. Results obtained by considering this system are also applicable to imaging and beam-projection systems. When anisoplanatism is present in an interferometric system, compensation performance is shown to be degraded from the limiting performance of an ideal system. Using optimal compensation, part of the performance degradation may be recovered. In order to construct the optimal estimator of conjugate phase, the modal correlation of object and beacon wave-front phase must be quantified. An analysis geometry is introduced in Section 3.3 to model the most general form of anisoplanatism required for imaging, beam-projection, and interferometric system analysis. For this generalized geometry, the cross-correlation of the object and beacon wave-front phase coefficients is calculated. The resulting cross-correlation expression is then validated by comparison with published theoretical results and by reduction and analysis of laboratory phase measurements. The chapter is summarized in Section 3.4.

3.2 Optimal modal compensation in adaptive optics

The discussion of atmospheric compensation in Chapter II focused on the performance of an ideal AO system, demonstrating how performance is degraded when anisoplanatism is present. Anisoplanatism causes beacon phase coefficients to be only partially correlated with the phase coefficients for the object of interest. As a result, the residual phase after wave-front correction is increased, resulting in reduced system performance. If the correlation of object and beacon phase coefficients can be quantified for the form of anisoplanatism present in the system, then optimal estimation theory [43] can be applied to the wave-front compensation problem. In the context of optimal estimation theory, beacon phase measurements are not used directly, but rather the wave-front correction applied to

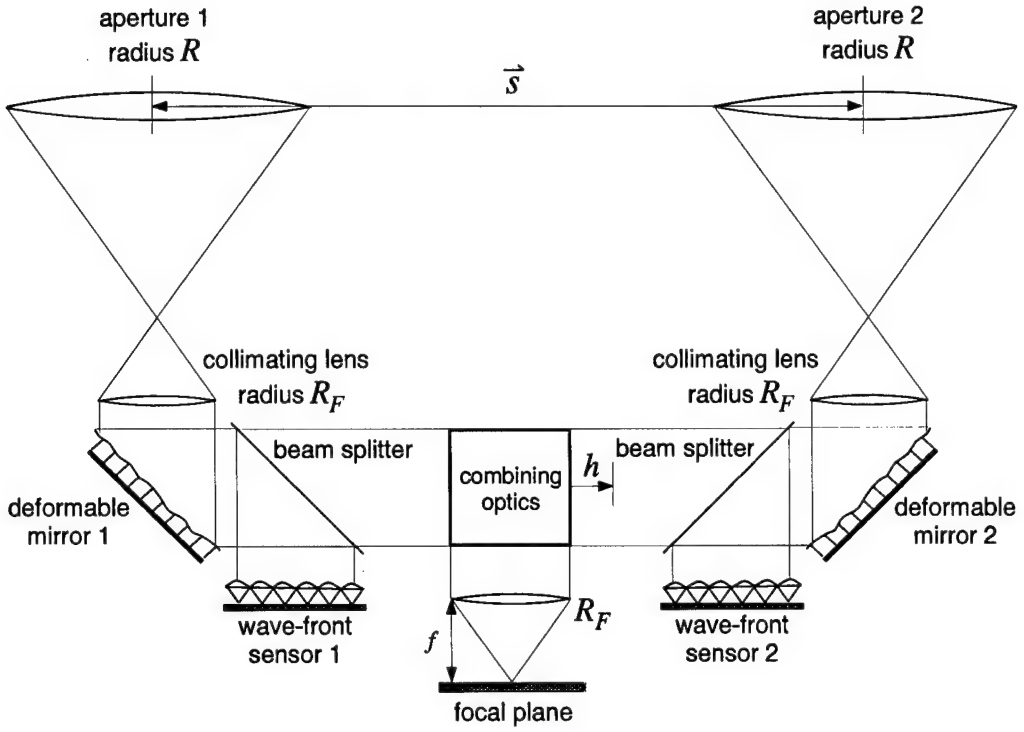

Figure 11. Schematic diagram of an AO system for an optical interferometer. If all system components associated with aperture 2 are removed, the remaining components represent a conventional AO system for imaging and beam-projection applications.

the DM is estimated from the beacon phase measurements, given the correlation of the beacon and object phase. The result is a partial recovery of the performance degradation due to anisoplanatism.

3.2.1 Wave-front compensation performance. The analysis of compensation performance for anisoplanatism in AO systems in the context of optimal estimation theory proceeds in parallel with the optical system performance analysis of Subsection 2.2.5. Here, we consider the effect of wave-front compensation applied to light incident in each aperture of an optical interferometer, as shown in Figure 11. Again, if all system components associated with aperture 2 are removed, the remaining components represent a conventional AO system for imaging and beam-projection applications.

As was shown in Chapter II, the performance of the interferometric system depends upon the aperture-averaged differential phase variance δ^2. For modal compensation through order N, the aperture-averaged residual differential phase variance, designated δ_N^2 is calculated from Eq. (74) as:

$$\begin{aligned}\delta_N^2 &= \int \mathrm{d}\vec{\rho}\, W(\vec{\rho}) \left\langle [\phi_{o1}(R\vec{\rho}) - \phi_{o2}(R\vec{\rho})]^2 \right\rangle - \sum_{i=2}^{N} \left\langle (\Delta a_{oi})^2 \right\rangle \\ &\quad + \sum_{i=2}^{N} \left\langle [\Delta a_{oi} - \Delta \tilde{a}_{oi}]^2 \right\rangle, \end{aligned} \tag{96}$$

where Δa_{oi} and $\Delta \tilde{a}_{oi}$ are defined as the difference in Zernike phase coefficients between aperture 1 and aperture 2 for the object and conjugate phase, respectively:

$$\Delta a_{oi} \equiv a_{o1i} - a_{o2i}, \tag{97}$$

$$\Delta \tilde{a}_{oi} \equiv \tilde{a}_{o1i} - \tilde{a}_{o2i}. \tag{98}$$

In the definition of Δa_{oi} and $\Delta \tilde{a}_{oi}$, a_{o1i} and a_{o2i} are the object phase coefficients in each aperture, whereas $\tilde{a}_{o1i}$ and $\tilde{a}_{o2i}$ are the conjugate phase coefficients applied to DM 1 and DM 2, respectively. Note that the form of δ_N^2 in Eq. (96) is the same as ε_N^2 in Eq. (86) with ϕ_o replaced by $(\phi_{o1} - \phi_{o2})$, a_{oi} replaced by Δa_{oi}, and $\tilde{a}_{oi}$ replaced by $\Delta \tilde{a}_{oi}$. Thus, by use of Eq. (76), for Nth order atmospheric compensation in an interferometer, the fringe Strehl ratio is given by:

$$\mathrm{FSR} = \exp\left(-\frac{1}{2}\,\delta_N^2\right). \tag{99}$$

The goal of an AO system is to maximize the optical performance, which, according to Eq. (99), is equivalent to minimizing δ_N^2. Considering the form of Eq. (96), δ_N^2 is minimized whenever $\langle [\Delta a_{oi} - \Delta \tilde{a}_{oi}]^2 \rangle$ is minimized for all i. For an ideal AO system, $\Delta \tilde{a}_{oi} \to \Delta a_{oi}$ for all i, and therefore $\langle [\Delta a_{oi} - \Delta \tilde{a}_{oi}]^2 \rangle \to 0$. Thus, in an ideal AO system, δ_N^2 reaches its limiting value given by:

$$\lim_{\Delta \tilde{a}_{oi} \to \Delta a_{oi}} \delta_N^2 = \int \mathrm{d}\vec{\rho}\, W(\vec{\rho}) \left\langle [\phi_{o1}(R\vec{\rho}) - \phi_{o2}(R\vec{\rho})]^2 \right\rangle - \sum_{i=2}^{N} \left\langle (\Delta a_{oi})^2 \right\rangle. \tag{100}$$

For a non-ideal AO system, the differential compensation $\Delta\tilde{a}_{oi}$ will not generally be equal to the differential phase coefficient Δa_{oi}, and δ_N^2 will be larger than the limiting value given in Eq. (100).

If optimal modal wave-front compensation is defined as that correction corresponding to a minimization of δ_N^2, then the optimality criterion is to minimize $\langle[\Delta a_{oi} - \Delta\tilde{a}_{oi}]^2\rangle$ for all i. Put another way, we must find $\Delta\hat{a}_{oi}$ such that $\langle(\Delta a_{oi} - \Delta\hat{a}_{oi})^2\rangle$ is minimized. Thus, setting $\Delta\tilde{a}_{oi} = \Delta\hat{a}_{oi}$ provides optimal wave-front compensation. The optimality criterion of minimizing $\langle(\Delta a_{oi} - \Delta\hat{a}_{oi})^2\rangle$ corresponds to developing the minimum-mean-square-error (MMSE) estimator [43] of Δa_{oi}. The MMSE estimate $\Delta\hat{a}_{oi}$ is an estimate based upon some measured data that is related statistically to Δa_{oi}. The form of the estimator and the minimal value of $\langle(\Delta a_{oi} - \Delta\hat{a}_{oi})^2\rangle$ are determined completely by the statistical relationship between Δa_{oi} and the data used to estimate that differential phase coefficient.

As discussed in Chapter II, for a typical modal compensation scheme, measured coefficients from the AO beacon are applied directly in the wave-front correction. In our notation, this is to say that:

$$\Delta\tilde{a}_{bi} = a_{b1i} - a_{b2i}, \tag{101}$$

where a_{b1i} and a_{b2i} are the modal coefficients of order i for the beacon phase in aperture 1 and aperture 2, respectively. Due to anisoplanatism, Δa_{oi} and Δa_{bi} will only be partially correlated, and the MMSE estimate $\Delta\hat{a}_{oi}$ will not, in general, be equal to Δa_{bi}. Thus, the use of Δa_{bi} directly for wave-front compensation will not minimize δ_N^2 for any order of modal correction. This implies that the wave-front compensation can be optimized only by estimating coefficients Δa_{oi} given measurements Δa_{bi}, not by using the measurements directly as the conjugate phase. This fact has been pointed out previously by Valley and Wandzura [88] and explored in-depth by Whiteley et al. [96] in the case of single aperture systems, a special case of the more-general analysis presented here.

3.2.2 Minimum-mean-square-error (MMSE) estimation. In this subsection, the form of the modal differential coefficient estimates $\Delta\hat{a}_{oi}$ which optimize the wave-front compensation is developed. Here, we define the column vector $\mathbf{y}$ whose components are the differential modal coefficients associated with the object of interest of order 1 through

N:

$$\mathbf{y} = \begin{bmatrix} \Delta a_{o1} \\ \Delta a_{o2} \\ \Delta a_{o3} \\ \vdots \\ \Delta a_{oN} \end{bmatrix} = \begin{bmatrix} a_{o11} - a_{o21} \\ a_{o12} - a_{o22} \\ a_{o13} - a_{o23} \\ \vdots \\ a_{o1N} - a_{o2N} \end{bmatrix}. \tag{102}$$

The MMSE estimate of $\mathbf{y}$, designated $\hat{\mathbf{y}}$,is the column vector whose components are the MMSE estimates of the differential modal coefficients:

$$\hat{\mathbf{y}} = \begin{bmatrix} \Delta \hat{a}_{o1} \\ \Delta \hat{a}_{o2} \\ \Delta \hat{a}_{o3} \\ \vdots \\ \Delta \hat{a}_{oN} \end{bmatrix}. \tag{103}$$

The vector $\mathbf{x}$ is composed of the corresponding beacon differential phase coefficient measurements:

$$\mathbf{x} = \begin{bmatrix} \Delta a_{b1} \\ \Delta a_{b2} \\ \Delta a_{b3} \\ \vdots \\ \Delta a_{bN} \end{bmatrix} = \begin{bmatrix} a_{b11} - a_{b21} \\ a_{b12} - a_{b22} \\ a_{b13} - a_{b23} \\ \vdots \\ a_{b1N} - a_{b2N} \end{bmatrix}. \tag{104}$$

Given the measurement vector $\mathbf{x}$, we can form the MMSE estimator of $\mathbf{y}$ [43]. The estimate $\hat{\mathbf{y}}$ is the conditional expectation given the measurement vector $\mathbf{x}$:

$$\hat{\mathbf{y}} = \langle \mathbf{y} | \mathbf{x} \rangle , \tag{105}$$

where the expectation is with respect to the posterior probability density function $p(\mathbf{y}|\mathbf{x})$. In order to construct the MMSE estimator of $\mathbf{y}$, the joint PDF of $\mathbf{x}$ and $\mathbf{y}$ must be known. Since the Zernike coefficients of the object and beacon phase are zero-mean Gaussian, and the components of $\mathbf{x}$ and $\mathbf{y}$ are the difference of these coefficients, then $\mathbf{x}$ and $\mathbf{y}$ are also zero-mean and jointly Gaussian [36].

For $\mathbf{x}$ and $\mathbf{y}$ zero-mean and jointly Gaussian, it has been shown [43] that the MMSE estimate of $\mathbf{y}$ is given by:

$$\hat{\mathbf{y}} = C_{yx}C_{xx}^{-1}\mathbf{x}. \tag{106}$$

where C_{yx} and C_{xx} are the covariance matrices of $\mathbf{y}$ with $\mathbf{x}$ and $\mathbf{x}$ with $\mathbf{x}$, respectively, which for zero mean vectors $\mathbf{y}$ and $\mathbf{x}$ are given by:

$$C_{yx} = \langle \mathbf{y}\mathbf{x}^T \rangle, \tag{107}$$

$$C_{xx} = \langle \mathbf{x}\mathbf{x}^T \rangle, \tag{108}$$

where $\mathbf{x^T}$ is the vector transpose of $\mathbf{x}$. The form of the estimator given in Eq. (106) will be used throughout the remainder of this paper. Note that $\hat{\mathbf{y}} = \mathbf{x}$ only if $C_{yx}C_{xx}^{-1} = I$.

The value of δ_N^2 given in Eq. (96) depends upon the choice of conjugate differential phase coefficients $\Delta\tilde{a}_{oi}$. In the case of MMSE estimation, $\Delta\tilde{a}_{oi} = \Delta\hat{a}_{oi}$. These coefficient estimates are the elements of $\hat{\mathbf{y}}$, and minimize the so-called Bayesian mean square error $\langle(\Delta a_{oi} - \Delta\hat{a}_{oi})^2\rangle$ [43]. Accordingly, the summation over i is minimized as well, and may be computed directly as:

$$\sum_{i=1}^{N} \langle(\Delta a_{oi} - \Delta\hat{a}_{oi})^2\rangle = \mathrm{TR}\left[C_{yy} - C_{yx}C_{xx}^{-1}C_{xy}\right]. \tag{109}$$

where TR$[\cdot]$ designates the matrix trace operation C_{yy} is the covariance matrix of $\mathbf{y}$ with $\mathbf{y}$, and C_{xy} is the matrix transpose of C_{yx}.

If the beacon measurements are used directly for wave-front compensation, then $\Delta\tilde{a}_{oi} = \Delta a_{bi}$ in Eq. (96). The differential phase coefficients Δa_{bi} are the elements of $\mathbf{x}$, and will not generally minimize $\langle(\Delta a_{oi} - \Delta a_{bi})^2\rangle$, nor will the summation over i be minimized. However, the summation can be quantified using the same notation as above:

$$\sum_{i=1}^{N} \langle(\Delta a_{oi} - \Delta a_{bi})^2\rangle = \mathrm{TR}\left[C_{yy} + C_{xx} - 2C_{yx}\right]. \tag{110}$$

Using the matrix expression for the MMSE estimator performance given in Eq. (109), δ_N^2 is given by:

$$\text{MMSE: } \delta_N^2 = \int \mathrm{d}\vec{\rho}\, W(\vec{\rho}) \left\langle [\phi_{o1}(R\vec{\rho}) - \phi_{o2}(R\vec{\rho})]^2 \right\rangle - \mathrm{TR}\left[C_{yx} C_{xx}^{-1} C_{xy}\right]. \tag{111}$$

If the measured beacon differential phase coefficients are used, then from Eq. (110), δ_N^2 is given by:

$$\text{measured: } \delta_N^2 = \int \mathrm{d}\vec{\rho}\, W(\vec{\rho}) \left\langle [\phi_{o1}(R\vec{\rho}) - \phi_{o2}(R\vec{\rho})]^2 \right\rangle - \mathrm{TR}\left[2C_{yx} - C_{xx}\right]. \tag{112}$$

The performance of imaging and beam-projection systems is quantified by calculating the aperture-averaged residual phase variance ε_N^2, which is computed from Eq. (111) and Eq. (112) by replacing $(\phi_{o1} - \phi_{o2})$ with ϕ_o, and by setting $a_{o2i}, a_{b2i} = 0$ in the definition of $\mathbf{y}$ and $\mathbf{x}$. In this case, the subscript 1 is dropped from a_{o1i} and a_{b1i}, and the object and beacon phase coefficients are designated a_{oi} and a_{bi}, respectively. Thus, $\Delta a_{oi} = a_{oi}$ and $\Delta a_{bi} = a_{bi}$. In addition, the piston component is excluded in $\mathbf{y}$ and $\mathbf{x}$, and all summations begin with $i = 2$. The form of the MMSE estimator is unchanged, and the optimal modal compensation theory may be applied directly to single-aperture systems.

3.3 Spatial cross-correlation of Zernike coefficients

In the Subsection 3.2.2, the MMSE estimate of the object differential phase coefficients $\mathbf{y}$ given beacon differential phase coefficient measurements $\mathbf{x}$ depended upon the covariance matrices C_{yx} and C_{xx}. Since $y_m = (a_{o1m} - a_{o2m})$ and $x_n = (a_{b1n} - a_{b2n})$, the mn-th element of C_{yx} is given by:

$$\begin{aligned} [C_{yx}]_{mn} &= \langle (a_{o1m} - a_{o2m})(a_{b1n} - a_{b2n}) \rangle \\ &= \langle a_{o1m} a_{b1n} \rangle - \langle a_{o1m} a_{b2n} \rangle - \langle a_{o2m} a_{b1n} \rangle + \langle a_{o2m} a_{b2n} \rangle . \end{aligned} \tag{113}$$

Likewise, since $x_m = (a_{b1m} - a_{b2m})$ and $x_n = (a_{b1n} - a_{b2n})$, the mn-th element of C_{xx} is given by:

$$\begin{aligned}[C_{xx}]_{mn} &= \langle (a_{b1m} - a_{b2m})(a_{b1n} - a_{b2n}) \rangle \\ &= \langle a_{b1m} a_{b1n} \rangle - \langle a_{b1m} a_{b2n} \rangle - \langle a_{b2m} a_{b1n} \rangle + \langle a_{b2m} a_{b2n} \rangle . \end{aligned} \tag{114}$$

Similarly, the matrix elements of C_{yy} correspond to the cross-correlation of the appropriate Zernike coefficients. Thus, in order to compute the matrix elements of the MMSE estimator given in Eq. (106), and to measure compensation performance as specified in Eq. (111) and Eq. (112), the cross-correlation of the appropriate Zernike coefficients must be computed.

3.3.1 Analysis geometry. Evaluation of the covariance matrices C_{yy}, C_{xx}, and C_{yx} involves the calculation of modal cross-correlations which have the following general form:

$$\langle a_{u1i} a_{v2j} \rangle = B_{a_{u1i} a_{v2j}}(\vec{r}_{su}, \vec{r}_{a1}, \vec{r}_{sv}, \vec{r}_{a2}), \tag{115}$$

where $B_{a_{u1i} a_{v2j}}$ represents the spatial cross-correlation of a_{u1i} with a_{v2j} as a function of the optical source locations $\vec{r}_{su}$, $\vec{r}_{sv}$ and the aperture locations $\vec{r}_{a1}$, $\vec{r}_{a2}$. Spatial cross-correlations of this form address all types of anisoplanatism present in imaging, beam-projection, and interferometric systems. Thus, to develop an expression for $B_{a_{u1i} a_{v2j}}$, consider a geometry with two spatially-separated apertures and two spatially-separated sources, as depicted in Figure 12. This geometry shows two apertures of radius R, with locations given by $\vec{r}_{a1}$ and $\vec{r}_{a2}$. The separation of the apertures is designated $\vec{s} \equiv \vec{r}_{a2} - \vec{r}_{a1}$. Two optical sources are located by $\vec{r}_{su}$ and $\vec{r}_{sv}$. The position vectors of the two apertures and the two sources share a fixed coordinate system specified by the unit vectors $\hat{x}$, $\hat{y}$, and $\hat{z}$.

A single turbulent atmospheric layer, parallel to the $\hat{x} - \hat{y}$ plane, is indexed by the subscript l, located by the vector $\vec{z}_l$, and has thickness Δz_l. Light rays propagating from the source to each point in the aperture will intersect the turbulent layer at height z_l, thus defining the projection of each aperture in that layer, as is indicated in Figure 12.

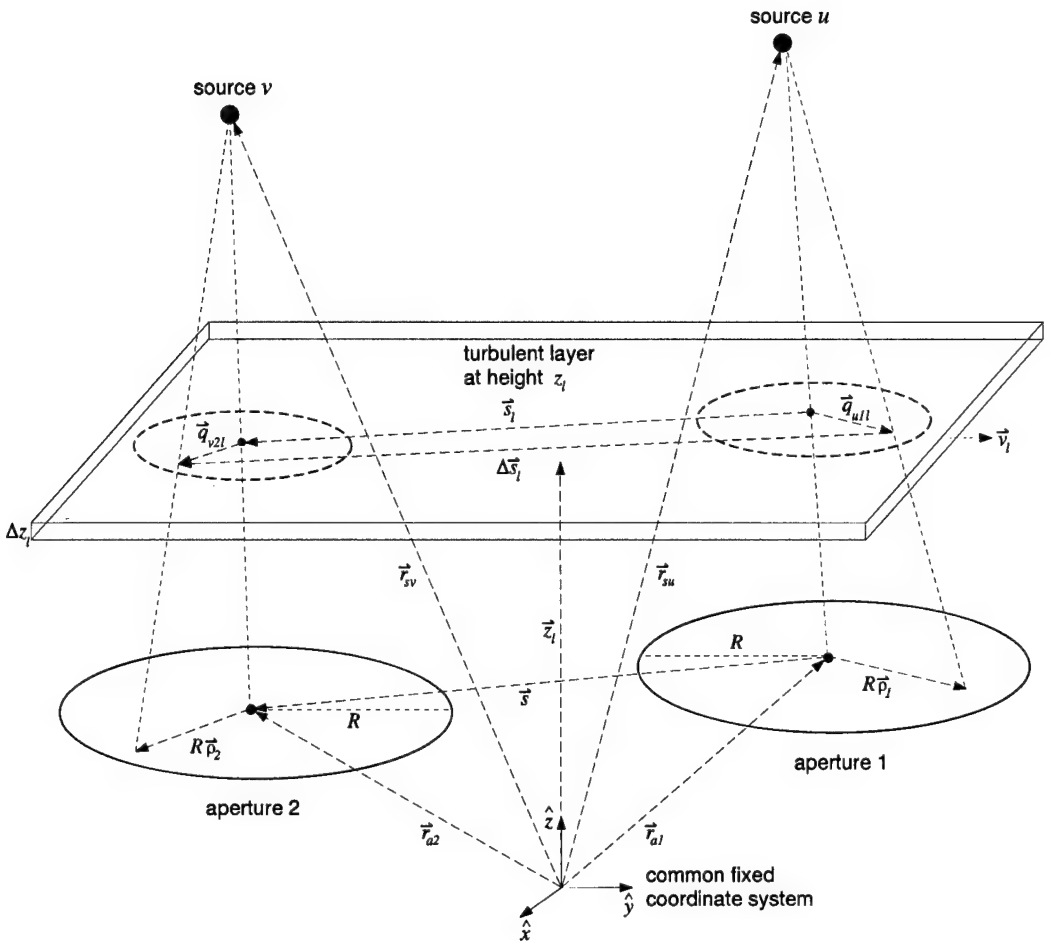

Figure 12. Analysis geometry used for computing the spatial cross-correlation of Zernike expansion coefficients.

Consider the vectors $R\vec{\rho}_1$ and $R\vec{\rho}_2$, which locate points in aperture 1 and aperture 2, respectively, relative to the aperture centers. The projection of $R\vec{\rho}_1$ for source u and the projection of $R\vec{\rho}_2$ for source v into the lth layer are designated by $\vec{q}_{u1l}$ and $\vec{q}_{v2l}$, respectively. The projected aperture vectors $\vec{q}_{u1l}$ and $\vec{q}_{v2l}$ are related to $R\vec{\rho}_1$, $R\vec{\rho}_2$, $\vec{r}_{a1}$, $\vec{r}_{a2}$, $\vec{r}_{su}$, $\vec{r}_{sv}$, and z_l as follows:

$$\vec{q}_{u1l} = (1 - A_{u1l})R\vec{\rho}_1, \tag{116}$$

$$\vec{q}_{v2l} = (1 - A_{v2l})R\vec{\rho}_2, \tag{117}$$

where the layer scaling factors A_{u1l} and A_{v2l} are given by:

$$A_{u1l} = \frac{z_l - (\vec{r}_{a1} \cdot \hat{z})}{(\vec{r}_{su} - \vec{r}_{a1}) \cdot \hat{z}}, \tag{118}$$

$$A_{v2l} = \frac{z_l - (\vec{r}_{a2} \cdot \hat{z})}{(\vec{r}_{sv} - \vec{r}_{a2}) \cdot \hat{z}}. \tag{119}$$

An important quantity in the development of an expression for $B_{a_{u1i}a_{v2j}}$ is the projected separation of the aperture centers in the lth layer, designated $\vec{s}_l$. In terms of the aperture and source position vectors, and the layer scaling factors, $\vec{s}_l$ is given by:

$$\vec{s}_l = \vec{s} + A_{v2l}(\vec{r}_{sv} - \vec{r}_{a2}) - A_{u1l}(\vec{r}_{su} - \vec{r}_{a1}). \tag{120}$$

Another important quantity is the vector separation of the projected aperture vectors in the lth layer, designated $\Delta\vec{s}_l$. As can be seen in figure 12, $\Delta\vec{s}_l$ is related to $\vec{s}_l$, $\vec{q}_{u1l}$, and $\vec{q}_{v2l}$ as follows:

$$\Delta\vec{s}_l = \vec{q}_{v2l} + \vec{s}_l - \vec{q}_{u1l}. \tag{121}$$

If source u is at an infinite range, and source v remains at a finite range, then:

$$A_{u1l} = 0, \tag{122}$$

$$\vec{s}_l = \vec{s} + A_{v2l}(\vec{r}_{sv} - \vec{r}_{a2}) - [z_l - (\vec{r}_{a1} \cdot \hat{z})](\tan\theta_u \cos\phi_u \hat{x} + \tan\theta_u \sin\phi_u \hat{y}), \tag{123}$$

where θ_u is the angular direction of source u with respect to the unit vector normal to aperture 1, and ϕ_u is the angular direction of the source u with respect to $\hat{x}$. Similarly, if source v is at an infinite range, and source u is at a finite range, then:

$$A_{v2l} = 0, \tag{124}$$

$$\vec{s}_l = \vec{s} + [z_l - (\vec{r}_{a2} \cdot \hat{z})](\tan\theta_v \cos\phi_v \hat{x} + \tan\theta_v \sin\phi_v \hat{y}) - A_{u1l}(\vec{r}_{su} - \vec{r}_{a1}), \tag{125}$$

where θ_v is the angular direction of source v with respect to the unit vector normal to aperture 2, and ϕ_v is the angular direction of source v with respect to $\hat{x}$. If source u and source v both lie at an infinite range, then:

$$A_{u1l} = 0, \tag{126}$$

$$A_{v2l} = 0, \tag{127}$$

$$\begin{aligned} \vec{s}_l &= \vec{s} + [z_l - (\vec{r}_{a2} \cdot \hat{z})][(\tan\theta_v \cos\phi_v)\hat{x} + (\tan\theta_v \sin\phi_v)\hat{y}] \\ &\quad -[z_l - (\vec{r}_{a1} \cdot \hat{z})][(\tan\theta_u \cos\phi_u)\hat{x} + (\tan\theta_u \sin\phi_u)\hat{y}]. \end{aligned} \tag{128}$$

3.3.2 Spatial cross-correlation calculation. Using the analysis geometry introduced in Section 3.3.1, we now derive an expression for the spatial cross-correlation of the Zernike expansion coefficients. The optical phase from source u in aperture 1 and the optical phase from source v in aperture 2, designated $\phi_{u1}(R\vec{\rho}_1)$ and $\phi_{v2}(R\vec{\rho}_2)$, respectively, may be expanded with respect to the Zernike polynomials:

$$\phi_{u1}(R\vec{\rho}_1) = \sum_i a_{u1i} Z_i(\vec{\rho}_1), \tag{129}$$

$$\phi_{v2}(R\vec{\rho}_2) = \sum_j a_{v2j} Z_j(\vec{\rho}_2), \tag{130}$$

where a_{u1i} and a_{v2j} are the Zernike coefficient of the phase from source u in aperture 1 of order i and the Zernike coefficient of the phase from source v in aperture 2 of order j, respectively. These coefficients are obtained by projecting the phase onto the corresponding Zernike polynomial as follows:

$$a_{u1i} = \int d\vec{\rho}_1 \, \phi_{u1}(R\vec{\rho}_1) Z_i(\vec{\rho}_1) W(\vec{\rho}_1), \tag{131}$$

$$a_{v2j} = \int d\vec{\rho}_2 \, \phi_{v2}(R\vec{\rho}_2) Z_j(\vec{\rho}_2) W(\vec{\rho}_2), \tag{132}$$

where $W(\vec{\rho})$ is the aperture weighting function defined in Eq. (65).

The spatial cross-correlation of Zernike coefficient a_{u1i} with Zernike coefficient a_{v2j} is given by:

$$B_{a_{u1i}a_{v2j}} = \langle a_{u1i}a_{v2j} \rangle . \tag{133}$$

Substituting Eq. (131) and Eq. (132) into Eq. (133) yields the following:

$$B_{a_{u1i}a_{v2j}} = \left\langle \int \mathrm{d}\vec{\rho}_1 \int \mathrm{d}\vec{\rho}_2 \, \phi_{u1}(R\vec{\rho}_1)\phi_{v2}(R\vec{\rho}_2)Z_i(\vec{\rho}_1)Z_j(\vec{\rho}_2)W(\vec{\rho}_1)W(\vec{\rho}_2) \right\rangle . \tag{134}$$

Since ϕ_{u1} and ϕ_{v2} are the only random quantities in Eq. (134), the expectation operator may be taken inside the integral as follows:

$$B_{a_{u1i}a_{v2j}} = \int \mathrm{d}\vec{\rho}_1 \int \mathrm{d}\vec{\rho}_2 \, \langle \phi_{u1}(R\vec{\rho}_1)\phi_{v2}(R\vec{\rho}_2) \rangle \, Z_i(\vec{\rho}_1)Z_j(\vec{\rho}_2)W(\vec{\rho}_1)W(\vec{\rho}_2). \tag{135}$$

Thus, to evaluate the integral of Eq. (135), $\langle \phi_{u1}(R\vec{\rho}_1)\phi_{v2}(R\vec{\rho}_2) \rangle$ must first be evaluated.

Using a layered atmospheric model, ϕ_{u1} and ϕ_{v2} are expressed as:

$$\phi_{u1}(R\vec{\rho}_1) = \left(\frac{2\pi}{\lambda}\right) \sum_{l_1} \Delta z_{l_1} \, n'_{l_1}(\vec{q}_{u1l_1}) \tag{136}$$

$$\phi_{v2}(R\vec{\rho}_2) = \left(\frac{2\pi}{\lambda}\right) \sum_{l_2} \Delta z_{l_2} \, n'_{l_2}(\vec{q}_{v2l_2}), \tag{137}$$

where Δz_{l_1} and Δz_{l_2} are the thickness of the atmospheric layers indexed by l_1 and l_2, and $n'_{l_1}(\vec{q}_{u1l_1})$ and $n'_{l_2}(\vec{q}_{v2l_2})$ are the index of refraction fluctuations in the layers indexed by l_1 and l_2 at position $\vec{q}_{u1l_1}$ and $\vec{q}_{v2l_2}$, respectively. If the index of refraction fluctuations are uncorrelated layer to layer [61, 68, 81], that is,

$$\langle n'_{l_1}(\vec{q}_{u1l_1})n'_{l_2}(\vec{q}_{v2l_2}) \rangle \propto \delta_{l_1 l_2}, \tag{138}$$

where δ is the Kronecker delta, it follows that:

$$\langle \phi_{u1}(R\vec{\rho}_1)\phi_{v2}(R\vec{\rho}_2) \rangle = \left(\frac{2\pi}{\lambda}\right)^2 \sum_{l} {\Delta z_l}^2 \, \langle n'_l(\vec{q}_{u1l})n'_l(\vec{q}_{v2l}) \rangle . \tag{139}$$

Recognizing that the quantity $\langle n_l'(\vec{q}_{u1l})n_l'(\vec{q}_{v2l})\rangle$ is the spatial autocorrelation of the index of refraction fluctuations in the lth layer, designated $B_{n'}(\vec{q}_{u1l},\vec{q}_{v2l})$, we see that:

$$\langle \phi_{u1}(R\vec{\rho}_1)\phi_{v2}(R\vec{\rho}_2)\rangle = \sum_l \left[\left(\frac{2\pi}{\lambda}\right)^2 \Delta z_l{}^2 B_{n'}(\vec{q}_{u1l},\vec{q}_{v2l})\right]. \tag{140}$$

At this point, we note that the quantity in the square braces of Eq. (140) is the spatial autocorrelation of the optical phase in the lth layer, designated $B_\phi(\vec{q}_{u1l},\vec{q}_{v2l})$. Thus, Eq. (140) may be written:

$$\langle \phi_{u1}(R\vec{\rho}_1)\phi_{v2}(R\vec{\rho}_2)\rangle = \sum_l B_\phi(\vec{q}_{u1l},\vec{q}_{v2l}). \tag{141}$$

For spatially wide-sense stationary statistics, B_ϕ will be a function only of the vector separation of points specified by the projected aperture vectors $\vec{q}_{u1l}$ and $\vec{q}_{v2l}$ [32]. From Eq. (121), the vector separation is $\Delta\vec{s}_l$, and it can be said that:

$$B_\phi(\Delta\vec{s}_l) = B_\phi(\vec{q}_{v2l} + \vec{s}_l - \vec{q}_{u1l}). \tag{142}$$

Hence, we conclude that:

$$\langle \phi_{u1}(R\vec{\rho}_1)\phi_{v2}(R\vec{\rho}_2)\rangle = \sum_l B_\phi(\vec{q}_{v2l} + \vec{s}_l - \vec{q}_{u1l}). \tag{143}$$

Substituting Eq. (143) into Eq. (135), yields the following expression for $B_{a_{u1i}a_{v2j}}$:

$$B_{a_{u1i}a_{v2j}} = \int \mathrm{d}\vec{\rho}_1 \int \mathrm{d}\vec{\rho}_2 \left[\sum_l B_\phi(\vec{q}_{v2l} + \vec{s}_l - \vec{q}_{u1l})\right] Z_i(\vec{\rho}_1)Z_j(\vec{\rho}_2)W(\vec{\rho}_1)W(\vec{\rho}_2). \tag{144}$$

Exchanging the order of summation and integration and transforming the integration variables to the projected aperture vectors $\vec{q}_{u1l}$ and $\vec{q}_{v2l}$ yields the following:

$$\begin{aligned} &B_{a_{u1i}a_{v2j}}(\vec{r}_{su},\vec{r}_{a1},\vec{r}_{sv},\vec{r}_{a2}) \\ &= \sum_l [R^2(1-A_{u1l})(1-A_{v2l})]^{-1} \int \mathrm{d}\vec{q}_{u1l} \int \mathrm{d}\vec{q}_{v2l}\, B_\phi(\vec{q}_{v2l} + \vec{s}_l - \vec{q}_{u1l}) \\ &\quad \times Z_i\left[\frac{\vec{q}_{u1l}}{R(1-A_{u1l})}\right] Z_j\left[\frac{\vec{q}_{v2l}}{R(1-A_{v2l})}\right] W\left[\frac{\vec{q}_{u1l}}{R(1-A_{u1l})}\right] W\left[\frac{\vec{q}_{v2l}}{R(1-A_{v2l})}\right]. \end{aligned} \tag{145}$$

By employing Parseval's theorem and the Wiener-Khinchin theorem [32], and the scaling and shifting properties of Fourier transforms [30], as in detailed in Appendix A, Eq. (145) can be written as:

$$\begin{aligned} & B_{a_{u1i}a_{v2j}}(\vec{r}_{su}, \vec{r}_{a1}, \vec{r}_{sv}, \vec{r}_{a2}) \\ &= \sum_l \int \mathrm{d}\vec{k}\, W_\phi(\vec{k}, z_l) \exp(-j2\pi\vec{k}\cdot\vec{s}_l) Q_i\left[R(1-A_{u1l})\vec{k}\right] Q_j^*\left[R(1-A_{v2l})\vec{k}\right], \end{aligned} \quad (146)$$

where $\vec{k}$ is a two-dimensional spatial frequency vector, $W_\phi(\vec{k}, z_l)$ is the spatial PSD of the optical phase in the turbulent layer at height z_l, $\vec{s}_l$ is the separation of the projected aperture centers given in Eq. (120), and $Q_i(\vec{f})$ is the Fourier transform of $Z_i(\vec{\rho})W(\vec{\rho})$.

Integrating Eq. (146) over the azimuthal component of $\vec{k}$, as detailed in Appendix B, yields the following result:

$$\begin{aligned} & B_{a_{u1i}a_{v2j}}(\vec{r}_{su}, \vec{r}_{a1}, \vec{r}_{sv}, \vec{r}_{a2}) \\ &= \frac{4}{\pi} D^{-2} F \sum_l [(1-A_{u1l})(1-A_{v2l})]^{-1} \\ &\quad \times \left\{ \begin{array}{l} G\int_0^\infty \frac{dx}{x} W_\phi\left(\frac{x}{\pi D}, z_l\right) J_{(m_i+m_j)}\left[\frac{2s_l}{D}x\right] \\ \qquad \times J_{(n_i+1)}[(1-A_{u1l})x] J_{(n_j+1)}[(1-A_{v2l})x] \\ +H\int_0^\infty \frac{dx}{x} W_\phi\left(\frac{x}{\pi D}, z_l\right) J_{|m_i-m_j|}\left[\frac{2s_l}{D}x\right] \\ \qquad \times J_{(n_i+1)}[(1-A_{u1l})x] J_{(n_j+1)}[(1-A_{v2l})x], \end{array} \right. \end{aligned} \quad (147)$$

where $D = 2R$ is the diameter of the aperture, $J_\kappa(\cdot)$ is the Bessel function of the first kind of order κ, $x \equiv \pi D k$, $s_l = |\vec{s}_l|$, and the functions F, G, and H are defined as:

$$F \equiv [(n_i+1)(n_j+1)]^{\frac{1}{2}} (-1)^{\frac{1}{2}(n_i+n_j)} 2^{[1-\frac{1}{2}(\delta_{m_i0}+\delta_{m_j0})]} (-1)^{m_j}, \quad (148)$$

$$\begin{aligned} G \equiv\ & (-1)^{\frac{3}{2}(m_i+m_j)} \cos\left[(m_i+m_j)\theta_{s_l}\right. \\ & \left. +\pi/4\left\{(1-\delta_{m_i0})[(-1)^i-1] + (1-\delta_{m_j0})[(-1)^j-1]\right\}\right], \end{aligned} \quad (149)$$

$$\begin{aligned} H \equiv\ & (-1)^{\frac{3}{2}|m_i-m_j|} \cos\left[(m_i-m_j)\theta_{s_l}\right. \\ & \left. +\pi/4\left\{(1-\delta_{m_i0})[(-1)^i-1] - (1-\delta_{m_j0})[(-1)^j-1]\right\}\right], \end{aligned} \quad (150)$$

where n_i, m_i and n_j, m_j are the radial and azimuthal orders of the ith and jth Zernike polynomial, respectively, and θ_{s_l} is the angle between $\vec{s}_l$ and $\hat{x}$.

The expression for $B_{a_{u1i}a_{v2j}}$ in Eq. (147) is valid for any wide-sense stationary and isotropic statistical model for the turbulence-induced phase given by W_ϕ. For this work, the von Kármán spectrum given in Eq. (31) is employed. According to Eq. (36), $W_\phi(k = x/\pi D, z_l)$ is given by:

$$W_\phi(x/\pi D, z_l) = \frac{\pi}{4} D^2 \left(\frac{D}{r_0}\right)^{5/3} \sqrt{3}\,\Gamma(8/3)\, 2^{-5/3} \frac{6.88}{2.91}\, w_l\, (x^2 + x_0^2)^{-11/6}, \tag{151}$$

where $x_0 \equiv \pi D/L_0$. Substituting Eq. (151) into Eq. (147) yields the following expression for $B_{a_{u1i}a_{v2j}}$:

$$\begin{aligned} &B_{a_{u1i}a_{v2j}}(\vec{r}_{su}, \vec{r}_{a1}, \vec{r}_{sv}, \vec{r}_{a2}) \\ &= \left(\frac{D}{r_0}\right)^{5/3} \sqrt{3}\,\Gamma(8/3)\, 2^{-5/3} \frac{6.88}{2.91}\, F \sum_l w_l\, [(1 - A_{u1l})(1 - A_{v2l})]^{-1} \\ &\times \left\{ \begin{array}{l} G \int_0^\infty \frac{dx}{x} (x^2 + x_0^2)^{-11/6} J_{(m_i+m_j)} \left[\frac{2s_l}{D} x\right] \\ \qquad \times J_{(n_i+1)}[(1 - A_{u1l})x] J_{(n_j+1)}[(1 - A_{v2l})x] \\ +H \int_0^\infty \frac{dx}{x} (x^2 + x_0^2)^{-11/6} J_{|m_i-m_j|} \left[\frac{2s_l}{D} x\right] \\ \qquad \times J_{(n_i+1)}[(1 - A_{u1l})x] J_{(n_j+1)}[(1 - A_{v2l})x]. \end{array} \right. \end{aligned} \tag{152}$$

According to Eq. (152), the total cross-correlation can be viewed as the sum of layer contributions weighted by the factor w_l given by Eq. (34). The layer contribution is determined by the relative projected aperture separation s_l/D, and by the relative outer scale L_0/D using the parameter x_0. Eq. (152) serves throughout the remainder of this work as the primary means of calculating the cross-correlation of the Zernike coefficients for a given set of aperture and source locations. This expression and the accompanying geometry in Figure 12 can be adapted to model all types of spatial and temporal anisoplanatic effects considered in this research.

3.3.3 Theoretical validation. To verify the validity of the spatial cross-correlation expression developed here, Eq. (152) can be compared directly with published results for a

specific case of the analysis geometry. Takato and Yamaguchi [76] developed an expression for the spatial correlation of Zernike coefficients with finite outer scale. Their development was for plane-wave propagation from a single source, with two apertures separated by $\vec{s}$. In the notation of the present analysis, this corresponds to $A_{u1l}, A_{v2l} = 0$ and $\vec{s}_l = \vec{s}$. Thus, the spatial cross-correlation is derived from Eq. (152) as:

$$\begin{aligned}\langle a_i a_j \rangle (s) &= \left(\frac{D}{r_0}\right)^{5/3} \sqrt{3}\,\Gamma(8/3)\, 2^{-5/3} \frac{6.88}{2.91} F \\ &\times \begin{cases} G \int_0^\infty \frac{dx}{x} (x^2 + x_0^2)^{-11/6} J_{(m_i+m_j)} \left[\frac{2s}{D} x\right] J_{(n_i+1)}(x) J_{(n_j+1)}(x) \\ +H \int_0^\infty \frac{dx}{x} (x^2 + x_0^2)^{-11/6} J_{|m_i-m_j|} \left[\frac{2s}{D} x\right] J_{(n_i+1)}(x) J_{(n_j+1)}(x), \end{cases}\end{aligned} \tag{153}$$

where the source and aperture subscripts have been dropped from the Zernike coefficients, as the sources are coincident and the aperture is implied by the the subscripts i (aperture 1) and j (aperture 2). For a given aperture separation direction, $\langle a_i a_j \rangle$ depends upon the relative aperture separation s/D and the relative outer scale L_0/D.

For separation in the $\hat{x}$ direction, Takato and Yamaguchi [76] expressed results for the autocorrelation ($i = j$) of the Zernike modes in terms of a correlation coefficient defined as:

$$\rho_{a_i a_j}(s) \equiv \frac{\langle a_i a_j \rangle (s)}{\sqrt{\langle a_i a_i \rangle (0) \langle a_j a_j \rangle (0)}}. \tag{154}$$

Using the expression for $\langle a_i a_j \rangle$ given in Eq. (153), the results of reference [76] were replicated for piston, tilt, and defocus correlation with $L_0/D = 1, 10, 20, 50, 100$. These results are shown in Figure 13. The autocorrelation plots in Figure 13 demonstrate the general correlative properties characteristic of the Zernike coefficients for finite outer scale. For all modes, the correlation coefficient is 1 for coincident apertures, and drops off as the separation increases. The correlation coefficient falls more slowly for larger relative outer scale values. Of the low-order Zernike aberrations, piston and tilt are the only modes for which the correlation coefficient is significantly larger than 0 for $s/D > 1$.

Using Eq. (153), the cross-correlation ($i \neq j$) of the Zernike coefficients can also be quantified. The correlation coefficient $\rho_{a_i a_j}$ was computed according to Eq. (154) for $i = 2, j = 4$ and $i = 3, j = 5$ for the same relative outer scale values considered in Figure 13.

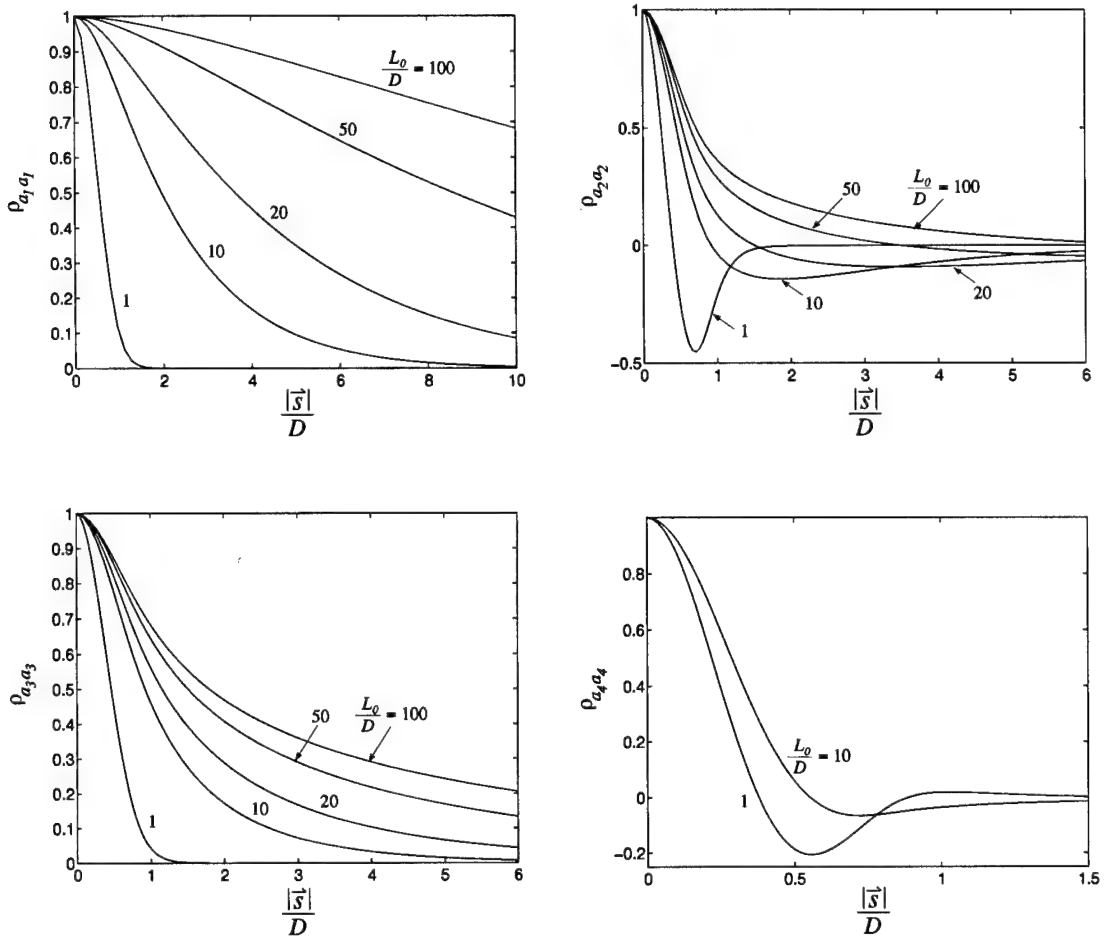

Figure 13. Spatial autocorrelation of low-order Zernike coefficients. Results are for plane-wave propagation from a single source with relative outer scale L_0/D, and relative aperture separation s/D.

The results of these calculations are shown in Figure 14. These results demonstrate an important characteristic of the cross-correlation of Zernike modes. While the mode combinations considered here ($i = 2, j = 4$ and $i = 3, j = 5$) are uncorrelated for $s/D = 0$ (also true for infinite outer scale, see Table 3), the magnitude of the cross-correlation increases through some maximum value as s/D increases, before going to 0 as $s/D \rightarrow \infty$. This cross-correlation effect will play a significant role when applying the optimal modal compensation theory developed earlier, as the enhanced cross-correlation between modes will affect compensation performance when anisoplanatism is present in an AO system.

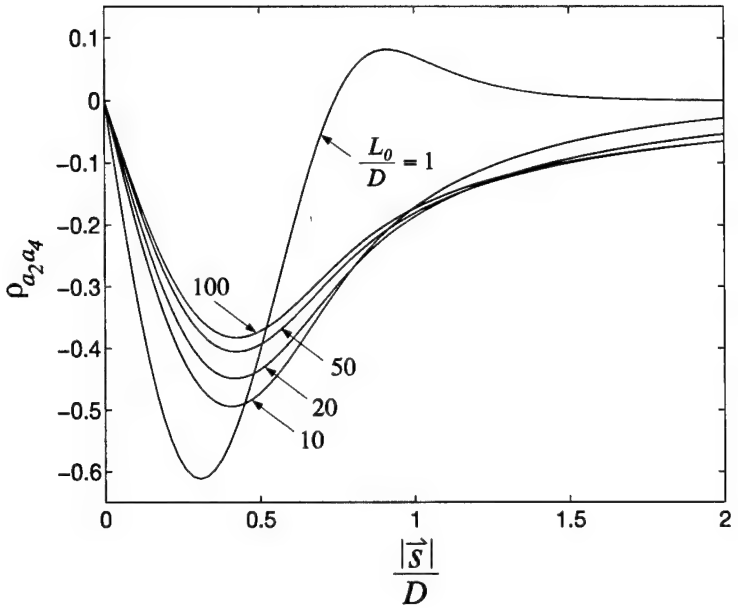

(a)

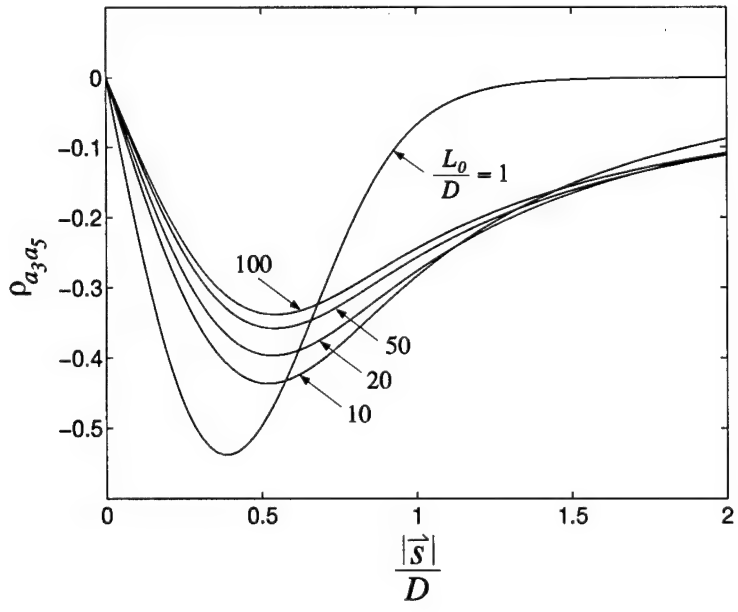

(b)

Figure 14. Spatial cross-correlation of low-order Zernike coefficients. (a) Cross-correlation of a_2 (x-tilt) with a_4 (defocus) and (b) cross-correlation of a_3 (y-tilt) with a_5 astigmatism. While these modes are uncorrelated for $s/D = 0$, the magnitude of the cross-correlation increases through some maximum value as s/D increases.

Integrals of the form contained in Eq. (153) can be evaluated analytically [71, 76]. The analytic expression is a series solution for which convergence is may be slow. Thus, in practice, it is often easier to evaluate these integrals numerically, as was done in reference [76] and for the results shown in Figure 13 and Figure 14. Throughout the remainder of this work, numerical integration is used to evaluate the generalized cross-correlation expression in Eq. (152).

3.3.4 Experimental validation. The spatial cross-correlation expression given in Eq. (152) can also be validated by comparison with experimental results. By invoking Taylor's frozen-flow hypothesis [61] to account for the effects of bulk motion of the turbulent medium, the spatial cross-correlation expression in Eq. (152) may be converted into an expression for the temporal cross-correlation of Zernike coefficients, designated $R_{a_i a_j}(\tau)$, where τ is the time delay between measurements [37,94]. In this case, $s_l = v_l \tau$ in Eq. (152) for a non-zero flow velocity in the lth layer specified by the vector $\vec{v}_l$. If a_i is the ith Zernike coefficient in the aperture at time t, and a_j is the jth Zernike coefficient in the aperture at time $t + \tau$, then the temporal cross-correlation of these coefficients, designated $R_{a_i a_j}$ is given by:

$$R_{a_i a_j}(\tau) = \left(\frac{D}{r_0}\right)^{5/3} \sqrt{3}\,\Gamma(8/3)\, 2^{-5/3} \left(\frac{6.88}{2.91}\right) F$$
$$\times \sum_l w_l \left\{ \begin{array}{l} G \int_0^\infty \frac{dx}{x} (x^2 + {x_0}^2)^{-11/6} J_{(m_i+m_j)} \left(\frac{2v_l\tau}{D} x\right) J_{(n_i+1)}(x) J_{(n_j+1)}(x) \\ +H \int_0^\infty \frac{dx}{x} (x^2 + {x_0}^2)^{-11/6} J_{|m_i-m_j|} \left(\frac{2v_l\tau}{D} x\right) J_{(n_i+1)}(x) J_{(n_j+1)}(x). \end{array} \right. \quad (155)$$

For comparison with theory, experimental measurements of turbulence-induced phase were obtained in the laboratory using the optical apparatus in Fig. 15. In this apparatus, a 2 cm diameter collimated laser beam is propagated through a channeled flow of turbulence generated by the mixing of helium and nitrogen gases. The velocity of the flow along the channel was approximately 4 m/s. The laser beam was centered approximately 10 cm from the exit of the turbulence generator, where the mixing layer of the two gases has just expanded to the width of the channel. A Hartmann wave-front sensor was used to measure the local gradient of the phase induced in the beam upon propagation through

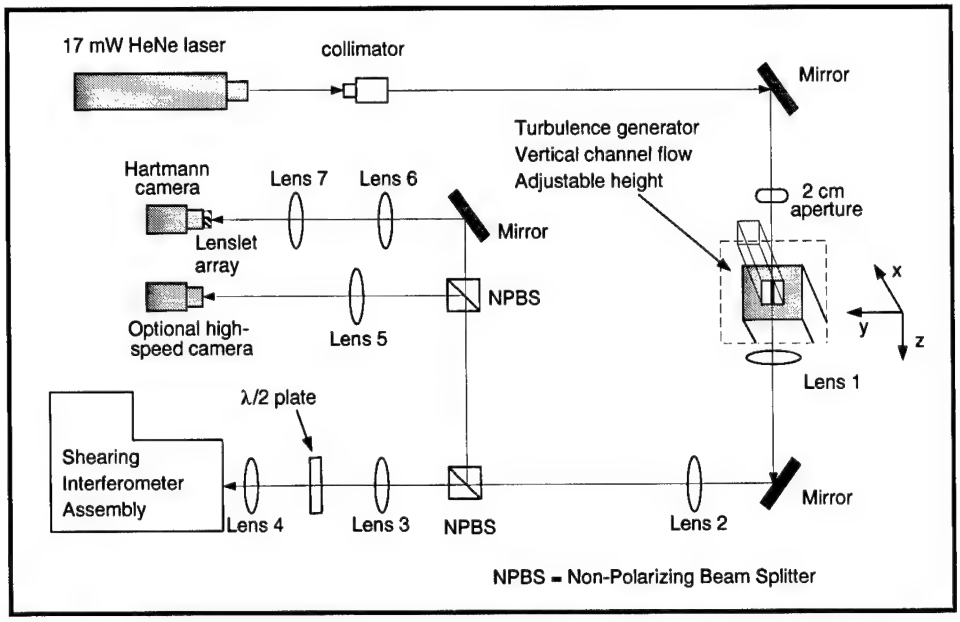

Figure 15. Optical bench used to obtain phase measurements for laser beam propagation through a turbulent mixing layer.

the turbulent flow. A thorough description of this apparatus and the experiments from which the data was obtained can be found in reference [28] and reference [67]. Phase measurements were obtained through a least-squares reconstructor [67], resulting in an ensemble of 255 phase realizations, each represented as a 41×41 array at 1 msec intervals. A sample of these experimental phase measurements is shown in Figure 16.

From the reconstructed phase measurements, the Zernike coefficient a_i at time t is calculated by projecting $\phi(x_m, y_n; t)$ onto the Zernike polynomial $Z_i(x_m, y_n)$ as follows:

$$a_i(t) = \frac{\sum_{m=1}^{41} \sum_{n=1}^{41} \phi(x_m, y_n; t) Z_i(x_m, y_n)}{\sum_{m=1}^{41} \sum_{n=1}^{41} Z_i^2(x_m, y_n)}, \tag{156}$$

where the ordered pair (x_m, y_n) designates the physical location specified by row m and column n in the data array. Likewise, the Zernike coefficient a_j at time $t + \tau$ is calculated by:

$$a_j(t+\tau) = \frac{\sum_{m=1}^{41} \sum_{n=1}^{41} \phi(x_m, y_n; t+\tau) Z_j(x_m, y_n)}{\sum_{m=1}^{41} \sum_{n=1}^{41} Z_j^2(x_m, y_n)}. \tag{157}$$

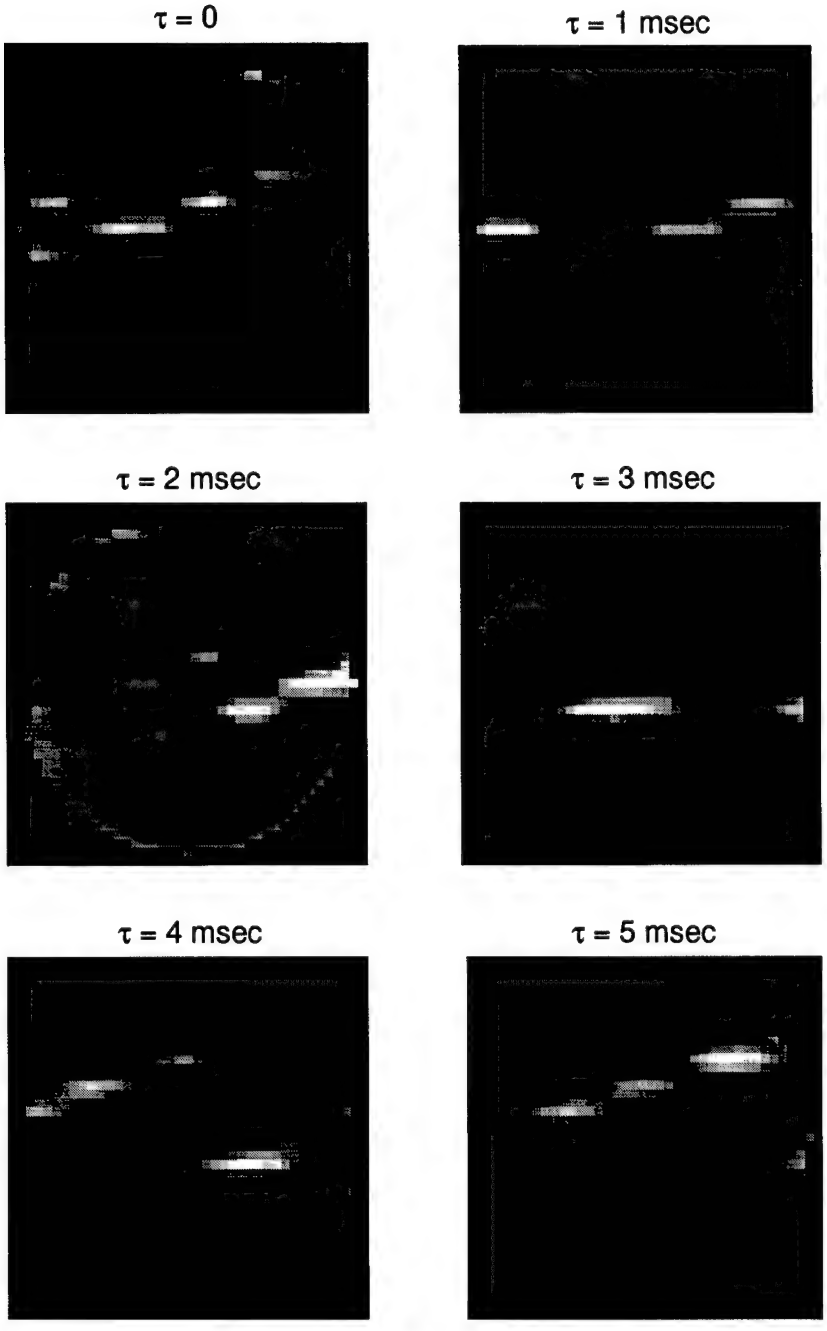

Figure 16. Sample of laboratory measurements of turbulence-induced phase. Deterministic optical system effects have been removed. Phase measurements were obtained on a 41 × 41 grid at 1 msec intervals.

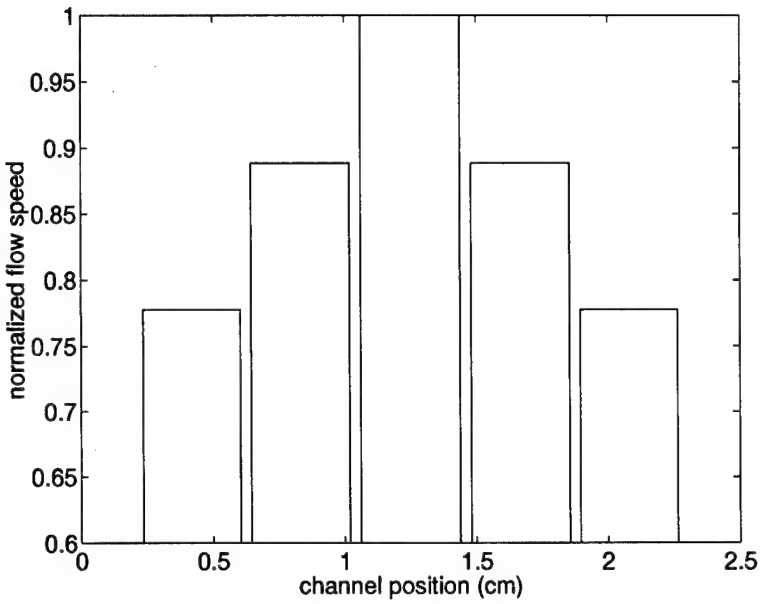

Figure 17. Turbulent flow speed profile for the 5-layer discrete turbulence model employed in calculating the theoretical values of the Zernike coefficient cross-correlation. The flow velocity in each layer is taken to be along the major axis of the flow channel. The flow speed in each layer is normalized to the maximum speed in the channel, $v_{\max}$.

Using these calculated Zernike coefficients, the estimated temporal cross-correlation of $a_i(t)$ with $a_j(t+p\tau_d)$, designated $\hat{R}_{a_i a_j}(p\tau_d)$, where p indexes the number of time steps between the phase measurements, was calculated as follows:

$$\hat{R}_{a_i a_j}(p\tau_d) = \frac{1}{255-p} \sum_{q=1}^{255-p} a_i[(q-1)\tau_d] a_j[(q-1+p)\tau_d]. \tag{158}$$

Thus, $\hat{R}_{a_i a_j}(p\tau_d)$ was determined at $\tau_d = 1$ msec intervals for the reconstructed phase measurements obtained in the laboratory.

Eq. (155) requires that the turbulent flow be modeled in a finite number of discrete layers, and that the parameters $\vec{v}_l$, w_l, and L_0 be specified for each of these layers. Based on laboratory measurements, the velocity in each of 5 discrete layers was taken to be in direction of the major axis of the flow channel. In these analysis efforts, the normalized flow speed profile shown in Fig. 17 was employed, where the speed of the turbulent flow in each layer is divided by the maximum speed $v_{\max}$ in the channel. To simplify the analysis

mode i	mode j	$v_{\max}$ (m/s)	L_0 (m)	L_0/D
2 (x-tilt)	2 (x-tilt)	4.8	0.035	1.75
3 (y-tilt)	3 (y-tilt)	6.4	0.020	1.00
2 (x-tilt)	4 (defocus)	3.5	0.050	2.50
2 (x-tilt)	8 (coma)	3.0	0.035	1.75
3 (y-tilt)	7 (coma)	3.5	0.035	1.75

Table 4. Maximum flow speed ($v_{\max}$) and outer scale (L_0) parameters selected to fit the theoretical cross-correlation results to the experimental data.

efforts, an equal weighting for each layer was assumed; that is, $w_l = 0.2$. The outer scale L_0 is also assumed to be the same for all layers.

The temporal cross-correlation of the Zernike coefficients was estimated from the experimental data according to Eq. (158) and calculated using the theoretical expression given in Eq. (155). For each of the results presented in this section, the maximum flow speed, $v_{\max}$, and the outer scale L_0 were chosen to fit the theoretical curves with the experimental measurements. These quantities determine the free parameters v_l and x_0 in Eq. (155). The values of $v_{\max}$ and L_0 chosen for each combination of modes i and j presented in this section are summarized in Table 4. The velocities resulting from the fit correspond well with the mean velocity of 4 m/s measured in the laboratory. The magnitude of the outer scale values resulting from the fit ($L_0/D \sim 1 - 3$) indicate that finite outer scale effects are present in the data and that the turbulence cannot be modeled adequately with an infinite outer scale (Kolmogorov) spectrum.

The experimental estimates for the temporal autocorrelation of the orthogonal components of tilt (Zernike 2 and 3) are shown with error bars in Figure 18(a)-(b). For reference, the theoretical autocorrelation is shown by the solid curves. Both the experimental and theoretical autocorrelation have been normalized to yield a correlation coefficient in the range -1 to 1. From these results, it is apparent that the temporal autocorrelation of the orthogonal components of tilt are well-modeled by Eq. (155) for $\tau \leq 5$ msec. For $\tau > 5$ msec, it is obvious that the frozen-flow hypothesis upon which Eq. (155) is constructed does not fully account for the temporal evolution of the turbulence.

The experimental and theoretical cross-correlation of tilt with defocus (Zernike 4) and orthogonal components of coma (Zernike 7 and 8) is shown in Figure 19. Only the cross-

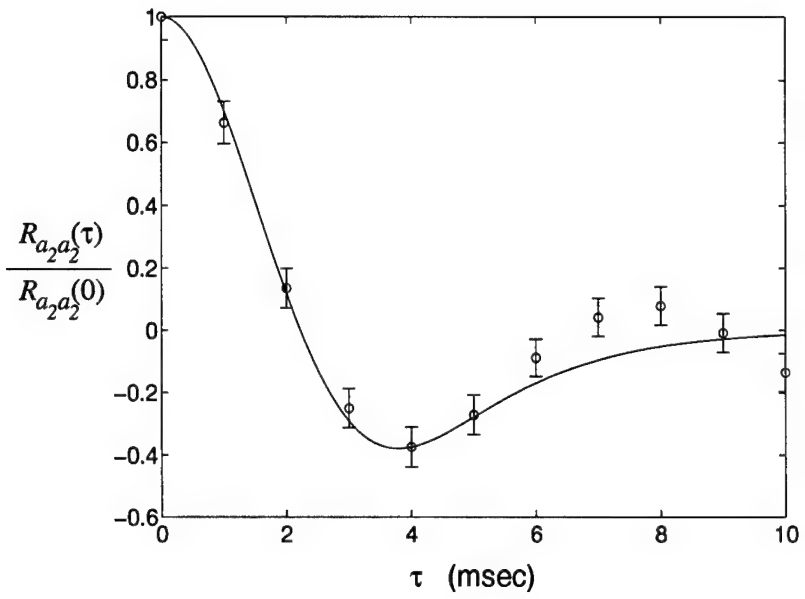

(a)

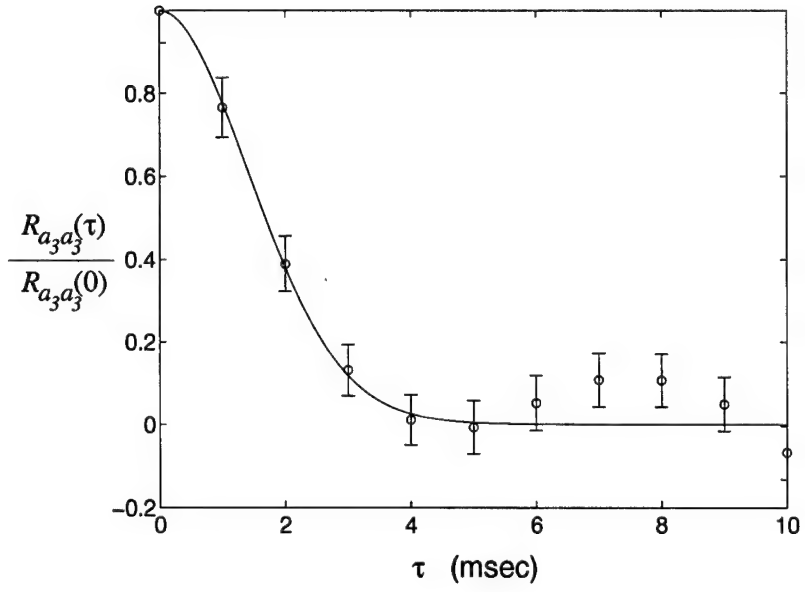

(b)

Figure 18. Comparison of theoretical and experimental temporal autocorrelation results for tilt components. (a) Temporal autocorrelation of the x-tilt (Zernike 2) and (b) temporal autocorrelation of the y-tilt (Zernike 3) for the reconstructed phase measurements studied. Experimental results are shown with error bars, and theoretical results are indicated by the solid curves.

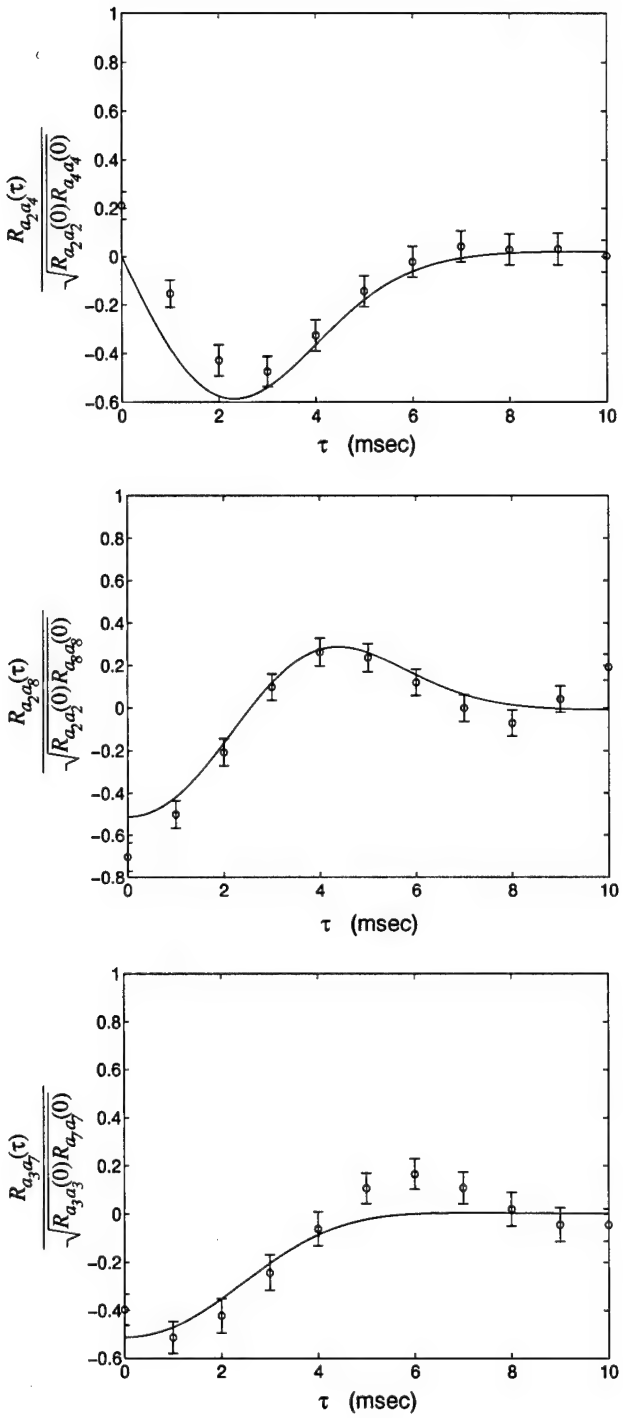

Figure 19. Comparison of theoretical and experimental temporal cross-correlation results. Experimental results are shown with error bars, and theoretical results are indicated by the solid curves.

correlation of x-tilt with defocus is shown as the cross-correlation of y-tilt with defocus is zero for all values of τ. Similarly, x-tilt is uncorrelated with Zernike 7 and y-tilt is uncorrelated with Zernike 8.

As is shown by the theoretical cross correlation curves, tilt is uncorrelated with defocus at $\tau = 0$, as is conventionally reported [54] (also see Table 3). As τ increases, however, the magnitude of the cross-correlation increases through some maximum value before going to zero for larger values of τ. The experimental cross-correlation of tilt with defocus follows the same trend, and is well-modeled by theory over a range of τ values. The theoretical curves in Figure 19 also demonstrate that the tilt components are correlated with orthogonal coma components at $\tau = 0$ as the conventional analysis indicates [54]. Tilt remains correlated with coma for $\tau > 0$ before becoming uncorrelated at larger values of τ.

While the theoretical cross-correlation results shown in Figure 19 generally agree with the experiment considering measurement error, there is a noted difference between theory and experiment at smaller values of τ. As this was not the case for the autocorrelation results in Figure 18, validity of the frozen flow hypothesis cannot be questioned in explaining this disagreement. Instead, differences between the experimental and theoretical results are due to statistical anisotropy, which has been noted to exist in mixing layers [28, 29].

3.4 Summary

This chapter extends the analysis of optical system performance degraded by turbulence-induced anisoplanatism. By considering the form of the aperture-averaged residual differential phase variance δ_N^2 for Nth-order modal compensation, system performance was shown to be suboptimal when beacon modal phase measurements are used directly for wave-front correction. To achieve optimal (but not necessarily ideal) performance, the modal correction must be estimated from the beacon phase coefficients, given knowledge of the correlation of object and beacon phase. The optimality criterion determined by the form of δ_N^2 corresponds to MMSE estimation, where the mean value of the squared difference between the object and conjugate phase coefficients is minimized for all modes.

The formalism and notation associated with MMSE estimation was introduced, and the performance of the estimator was quantified in terms of covariance matrices for the beacon and object phase coefficients.

In order to calculate the MMSE estimator matrix, the spatial cross-correlation of the object and beacon phase coefficients must be quantified. To model the full range of anisoplanatic effects in imaging, beam-projection, and interferometric systems, the cross-correlation of Zernike coefficients in spatially-separated apertures from spatially-separated optical sources must be quantified. An analysis geometry was introduced to model these effects, and the cross-correlation calculation was performed for wide-sense stationary and isotropic phase statistics with finite outer scale. For a layered atmospheric model, the total cross-correlation is a weighted sum of the cross-correlation in each layer. For each layer, the cross-correlation depends upon the ratio s_l/D, where s_l is the projected aperture separation in the lth layer, and D is the diameter of the apertures. The cross-correlation also depends upon the relative outer scale L_0/D.

The expression resulting from the cross-correlation calculation may be tailored for analysis of a system-specific geometry. To test the validity of the cross-correlation analysis, the results of this calculation were compared to published theoretical results [76], and were found to be in exact agreement. The expression for the cross-correlation also predicts that while most low-order Zernike modes are uncorrelated at zero spatial separation, the magnitude of the cross-correlation increases through some maximum value before going to zero as the spatial separation becomes large relative to the aperture diameter. To test this prediction and to further confirm the validity of the cross-correlation expression, laboratory measurements of turbulence-induced phase were analyzed. Experimental measurements of the temporal autocorrelation where found to be in close agreement with theoretical predictions when frozen-flow assumptions were valid. The cross-correlation enhancement effect predicted by the theory was also confirmed by the experimental results.

IV. Ground-Based Adaptive-Optical Imaging

4.1 Introduction

In this chapter, the optimal modal compensation theory developed in Chapter III is applied to ground-based adaptive-optical imaging systems. Adaptive optics improve the resolution of ground-based imaging systems by conjugating the turbulence-induced phase incident in the system aperture. When anisoplanatism is present in the AO system, the imaging performance is degraded, since the incident and conjugate phase are only partially correlated. By accounting for the statistics of the turbulence-induced phase, part of the performance degradation may be recovered through optimal compensation.

The application of the optimal modal compensation theory is discussed in Section 4.2. The minimum-mean-square-error (MMSE) estimator for the optimal modal phase coefficients is discussed, and the performance of the estimator is given in terms of the statistics of the object and beacon phase. The spatial correlation of the object and beacon phase is given by a special case of the general correlation expression in Eq. (152). Thus, both angular and focal anisoplanatism effects may be accounted for in the optimal estimator.

The performance of natural-guide-star (NGS) and laser-guide-star (LGS) compensation with the optimal estimator is discussed in Section 4.3 and Section 4.4. For NGS compensation, the performance degradation resulting from angular anisoplanatism is shown to be reduced when the MMSE estimator of object phase coefficients is employed. Thus, the NGS beacon angular offset can be increased without degrading imaging performance. For the LGS beacon aided by a NGS beacon for tilt compensation, angular and focal anisoplanatic effects are reduced by the optimal estimator. Thus, the LGS beacon alititude can be decreased without degrading imaging performance.

Section 4.5 discusses how tilt compensation performance may be enhanced by incorporating higher-order modes in a MMSE estimator for wave-front tilt. For NGS tilt compensation, the maximum-permissible angular separation between the object and NGS is significantly increased. Recovery of object tilt components using only LGS beacon measurements is discussed. In this scheme, while only higher-order modal measurements can be obtained from the LGS, the cross-correlation of the higher-order modes with tilt com-

ponents can be utilized in the MMSE estimator to provide an estimate of wave-front tilt. The performance of the tilt estimator is quantified, demonstrating its ability to enhance imaging performance as well as practical limits to its application. Section 4.6 provides a brief summary of the chapter.

4.2 Application of theory to ground-based adaptive optics

The optimal modal compensation theory discussed in Section 3.2 may be applied directly to ground-based imaging with an AO system. Recall that a lower bound on the Strehl ratio of an imaging system is given in Eq. (90) as $\mathrm{SR} \geq \exp(-\varepsilon_N^2)$. The aperture-averaged residual phase variance ε_N^2 is computed using Eq. (86):

$$\varepsilon_N^2 = \int \mathrm{d}\vec{\rho}\, W(\vec{\rho}) \left\langle \phi_o^2(R\vec{\rho}) \right\rangle - \sum_{i=2}^{N} \left\langle a_{oi}^2 \right\rangle + \sum_{i=2}^{N} \left\langle (a_{oi} - \tilde{a}_{oi})^2 \right\rangle . \tag{159}$$

The Zernike coefficients of the conjugate phase are represented by $\tilde{a}_{oi}$, and are based upon measurements of the beacon phase ϕ_b. Suppose the modal coefficients a_{bi} are measured from the beacon phase incident in the system aperture:

$$a_{bi} \equiv \int \mathrm{d}\vec{\rho}\, W(\vec{\rho})\, \phi_b(R\vec{\rho})\, Z_i(\vec{\rho}). \tag{160}$$

Recognizing that ε_N^2 has the same mathematical form as δ_N^2 in Eq. (96), and considering the optimal modal compensation theory developed in Chapter III, ε_N^2 is minimized by setting $\tilde{a}_{oi} = \hat{a}_{oi}$, where $\hat{a}_{oi}$ is the MMSE estimate of a_{oi} given a_{bi}. For imaging applications, we are concerned only with piston-removed phase. Thus, the vector $\mathbf{y}$ corresponding to Eq. (102) is composed of object phase coefficients of order 2 through N, whereas $\mathbf{x}$ is composed of the corresponding Zernike phase coefficients measured from the NGS or LGS beacon:

$$\mathbf{y} = \begin{bmatrix} a_{o2} \\ a_{o3} \\ a_{o4} \\ \vdots \\ a_{oN} \end{bmatrix} \qquad \mathbf{x} = \begin{bmatrix} a_{b2} \\ a_{b3} \\ a_{b4} \\ \vdots \\ a_{bN} \end{bmatrix} . \tag{161}$$

The components of $\hat{\mathbf{y}}$ are the MMSE estimates of the object phase:

$$\hat{\mathbf{y}} = \begin{bmatrix} \hat{a}_{o2} \\ \hat{a}_{o3} \\ \hat{a}_{o4} \\ \vdots \\ \hat{a}_{oN} \end{bmatrix}. \tag{162}$$

According to Eq. (106), $\hat{\mathbf{y}}$ is related to $\mathbf{x}$ by:

$$\hat{\mathbf{y}} = C_{yx} C_{xx}^{-1} \mathbf{x}, \tag{163}$$

where C_{yx} is the covariance matrix of $\mathbf{y}$ with $\mathbf{x}$ and C_{xx} is the covariance matrix of $\mathbf{x}$ with $\mathbf{x}$, as in Eq. (107) and Eq. (108), respectively. When the optimal coefficients are used in modal compensation, then according to Eq. (109), ε_N^2 is given by:

$$\text{MMSE: } \varepsilon_N^2 = \int \mathrm{d}\vec{\rho}\, W(\vec{\rho})\, \langle \phi_o^2(R\vec{\rho}) \rangle - \mathrm{TR}\left[C_{yx} C_{xx}^{-1} C_{xy} \right]. \tag{164}$$

If the measured beacon phase coefficients are used directly to form the conjugate phase (no optimal estimation), then according to Eq. (110), ε_N^2 is given by:

$$\text{measured: } \varepsilon_N^2 = \int \mathrm{d}\vec{\rho}\, W(\vec{\rho})\, \langle \phi_o^2(R\vec{\rho}) \rangle - \mathrm{TR}\left[2C_{yx} - C_{xx} \right]. \tag{165}$$

The matrix elements of C_{yy}, C_{xx} and C_{yx} are given by evaluating the spatial cross-correlation expression of Eq. (152) for a geometric specification consistent with a ground-based imaging system. This special case of the generalized analysis geometry in Figure 12 is shown in Figure 20, where $\vec{r}_{a1} = \vec{r}_{a2} = \vec{r}_a$. For the single-aperture case, the aperture separation $\vec{s} = 0$, and the projected aperture separation $\vec{s}_l$ is given by Eq. (120).

4.3 Natural-guide-star compensation

To quantify NGS compensation performance, ε_N^2 must be calculated according to Eq. (164) for MMSE-estimates of the object phase, and by Eq. (165) for employing beacon

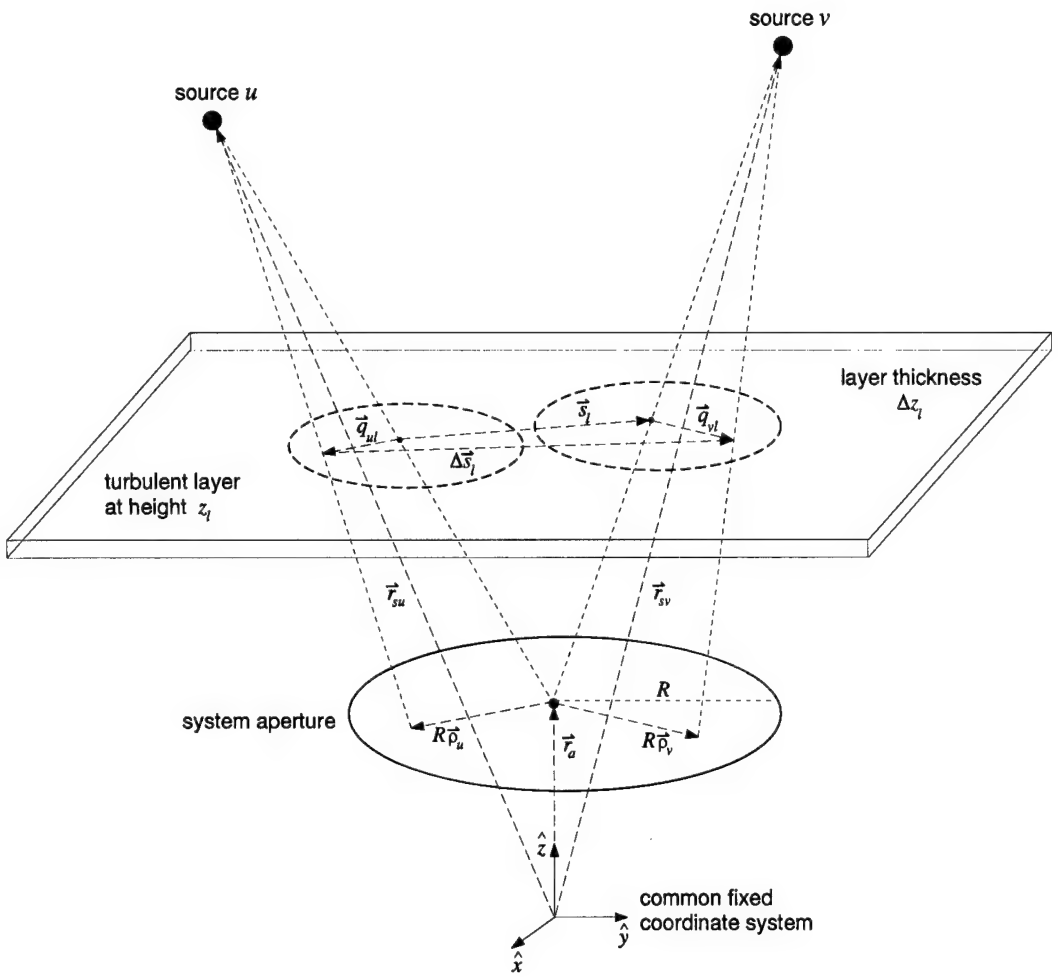

Figure 20. Special case of analysis geometry for ground-based imaging systems.

phase measurements directly. The first term of ε_N^2 is the aperture-averaged piston-removed phase variance, which for finite outer scale L_0 is given by:

$$\int \mathrm{d}\vec{\rho}\, W(\vec{\rho})\, \langle \phi_o^2(R\vec{\rho}) \rangle = \left(\frac{D}{r_0}\right)^{5/3} \sqrt{3}\, \Gamma(8/3)\, 2^{-5/3} \left(\frac{6.88}{2.91}\right) \times \left[\frac{3}{10} x_0^{-5/3} - 2\int_0^\infty \frac{dx}{x} (x^2 + {x_0}^2)^{-11/6} J_1^2(x)\right], \quad (166)$$

where $x_0 \equiv \pi D/L_0$, as in Eq. (152). Since each term of Eq. (164) and Eq. (165) is proportional to $(D/r_0)^{5/3}$ [see Eq. (152)], compensation performance may be quantified by the normalized aperture-averaged residual phase variance, $\varepsilon_N^2 (D/r_0)^{-5/3}$. When normalized in

this fashion, ε_N^2 will depend only on the parameter x_0, which is fully specified by the relative outer scale L_0/D. For the results which follow, a 1 m aperture diameter is assumed, and angular offsets are normalized to the isoplanatic angle θ_0 defined in Eq. (91).

Figure 21(a) shows the value of $\varepsilon_N^2(D/r_0)^{-5/3}$ for compensation using an NGS with angular offset $\theta_b/\theta_0 = 0$ to 10 for $N = 6, 10, 15, 21$, and $L_0/D = 100$. Similarly, Figure 22(a) shows the value of $\varepsilon_N^2(D/r_0)^{-5/3}$ for compensation using an NGS with angular offset $\theta_b/\theta_0 = 0$ to 2 for $N = 28, 36, 45, 55$, and $L_0/D = 50$. The dashed horizontal lines in Figure 21(a) and Figure 22(a) correspond to $\varepsilon_N^2 = 1$ rad^2 for each value of the relative aperture diameter D/r_0 considered. For each relative aperture diameter, the normalized error must be less than the value indicated for Strehl ratio performance greater than 0.37. Performance results for the MMSE estimator are shown by the solid curves for each correction order. Performance results for coefficients measured directly from the NGS are shown by the dashed curve. As is illustrated in Figure 21(a) and Figure 22(a), the normalized error from the MMSE estimator is always less than or equal to the normalized error using phase coefficients directly as the conjugate phase.

Figure 21(b) shows the Strehl ratio of an AO system with $D/r_0 = 5$ corresponding to the results in Figure 21(a). The MMSE estimator is shown to yield imaging performance greater than or equal to the imaging performance when beacon phase coefficients are used directly in the compensation. For the orders of correction considered in Figure 21(b), the difference between the imaging performance of the MMSE compensation and the imaging performance using beacon measurements directly is appreciable for $\theta_b/\theta_0 > 2$.

Figure 22(b) shows the Strehl ratio performance of an AO system with $D/r_0 = 10$ corresponding to the results in Figure 22(a). Again, the MMSE estimator yields imaging performance greater than or equal to the imaging performance when beacon phase coefficients are used directly in the AO compensation. For the orders of correction considered in Figure 22(b), the difference between the imaging performance of the MMSE compensation and the imaging performance using beacon measurements directly is appreciable for $\theta_b/\theta_0 > 0.5$. For $N = 55$, the MMSE estimator can provide equivalent imaging performance at beacon offset angles approximately 10% larger than when beacon measurements are used directly in the compensation.

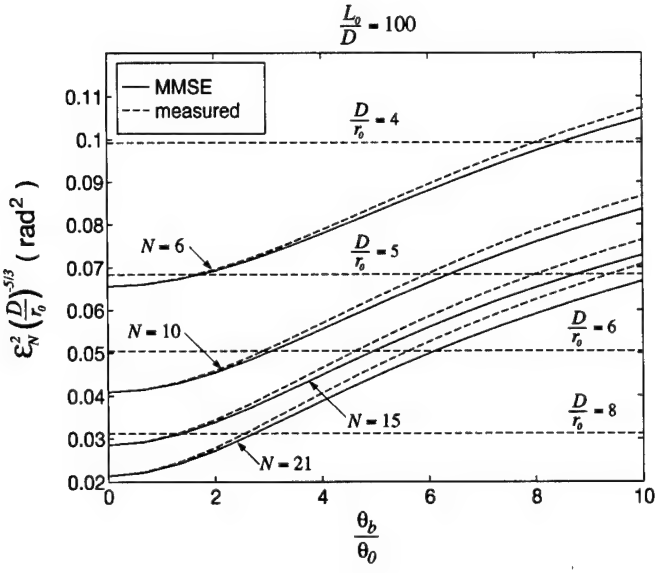

(a)

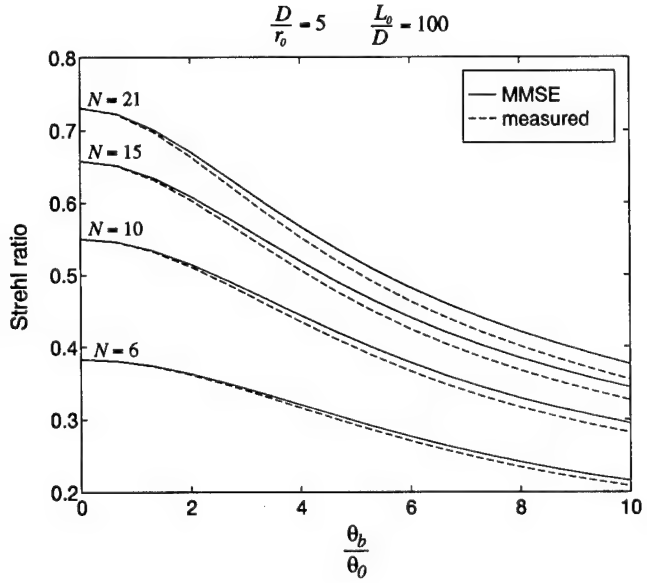

(b)

Figure 21. Comparison of lower-order NGS optimal compensation performance with conventional compensation performance. (a) Value of $\varepsilon_N^2 (D/r_0)^{-5/3}$, for the NGS beacon offset θ_b/θ_0 using the MMSE estimator (solid line) and using beacon measurements directly (dashed line). Horizontal lines indicate levels at which $\varepsilon_N^2 = 1$ rad^2 for each value of D/r_0. (b) Corresponding Strehl ratio performance with relative aperture diameter $D/r_0 = 5$.

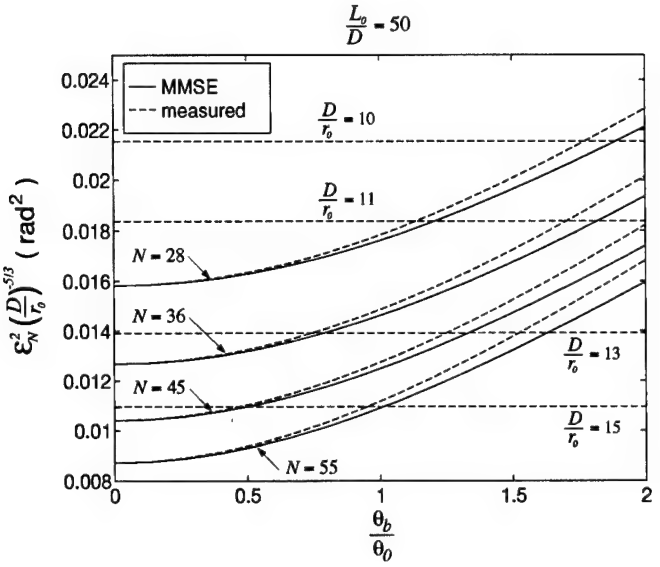

(a)

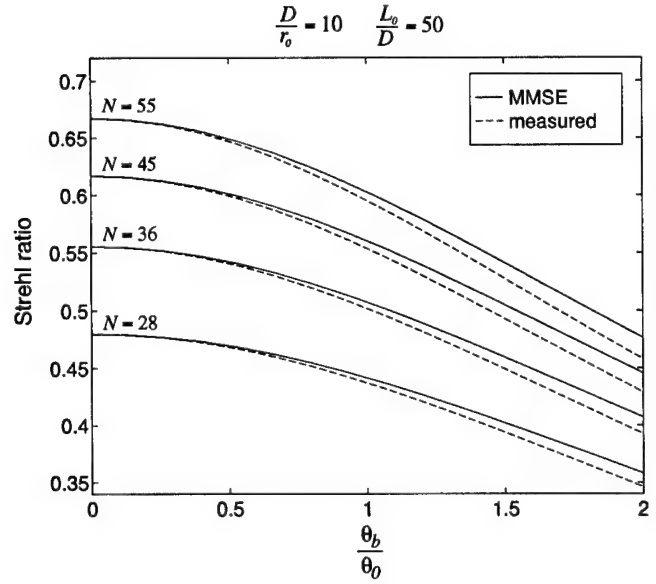

(b)

Figure 22. Comparison of higher-order NGS optimal compensation performance with conventional compensation performance. (a) Value of $\varepsilon_N^2(D/r_0)^{-5/3}$, for the NGS beacon offset θ_b/θ_0 using the MMSE estimator (solid line) and using beacon measurements directly (dashed line). Horizontal lines indicate levels at which $\varepsilon_N^2 = 1$ rad^2 for each value of D/r_0. (b) Corresponding Strehl ratio performance with relative aperture diameter $D/r_0 = 10$.

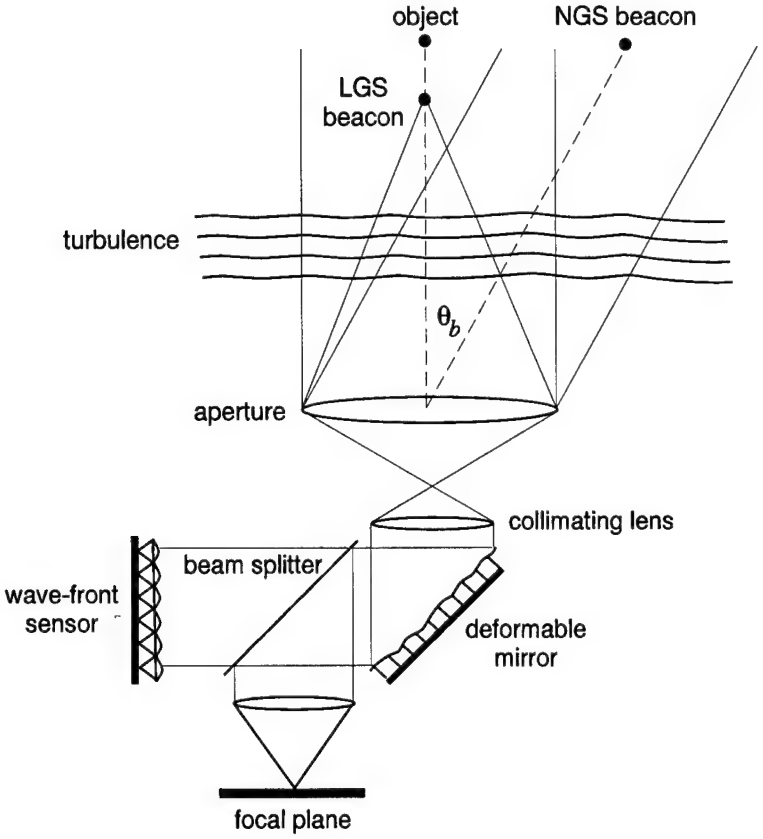

Figure 23. Schematic diagram of an AO system with LGS compensation aided by an off-axis NGS for tilt compensation.

4.4 Natural-guide-star aided laser-guide-star compensation

When investigating LGS compensation, we must consider the effect of using an off-axis NGS for tilt compensation along with an on-axis LGS for higher-order modes. An AO system in which the LGS is aided by an NGS for tilt compensation is shown in Figure 23. The LGS beacon is formed at some finite altitude and the NGS has an angular offset θ_b with respect to the optical axis. In this configuration, the beacon phase coefficient measurements a_{bi} are decorrelated from the object phase coefficients a_{oi} due to both angular anisoplanatism (NGS effect) and focal anisoplanatism (LGS effect). The form of the beacon measurement vector does not change, but the tilt components a_{b2} and a_{b3} are associated with the NGS.

One conceptual difficulty that arises in modeling LGS effects with the geometry shown in Figure 20 is the notion of specifying a fixed position vector for the LGS. When an on-axis laser beam propagates upward through the atmosphere to form the beacon, a random deflection is induced by the turbulence. Thus, the angle associated with the vector location of the beacon is a random quantity. Tyler [85] has estimated the variance of this random deflection, σ_θ^2, to be given by:

$$\sigma_\theta^2 = 0.182(\lambda/D)^2(D/r_0)^{5/3}. \tag{167}$$

For $D = 1$ m, $\lambda = 500$nm, and $D/r_0 < 10$, σ_θ is less than 2 μrad. Since the angular offset between the LGS and tilt NGS considered in these results is more than an order of magnitude larger than σ_θ, the random deflection of the beam is negligible, and the LGS is considered to be fixed on-axis at the specified altitude.

Figure 24(a) shows the value of $\varepsilon_N^2(D/r_0)^{-5/3}$ for compensation using an LGS at altitude 10 to 30 km for $N = 6, 10, 15, 21$, with NGS offset $\theta_b/\theta_0 = 5$ and $L_0/D = 100$. Similarly, Figure 25(a) shows the value of $\varepsilon_N^2(D/r_0)^{-5/3}$ for compensation using an LGS at altitude 10 to 30 km for $N = 28, 36, 45, 55$, with NGS offset $\theta_b/\theta_0 = 5$ and $L_0/D = 50$. As was the case in the NGS compensation results, the dashed horizontal lines in Figure 24(a) and Figure 25(a) correspond to $\varepsilon_N^2 = 1$ rad^2 for each value of the relative aperture diameter D/r_0 considered. Performance results obtained with the MMSE estimator are shown by the solid curves. The dashed curves indicate the compensation performance when beacon phase measurements are used directly for the conjugate phase. These results show that the normalized error associated with the MMSE estimator is always less than the normalized error associated with using phase coefficients directly at all LGS altitudes, and for all orders of correction. The results in Figure 24(a) show that the relative error reduction with the MMSE estimator is small for the lower orders of correction ($N = 6, 10, 15, 21$). For the higher orders of correction ($N = 28, 36, 45, 55$) shown in Figure 25(a), the relative error reduction with the MMSE estimator is greater, with enhanced compensation performance evident at all LGS altitudes.

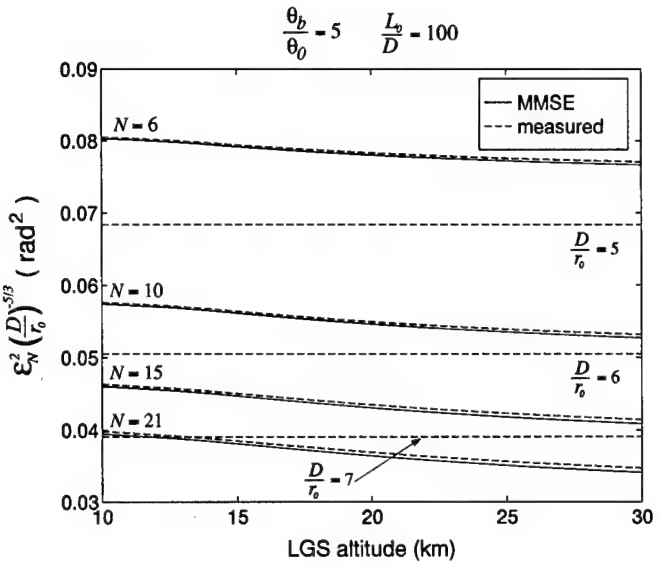

(a)

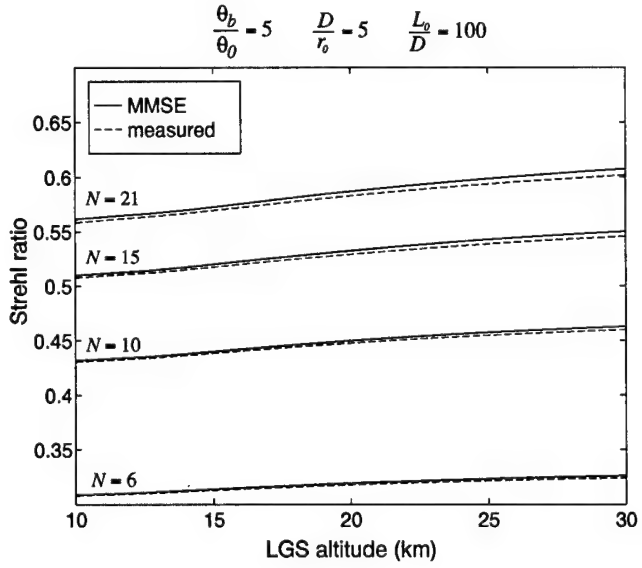

(b)

Figure 24. Comparison of lower-order LGS optimal compensation performance with conventional compensation performance. (a) Value of $\varepsilon_N^2(D/r_0)^{-5/3}$, for an on-axis LGS at altitude 10 to 30 km and a tilt-compensation NGS offset by $\theta_b/\theta_0 = 5$ using the MMSE estimator (solid line) and using beacon measurements directly (dashed line). Horizontal lines indicate levels at which $\varepsilon_N^2 = 1$ rad^2 for each value of D/r_0. (b) Corresponding Strehl ratio performance with relative aperture diameter $D/r_0 = 5$.

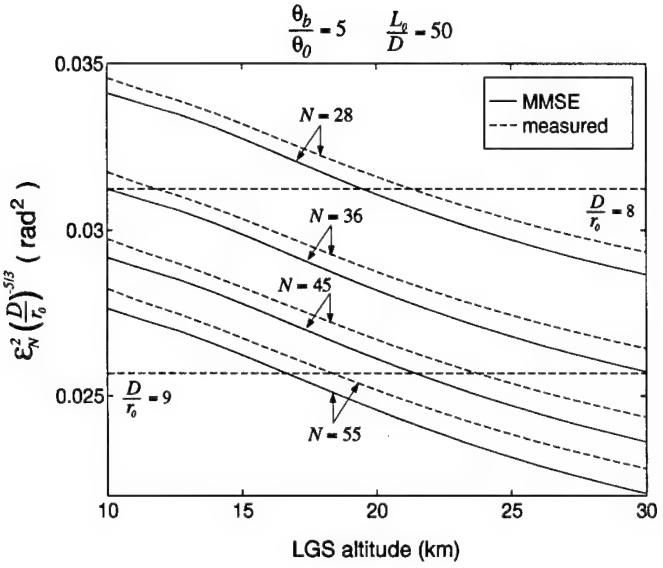

(a)

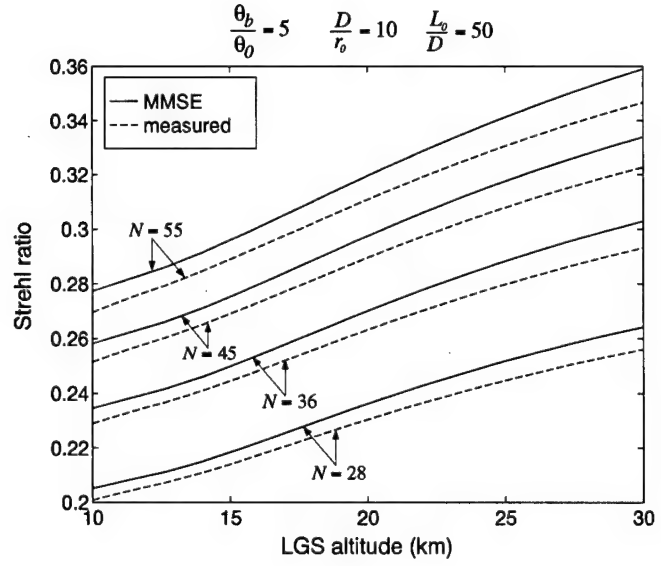

(b)

Figure 25. Comparison of higher-order LGS optimal compensation performance with conventional compensation performance. (a) Value of $\varepsilon_N^2(D/r_0)^{-5/3}$, for an on-axis LGS at altitude 10 to 30 km and a tilt-compensation NGS offset by $\theta_b/\theta_0 = 5$ using the MMSE estimator (solid line) and using beacon measurements directly (dashed line). Horizontal lines indicate levels at which $\varepsilon_N^2 = 1$ rad^2 for each value of D/r_0. (b) Corresponding Strehl ratio performance with relative aperture diameter $D/r_0 = 10$.

Figure 24(b) shows the Strehl ratio of the LGS/NGS AO system with $D/r_0 = 5$ corresponding to the results in Figure 24(a). Figure 25(b) shows the Strehl ratio of the LGS/NGS AO system with $D/r_0 = 10$ corresponding to the results in Figure 25(a). For all orders of correction and at all LGS altitudes, the MMSE compensation yields better imaging performance than when beacon measurements are used directly for compensation. For the higher correction orders ($N = 28, 36, 45, 55$), the MMSE estimator reduces the effect of focal anisoplanatism, recovering some of the imaging performance lost by using a lower-altitude LGS. For $N = 55$, the MMSE estimator can provide equivalent imaging performance at LGS altitudes approximately 20% lower than when beacon measurements are used directly in the compensation.

4.5 Tilt compensation enhancement

For ground-based AO imaging applications, accurate compensation for wave-front tilt is critical, since the variance of the tilt phase is large compared to higher-order modes. As stated in Eq. (88), the aperture-averaged piston-removed phase variance for Kolmogorov turbulence (infinite outer scale) is $1.0299(D/r_0)^{5/3}$. From the covariance matrix shown in Table 3, the sum of the variance of the tilt components $\langle a_{o2}^2 \rangle + \langle a_{o3}^2 \rangle = 0.896(D/r_0)^{5/3}$. Thus, the wave-front tilt components account for nearly 87% of the total aperture-averaged piston-removed phase variance. For finite outer scale (von Kármán) turbulence, the percentage of the piston-removed phase variance represented by tilt will be smaller than for Kolmogorov turbulence, but will still be large compared to all higher-order modes.

When anisoplanatism is present in an AO system, tilt compensation performance will be degraded. Using the optimal modal compensation theory, however, some of the performance degradation may be recovered when the partial correlation of the tilt components is properly accounted for in the MMSE estimator for tilt. The MMSE estimator also provides a framework for further enhancing tilt compensation performance. If the object phase coefficient vector $\mathbf{y}$ contains only tilt components a_{o2} and a_{o3}, and the beacon measurement vector contains tilt plus higher-order modes $a_{b2}, a_{b3}, a_{b4} \ldots, a_{bN}$, then any cross-correlation between tilt and the higher-order modes will further reduce the value of ε_N^2 given in Eq. (164) over the value of ε_N^2 when only tilt measurements are employed.

As discussed in Subsection 3.3.3, while tilt is uncorrelated with most higher-order modes for concurrent apertures, the magnitude of cross-correlation of tilt and many of the higher-order modes is enhanced for moderate values of the relative aperture separation s/D. A similar effect occurs when there is an angular separation between the object and the beacon in an AO system. This angular offset produces an effective aperture separation in the turbulence layers above the system aperture, as depicted in Figure 20. The resulting cross-correlation between the object wave-front tilt and the beacon wave-front higher-order modes can be used to enhance tilt compensation performance from an off-axis beacon, as is illustrated in the remainder of this section.

4.5.1 Single-layer turbulence model. The analysis associated with the cross-correlation between tilt and higher-order modes for an angular separation between the object and beacon can be simplified and the results can be generalized if a single-layer model is invoked for the turbulence [93]. For a single-layer model, the turbulence is regarded as being concentrated at a particular altitude above the aperture. Since the turbulence is concentrated within a single layer, the weight for that layer is $w_l = 1$. Note that many of the turbulence profiles presented in Table 1 are highly concentrated in a single layer. For instance, for the HV-21 profile, the layer at altitude 200 m has an associated weight of 0.8902.

The aperture and source geometry for a single-layer turbulence model is shown in Figure 26. The turbulence layer is located at an altitude z_l above the aperture of diameter D. The beacon is located at an altitude h_b above the aperture, and is displaced by the angle θ_b from the direction of the object (the optical axis of the system). Consider identifying the distant object in Figure 26 with source u in Figure 20, and identifying the beacon with source v. Accordingly, since the object is at an infinite range, the layer scaling factor associated with the object is $A_{u1l} = 0$. From Eq. (119), the layer scaling factor associated with the beacon is $A_{v2l} = z_l/h_b$. For θ_b in the $\hat{x}$ direction, the projected aperture separation in the layer is given by $s_l = z_l \tan\theta_b$. Thus, from Eq. (152), the cross-correlation of on-axis

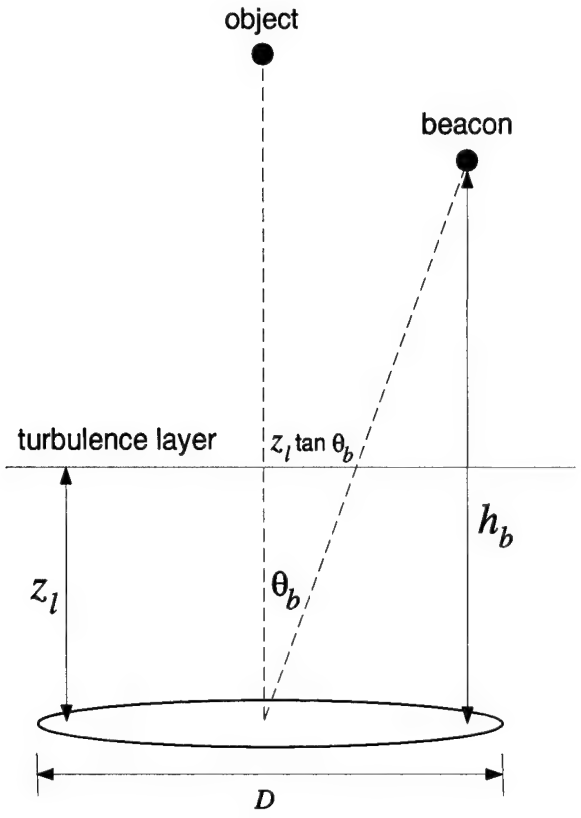

Figure 26. Geometry for a single-layer turbulence model. Projected aperture separation is given by $s_l = z_l \tan\theta_b$ for turbulence layer altitude z_l and beacon angle θ_b.

object phase coefficients a_{oi} with the off-axis beacon coefficients a_{bj} is given by:

$$\begin{aligned}\langle a_{oi} a_{bj} \rangle \;=\; & \left(\frac{D}{r_0}\right)^{5/3} \sqrt{3}\,\Gamma(8/3)\,2^{-5/3}\frac{6.88}{2.91}\,F\,(1 - z_l/h_b)^{-1} \\ & \times \left\{ \begin{array}{l} G\int_0^\infty \frac{dx}{x}(x^2 + x_0^2)^{-11/6} J_{(m_i+m_j)}\left[\frac{2z_l \tan\theta_b}{D}x\right] \\ \qquad \times J_{(n_i+1)}[x] J_{(n_j+1)}[(1 - z_l/h_b)x] \\ +H\int_0^\infty \frac{dx}{x}(x^2 + x_0^2)^{-11/6} J_{|m_i-m_j|}\left[\frac{2z_l \tan\theta_b}{D}x\right] \\ \qquad \times J_{(n_i+1)}[x] J_{(n_j+1)}[(1 - z_l/h_b)x], \end{array} \right. \end{aligned} \tag{168}$$

where F, G, and H are evaluated according to Eq. (148)-(150) with $\theta_{s_l} = 0$. As can be seen from Eq. (168), for a given mode combination the cross-correlation is parameterized by ratio of the layer altitude to the beacon altitude, z_l/h_b, the projected separation relative to the aperture diameter, $(z_l \tan\theta_b)/D$, and $x_0 = \pi D/L_0$. The parameter z_l/h_b characterizes

focal anisoplanatism, $(z_l \tan\theta_b)/D$ characterizes angular anisoplanatism, and x_0 accounts for the finite outer scale of the turbulence.

4.5.2 Higher-order modal cross-correlation. The cross-correlation between the object wave-front tilt and modal beacon measurements is shown in Figure 27. In these figures, a_{oi} $(i = 2, 3)$ represent the tilt components of the object wave-front, whereas a_{bj} $(j = 2, 3, \ldots, 15)$ represent the modal measurements from the beacon for tilt through Zernike 15. The cross-correlation is expressed by the correlation coefficient $\rho_{a_{oi}a_{bj}}$ computed as in Eq. 154. The autocorrelation results $(i = j)$ shown in Figure 27 illustrate the expected behavior of maximum correlation at $\theta_b = 0$ and decreasing correlation with increasing beacon angular offset. As indicated in these figures, at $\theta_b = 0$ all higher-order modes considered here are uncorrelated with tilt except the orthogonal components of coma $(j = 7, 8)$. The magnitude of the correlation coefficient for all other modes increases as $(z_l \tan\theta_b)/D$ increases, passing through some maximum value before going to 0 at large values of $(z_l \tan\theta_b)/D$. The enhanced cross-correlation between tilt and higher-order modes for $(z_l \tan\theta_b)/D > 0$ indicates that the higher-order measurements from an off-axis beacon may be used in the MMSE estimator for the object tilt components to improve tilt-compensation performance.

4.5.3 Natural-guide-star tilt compensation. To quantify the tilt-compensation performance enhancement obtained by including higher-order modes in the MMSE tilt estimator, the value of the aperture-averaged residual phase error after tilt correction is computed. This quantity is designated ε_T^2 (subscript T indicates tilt compensation only), and is equal to ε_N^2 for $N = 3$ calculated by use of Eq. (164). Thus, ε_T^2 is proportional to $(D/r_0)^{5/3}$ [see Eq. (166) and Eq. (168)], and compensation performance may be quantified by the normalized aperture-averaged residual phase variance after tilt correction, $\varepsilon_T^2(D/r_0)^{-5/3}$.

Figure 28(a) shows the value of $\varepsilon_T^2(D/r_0)^{-5/3}$ for an off-axis NGS employed as the AO beacon with $z_l/h_b = 0$. These results are obtained for the single-layer turbulence model with $L_0/D = 100$ and beacon angular offsets $(z_l \tan\theta_b)/D$ in the range from 0 to 0.5. The dashed curve shows the compensation performance when the NGS beacon

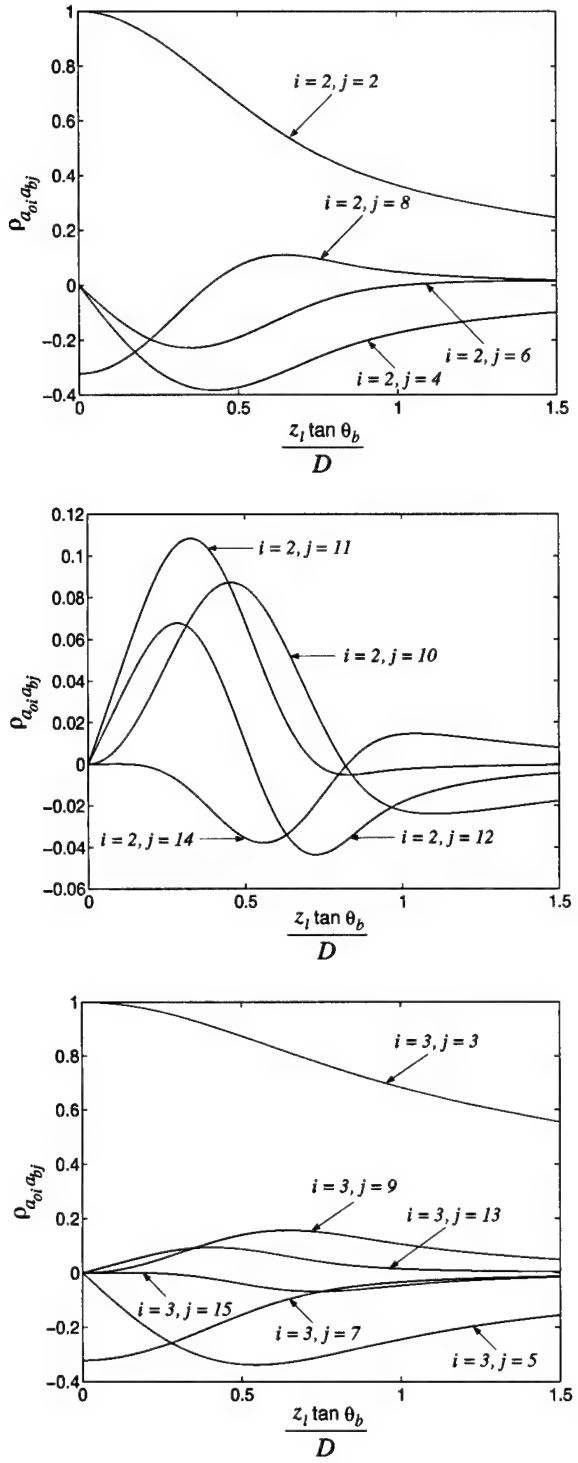

Figure 27. Cross-correlation of tilt with higher-order modes for angular beacon offset with single-layer turbulence model. Results are shown for the object wavefront tilt components with beacon measurements through Zernike 15 with $z_l/h_b = 0$ and $L_0/D = 100$ (uncorrelated modes omitted).

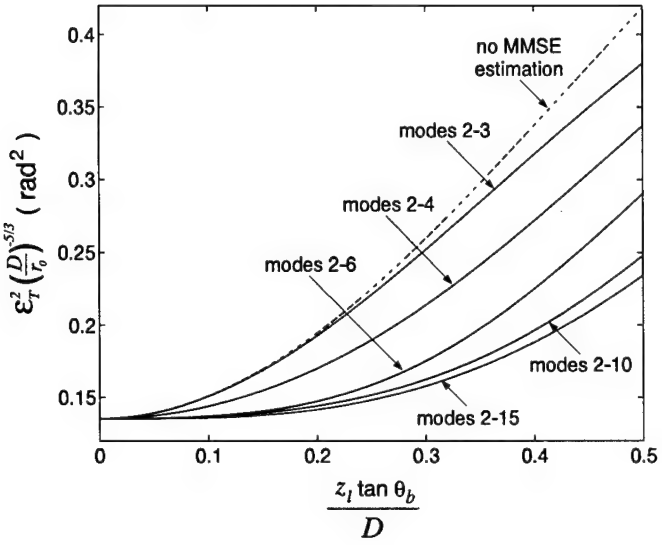

(a)

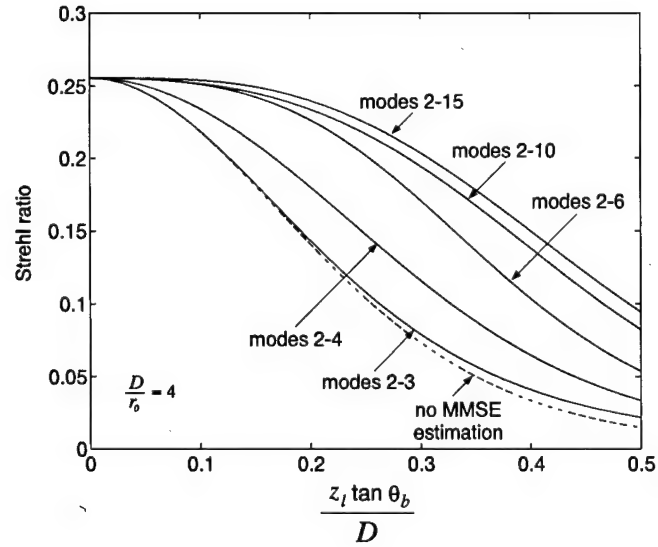

(b)

Figure 28. NGS tilt compensation performance with MMSE estimator including higher-order modes. (a) Value of $\varepsilon_T^2(D/r_0)^{-5/3}$ for the NGS beacon offset $(z_l \tan\theta_b)/D$ using the MMSE estimator for tilt (solid lines) and using tilt measurements directly (dashed line). (b) Corresponding Strehl ratio performance with relative aperture diameter $D/r_0 = 4$. Results shown are for $L_0/D = 100$, $z_l/h_b = 0$.

tilt measurements are used directly for wave-front tilt correction (no MMSE estimation employed). The solid curves show the effect of using the MMSE tilt estimator with the modal beacon measurements indicated. These results illustrate that if only tilt measurements are used in the MMSE estimator, optimal compensation will reduce the value of $\varepsilon_T^2(D/r_0)^{-5/3}$ at larger values of the NGS offset. When higher-order modes are included in the tilt estimator, $\varepsilon_T^2(D/r_0)^{-5/3}$ may be reduced significantly, especially at larger values of $(z_l \tan\theta_b)/D$.

Figure 28(b) shows the Strehl ratio performance corresponding to each curve in Figure 28 for $D/r_0 = 4$. For including modal measurements through Zernike 15 in the MMSE tilt estimator, the Strehl ratio remains within 1% of the limiting performance (at zero angular offset) out to $(z_l \tan\theta_b)/D = 0.15$. For using only tilt measurements in the estimator, the corresponding limiting performance angle is $(z_l \tan\theta_b)/D = 0.05$ (only 1/3 as great). For the largest NGS offset angle considered, using the beacon measurements directly for tilt compensation results in SR < 0.02. By incorporating beacon modal measurements through Zernike 15 in the tilt estimator, the Strehl ratio is increased by nearly 5 times to SR ~ 0.1. As the results in Figure 28 illustrate, for a fixed NGS offset, the tilt compensation performance may be enhanced by including higher-order modes in the tilt estimator. Correspondingly, an equivalent level of tilt compensation performance may be obtained at larger beacon offset angles when an optimal compensation is applied by the AO system.

4.5.4 Laser-guide-star tilt estimation. As was discussed in Section 2.3, the LGS signal does not contain tilt phase information since the tilt components of the LGS wave-front are naturally compensated by the reciprocal propagation from the beacon to the receiving aperture. This imposes a limitation on the use of the LGS in adaptive optics. In practice, therefore, the LGS is used for higher-order compensation, with tilt compensation provided by means of a nearby NGS.

Within the past few years, research has been conducted to develop methods of measuring tilt from the LGS. Belen'kii has proposed several techniques [5–7] in which LGS tilt is sensed by observing the upward propagation of the laser beam with auxiliary telescopes separated from the transmitter in transverse directions. Belen'kii has argued that the tilt

contribution from the downward path to the auxiliary telescope may be reduced by averaging over the angular extent of the beacon, thus singling out only the tilt induced in the upward path. This tilt measurement corresponds to the tilt induced in light incident from the astronomical object of interest. Belen'kii has also proposed a modification to this LGS tilt sensing method [8], which involves averaging the LGS image over the position of the auxiliary telescope in an array, and averaging over subaperture positions within the auxiliary telescopes. Ragazzoni et al. [57–59] have also proposed techniques for LGS tilt sensing that involve observing or transmitting the beacon from auxiliary telescopes located in transverse directions. Recently, Lukin [50] has reported on a method for optimal tilt correction using tilt measurements from monostatic and bistatic LGS adaptive optics configurations.

The method for LGS tilt estimation proposed in this research is substantially different from the methods of Belen'kii, Ragazzoni et al., and Lukin. Since the methods proposed previously attempt to measure tilt directly from the LGS signal, efforts must be made to overcome the beam reciprocity effect, thus leading to the bistatic configurations proposed. These configurations in turn induce tilt measurement inaccuracies which must be overcome through novel methods (angular, multiple aperture, and subaperture averaging in Belen'kii's method; concurrent NGS tilt sensing in Ragazzoni's method; optimal estimation in Lukin's method). In the method proposed here, we ignore the tilt components associated with the LGS completely, measuring only higher-order modal aberrations, which are assumed to be unaffected by beam reciprocity. When a LGS is positioned off-axis, the correlation between the on-axis tilt components from an astronomical object and the higher-order LGS modes is sufficiently strong to provide for tilt sensing using the MMSE tilt estimator. Thus, wave-front tilt components are not measured directly from the LGS signal, but instead, the higher-order measurements are used exclusively to estimate the wave-front tilt.

According to Eq. 164, the performance of the MMSE tilt estimator depends upon the cross-correlation of the object tilt components with higher-order beacon measurements (C_{yx}) as well as the cross-correlation of the beacon modes (C_{xx}). Considering the cross-correlation results in Figure 27, the performance of a tilt estimator based only on beacon

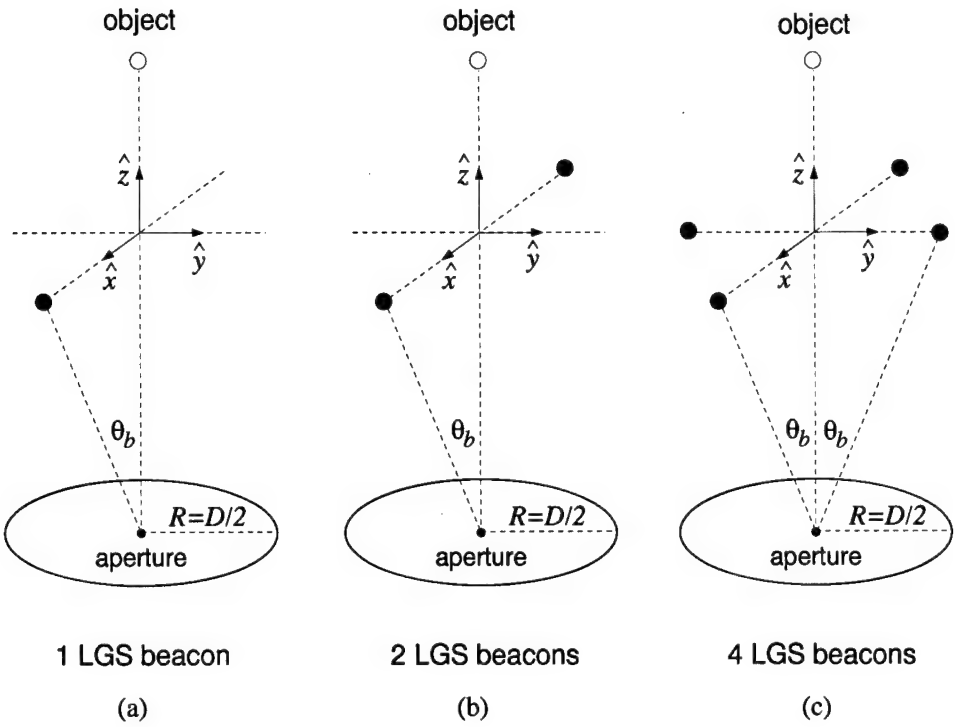

Figure 29. Off-axis deployment geometry for LGS tilt estimation. (a) Single beacon at angle θ_b in $\hat{x}$ direction. (b) Two beacon configuration along the $\hat{x}$ direction, both at angle θ_b. (c) Four LGS configuration with beacons offset along $\hat{x}$ and $\hat{y}$ axes, each at angle θ_b.

measurements beginning with Zernike 4 will be highly dependent upon the geometry of the LGS deployment. Consider the three off-axis LGS deployment configurations shown in Figure 29. These diagrams show (a) the LGS geometry for the case of a single beacon offset angularly in the $\hat{x}$ direction, (b) two beacons offset symmetrically along the $\hat{x}$ direction, and (c) four beacons offset along the $\hat{x}$ and $\hat{y}$ directions, each at angle θ_b.

In order to quantify performance for each configuration shown in Figure 29, we will consider all wave-front distortion higher than tilt to be perfectly compensated (presumably by an on-axis LGS not shown). Therefore, the residual phase variance after tilt compensation is due only to errors in estimating the actual tilt components associated with the on-axis object of interest. In this case, ε_T^2 is given by:

$$\varepsilon_T^2 = \mathrm{TR}\left[C_{yy} - C_{yx}C_{xx}^{-1}C_{xy}\right], \tag{169}$$

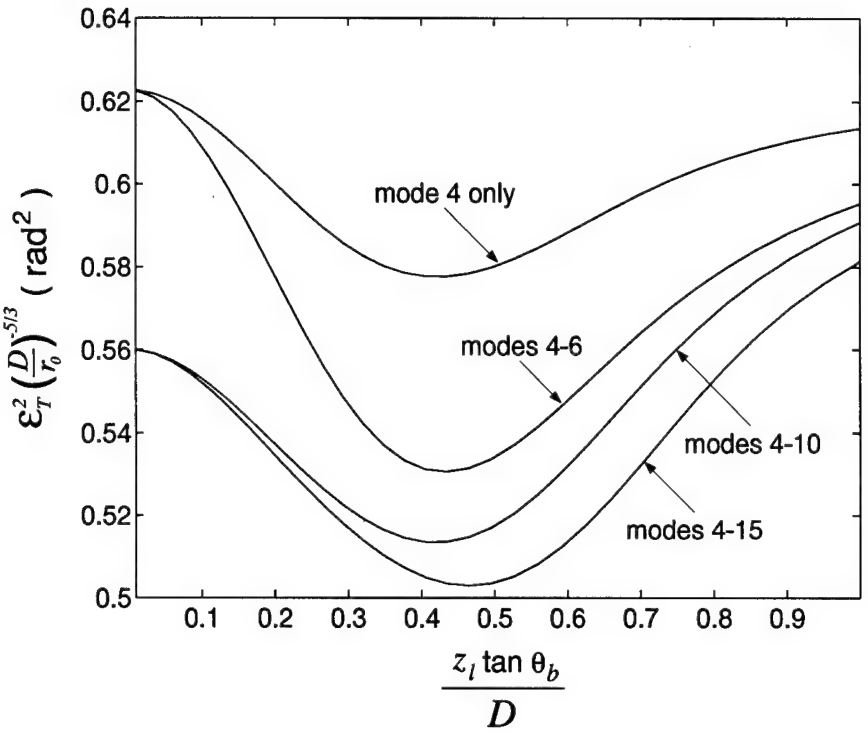

Figure 30. Tilt compensation performance from a single LGS. Value of $\varepsilon_T^2(D/r_0)^{-5/3}$ has been quantified using the beacon modal measurements indicated in the MMSE tilt estimator. Results shown are for $L_0/D = 100$ and $z_l/h_b = 0.01$.

where $\mathbf{y}$ represents the on-axis tilt components associated with the object and $\mathbf{x}$ represents higher-order measurements associated with each LGS. Again, since all matrix elements in Eq. (169) are proportional to $(D/r_0)^{5/3}$, the normalized residual phase variance $\varepsilon_T^2(D/r_0)^{-5/3}$ is considered in the results which follow.

The tilt estimation performance for the single LGS configuration is shown in Figure 30. The value of $\varepsilon_T^2(D/r_0)^{-5/3}$ was computed for $(z_l \tan\theta_b)/D$ in the range 0 to 1. Each curve corresponds to the residual phase variance after applying the tilt correction estimated from the higher-order beacon measurements indicated. For all mode combinations considered, $\varepsilon_T^2(D/r_0)^{-5/3}$ attains its smallest value at an LGS angle $(z_l \tan\theta_b)/D \sim 0.5$, the exact value depending upon the particular modal measurement combination employed. The general effect of including higher-order modes through Zernike 15 is to reduce the value of the normalized residual phase variance. Notice that inclusion of the coma components

(Zernike 7 and 8) reduces the error at $(z_l \tan\theta_b)/D = 0$, since these modes are correlated with the tilt components at zero angular offset (see Figure 27).

Tilt estimation performance results are shown in Figure 31(a)-(b) for the multiple-LGS beacon configurations depicted in Figure 29(b)-(c). Each curve represents the performance obtained by incorporating the modes indicated into the measurement vector, beginning with Zernike 4 (defocus) and continuing through Zernike 15. These results illustrate that increasing the number of LGS beacons will enhance the performance of the tilt estimator, as the higher-order modes from each beacon are correlated with the on-axis tilt components. The smallest value of $\varepsilon_T^2(D/r_0)^{-5/3}$ occurs for beacon offsets of $(z_l \tan\theta_b)/D = 0.4 - 0.6$, depending upon the modes included in the measurement vector $\mathbf{x}$.

The magnitude of the turbulence outer scale also has a significant effect on tilt compensation performance using the LGS measurements. Recall that the cross-correlation of Zernike coefficients in Eq. (168) depends upon the parameter $x_0 = \pi D/L_0$. Thus, the value of ε_T^2 will vary depending upon the value of the relative outer scale L_0/D. For the four-LGS beacon configuration, estimating tilt by measuring Zernike modes 4 to 15 from each beacon, ε_T^2 was quantified for $L_0/D = 10, 20, 50, 100$. These results are shown in Figure 32(a). As indicated in this figure, ε_T^2 decreases at all values of $(z_l \tan\theta_b)/D$ with decreasing values of L_0/D. Figure 32(b) shows the Strehl ratio performance corresponding to each curve in Figure 32(a) for the relative aperture diameter $D/r_0 = 4$. For $L_0/D = 100$, the Strehl ratio is no greater than 0.02 for any beacon offset angle. For smaller values of L_0/D, increased Strehl ratio performance is noted at all beacon offset angles. For $L_0/D = 10$, the Strehl ratio is over 0.3 for $(z_l \tan\theta_b)/D \sim 0.6$. Considering that the majority of experimental studies [2] have measured outer scale values in the range from 5 m to 100 m, smaller values of L_0/D may often be the case in practice. Thus, the LGS tilt estimation method considered here may offer a significant gain in imaging performance when tilt information is otherwise unavailable.

As was mentioned in Subsection 4.5.1, the parameter z_l/h_b characterizes the effect of focal anisoplanatism on the Zernike coefficient cross-correlation in Eq. (168). This parameter specifies the altitude of the effective turbulence layer relative to the altitude

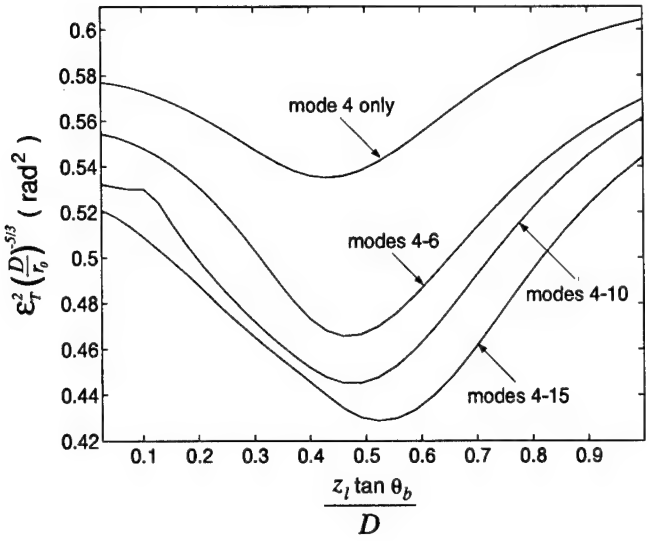

(a)

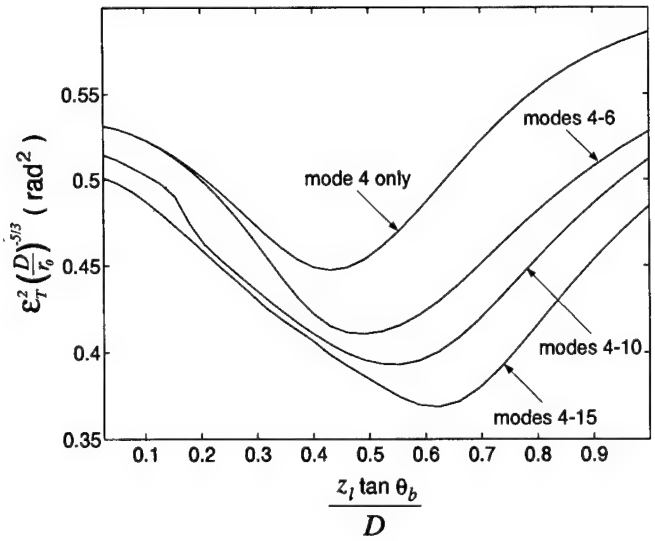

(b)

Figure 31. Tilt compensation performance for multiple LGS configurations for beacon measurements indicated on each curve. (a) $\varepsilon_T^2(D/r_0)^{-5/3}$ for two-LGS configuration, and (b) $\varepsilon_T^2(D/r_0)^{-5/3}$ for four-LGS beacon configuration. Results shown are for $L_0/D = 100$ and $z_l/h_b = 0.01$.

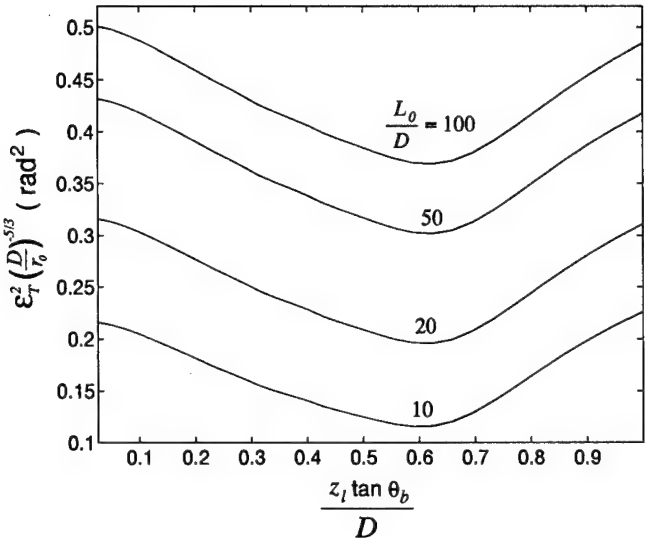

(a)

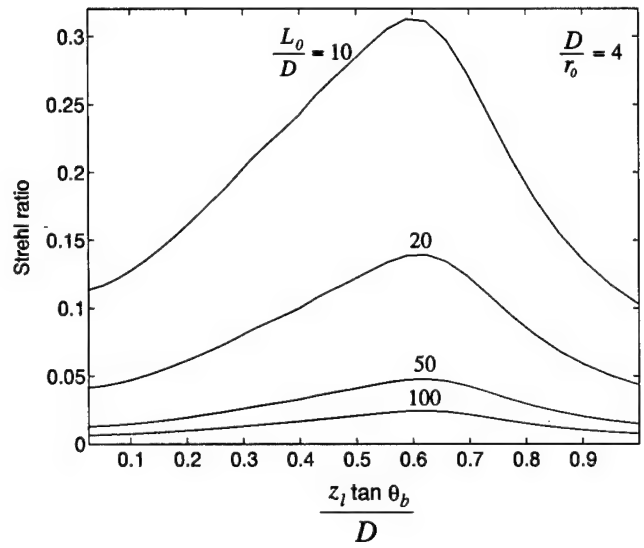

(b)

Figure 32. Effect of finite outer scale on LGS tilt compensation performance. (a) Normalized residual phase variance $\varepsilon_T^2(D/r_0)^{-5/3}$ and (b) Strehl ratio for beacon angular offset $(z_l \tan\theta_b)/D$. Results shown for four-LGS beacon configuration using Zernike modes 4 to 15 in the measurement vector for tilt estimation with $z_l/h_b = 0.01$.

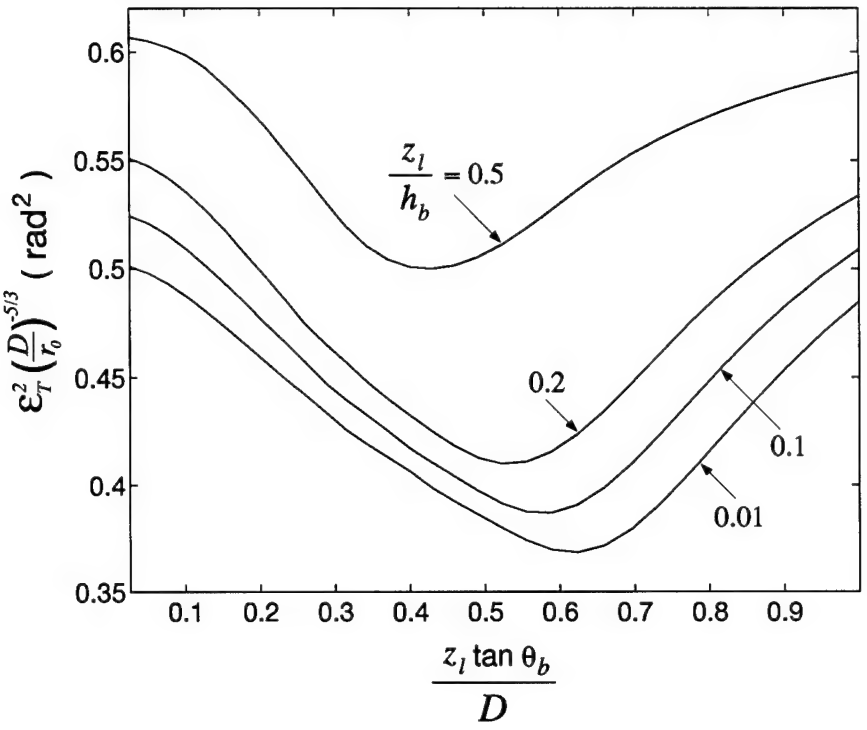

Figure 33. Effect of focal anisoplanatism on LGS tilt compensation performance. Results are shown for the four-LGS beacon configuration using Zernike modes 4 to 15 in the measurement vector for tilt estimation with $L_0/D = 100$.

of the beacon. For the results presented thus far, $z_l/h_b = 0.01$ has been employed in all calculations. This value of z_l/h_b was chosen since effective layer altitudes are typically on the order of 0.1 km to 1 km, whereas LGS beacon altitudes are on the order of 10 km to 100 km. If the effective layer altitude is higher, or the beacon altitude is lower, then focal anisoplanatism will effect the performance of LGS tilt estimation. This effect was quantified by calculating the value of ε_T^2 for $z_l/h_b = 0.01, 0.1, 0.2, 0.5$ using the four-LGS beacon configuration, estimating tilt by measuring Zernike modes 4 to 15 from each beacon. These results are shown in Figure 33, illustrating that focal anisoplanatism degrades the performance of LGS tilt estimation, since ε_T^2 increases for increasing values of z_l/h_b. This performance degradation comes about due to the reduced correlation of the on-axis object tilt with higher-order beacon modal measurements in the MMSE tilt estimator.

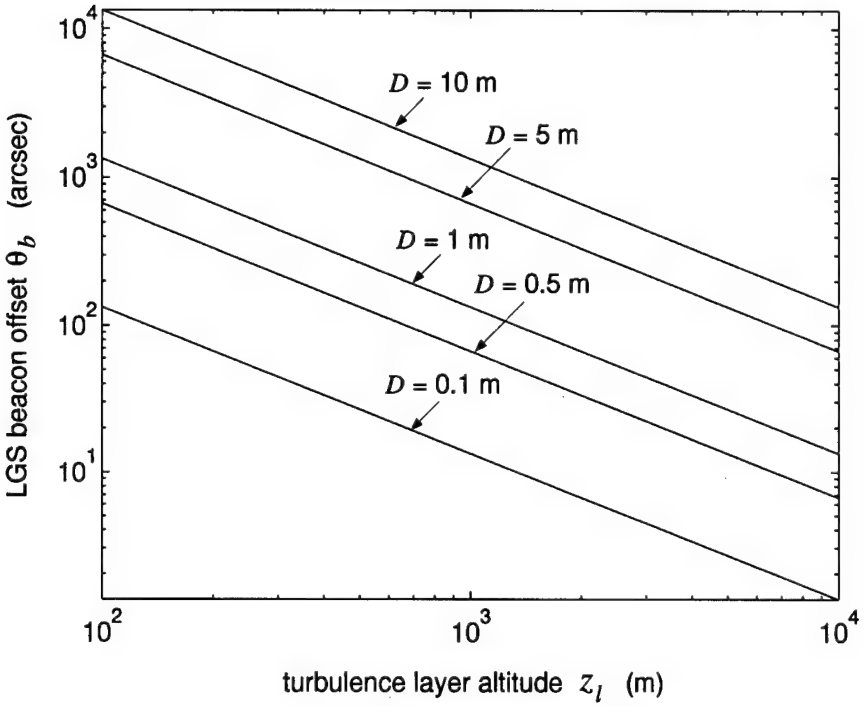

Figure 34. Beacon angular offset for peak LGS tilt estimation performance. Each curve shows the turbulence layer altitude z_l and beacon offset θ_b consistent with $(z_l \tan\theta_b)/D = 0.6$ for each value of aperture diameter D indicated.

For tilt estimation using the four-LGS beacon configuration with Zernike modes 4 to 15 in the measurement vector, tilt estimation performance is maximized at a non-zero beacon offset angle, as is illustrated in Figure 31(b) and Figure 32. This angle is determined by the combined effect of the enhanced cross-correlation between the on-axis object tilt and the off-axis higher-order beacon measurements. As is illustrated in Figure 32, for the range of relative outer scale values considered, the tilt compensation performance reaches its peak near $(z_l \tan\theta_b)/D = 0.6$. Thus, to achieve the greatest possible tilt compensation performance with the method discussed here, the LGS beacon offset angle should be such that:

$$\theta_b = \tan^{-1}\left(\frac{0.6D}{z_l}\right). \tag{170}$$

For a given aperture diameter D, Eq. (170) establishes a relationship between z_l and θ_b. This relationship is shown graphically in Figure 34 for several values of D. Figure 34

indicates that for $z_l = 1$ km, θ_b should be on the order of 10 arcsec when $D = 0.1$ m. When $D = 10$ m, however, θ_b should be approximately 2,000 arcsec (over 0.5 deg) for $z_l = 1$ km. Intermediate aperture diameters will require θ_b to be approximately 100 arcsec to 1,000 arcsec. Since 1 arcsec = 4.85 μrad, and the isoplanatic angle θ_0 is nominally 7 μrad for the HV-21 C_n^2 profile, then θ_b for peak LGS tilt compensation performance may be as much as several hundred times θ_0.

4.6 Summary

In this chapter, the optimal modal compensation theory developed in Chapter III was applied to AO compensation for ground-based imaging systems. The turbulence-induced phase from an NGS or LGS beacon is only partially correlated with the phase from the object of interest when the beacon is offset from the optical axis or at finite altitude. Thus, the wave-front compensation performance obtained by applying beacon phase measurements directly in an AO system is sub-optimal. Instead, to achieve optimal compensation performance, the object phase must be estimated using the MMSE estimator given modal beacon measurements.

For the off-axis NGS, the MMSE estimator resulted in compensation performance that was equal to or better than the compensation performance using beacon measurements directly for all orders of correction and at all beacon offset angles. For the correction orders $N = 6, 10, 15, 21$ with a 1 m aperture, the MMSE estimator provides enhanced performance for beacon offsets greater than $2\,\theta_0$. For $N = 28, 36, 45, 55$ with a 1 m aperture, the MMSE estimator provides enhanced performance for beacon offsets greater than $0.5\,\theta_0$. For the highest-order correction studied, the MMSE estimator can provide equivalent imaging performance at NGS offset angles 10% larger than when NGS measurements are used directly for compensation.

For the case of an on-axis LGS with an off-axis NGS for tilt compensation, the MMSE estimator resulted in enhanced compensation performance over using beacon measurements directly throughout the entire range of LGS altitudes considered. The relative performance enhancement was greater for the higher correction orders. The MMSE estimator partially reduces the effect of focal anisoplanatism. For the highest-order correction studied, the

MMSE estimator can provide equivalent imaging performance at altitudes 20% lower than when beacon measurements are using directly for wave-front compensation.

The MMSE estimator was also employed in order to enhance tilt compensation from an off-axis NGS. Using the MMSE estimator for object tilt components, higher-order modes can be included in the beacon measurement vector. For an off-axis NGS, many of these higher-order modes are correlated with the on-axis tilt components. Thus, including these modes in the tilt estimator results in increased Strehl ratio performance over using tilt measurements only. For tilt compensation from an off-axis NGS using beacon Zernike modes 2 to 15, it was shown that the maximum beacon offset angle for nearly-limiting performance is 3 times larger than when only tilt measurements are used. Equivalently, for a given beacon offset, the Strehl ratio is increased by incorporating higher-order modes.

While tilt components cannot be measured conventionally from the LGS wave-front due to beam reciprocity effects, the MMSE tilt estimator permits the tilt components to be estimated using only higher-order measurements from the LGS beacon. Since the higher-order modes from an off-axis LGS beacon are correlated with on-axis tilt, the off-axis higher-order beacon measurements enable estimation of the on-axis tilt components. The performance of such an estimator depends upon the geometric configuration of the LGS beacons, which beacon modes are used, the relative turbulence outer scale L_0/D, and the extent of focal anisoplanatism degradation. It was shown that for a constellation of four LGS beacons offset orthogonally from the optical axis, using measurements of Zernike modes 4 to 15 from each beacon, the Strehl ratio can be over 0.3 for $D/r_0 = 4$ and $L_0/D = 10$. Performance is degraded for larger values of L_0/D. The tilt estimation performance is degraded further when focal anisoplanatism reduces the cross-correlation between tilt and the higher-order modal measurements. Peak LGS tilt estimation performance occurs at an angle which depends upon the diameter of the aperture and the height of the effective turbulence layer. This peak angle was shown to be significantly larger than the isoplanatic angle θ_0 for typical AO systems.

V. *Airborne Laser Beam-Steering Adaptive Optics*

5.1 Introduction

For a system such as Airborne Laser (ABL) [11, 26], which attempts to project a laser beam through the atmosphere onto a distant object over an extended period of time, turbulence-induced phase aberrations degrade system performance. Random angular beam deflections result in reduced energy deposition on the surface of the target object, whereas spatial dispersion reduces the incident beam energy density. Therefore in ABL target engagements, beam steering should account for the effects of turbulence-induced wave-front tilt. This chapter describes the application of the optimal modal compensation theory developed in Chapter III to beam-steering adaptive optics for the ABL.

Due to the finite temporal response of adaptive-optical systems, steering commands must be based upon time-delayed wave-front measurements. The dynamics of the ABL target engagement scenario and turbulence-induced anisoplanatism cause the time-delayed wave-front measurements to be decorrelated from the required wave-front tilt correction. This decorrelation leads to suboptimal beam-steering performance when time-delayed wave-front measurements are used directly for compensation. In Section 5.2, optimal modal compensation theory is applied to the ABL target engagement scenario for optimal compensation by an AO system, illustrating the necessity to quantify the temporal cross-correlation of Zernike coefficients for a dynamic system. Section 5.3 discusses how aperture and source motion effects are modeled in the analysis geometry associated with the optimal compensation theory. ABL target engagement results are presented in Section 5.4, demonstrating that beam-steering performance is enhanced by incorporating tilt plus higher-order time-delayed measurements in the MMSE estimator for wave-front tilt. The chapter is summarized in Section 5.5.

5.2 Application of theory to Airborne Laser beam-steering adaptive optics

As was discussed in Chapter II, the performance of a beam-projection system such as the Airborne Laser is also quantified by a Strehl ratio which depends upon the aperture-averaged phase variance. When a conjugate phase is applied to the wave-front prior to

beam propagation, the residual phase variance determines the performance. In the case of adaptive-optical beam steering control, a conjugate tilt phase $\tilde{\phi}_o$ is applied to the outgoing beam, and the performance of the system depends upon the aperture-averaged residual phase variance after tilt correction, designated ε_T^2, and calculated as:

$$\varepsilon_T^2 = \int \mathrm{d}\vec{\rho}\, W(\vec{\rho})\, \left\langle [\phi_o(R\vec{\rho},t) - \tilde{\phi}_o(R\vec{\rho},t)]^2 \right\rangle . \tag{171}$$

The corresponding lower bound on Strehl ratio is given by:

$$\mathrm{SR} \geq \exp(-\varepsilon_T^2). \tag{172}$$

The tilt correction phase $\tilde{\phi}_o(R\vec{\rho},t)$ may be expanded in terms of the orthogonal components of tilt, $\tilde{a}_{o2}(t)$ and $\tilde{a}_{o3}(t)$ (Noll's ordering [54]). By employing the orthonormality property of the Zernike polynomials on the unit circle, ε_T^2 may be expressed as:

$$\varepsilon_T^2 = \int \mathrm{d}\vec{\rho}\, W(\vec{\rho})\, \langle \phi_o^2(R\vec{\rho},t)\rangle - \sum_{i=2}^{3} \langle a_{oi}^2(t)\rangle + \sum_{i=2}^{3} \langle [a_{oi}(t) - \tilde{a}_{oi}(t)]^2 \rangle , \tag{173}$$

where $a_{oi}(t)$ is the coefficient of the expansion of $\phi_o(R\vec{\rho},t)$ with respect to the Zernike polynomials:

$$a_{oi}(t) \equiv \int \mathrm{d}\vec{\rho}\, W(\vec{\rho})\, \phi_o(R\vec{\rho},t) Z_i(\vec{\rho}). \tag{174}$$

The expression for ε_T^2 has the same form as δ_N^2 in Chapter III, and therefore the optimal modal compensation theory may also be applied to AO compensation in ABL beam steering.

In ABL target engagements, the conjugate tilt coefficients $\tilde{a}_{o2}(t)$ and $\tilde{a}_{o3}(t)$ are determined by measurements from a beacon source. Due to the finite temporal response of the AO system, a time delay exists between the beacon measurements at time $t-\tau$ and the tilt correction applied to the outgoing laser beam at time t. The measured beacon tilt coefficients, designated $a_{b2}(t-\tau)$ and $a_{b3}(t-\tau)$, are determined by the projection of the beacon phase $\phi_b(R\vec{\rho},t-\tau)$ onto the appropriate Zernike polynomials:

$$a_{bi}(t-\tau) = \int \mathrm{d}\vec{\rho}\, W(\vec{\rho}) \phi_b(R\vec{\rho},t-\tau) Z_i(\vec{\rho}), \text{ for } i = 2,3. \tag{175}$$

Due to aperture and source motion within the delay period τ, $a_{bi}(t-\tau)$ will be decorrelated from $a_{oi}(t)$ [94]. Thus, if the beacon measurements are used directly for the conjugate tilt, that is $\tilde{a}_{oi}(t) = a_{bi}(t-\tau)$, then the compensation will be suboptimal. Optimal performance may be obtained by estimating the coefficients $a_{oi}(t)$ given measurements $a_{bi}(t-\tau)$ using an MMSE estimator for the object wave-front tilt components.

The notation associated with MMSE tilt estimation follows that of the MMSE estimator introduced in Subsection 3.2.2. For the beam-steering application, however, only the wave-front tilt components need to be estimated. The tilt acquired by the laser beam as it propagates to the target object is described by the tilt vector $\mathbf{y}$ whose elements are the orthogonal components of the wave-front tilt at time t:

$$\mathbf{y} = \begin{bmatrix} a_{o2}(t) \\ a_{o3}(t) \end{bmatrix}. \tag{176}$$

The beacon measurement vector $\mathbf{x}$ may contain tilt plus higher-order modal components measured at time $t-\tau$:

$$\mathbf{x} = \begin{bmatrix} a_{b2}(t-\tau) \\ a_{b3}(t-\tau) \\ a_{b4}(t-\tau) \\ \vdots \\ a_{bN}(t-\tau) \end{bmatrix}. \tag{177}$$

The tilt estimate vector $\hat{\mathbf{y}}$ applied at time t based on measurements at time $t-\tau$ will contain two elements corresponding to the MMSE estimates of the tilt acquired by the propagating laser beam:

$$\hat{\mathbf{y}} = \begin{bmatrix} \hat{a}_{o2}(t,\tau) \\ \hat{a}_{o3}(t,\tau) \end{bmatrix}. \tag{178}$$

According to Eq. (106), $\hat{\mathbf{y}}$ is related to $\mathbf{y}$ and $\mathbf{x}$ by:

$$\hat{\mathbf{y}} = C_{yx}C_{xx}^{-1}\mathbf{x}. \tag{179}$$

When the MMSE estimator is used in the tilt compensation, according to Eq. (109), ε_T^2 is given by:

$$\varepsilon_T^2 = \int \mathrm{d}\vec{\rho}\, W(\vec{\rho})\, \langle \phi_o^2(R\vec{\rho}, t)\rangle - \mathrm{TR}\left[C_{yx} C_{xx}^{-1} C_{xy}\right]. \tag{180}$$

The MMSE estimate of the phase coefficients $\mathbf{y}$ given time-delayed phase coefficient measurements $\mathbf{x}$ depends upon the covariance matrices C_{yx} and C_{xx}. Since $y_m = a_{o(m+1)}(t)$ and $x_n = a_{b(n+1)}(t-\tau)$, the mn-th element of C_{yx} is given by:

$$[C_{yx}]_{mn} = \langle a_{o(m+1)}(t) a_{b(n+1)}(t-\tau)\rangle = R_{a_{(m+1)}a_{(n+1)}}(\tau), \tag{181}$$

where $R_{a_{(m+1)}a_{(n+1)}}(\tau)$ is the temporal cross-correlation of $a_{o(m+1)}(t)$ with $a_{b(n+1)}(t-\tau)$. Likewise, since $x_m = a_{b(m+1)}(t-\tau)$ and $x_n = a_{b(n+1)}(t-\tau)$, the mn-th element of C_{xx} is given by:

$$[C_{xx}]_{mn} = \langle a_{b(m+1)}(t-\tau) a_{b(n+1)}(t-\tau)\rangle = R_{a_{(m+1)}a_{(n+1)}}(0). \tag{182}$$

Similarly, the matrix elements of C_{yy} and C_{xy} correspond to the temporal cross-correlation of the appropriate Zernike coefficients.

5.3 Temporal cross-correlation for aperture and source motion

The temporal cross-correlation of Zernike coefficients when aperture and source motion are present has been developed previously by Whiteley et al. [94]. The analysis geometry and cross-correlation results are summarized in this section. Figure 35 shows an aperture of radius R whose position vector at times separated by a period τ is designated by $\vec{r}_a(t-\tau)$ and $\vec{r}_a(t)$. An optical source is located at times separated by a period τ by the vectors $\vec{r}_s(t-\tau)$ and $\vec{r}_s(t)$, respectively. Atmospheric layers are indexed by the subscript l, located at height z_l, have thickness Δz_l, and a wind velocity $\vec{v}_l$. At a given time, light rays propagating from the source to each point in the aperture will intersect each layer, thus defining the temporal projections of the aperture in that layer, as is indicated in Figure 35. Due to the aperture and source motion during the time-delay period τ, the analysis geometry in Figure 35 corresponds exactly with the analysis geometry for the interferometric system in Figure 12. This correspondence indicates that the anisoplanatism introduced by

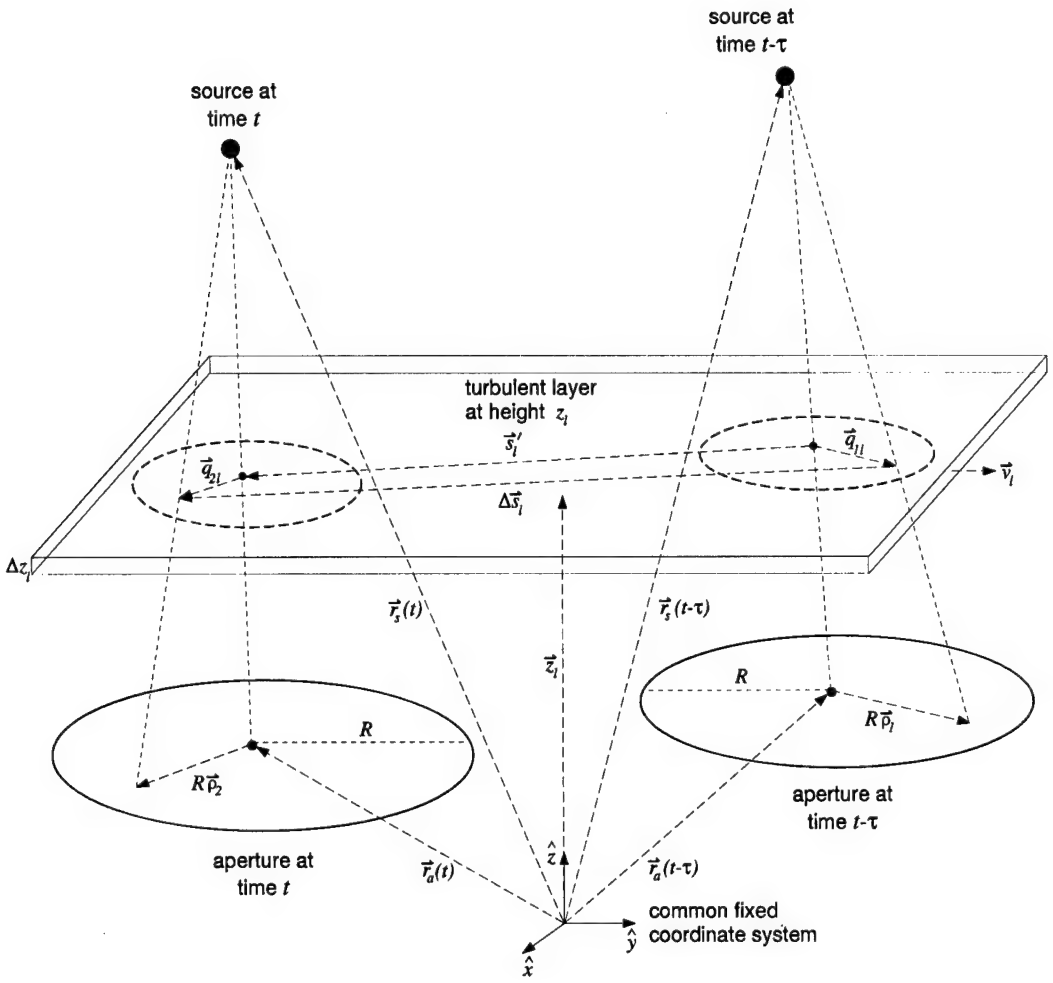

Figure 35. Analysis geometry used for computing the temporal cross-correlation of Zernike coefficients for aperture and source motion.

time-delay in a dynamic system is a generalized form of spatial anisoplanatism. Therefore, the spatial cross-correlation analysis associated with Figure 12 may be applied directly to Figure 35 with proper accounting for the aperture and source motion.

Consider the case where the aperture and source velocities, designated $\vec{v}_a$ and $\vec{v}_s$, are constant with respect to the period τ. Accordingly, the position vectors of the aperture and source at time $t-\tau$ and time t are related as follows:

$$\vec{r}_a(t) = \vec{r}_a(t-\tau) + \vec{v}_a\tau, \tag{183}$$

$$\vec{r}_s(t) = \vec{r}_s(t-\tau) + \vec{v}_s\tau, \tag{184}$$

Comparing the analysis geometry in Figure 35 to Figure 12, we recognize that $\vec{r}_a(t-\tau)$ corresponds to aperture location $\vec{r}_{a1}$, $\vec{r}_a(t)$ corresponds to aperture location $\vec{r}_{a2}$, $\vec{r}_s(t-\tau)$ corresponds to source location $\vec{r}_{s1}$, and $\vec{r}_s(t)$ corresponds to source location $\vec{r}_{s2}$. The effective projected aperture separation in the lth layer as a function of τ, designated $\vec{s}_l\,'(\tau)$, is obtained using Eq. (120), with $\vec{r}_{a2}$, $\vec{r}_{a1}$ and $\vec{r}_{s2}$, $\vec{r}_{s1}$ related by:

$$\vec{r}_{a2} = \vec{r}_{a1} + \vec{v}_a\tau, \tag{185}$$

$$\vec{r}_{s2} = \vec{r}_{s1} + \vec{v}_s\tau. \tag{186}$$

By employing Taylor's frozen-flow hypothesis to account for the temporal effects of the wind velocity v_l, $\vec{s}_l\,'(\tau)$ is given by [94]:

$$\vec{s}_l\,'(\tau) = \vec{v}_a\tau + [A_l(\tau) - A_l(0)](\vec{r}_s - \vec{r}_a) + A_l(\tau)(\vec{v}_s - \vec{v}_a)\tau - \vec{v}_l\tau, \tag{187}$$

where the layer aperture scaling factor $A_l(\tau)$ is given by:

$$A_l(\tau) = \frac{(z_l - \vec{r}_a\cdot\hat{z}) - (\vec{v}_a\cdot\hat{z})\tau}{(\vec{r}_s - \vec{r}_a)\cdot\hat{z} + [(\vec{v}_s - \vec{v}_a)\cdot\hat{z}]\tau}, \tag{188}$$

and $\vec{r}_a$, $\vec{r}_s$ are understood to be the position vectors of the aperture and source at time $t-\tau$.

An expression for the temporal cross-correlation $R_{a_ia_j}(\tau)$ is obtained using the spatial cross-correlation expression in Eq. (152) by substituting $\vec{s}_l\,'(\tau)$ for $\vec{s}_l$, substituting $A_l(\tau)$ for A_{v2l}, and substituting $A_l(0)$ for A_{u1l}:

$$\begin{aligned}
&R_{a_ia_j}(\tau;\vec{r}_a,\vec{r}_s;\vec{v}_a,\vec{v}_s;\vec{v}_l)\\
&= \left(\frac{D}{r_0}\right)^{5/3}\sqrt{3}\,\Gamma(8/3)\,2^{-5/3}\left(\frac{6.88}{2.91}\right)F\sum_l w_l\,\{[1-A_l(0)][1-A_l(\tau)]\}^{-1}\\
&\times\left\{\begin{array}{l}
G\displaystyle\int_0^\infty \tfrac{dx}{x}(x^2+{x_0}^2)^{-11/6}J_{(m_i+m_j)}\left[\tfrac{2s_l\,'(\tau)}{D}x\right]\\
\qquad\times J_{(n_i+1)}\{[1-A_l(0)]x\}J_{(n_j+1)}\{[1-A_l(\tau)]x\}\\
+H\displaystyle\int_0^\infty \tfrac{dx}{x}(x^2+{x_0}^2)^{-11/6}J_{|m_i-m_j|}\left[\tfrac{2s_l\,'(\tau)}{D}x\right]\\
\qquad\times J_{(n_i+1)}\{[1-A_l(0)]x\}J_{(n_j+1)}\{[1-A_l(\tau)]x\}.
\end{array}\right.
\end{aligned} \tag{189}$$

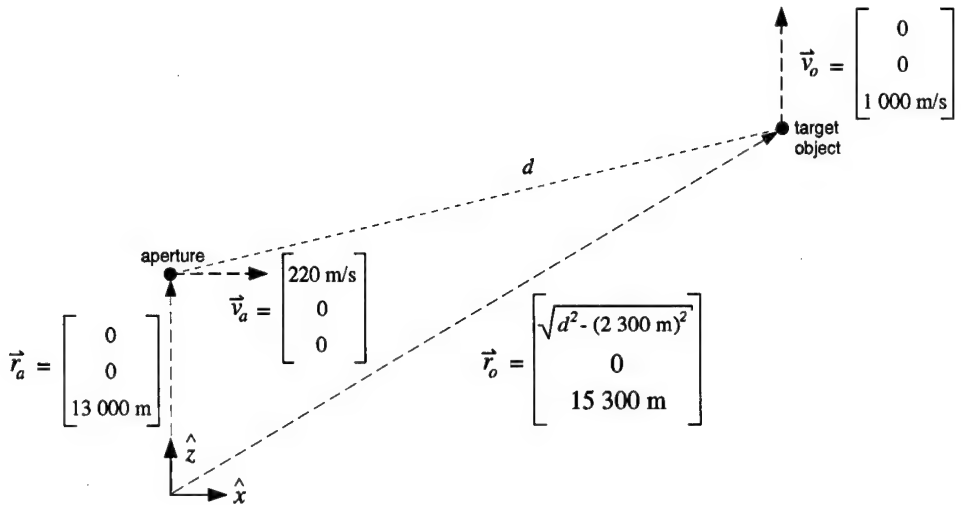

Figure 36. ABL target engagement scenario. This figure illustrates the particular aperture and target positions and velocities used to quantify temporal cross-correlation of the Zernike coefficients used in the MMSE tilt estimator. The position of the target object is specified relative to the position of the aperture by the parameter d, which represents the distance between the target and aperture.

The functions F, G, and H are computed as in Eq. (148)-(150), with θ_{s_l} replaced by $\theta_{s_l'}(\tau)$, which is the angle between $\vec{s}_l\,'(\tau)$ and $\hat{x}$.

5.4 Beam-steering performance enhancement

The expression for the temporal cross-correlation given in Eq. (189) may be used to quantify the elements of the MMSE tilt estimator in Eq. (179). In order to perform these calculations, a certain geometric specification must be made. The geometry used to obtain the results presented in this section is shown in figure 36. This geometry models the expected target engagement for an ABL system [10].

In this geometry, the aperture is located at a height of 13,000 m above a fixed origin specified by the unit vectors $\hat{x}$, $\hat{y}$, and $\hat{z}$. The $\hat{x}$ vector is in the direction of the aperture's velocity vector, $\vec{v}_a$, whose magnitude is 220 m/s. The target object is located at a height of 15,300 m. The component of the target position vector in the $\hat{y}$ direction is 0. The $\hat{x}$ component of the target's position is specified by the parameter d, representing the

distance between the transmitting aperture and the target object. Since the difference in the $\hat{z}$ components of $\vec{r}_o$ and $\vec{r}_a$ is fixed to be 2,300 m, and the $\hat{y}$ component of $\vec{r}_o$ is always 0, then the $\hat{x}$ component of $\vec{r}_o$ is given by:

$$\vec{r}_o \cdot \hat{x} = \sqrt{d^2 - (2300 \text{ m})^2}. \tag{190}$$

For all calculations, the aperture diameter is 1.75 m, and the wind velocity, $\vec{v}_l$ was set to 0, and $d = 100$ km. The velocity of the target object, $\vec{v}_o$, is 1,000 m/s in the $\hat{z}$ direction.

In ABL target engagements, a beacon signal (measured at time $t - \tau$) is generated by laser reflection from the leading surface of the target object. The system attempts to steer the transmitted beam at time t to the same physical location from which the beacon was received, with the forward motion of the target determining the impact point on the object's body (the target's displacement is $v_o\tau$). Thus, it may be said that $\vec{r}_o(t) = \vec{r}_b(t-\tau)$. This scenario corresponds to $\vec{v}_s = 0$, which implies that $\vec{r}_s(t) = \vec{r}_s(t - \tau)$ in Figure 35. Thus, the temporal dependence of the cross-correlation is determined primarily by the aperture velocity $\vec{v}_a$.

5.4.1 Turbulence model. The expression for $R_{a_i a_j}(\tau)$ given in Eq. (189) requires the optical turbulence to be modeled in a finite number of discrete layers with the parameters w_l, and L_0. For the ABL target engagement considered here, we have chosen to use Hufnagel-Valley (HV-21) $C_n^2(z)$ profile. The weights shown in Table 1 are not adequate for modeling the turbulence since C_n^2 is distributed differently between the aperture and target than was the case for the HV-21 weights. Over the altitudes considered here, C_n^2 decreases in a nearly linear fashion with z. Hence, the atmosphere was divided into 10 evenly-spaced layers between the aperture altitude (13,000 m) and the target altitude (15,300 m). The altitude and weight for each layer is shown in Table 5. For the results shown in this chapter, a constant value of $L_0 = 100$ m was chosen for all layers.

5.4.2 Higher-order modal cross-correlation. Since the projected aperture separation $s_l{}'(\tau)$ is non-zero for $\tau > 0$, then the cross-correlation effect discussed in Chapter III will also be manifested in the cross-correlation of tilt with higher-order modes in

layer l	altitude z_l (m)	w_l	layer l	altitude z_l (m)	w_l
1	13,209	0.1281	6	14,255	0.0963
2	13,418	0.1216	7	14,464	0.0904
3	13,627	0.1151	8	14,673	0.0846
4	13,836	0.1087	9	14,882	0.0791
5	14,045	0.1024	10	15,091	0.0738

Table 5. Turbulence modeling for ABL target engagement. Altitudes and weighting factors associated with 10 discrete layers used to model the atmosphere between the aperture and the target.

an ABL target engagement. Using Eq. (189) and the target engagement geometry shown in Figure 36, it can be demonstrated that for many higher-order modes, the magnitude of cross-correlation with tilt increases from 0 at zero time delay through some maximum value before decreasing to 0 at long time delays. Thus, including these higher-order modes in the MMSE tilt estimator will enhance its performance at moderate time delays.

The cross-correlation between the tilt acquired by the transmitted beam upon propagation to the target object and time-delayed modal measurements from a beacon source are shown in Figure 37. In these figures, a_i $(i = 2, 3)$ represent the tilt components for propagation to the target object at time t, whereas a_j $(j = 2, 3, \ldots, 15)$ represent the modal measurements from the beacon for tilt through Zernike 15 at time $(t - \tau)$. The cross-correlation has been normalized as indicated on the figures to express a correlation coefficient in the range -1 to 1. The autocorrelation of the tilt components $(i = j)$ shown in Figure 37 illustrate the expected behavior of maximum correlation at $\tau = 0$ and decreasing correlation with increasing time delay. As indicated in these figures, at $\tau = 0$ all higher-order modes considered here are uncorrelated with tilt except the orthogonal components of coma $(j = 7, 8)$. The magnitude of the correlation coefficient for all other modes increases as τ increases, passing through some maximum value before going to 0 at large τ. The enhanced cross-correlation between tilt and higher-order modes for $\tau > 0$ indicates that time-delayed higher-order measurements may be used in the MMSE tilt estimator to improve its performance.

5.4.3 Tilt compensation performance results. To study the effect of higher-order modes in the MMSE tilt estimator, let us consider the value of ε_T^2 as the modal

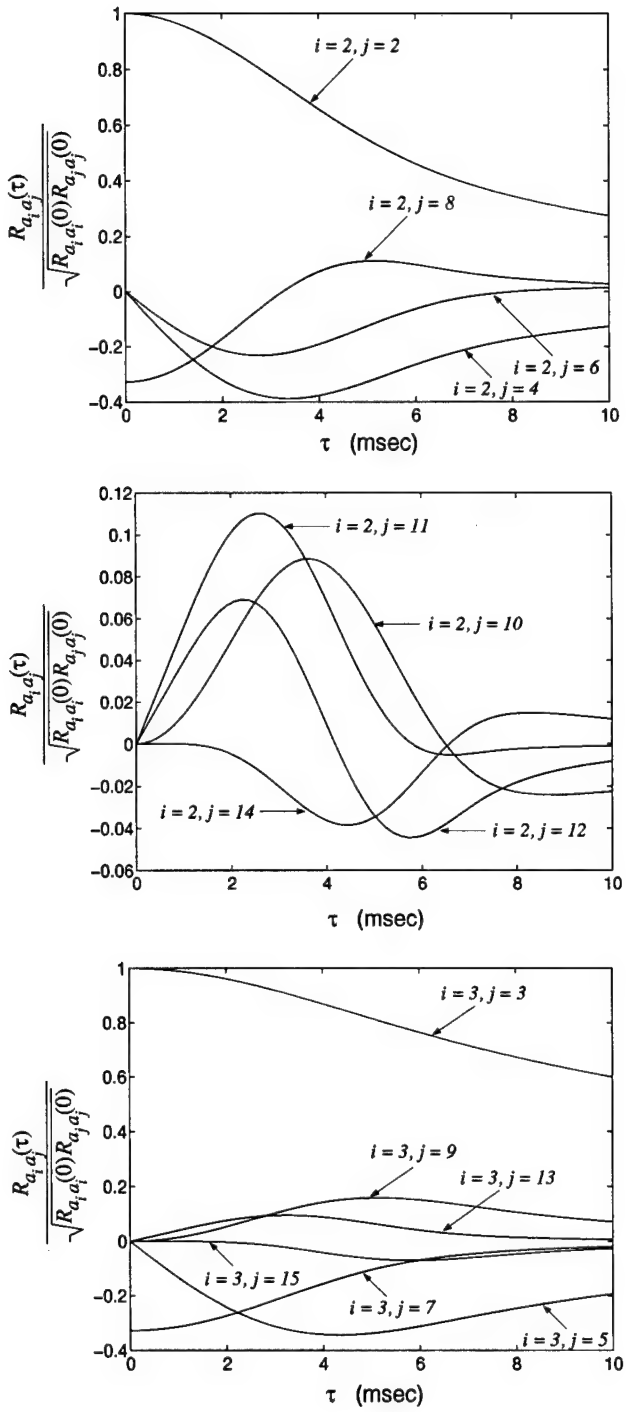

Figure 37. Cross-correlation of tilt with higher-order modes for ABL target engagement. Correlation results are shown for the tilt acquired by the transmitted beam upon propagation to the target object at time t with beacon measurements through Zernike 15 at time $t - \tau$ (uncorrelated modes omitted).

measurements are included. For the target engagement scenario shown in Figure 36, the aperture-averaged piston-removed phase variance is given by:

$$\int \mathrm{d}\vec{\rho}\, W(\vec{\rho})\, \langle \phi_o^2(R\vec{\rho}, t)\rangle = 0.3828 \left(\frac{D}{r_0}\right)^{5/3}. \tag{191}$$

Since all elements of the covariance matrices C_{yx}, C_{xx}, and C_{xy} are proportional to $(D/r_0)^{5/3}$ [see Eq. (189)], ε_T^2 may be normalized for the relative aperture diameter and calculated as follows:

$$\varepsilon_T^2 \left(\frac{D}{r_0}\right)^{-5/3} = 0.3828 - \left(\frac{D}{r_0}\right)^{-5/3} \mathrm{TR}\left[C_{yx} C_{xx}^{-1} C_{xy}\right]. \tag{192}$$

The normalized aperture-averaged residual phase variance was quantified according to Eq. (192) for a range of time delay τ using various mode combinations in the measurement vector $\mathbf{x}$. The result of these calculations is shown in Figure 38. For all correction schemes, as $\tau \to 0$, $\varepsilon_T^2 (D/r_0)^{-5/3}$ approaches its limiting value of 0.1342, indicating ideal tilt correction. For $\tau > 0$, the normalized error increases with increasing τ. When higher-order modal measurements are incorporated into the MMSE tilt estimator, however, $\varepsilon_T^2 (D/r_0)^{-5/3}$ increases more slowly with τ than when tilt measurements are used alone.

To compare performance for the correction schemes studied, consider the time delay at which each scheme yields $\varepsilon_T^2 (D/r_0)^{-5/3} = 0.1356$; that is, the time delay at which the normalized error is 1% larger than the limiting value of 0.1342. Let us call this time delay the *tilt correction interval*, and designate it τ_c. If tilt correction corresponding to $\varepsilon_T^2 (D/r_0)^{-5/3} \leq 0.1356$ is required for ABL beam steering, then τ_c represents the maximum interval between AO correction updates. Thus, we may think of $f_c \equiv 1/\tau_c$ as the operating frequency or bandwidth of the AO system. The values of τ_c and f_c corresponding to the results in Figure 38 are presented in Table 6. As higher order modes are included in the MMSE tilt estimator, τ_c is increased, corresponding to a reduced value for f_c. The bandwidth reduction, as a percentage of the bandwidth using tilt measurements only (modes 2-3), is shown in the last column of Table 6. When tilt plus higher order modal measurements through Zernike 15 are included in the tilt estimator, τ_c is over 3 times longer

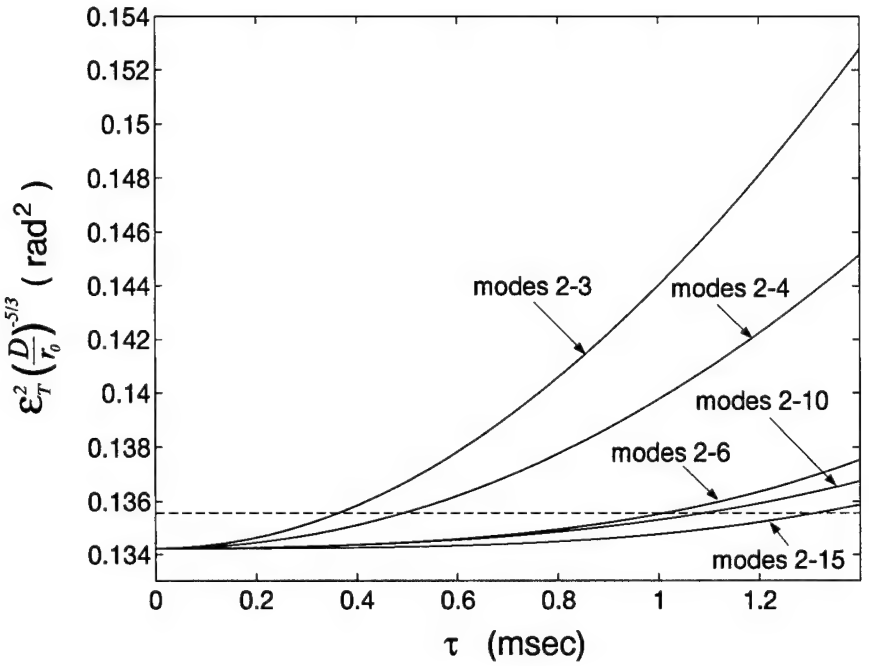

Figure 38. Normalized aperture-averaged residual phase variance after tilt correction for the ABL target engagement. The value of ε_T^2 is normalized to $(D/r_o)^{5/3}$ as a function of beacon measurement time delay τ for the MMSE tilt estimator using the modal measurements indicated. The dashed line shows a normalized error that is 1% larger than the limiting value of 0.1342.

than when tilt measurements alone are included. Correspondingly, the AO beam-steering bandwidth is reduced by over 70%.

For a given value of the relative aperture diameter D/r_0, the Strehl ratio performance of an ABL beam-steering AO system may be quantified according to Eq. (172). The results shown in Figure 38 for $\varepsilon_T^2(D/r_0)^{-5/3}$ were applied to a propagation scenario for which $D/r_0 = 5$. The corresponding Strehl ratio performance is shown in Figure 39 as a function of the beacon measurement time delay τ.

As is illustrated in Figure 39, greater beam-projection performance is maintained at longer beacon measurement time delays when higher-order modes are incorporated into the MMSE tilt estimator. At a fixed value of τ, the Strehl ratio is increased by using the correlated higher-order modes. In order to maintain a particular value of the Strehl ratio, longer measurement time delays may be used in the system if higher-order modes

MMSE modes	τ_c (msec)	f_c (kHz)	bandwidth reduction
2-3	0.3839	2.6048	...
2-4	0.4742	2.1088	19.04%
2-6	1.0161	0.9842	62.22%
2-10	1.1065	0.9038	65.30%
2-15	1.3323	0.7506	71.18%

Table 6. ABL AO bandwidth reduction using the MMSE estimator. The tilt correction interval τ_c corresponds to value of $\varepsilon_T^2(D/r_0)^{-5/3}$ that is 1% larger than the limiting value of 0.1342 using modal measurements in the MMSE tilt estimator as indicated.

are utilized in estimating the tilt components. The limiting value of the Strehl ratio (approximately 0.14) after tilt compensation for the relative aperture diameter $D/r_0 = 5$ indicates that in many practical target engagements, higher-order compensation may be required in the ABL AO system to maintain beam-projection performance. If higher-order compensation is required, the MMSE estimator will provide for enhanced performance when the effect of measurement time delay is significant.

5.5 Summary

Beam steering for ABL target engagements should include adaptive-optical tilt corrections to compensate for the degrading effect of phase aberrations induced by turbulence upon propagation from the system aperture to the target object. Due to the finite bandwidth of any such AO system, the tilt correction will be based upon time-delayed measurements of the beacon phase. The analysis presented in this chapter indicates that due to anisoplanatism, tilt correction is suboptimal when time-delayed tilt measurements are used directly in the beam-steering AO system. Optimal correction is realized only when tilt components are obtained using an MMSE estimator given time-delayed beacon measurements. The MMSE estimator permits the use of tilt plus higher-order modal measurements in forming the tilt estimate. The elements of the MMSE estimator may be quantified by calculating the cross-correlation of target object and beacon Zernike modes as a function of the time delay τ.

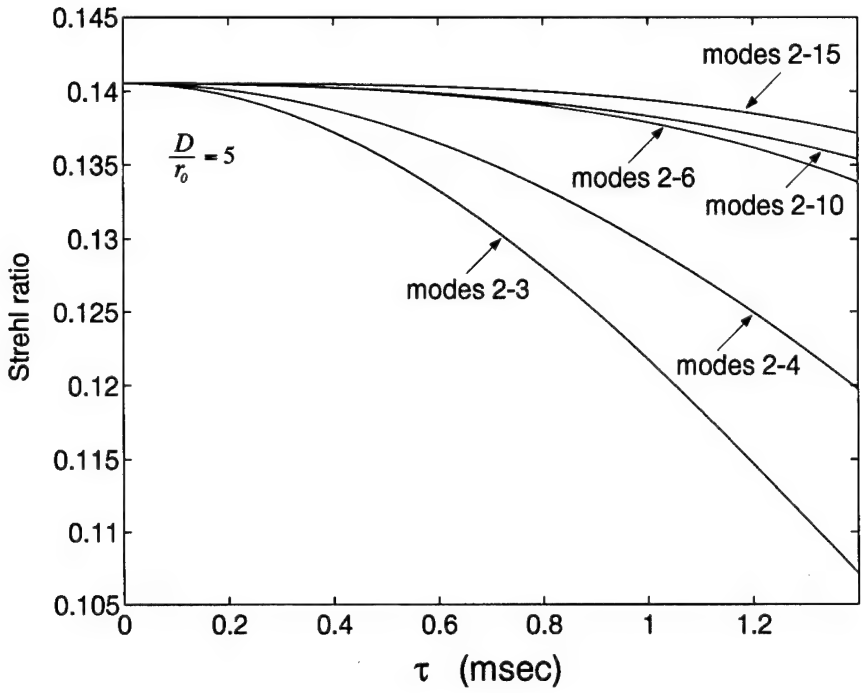

Figure 39. Strehl ratio performance of ABL beam-steering AO system for $D/r_0 = 5$. Performance is quantified as a function of the measurement time delay τ for MMSE tilt estimation using the modal measurements indicated.

The analysis presented in this chapter for an ABL target engagement demonstrates that while tilt is uncorrelated with most higher-order modes at $\tau = 0$, the correlation passes through some extremum at $\tau > 0$ before going to 0 at large values of τ. Thus, incorporating higher-order modes in the tilt estimator will enhance tilt correction performance. For the ABL target engagement scenario, tilt correction performance was quantified when various mode combinations were included in the MMSE tilt estimator. These results illustrate that enhanced performance is obtained by including delayed modal measurements through Zernike 15. Hence, longer measurement time delays may be used while maintaining a normalized residual phase variance that is 1% larger than its limiting value. Correspondingly, the ABL beam-steering AO bandwidth may be reduced when higher-order modes are included the MMSE tilt estimator. By including beacon measurements through Zernike 15, the beam-steering AO bandwidth is reduced by over 70% from the bandwidth when

using tilt measurements alone. At a fixed bandwidth, the Strehl ratio is increased by incorporating higher-order modes into the MMSE estimator for wave-front tilt.

VI. Adaptive-Optical Interferometry

6.1 Introduction

Michelson stellar interferometry, also referred to as amplitude interferometry, provides for imaging of astronomical objects with higher-resolution than can be achieved using single aperture systems [32,60,77]. This imaging technique is based upon the Van Cittert-Zernike theorem [9], which relates the visibility and phase of a fringe in the interferometer (referred to as the complex visibility) to the normalized Fourier transform of the irradiance distribution associated with the object of interest. Mathematically, the Van Cittert-Zernike theorem implies that [32]:

$$|\hat{\mu}_o(\vec{s})| = \left| \frac{\int \mathrm{d}\vec{\eta}\, I_o(\vec{\eta}) \exp\left(j\frac{2\pi}{\lambda L}\vec{s}\cdot\vec{\eta}\right)}{\int \mathrm{d}\vec{\eta}\, I_o(\vec{\eta})} \right|, \tag{193}$$

where $\hat{\mu}_o$ is the normalized mutual intensity of the object of interest, $\vec{s}$ is the baseline of the interferometer, I_o is the object irradiance, λ is the observation wavelength, and L is the distance from the object to the interferometer plane. Recall from Eq. (71) that when an interferometer is unaffected by turbulence, then the fringe visibility $V = |\hat{\mu}_o(\vec{s})|$. From Eq. (193), it can be concluded that V for a given baseline $\vec{s}$ is equal to the modulus of the normalized object spectrum evaluated at the spatial frequency $\vec{s}/\lambda L$. Thus, measurement of the fringe visibility at many baseline values provides for reconstruction of the object spectrum.

Interferometers have been constructed and operated at many locations throughout the world for the purpose of interferometric imaging [13,52,73]. The use of large apertures in interferometric applications at optical wavelengths is limited by the degrading effects of atmospheric turbulence. When atmospheric turbulence is present, the fringe pattern in the interferometer moves randomly, corrupting the relationship between the phase of the fringe and the phase of the Fourier transform of the object irradiance, and reducing fringe visibility measurements for long-exposure fringe measurement [66]. To enhance interferometer performance in the presence of atmospheric turbulence, adaptive-optics phase compensation has been proposed [48] and implemented. Many of these applications involve fringe-tracking methods for control of the AO systems [12,46].

In this chapter, practical limitations to the use of AO compensation in interferometry are explored. The effects of angular anisoplanatism are investigated in Section 6.2. The performance degradation related to angular anisoplanatism is quantified for various levels of modal compensation. In Section 6.3, drawing upon the optimal compensation theory developed in Chapter III, estimation theory is applied to AO compensation for interferometry to partially recover the performance degradation due to anisoplanatism. Results are presented in Section 6.4 to quantify the visibility enhancement obtained when optimal AO compensation is employed. The chapter is summarized in Section 6.5

6.2 Angular anisoplanatism in adaptive optics for interferometry

Interferometric techniques are often employed for high-spatial-resolution imaging of astronomical objects. These objects are typically dim, and therefore may not be bright enough to provide for wave-front sensing. In this case, a nearby NGS may be used as the AO beacon. Since there is an angular separation between the beacon and object of interest, turbulence-induced anisoplanatism will affect AO compensation performance in each aperture of the interferometer. To quantify the effect of angular anisoplanatism in an interferometric system, consider the system diagram in Figure 40, which shows an adaptive-optical interferometer affected by angular anisoplanatism. For simplicity, the object is located on the zenith, with the beacon located at an angle θ_b with respect to the object in the direction of the aperture separation vector $\vec{s}$.

The performance of the interferometer is quantified by the fringe Strehl ratio, which according to Eq. (99) is determined by the aperture-averaged residual differential phase variance δ_N^2 for compensation for piston through the Nth-order Zernike mode. Recall that the FSR decreases with increasing values of δ_N^2. Suppose that the beacon modal phase measurements in each aperture are used as the conjugate phase for each DM. In this case, the difference of the conjugate phase coefficients $\Delta\tilde{a}_{oi}$ is given by $\Delta\tilde{a}_{oi} = a_{b1i} - a_{b2i}$. Thus, from Eq. (96), δ_N^2 is expanded as:

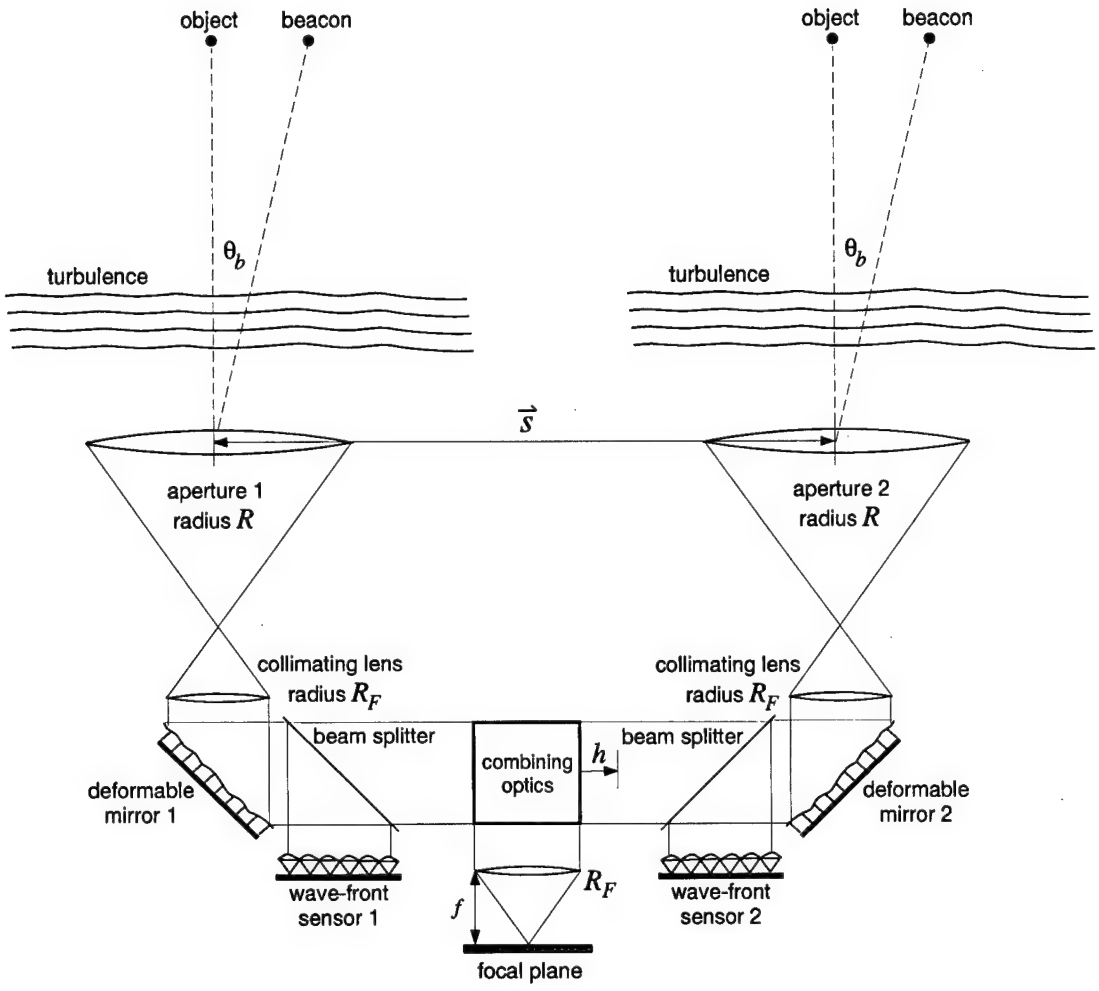

Figure 40. Angular anisoplanatism in adaptive optics for interferometry. When an off-axis source is used for wave front sensing, angular anisoplanatism is introduced into each adaptive-optics system, resulting in reduced fringe visibility.

$$\delta_N^2 = \int \mathrm{d}\vec{\rho}\, W(\vec{\rho}) \left\langle [\phi_{o1}(R\vec{\rho}) - \phi_{o2}(R\vec{\rho})]^2 \right\rangle - \sum_{i=2}^{N} \left\langle (a_{o1i} - a_{o2i})^2 \right\rangle + \sum_{i=2}^{N} \left\langle [(a_{o1i} - a_{o2i}) - (a_{b1i} - a_{b2i})]^2 \right\rangle, \tag{194}$$

If the terms inside the summation of Eq. (194) are expanded, the expression for δ_N^2 is simplified as follows:

$$\begin{aligned} \delta_N^2 = & \int \mathrm{d}\vec{\rho}\, W(\vec{\rho}) \left\langle \left[[\phi_{o1}(\vec{R}\rho) - \phi_{o2}(\vec{R}\rho) \right]^2 \right\rangle \\ & - \sum_{i=1}^{N} \{ 2 \left[\langle a_{o1i} a_{b1i} \rangle - \langle a_{o1i} a_{b2i} \rangle - \langle a_{o2i} a_{b1i} \rangle + \langle a_{o2i} a_{b2i} \rangle \right] \\ & - \langle a_{b1i}^2 \rangle + 2 \langle a_{b1i} a_{b2i} \rangle - \langle a_{b2i}^2 \rangle \}. \end{aligned} \tag{195}$$

Using the expression in Eq. (152), for the spatial cross-correlation of Zernike coefficients $B_{a_{u1i}a_{v2j}}$, each of the terms of Eq. (195) can be quantified. If the position of the object of interest is designated $\vec{r}_o$, and the position of the beacon is designated $\vec{r}_b$, then the correlation calculations required in Eq. (195) are as follows:

$$\begin{aligned} & \langle a_{o1i} a_{b1i} \rangle = B_{a_{u1i}a_{v2i}}(\vec{r}_o, \vec{r}_{a1}, \vec{r}_b, \vec{r}_{a1}), \quad \langle a_{o1i} a_{b2i} \rangle = B_{a_{u1i}a_{v2i}}(\vec{r}_o, \vec{r}_{a1}, \vec{r}_b, \vec{r}_{a2}), \\ & \langle a_{o2i} a_{b1i} \rangle = B_{a_{u1i}a_{v2i}}(\vec{r}_o, \vec{r}_{a2}, \vec{r}_b, \vec{r}_{a1}), \quad \langle a_{o2i} a_{b2i} \rangle = B_{a_{u1i}a_{v2i}}(\vec{r}_o, \vec{r}_{a2}, \vec{r}_b, \vec{r}_{a2}), \\ & \langle a_{b1i}^2 \rangle = B_{a_{u1i}a_{v2i}}(\vec{r}_b, \vec{r}_{a1}, \vec{r}_b, \vec{r}_{a1}), \qquad \langle a_{b1i} a_{b2i} \rangle = B_{a_{u1i}a_{v2i}}(\vec{r}_b, \vec{r}_{a1}, \vec{r}_b, \vec{r}_{a2}), \\ & \text{and} \quad \langle a_{b2i}^2 \rangle = B_{a_{u1i}a_{v2i}}(\vec{r}_b, \vec{r}_{a2}, \vec{r}_b, \vec{r}_{a2}). \end{aligned} \tag{196}$$

Eq. (195) also requires the aperture-averaged differential phase variance associated with the object of interest to be quantified. Including the effects of finite outer scale L_0, this term is calculated as follows:

$$\int \mathrm{d}\vec{\rho}\, W(\vec{\rho}) \left\langle [\phi_{o1}(R\vec{\rho}) - \phi_{o2}(R\vec{\rho})]^2 \right\rangle$$
$$= \left(\frac{D}{r_0}\right)^{5/3} \sqrt{3}\,\Gamma(8/3)\, 2^{-5/3} \left(\frac{6.88}{2.91}\right)$$
$$\times \left[\frac{3}{5} x_0^{-5/3} - \int_0^\infty \mathrm{d}x\, x\, (x^2 + {x_0}^2)^{-11/6} J_0\left(\frac{2s}{D} x\right)\right], \qquad (197)$$

where s/D is the relative aperture separation and $x_0 \equiv \pi D/L_0$, as in Eq. (152).

As indicated in Eq. (197), the aperture-averaged differential phase variance is proportional to $(D/r_0)^{5/3}$. From Eq. (152), it can be seen that each term of Eq. (195) is proportional to $(D/r_0)^{5/3}$. Thus, δ_N^2 is also proportional to $(D/r_0)^{5/3}$, and compensation performance can be quantified in terms of the normalized aperture-averaged residual differential phase variance, $\delta_N^2 (D/r_0)^{-5/3}$.

For a range of beacon angular offset θ_b, $\delta_N^2 (D/r_0)^{5/3}$ was calculated according to Eq. (195) for modal compensation through order $N = 15$, $N = 36$, $N = 66$, $N = 105$, and $N = 153$, corresponding to Zernike polynomial radial order $n = 4$, $n = 7$, $n = 10$, $n = 13$, and $n = 16$, respectively. The results of these calculations are shown in Figure 41(a)-(b) for interferometer baselines $s = |\vec{s}|$ corresponding to $s/D = 4$ and $s/D = 6$. The results for interferometer baselines $s/D = 8$ and $s/D = 10$ are shown in Figure 42(a)-(b). All results have been calculated with an aperture diameter $D = 1$ m, and $L_0/D = 100$. The beacon angular offset θ_b has been normalized to the isoplanatic angle θ_0, which for the HV-21 turbulence profile employed in these calculations is approximately 7 μrad, as indicated in Table 1. The maximum angle considered in these results is $\theta_b = 4\,\theta_0$.

As can be seen in each graph of Figure 41 and Figure 42, at each baseline and for all orders of compensation, $\delta_N^2 (D/r_0)^{-5/3}$ increases with increasing beacon offset. This increase represents the magnitude of the angular anisoplanatic effect for the adaptive optical interferometer. For a given beacon offset, the angular anisoplanatic effect may be reduced by increasing the order N of the atmospheric compensation. For larger values of θ_b/θ_0, however, the marginal decrease in angular anisoplanatism with increasing N is small.

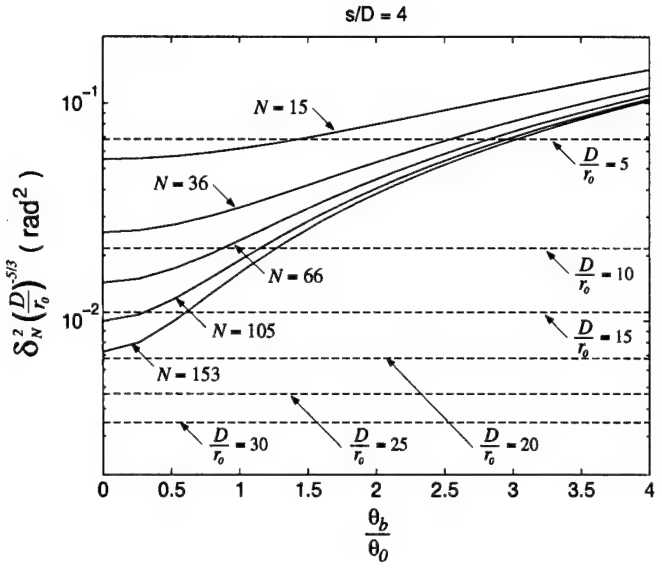

(a)

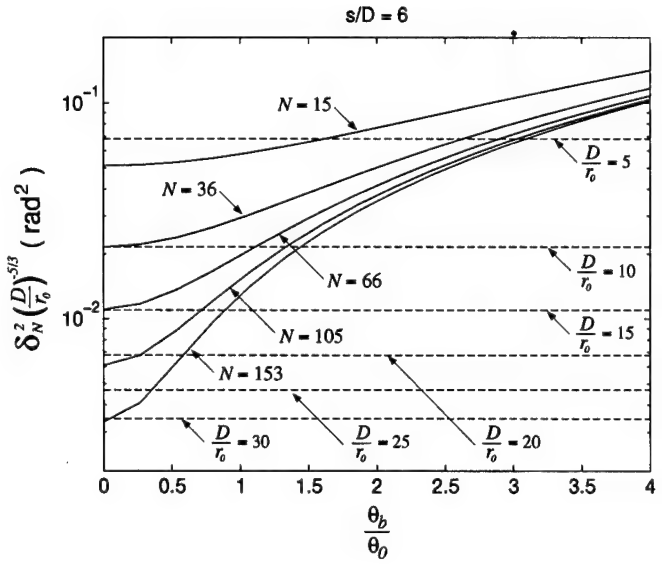

(b)

Figure 41. Effect of modal compensation on angular anisoplanatism in adaptive-optical interferometry for baselines $s/D = 4$ and $s/D = 6$. Normalized residual differential phase variance $\delta_N^2 (D/r_0)^{5/3}$ is shown for relative beacon offset θ_b/θ_0 with correction order $N = 15, 36, 66, 105, 153$. Dashed lines show $\delta_N^2 = 1$ rad^2 for $D/r_0 = 5, 10, 15, 20, 25$. Results are for $L_0/D = 100$.

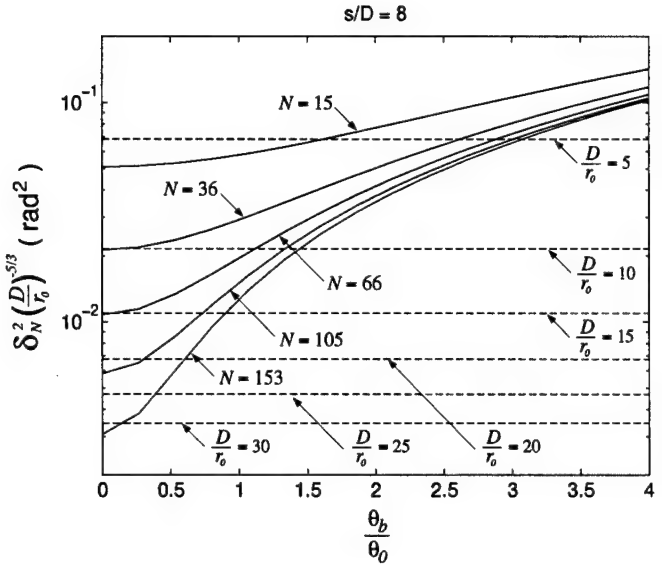

(a)

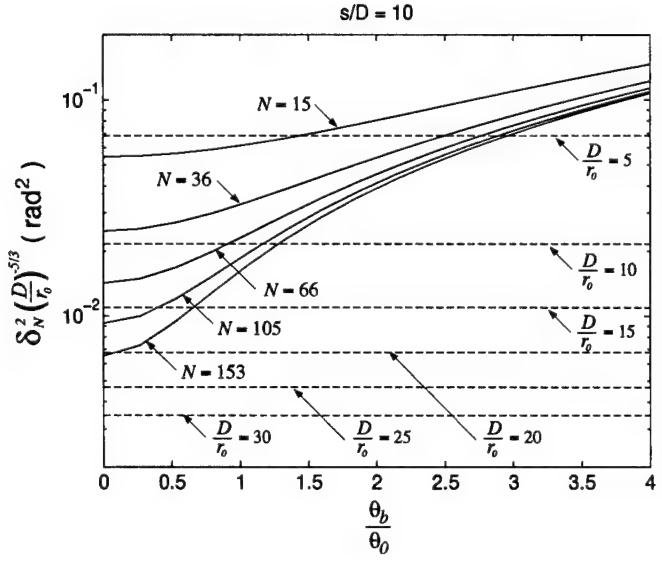

(b)

Figure 42. Effect of modal compensation on angular anisoplanatism in adaptive-optical interferometry for baselines (a) $s/D = 8$ and (b) $s/D = 10$. Normalized residual differential phase variance $\delta_N^2 (D/r_0)^{5/3}$ is shown for relative beacon offset θ_b/θ_0 with correction order $N = 15, 36, 66, 105, 153$. Dashed lines show $\delta_N^2 = 1$ rad^2 for $D/r_0 = 5, 10, 15, 20, 25$. Results are for $L_0/D = 100$.

Consider the maximum angle for which $\delta_N^2 \leq 1$ rad^2, which implies that FSR $\geq$ 0.6. This maximum angle specifies the range of angular offsets at which the FSR is not significantly reduced by turbulence-induced anisoplanatism in the AO system. The value of $\delta_N^2 (D/r_0)^{-5/3}$ corresponding to $\delta_N^2 = 1$ rad^2 is shown in each graph of Figure 41 and Figure 42 by dashed lines for the relative aperture diameters $D/r_0 = 5, 10, 15, 20, 25, 30$. For the 20 to 35 cm r_0 values experienced at the best observatory locations (for $\lambda = 500$ nm), these relative aperture diameters are applicable to 1 to 10 m class telescopes used as baseline apertures.

For the least stressing turbulence condition indicated in each graph of Figure 41 and Figure 42 ($D/r_0 = 5$), the lowest-order correction considered ($N = 15$) is an adequate level of compensation for $\theta_b < 1.5\,\theta_0$ at all baseline values studied. When the highest-order correction considered ($N = 153$) is employed for $D/r_0 = 5$, a beacon offset of up to $3\,\theta_0$ results in a FSR value no less than 0.6.

For the most stressing turbulence condition indicated ($D/r_0 = 30$), even the highest order correction considered ($N = 153$) is insufficient to provide $\delta_N^2 \leq 1$ rad^2 at any beacon offset for the baseline values $s/D = 4$ and $s/D = 10$. At $s/D = 6$, compensation through $N = 153$ reduces the residual variance to a sufficient level only when $\theta_b \sim 0$. At $s/D = 8$, the maximum allowable beacon offset for $N = 153$ is approximately $0.2\,\theta_0$.

It is curious and perhaps counter-intuitive that $\delta_N^2 (D/r_0)^{-5/3}$ should be smaller at the intermediate baseline values studied ($s/D = 6, s/D = 8$) than at $s/D = 4$ for $\theta_b/\theta_0 < 1$, as can be seen by comparing the results in Figure 41(b) and Figure 42(a) with Figure 41(a). This effect can be understood by considering the limiting form of δ_N^2 as $\theta_b/\theta_0 \to 0$, which is given in Eq. (100), and rewritten here in an expanded form:

$$\lim_{\Delta\tilde{a}_{oi} \to \Delta a_{oi}} \delta_N^2 = \int \mathrm{d}\vec{\rho}\, W(\vec{\rho}) \left\langle [\phi_{o1}(R\vec{\rho}) - \phi_{o2}(R\vec{\rho})]^2 \right\rangle - \sum_{i=2}^{N} \langle (a_{o1i})^2 \rangle - \sum_{i=2}^{N} \langle (a_{o2i})^2 \rangle + 2 \sum_{i=2}^{N} \langle a_{o1i} a_{o2i} \rangle \,. \tag{198}$$

As can be seen from Eq. (198), the interaperture correlation of the Zernike coefficients (the final summation) adds to the limiting value of δ_N^2. For relative outer scale $L_0/D = 100$, the

interaperture correlation of the x-tilt (Zernike 2) is negative and increasing in magnitude through some extremum value for intermediate values of s/D [76] (see also Figure 13). Thus, the interaperture term for $i = 2$ in Eq. 198 is negative and large compared to all other terms at the intermediate values of s/D. Therefore, δ_N^2 is reduced from its value at smaller relative baselines.

6.3 Application of theory to optical interferometric imaging

The results of Section 6.2 illustrate that angular anisoplanatism results in reduced FSR values by increasing the aperture-averaged residual differential phase between the baseline apertures. To recover some of the performance lost due to anisoplanatism, the optimal compensation theory developed in Chapter III can be applied directly. Recall that the optimal compensation theory was developed for the interferometric system shown in Figure 11. In Chapter IV and Chapter V, the general results of Chapter III were specialized to imaging and beam-projection systems. For an interferometric system, however, the results of the general analysis can be used immediately.

When modal beacon measurements a_{b1i} and a_{b2i} are obtained by wave-front sensing in aperture 1 and aperture 2, respectively, the minimum value of δ_N^2 is given by replacing $\Delta\tilde{a}_{oi}$ with $\Delta\hat{a}_{oi}$ in Eq. (96) as follows:

$$\begin{aligned}\min(\delta_N^2) &= \int \mathrm{d}\vec{\rho}\, W(\vec{\rho}) \left\langle [\phi_{o1}(R\vec{\rho}) - \phi_{o2}(R\vec{\rho})]^2 \right\rangle - \sum_{i=2}^{N} \langle (\Delta a_{oi})^2 \rangle \\ &\quad + \sum_{i=2}^{N} \langle [\Delta a_{oi} - \Delta\hat{a}_{oi}]^2 \rangle \,, \end{aligned} \tag{199}$$

where $\Delta\hat{a}_{oi}$ is the MMSE estimate of $\Delta a_{oi} = (a_{o1i} - a_{o2i})$, the difference of object phase coefficients between aperture 1 and aperture 2. The value of $\Delta\hat{a}_{oi}$ is estimated from the measured value of $\Delta a_{bi} = (a_{b1i} - a_{b2i})$ using the MMSE estimator of Eq. (106).

Since δ_N^2 depends only upon the difference of the conjugate phase applied to the DM in each aperture, then without loss of generality, the deformable mirror 2 may be removed and replaced with a plane mirror, as shown in Figure 43. Replacing the deformable mirror in aperture 2 with a plane mirror corresponds to setting $\tilde{a}_{o2i} = 0$, and hence, $\Delta\tilde{a}_{oi} = \tilde{a}_{o1i}$.

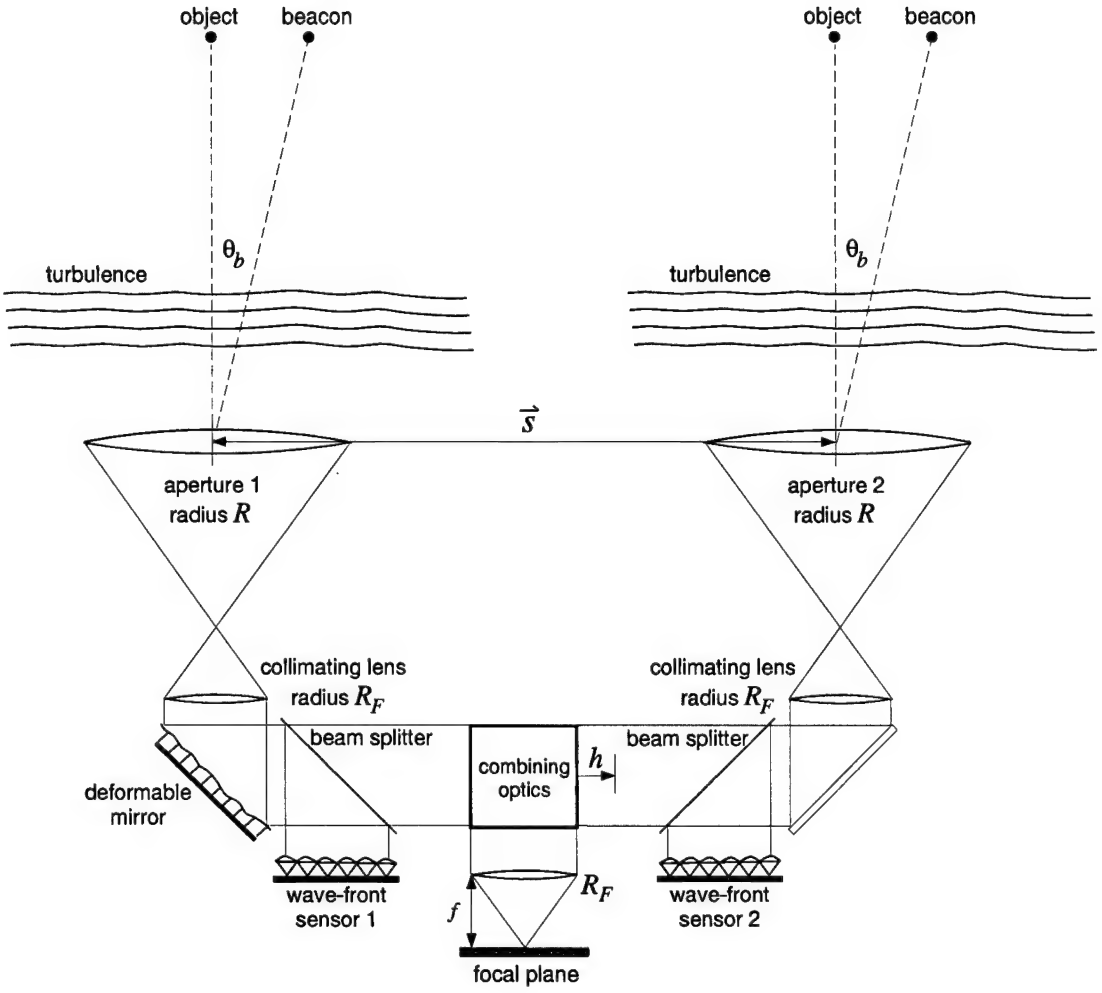

Figure 43. Optimal compensation for anisoplanatism in adaptive-optical interferometry. For optimal compensation, only one DM is employed. The conjugate phase placed on the DM is estimated from the difference in phase coefficients between wave-front sensor 1 and wave-front sensor 2.

Therefore, to obtain the minimal value of δ_N^2 given in Eq. (199), the MMSE estimates of $\Delta\hat{a}_{oi}$ represent the conjugate phase that should be placed on the single deformable mirror for optimal compensation in an adaptive-optical interferometer.

6.4 Fringe visibility enhancement through optimal atmospheric compensation

Figure 41 and Figure 42 illustrate the effect of angular anisoplanatism on the aperture-averaged residual differential phase variance δ_N^2. The results were normalized for the relative aperture D/r_0. For a given value of D/r_0, the fringe Strehl ratio is calculated according to Eq. (99), repeated here for clarity:

$$\text{FSR} = \exp\left(-\frac{1}{2}\,\delta_N^2\right). \tag{200}$$

From the results in Figure 41 and Figure 42, it can be determined that the relative aperture diameter $D/r_0 = 5$ requires modal compensation through approximately $N = 15$. Consider the FSR results shown in Figure 44. This plot gives the FSR value at $s/D = 8$ for $D/r_0 = 5$ and $L_0/D = 100$ with $N = 6, 10, 15, 21$ when beacon measurements are employed directly to form the conjugate phase. The beacon offset θ_b is normalized to θ_0, and the results were calculated using $D = 1$ m. As can be seen in Figure 44, the compensation orders indicated yield FSR values in the range from 0.4 to approximately 0.8 at $\theta_b/\theta_0 = 0$. The FSR for all compensation orders falls off as θ_b/θ_0 increases, resulting in a fringe Strehl ratio no greater than 0.5 for beacon offsets greater than $4\,\theta_0$. At the largest angular offset considered ($\theta_b/\theta_0 = 10$), the FSR is less than 0.05 for all compensation orders considered.

It is instructive to compare the effect of angular anisoplanatism on the fringe Strehl ratio in an interferometer with its effect on the Strehl ratio in an imaging system. This can be done by comparing the results shown in Figure 44 with the angular anisoplanatism degradation results of Figure 10(a) in Chapter II for each order of compensation considered. For convenience, Figure 45 shows the FSR performance curve for $N = 21$ in Figure 44 plotted with the SR performance curve for $N = 21$ in Figure 10(a). This graph illustrates that while the FSR is greater than the SR for $\theta_b/\theta_0 = 0$ (due to the interaperture tilt correlation effect discussed previously), the FSR degradation is more severe than

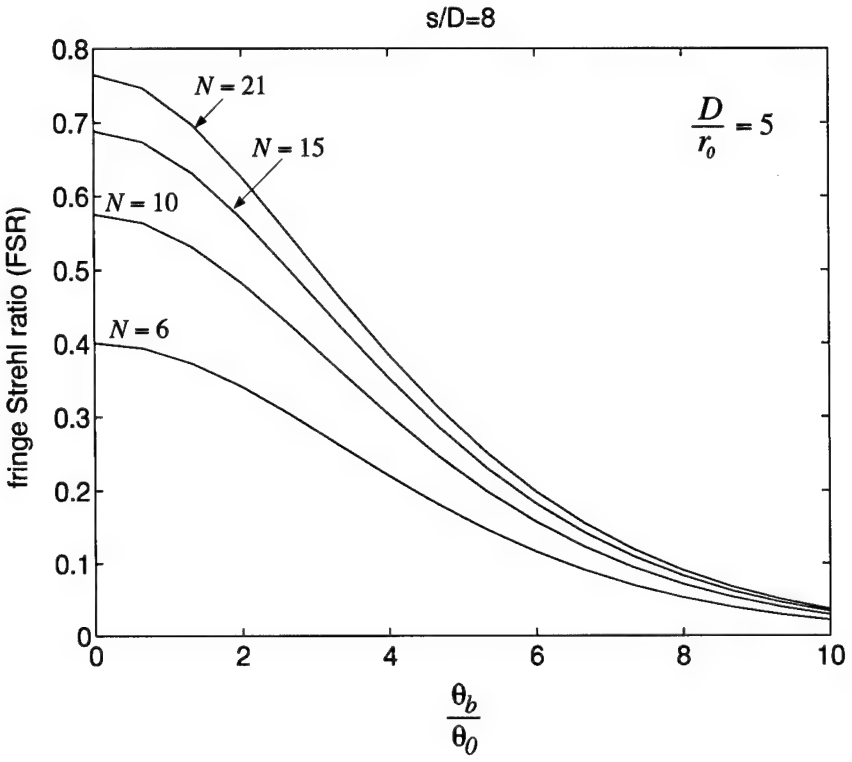

Figure 44. Effect of angular anisoplanatism on fringe Strehl ratio in adaptive optics for interferometry. Value of FSR is shown for relative beacon offset θ_b/θ_0 at interferometer baseline $s/D = 8$ with the compensation order indicated. Results are for $D/r_0 = 5$ and $L_0/D = 100$.

the SR degradation with increasing beacon offset angle. Thus, angular anisoplanatism imposes more severe beacon offset limits in interferometric applications than for imaging applications with adaptive optics.

As was illustrated by the results presented in Figure 44, angular anisoplanatism can significantly reduce the fringe visibility for beacon offsets that are several times the isoplanatic angle. The decreased fringe visibility limits the ability to recover object spectrum information for interferometric imaging applications. To mitigate the degrading effects of angular anisoplanatism, the optimal compensation theory may be applied, as was discussed in Section 6.3.

When the conjugate phase coefficients are estimated from beacon modal measurements, δ_N^2 is given by Eq. (111). If the measured beacon modal coefficients are used directly

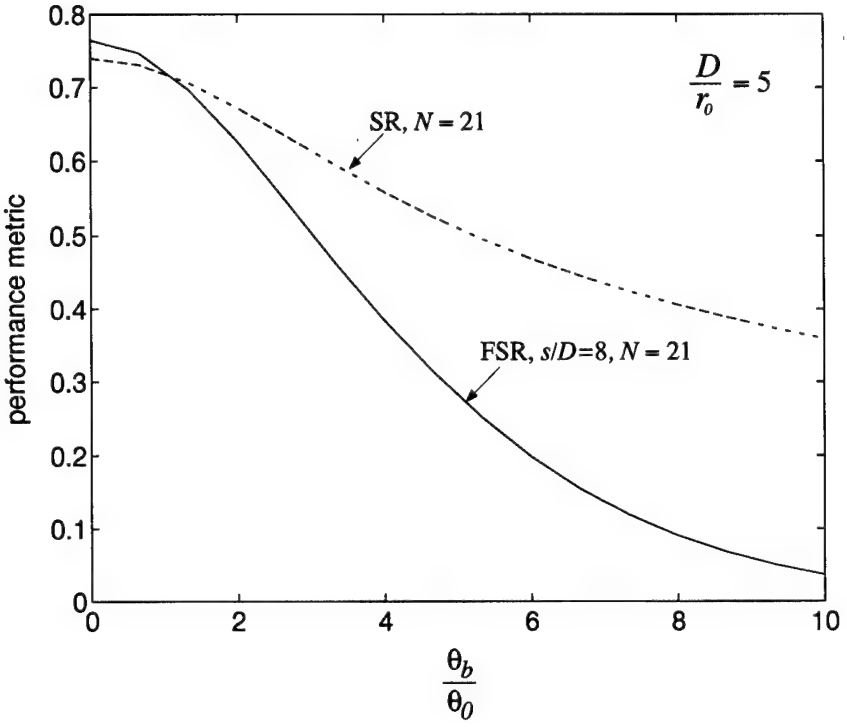

Figure 45. Comparison of angular anisoplanatism effect on performance of interferometric and imaging systems. The solid line shows the fringe Strehl ratio for an interferometer with $s/D = 8$ and compensation order $N = 21$. The dashed line shows the Strehl ratio of an imaging system with compensation order $N = 21$. Results are for $D/r_0 = 5$ and $L_0/D = 100$.

to form the conjugate phase, then δ_N^2 is given by Eq. (112). Since δ_N^2 is minimized by using the MMSE estimator, then the FSR will be larger when the estimator is employed than when the beacon measurements are employed directly. To express the increase in the fringe Strehl ratio that results from optimal compensation, the FSR gain G_{FSR} is defined as:

$$G_{\mathrm{FSR}} \equiv \frac{\exp\left[-\frac{1}{2}(\text{MMSE: } \delta_N^2)\right]}{\exp\left[-\frac{1}{2}(\text{measured: } \delta_N^2)\right]}. \tag{201}$$

From the expressions given in Eq. (111) and Eq. (112), G_{FSR} can be expressed using the vector notation defined in Chapter III:

$$G_{\mathrm{FSR}} = \exp\left\{-\frac{1}{2}\mathrm{TR}\left[2C_{yx} - C_{xx} - C_{yx}C_{xx}^{-1}C_{xy}\right]\right\}. \tag{202}$$

Since each element of C_{yx} and C_{xx} is proportional to $(D/r_0)^{5/3}$, then G_{FSR} will also depend upon the relative aperture diameter D/r_0.

The value of G_{FSR} was quantified for beacon offset angles from $\theta_b/\theta_0 = 0$ to $\theta_b/\theta_0 = 10$ for $D/r_0 = 5$ and $L_0/D = 100$. The results of these calculations are shown in Figure 46(a) and Figure 46(b) for $N = 6$ and $N = 10$, respectively. Figure 47(a) and Figure 47(b) show the FSR gain results for $N = 15$ and $N = 21$, respectively. These calculations were performed using $D = 1$ m with the 4-layer HV-21 turbulence profile in Table 1.

For modal compensation through $N = 6$ and $N = 10$, the plots in Figure 46 show the value of G_{FSR} for the relative interferometer baselines $s/D = 4, 6, 8, 10$. As can be seen from these plots, G_{FSR} is appreciably greater than 1 for beacon offset angles greater than θ_0. The FSR gain increases as the beacon angular offset increases for all relative baseline values. The gain is also higher for the lower values of s/D at all values of θ_b/θ_0, indicating that the enhanced cross-correlation of the beacon measurements and object phase coefficients at lower values of s/D reduces δ_N^2 using the MMSE estimator. At the largest beacon angular offsets considered ($\theta_b/\theta_0 = 10$), the FSR is increased by 15% to approximately 25%, depending upon the relative baseline s/D.

For modal compensation through $N = 15$ and $N = 21$, the plots in Figure 47 show the value of G_{FSR} for the relative interferometer baselines $s/D = 4, 6, 8, 10$. As was the case for $N = 6$ and $N = 10$, G_{FSR} is greater than 1 for beacon offset angles greater than θ_0 at all values of s/D. The FSR gain increases as the beacon angular offset increases for all relative baseline values. Again, the gain is higher for the lower values of s/D at all values of θ_b/θ_0. At $\theta_b/\theta_0 = 10$, the FSR is increased by over 25%, for $s/D = 4$. By comparing the plots of Figure 46 with the plots of Figure 47, it can be seen that the FSR gain is increased for the higher orders of compensation. This indicates that the MMSE estimator is able to partially recover some of the performance degradation due to anisoplanatism even for the highest aberration orders considered.

While the FSR gain is greatest for larger values of θ_b/θ_0, the actual increase in the FSR may be small, since the FSR is small for these beacon angular offset values (see

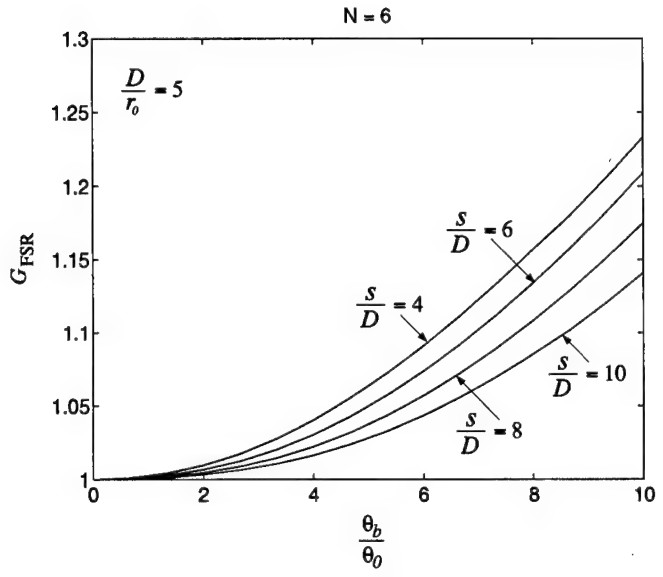

(a)

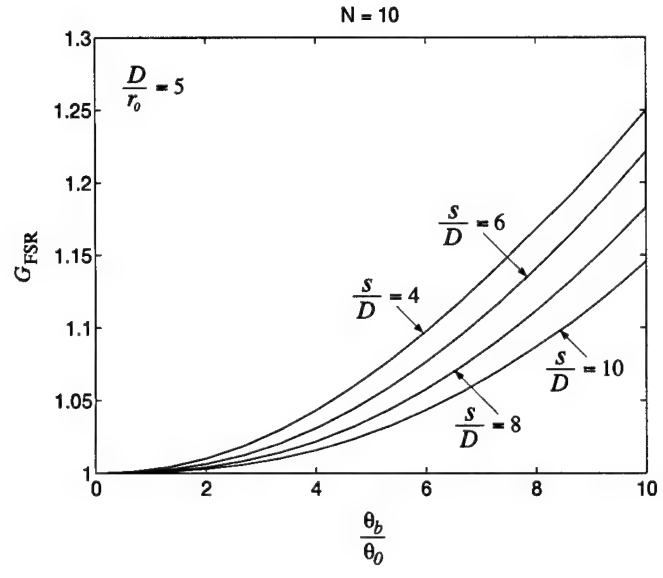

(b)

Figure 46. Fringe Strehl ratio gain for compensation order (a) $N = 6$ and (b) $N = 10$. FSR gain G_{FSR} is shown for relative beacon offset θ_b/θ_0 at interferometer baselines $s/D = 4, 6, 8, 10$ with $D/r_0 = 5$ and $L_0/D = 100$.

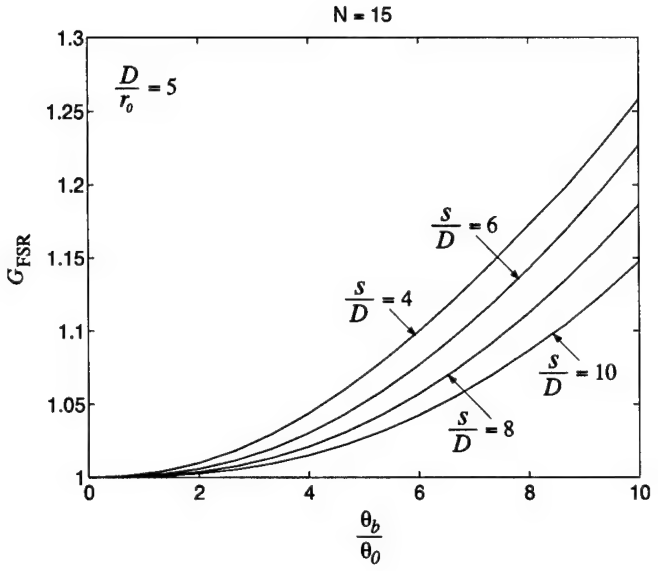

(a)

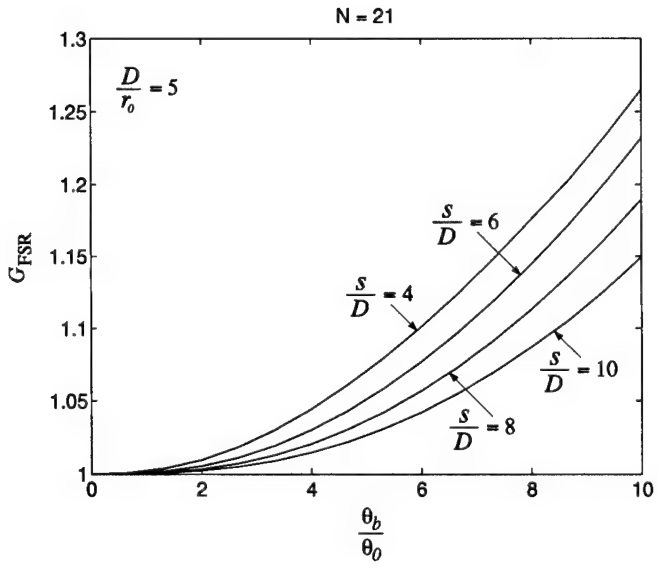

(b)

Figure 47. Fringe Strehl ratio gain for compensation order (a) $N = 15$ and (b) $N = 21$. FSR gain G_{FSR} is shown for relative beacon offset θ_b/θ_0 at interferometer baselines $s/D = 4, 6, 8, 10$ with $D/r_0 = 5$ and $L_0/D = 100$.

Figure 44). In fact, the FSR increase may be larger at moderate values of θ_b/θ_0, since the FSR value is larger. Regardless of the FSR increase, $G_{\mathrm{FSR}} > 1$ indicates an increase in the fringe visibility, and therefore a partial recovery of the performance degradation due to angular anisoplanatism. It should be pointed out here that since G_{FSR} depends upon D/r_0, the increase in FSR is expected to be greater for the higher orders of atmospheric compensation which are required for larger values of relative aperture diameter D/r_0.

6.5 Summary

High-resolution imagery is obtained from an optical interferometer by measuring the visibility of the fringe obtained when light from two apertures is combined, and the resulting irradiance pattern is measured on the focal plane of the system. According to the Van Cittert-Zernike theorem, the fringe visibility gives the normalized spectrum of the object irradiance distribution evaluated at a spatial frequency which is proportional to the baseline separation of the apertures. Thus, long baselines provide for high spatial-frequency sampling of the object spectrum. Large apertures may be employed to increase the irradiance on the focal plane of the system in order to enhance visibility measurements. Due to the increased magnitude of turbulence effects in large apertures (increased D/r_0), however, the fringe visibility is decreased, and object spectrum information cannot be accurately measured. In this case, adaptive optics may be employed to compensate for turbulence effects, restoring the benefits of using large apertures in the interferometer.

If the object being observed by an interferometer is too dim, then it may not be bright enough to provide for wave-front sensing in the AO loop. In this case, a nearby NGS beacon must be employed. The angular separation between the object of interest and the AO beacon results in a degradation of compensation performance due to anisoplanatism. In this chapter, the angular anisoplanatic effect was characterized using modal analysis techniques, where the performance degradation is quantified by the correlation of the appropriate object and beacon Zernike coefficients. For several values of the relative baseline s/D, the aperture-averaged residual differential phase variance δ_N^2 was calculated over a range of beacon angular offsets θ_b. The maximum-permissible beacon angular offset depends upon the relative aperture diameter D/r_0 and the order of compensation N. For

$D/r_0 = 5$, the beacon angular offset limit is between $1.5\,\theta_0$ and $3\,\theta_0$, depending upon the compensation order. For $D/r_0 = 30$, the angular limit was approximately $0.2\,\theta_0$ for the highest-order compensation considered ($N = 153$). In general, performance degradation due to angular anisoplanatism is more severe for interferometric applications than for imaging applications, as the fringe Strehl ratio drops off more rapidly with increasing beacon offset angle than the Strehl ratio of an imaging AO system.

The optimal compensation theory developed in Chapter III can be applied to provide enhanced fringe visibility in an adaptive-optical interferometer suffering performance degradation due to angular anisoplanatism. For optimal compensation, the beacon measurements are not used directly for compensation in each aperture, but instead, an optimal conjugate phase is formed in one aperture based upon the difference of beacon measurements in each aperture. Application of the optimal conjugate phase results in an increased FSR, quantified by the fringe Strehl ratio gain G_{FSR}. The value of G_{FSR} depends upon the compensation order N, the relative baseline s/D, and the relative aperture diameter D/r_0. It was shown that for $N = 21$ at the beacon offset $\theta_b/\theta_0 = 10$, optimal compensation results in an FSR increase of 15% to over 25%, depending upon the relative baseline s/D.

VII. Conclusions and Recommendations

7.1 Introduction

The principle objective of this research was to establish a common framework for the analysis of anisoplanatism in imaging, beam-projection, and interferometric adaptive-optical systems and to apply optimal AO compensation techniques in each application. This objective was motivated by the inadequacy of current analysis methods to address the degrading effects of anisoplanatism in emerging adaptive optics applications such as beam steering and control for the Airborne Laser and atmospheric compensation for high-resolution interferometric imaging. Specifically, this research was intended to assess the performance degradation caused by anisoplanatism, and to quantify the performance improvement that could be obtained using optimal atmospheric compensation.

In Chapter I of this dissertation, an overview of anisoplanatism in adaptive optics was presented, along with the historical background, research motivation, problem statement, and key research results. Chapter II provided background knowledge in atmospheric and adaptive optics, highlighting the effects of turbulence in optical systems. Optimal compensation theory was laid out in Chapter III, including the calculation of the spatial cross-correlation of Zernike phase coefficients, which characterizes anisoplanatism in a general sense. The application of the optimal compensation theory to ground-based adaptive optics for imaging was presented in Chapter IV. Chapter V was devoted to exploring the optimization of Airborne Laser beam-steering adaptive optics. Angular anisoplanatic effects and optimal compensation in adaptive-optical interferometry were discussed in Chapter VI. In the present chapter, the significant advances and results of this research are summarized, conclusions are drawn, and recommendations for future research are offered.

7.2 Significant advances

This research has resulted in the following significant advances regarding the understanding of anisoplanatism in adaptive optics:

- A *unified approach* to the analysis of anisoplanatism in imaging, dynamic beam-projection, and interferometric systems.

- An optimal compensation theory for adaptive-optical systems suffering *generalized* anisoplanatic degradation, based on modal decomposition of the turbulence-induced phase and established optimal estimation techniques.
- The *first known* theoretical and experimental validation of a modal cross-correlation enhancement effect that occurs in systems with moderate levels of anisoplanatic degradation.
- The *first published* analysis of temporal anisoplanatism for a dynamic system [94], and the *first analysis* of angular anisoplanatism in adaptive optics for interferometric imaging [95], establishing the fringe Strehl ratio as a *new metric* to quantify turbulence degradation.
- A *new class* of tilt-sensing techniques for laser guide star adaptive optics to obtain tilt information lost due to reciprocal compensation in the LGS signal.
- The *first known* use of tilt plus higher-order modal measurements to improve tilt compensation performance in anisoplanatic systems.
- A *simplified system design* for adaptive optics in interferometric imaging, where an optimal conjugate phase is placed on a single deformable mirror, based upon wavefront sensor measurements in each aperture.

7.3 Summary of results

The application of optimal modal compensation in adaptive-optical systems whose compensation performance is degraded by anisoplanatism yielded a variety of results. Key results associated with each of the system types considered are summarized in this section.

7.3.1 Ground-based adaptive-optical imaging results.

- For compensation from an off-axis NGS, MMSE estimation resulted in compensation performance improvement for all orders of correction and at all beacon offset angles. For the correction orders $N = 6, 10, 15, 21$ with a 1 m aperture, enhanced performance was noted for beacon offsets greater than $2\,\theta_0$. For $N = 28, 36, 45, 55$ with a 1 m aperture, enhanced performance was noted for beacon offsets greater than $0.5\,\theta_0$. For

compensation through $N = 55$, the MMSE estimator can provide equivalent imaging performance at NGS offset angles 10% larger than when NGS measurements are used directly for compensation.

- For compensation from an on-axis LGS with an off-axis NGS for wave-front tilt measurement, the optimal estimator resulted in enhanced compensation performance for all LGS altitudes considered. The MMSE estimator partially reduces the effect of focal anisoplanatism. For compensation through $N = 55$, the MMSE estimator can provide equivalent imaging performance at altitudes 20% lower than when beacon measurements are using directly for wave-front compensation.

- For an off-axis NGS, including higher-order modal measurements in the tilt estimator resulted in increased Strehl ratio performance over using tilt measurements only. For tilt compensation using beacon Zernike modes 2 to 15, it was shown that the maximum beacon offset angle for nearly-limiting performance is 3 times larger than when only tilt measurements are used. For a given beacon offset, the Strehl ratio is increased by incorporating higher-order modes.

- Wave-front tilt cannot be measured directly from the LGS signal due to natural compensation caused by beam reciprocity. Nonetheless, optimal compensation methods permit on-axis wave-front tilt components to be estimated using only higher-order measurements from off-axis LGS beacons. It was shown that for a constellation of four LGS beacons offset orthogonally from the optical axis, using measurements of Zernike modes 4 to 15 from each beacon, the Strehl ratio can be greater than 0.3 for $D/r_0 = 4$ and $L_0/D = 10$. Tilt estimation performance is degraded by focal anisoplanatism. Peak LGS tilt estimation performance occurs at an angle which depends upon the diameter of the aperture and the height of the effective turbulence layer. The peak angle can be significantly larger than the isoplanatic angle for typical AO systems.

7.3.2 Airborne Laser beam-steering adaptive optics results.

- Due to anisoplanatism, tilt correction is suboptimal when time-delayed tilt measurements are used directly in the beam-steering adaptive optics for the Airborne Laser system. Optimal correction is obtained using the MMSE estimator given time-delayed beacon measurements, which may include tilt plus higher-order modes.
- While tilt is uncorrelated with most higher-order modes at $\tau = 0$, the correlation passes through some extremum at $\tau > 0$ before going to 0 at large values of τ. Thus, incorporating higher-order modes in the tilt estimator will enhance tilt correction performance.
- For the ABL target engagement scenario, enhanced tilt compensation performance is obtained by including delayed modal measurements through Zernike 15. Thus, compensation performance may be maintained to within 1% of its limiting value at longer measurement time delays, resulting in a reduced AO bandwidth for the ABL. It was shown that by including beacon measurements through Zernike 15, the beam-steering AO bandwidth is reduced by over 70%. At a fixed bandwidth, the Strehl ratio is increased by incorporating higher-order modes into the MMSE estimator.

7.3.3 Adaptive-optical interferometry results.

- The angular anisoplanatic effect was characterized for adaptive optics in interferometric imaging using modal analysis techniques. For $D/r_0 = 5$, the beacon angular limit is between $1.5\,\theta_0$ and $3\,\theta_0$, depending upon the compensation order. For $D/r_0 = 30$, the beacon angular limit is approximately $0.2\theta_0$ with compensation through $N = 153$. This analysis demonstrates that performance degradation due to angular anisoplanatism is more severe for interferometric applications than for imaging applications.
- For optimal compensation in an interferometer, beacon measurements should not used directly to conjugate the phase in each aperture, but instead, an optimal phase should be formed on a deformable mirror in one aperture based upon the difference of beacon measurements in each aperture.

- Application of an optimal conjugate phase results in an increased fringe Strehl ratio, quantified by the FSR gain, G_{FSR}. The value of G_{FSR} depends upon the compensation order N, the relative baseline s/D, and the relative aperture diameter D/r_0. For $N = 21$ at the beacon offset $\theta_b/\theta_0 = 10$, optimal compensation resulted in an FSR increase of 15% to over 25%, depending upon the relative baseline s/D.

7.4 Conclusions drawn from research

Although anisoplanatism is manifested in diverse ways for different types of adaptive-optical systems, its physical origin is the same. Measured wave-front aberrations and the turbulence-induced phase from the object of interest are not conjugate, but instead only partially correlated in anisoplanatic systems. This effect results from differences in the turbulence volume sampled by beacon and object light. This generalized view of anisoplanatism serves as a unifying concept in the analysis of a broad class of adaptive optics for imaging, beam-projection, and interferometric systems.

In the context of modal analysis techniques, wave-front phase aberrations are described by projecting the turbulence-induced phase onto a basis set of Zernike polynomials. Thus, anisoplanatism is quantified by the spatial cross-correlation of Zernike coefficients. By considering a mathematical description of modal compensation performance, optimal estimation techniques can be applied to adaptive optics. The resulting optimal modal compensation theory indicates that when the performance of an AO system is degraded by anisoplanatism, the conjugate phase should be estimated from the wave-front measurements. Otherwise, direct application of the wave-front measurements in phase conjugation will result in suboptimal compensation performance.

The application of optimal modal compensation results in enhanced performance for ground-based AO imaging systems, dynamic beam-projection systems like the Airborne Laser, and adaptive-optical interferometers for high-resolution image reconstruction. For ground-based imaging systems, natural guide star beacons at larger angular offsets and lower-altitude laser guide star beacons may be employed without significantly reducing system performance. In addition, wave-front tilt estimates can be obtained from a laser guide star even though tilt cannot be measured directly from the LGS signal. For beam-

steering adaptive optics in the Airborne Laser, optimal tilt compensation permits longer measurement time delays, thus reducing the bandwidth of such a system. When adaptive optics are used with a spatial interferometer, optimal compensation results in increased fringe visibility at larger beacon offsets, reducing the degrading effects of angular anisoplanatism, and leading to better image reconstruction.

7.5 Recommendations for future research

The research activity presented in this dissertation presents a description of optimal compensation for anisoplanatism that is complete and consistent. While the research *answers* many important questions, it *asks* just as many, if not more. There were several considerations that were outside the scope of the current research effort that could be addressed in future research activity. These issues are outlined in the following paragraphs.

Turbulence modeling. The generalized concept of anisoplanatism espoused in this research focused on aperture and source spatial separations as the primary source of anisoplanatism. Indeed, this view is consistent with all previous conventional analysis efforts that assume statistical isotropy in turbulence modeling. It is recognized, however, that statistical *anisotropy* will change the correlative properties of all Zernike modes, especially the cross-correlation between different aberration orders. In this sense, statistical anisotropy would give rise to a performance degradation effect in AO systems similar to conventional or the generalized form of spatial anisoplanatism. By invoking reasonable models for anisotropic turbulence, the cross-correlation calculations for Zernike modes could be extended to account for this effect. As a result, the optimal compensation theory would help to mitigate the performance degradation resulting from anisotropic turbulence.

Measurement noise effects. In the development of the optimal compensation theory, it was assumed that apart from anisoplanatism, the wave-front sensing device was ideal. Therefore, the effects of sensor noise were not considered. If an appropriate noise model for the Zernike coefficients resulting from wave-front sensor measurements were developed, that model could be incorporated into the MMSE estimator, resulting in a reduced sensitivity to noise effects caused by low light levels or detector read noise.

Laser guide star tilt sensing. The method for wave-front tilt sensing developed in this research is innovative in that it takes advantage of the natural properties of anisoplanatism to obtain a tilt measurement indirectly from higher-order modal measurements. The particular off-axis LGS geometry investigated here is just one of many ways to utilize the cross-correlation between tilt and higher-order modes. Even if a single LGS is deployed on-axis, higher-order wave-front measurements from spatially-offset subregions of the aperture could be employed to estimate the full-aperture tilt. Although the LGS signal does not contain full-aperture tilt components, it does contain *local* wave-front gradients that correspond to sub-aperture tilts. Indeed these subaperture tilts are the fundamental signal used to reconstruct higher-order modes. It follows therefore that wave-front sensor subaperture tilts should be correlated with the full-aperture tilt. In this case, an optimal estimate of the full-aperture tilt could be formed on the basis of subaperture tilt measurements.

Higher-order compensation for ABL. The application of optimal compensation to adaptive optics for the Airborne Laser dealt only with beam-steering or tilt correction. While tilt compensation is the most important aberration correction in this system, higher-order compensation may be required, depending upon the relative aperture diameter D/r_0. In this case, optimal higher-order modal compensation would also result in increased Strehl ratio for the irradiance-on-target with extended propagation paths. The required modal cross-correlations can be obtained from the current expressions, with proper accounting for the effects of aperture and source motion.

Laser guide star in interferometry. When considering the effect of optimal compensation in adaptive optics for interferometric applications, the only effects investigated in this research were those associated with angular offsets of a natural guide star. Since the limits of angular anisoplanatism in interferometry are more severe than in conventional imaging, it is reasonable to assume that laser-guide-star adaptive optics may be required for reasonable sky coverage. In this case, focal anisoplanatism also will affect compensation performance. As was the case in conventional single-aperture imaging with LGS compensation, there will be limits placed on the beacon altitude by focal anisoplanatism. These limits, and the ability for optimal compensation to expand these limits could be investi-

gated using the current theory and cross-correlation expressions, with proper modeling to account for the finite altitude of the LGS beacon.

Appendix A. Conversion of spatial integral to a spectral integral in the Zernike coefficient cross-correlation calculation

In this appendix, the conversion of the spatial integral for $B_{a_{u1i}a_{v2j}}$ in Eq. (145) to the spectral integral in Eq. (146) is detailed. This development begins with the expression for the spatial cross-correlation given in Eq. (145):

$$\begin{aligned} & B_{a_{u1i}a_{v2j}}(\vec{r}_{su},\vec{r}_{a1},\vec{r}_{sv},\vec{r}_{a2}) \\ &= \sum_l [R^2(1-A_{u1l})(1-A_{v2l})]^{-1} \int \mathrm{d}\vec{q}_{u1l} \int \mathrm{d}\vec{q}_{v2l}\, B_\phi(\vec{q}_{v2l}+\vec{s}_l-\vec{q}_{u1l}) \\ &\quad \times Z_i\left[\frac{\vec{q}_{u1l}}{R(1-A_{u1l})}\right] Z_j\left[\frac{\vec{q}_{v2l}}{R(1-A_{v2l})}\right] W\left[\frac{\vec{q}_{u1l}}{R(1-A_{u1l})}\right] W\left[\frac{\vec{q}_{v2l}}{R(1-A_{v2l})}\right]. \end{aligned} \quad (203)$$

For spatial functions $f(\vec{r})$ and $g(\vec{r})$, Parseval's theorem [32] says that:

$$\int d\vec{r}\, f(\vec{r})g^*(\vec{r}) = \int d\vec{f}\, F(\vec{f})G^*(\vec{f}), \quad (204)$$

where $F(\vec{f})$ and $G(\vec{f})$ are the Fourier transforms of $f(\vec{r})$ and $g(\vec{r})$, respectively. The scaling properties of Fourier transforms applied to the spatial function $f(\vec{r})$ may be written as [30]:

$$\mathcal{FT}\left\{f(\frac{\vec{r}}{b})\right\} = |b|F(b\vec{f}), \quad (205)$$

where $\mathcal{FT}\{\cdot\}$ denotes the Fourier transform operation. Applying Parseval's theorem and the scaling properties of the Fourier transform to the integral over $\vec{q}_{2l}$ in Eq. (203) yields:

$$\begin{aligned} & B_{a_{u1i}a_{v2j}}(\vec{r}_{su},\vec{r}_{a1};\vec{r}_{sv},\vec{r}_{a2}) \\ &= \sum_l [R(1-A_{u1l})]^{-1} \int \mathrm{d}\vec{q}_{u1l} \int \mathrm{d}\vec{k}\, \mathcal{FT}\left\{B_\phi(\vec{q}_{v2l}+\vec{s}_l-\vec{q}_{u1l})\right\} \\ &\quad \times Z_i\left[\frac{\vec{q}_{u1l}}{R(1-A_{u1l})}\right] W\left[\frac{\vec{q}_{u1l}}{R(1-A_{u1l})}\right] Q_j^*\left[R(1-A_{v2l})\vec{k}\right], \end{aligned} \quad (206)$$

where $Q_j^*(\vec{f})$ is the Fourier transform of $Z_j^*(\vec{r})W(\vec{r})$.

The Wiener-Khinchin theorem says that for a spatially wide-sense stationary quantity $x(\vec{r})$, the spatial power spectral density of x, designated $W_x(\vec{k})$ is the Fourier transform of the spatial autocorrelation of x [32], designated $B_x(\Delta\vec{r})$. Since the phase in the lth layer

is spatially wide-sense stationary, then, by the Wiener-Khinchin theorem:

$$\mathcal{FT}\left\{B_\phi(\vec{q}_{v2l}+\vec{s}_l-\vec{q}_{u1l})\right\} = W_\phi(\vec{k},z_l)\exp\left[j2\pi\vec{k}\cdot(\vec{q}_{u1l}-\vec{s}_l)\right], \tag{207}$$

where the exponential term arises from the spatial shift property of the Fourier transform [30]. Thus, substituting Eq. (207) into Eq. (206) yields:

$$\begin{aligned} &B_{a_{u1i}a_{v2j}}(\vec{r}_{su},\vec{r}_{a1};\vec{r}_{sv},\vec{r}_{a2}) \\ &= \sum_l [R(1-A_{u1l})]^{-1}\int d\vec{q}_{u1l}\int d\vec{k}\, W_\phi(\vec{k},z_l)\exp\left[j2\pi\vec{k}\cdot(\vec{q}_{u1l}-\vec{s}_l)\right] \\ &\quad \times Z_i\left[\frac{\vec{q}_{u1l}}{R(1-A_{u1l})}\right] W\left[\frac{\vec{q}_{u1l}}{R(1-A_{u1l})}\right] Q_j^*\left[R(1-A_{v2l})\vec{k}\right]. \end{aligned} \tag{208}$$

Exchanging the order of integration over $\vec{q}_{u1l}$ and $\vec{k}$, and rearranging terms in the integral yields the following expression:

$$\begin{aligned} &B_{a_{u1i}a_{v2j}}(\vec{r}_{su},\vec{r}_{a1};\vec{r}_{sv},\vec{r}_{a2}) \\ &= [R(1-A_{u1l})]^{-1}\int d\vec{k}\, W_\phi(\vec{k},z_l)Q_j^*\left[R(1-A_{v2l})\vec{k}\right]\exp(-j2\pi\vec{k}\cdot\vec{s}_l) \\ &\quad \times \int d\vec{q}_{u1l} Z_i\left[\frac{\vec{q}_{u1l}}{R(1-A_{u1l})}\right] W\left[\frac{\vec{q}_{u1l}}{R(1-A_{u1l})}\right]\exp(j2\pi\vec{k}\cdot\vec{q}_{u1l}). \end{aligned} \tag{209}$$

At this point, it is recognized that the integral over $\vec{q}_{u1l}$ in Eq. (209) is the Fourier transform of $Z_i[\,\cdot\,]W[\,\cdot\,]$. Since, by the scaling property of Fourier transforms,

$$\mathcal{FT}\left\{Z_i\left[\frac{\vec{q}_{u1l}}{R(1-A_{u1l})}\right] W\left[\frac{\vec{q}_{u1l}}{R(1-A_{u1l})}\right]\right\} = R(1-A_{u1l})Q_i\left[R(1-A_{u1l})\vec{k}\right], \tag{210}$$

it is therefore concluded from Eq. (209) that:

$$\begin{aligned} &B_{a_{u1i}a_{v2j}}(\vec{r}_{su},\vec{r}_{a1},\vec{r}_{sv},\vec{r}_{a2}) \\ &= \sum_l \int d\vec{k}\, W_\phi(\vec{k},z_l)\exp(-j2\pi\vec{k}\cdot\vec{s}_l)Q_i\left[R(1-A_{u1l})\vec{k}\right] Q_j^*\left[R(1-A_{v2l})\vec{k}\right], \end{aligned} \tag{211}$$

which is the spectral integral of Eq. (146).

Appendix B. Integration of the azimuthal component of the Zernike coefficient cross-correlation expression

In this appendix, the integration of Eq. (146) with respect to the azimuthal component of $\vec{k}$ is performed to yield the expression in Eq. (147), which involves one-dimensional integration over the radial component of $\vec{k}$. The development begins by introducing the following expression for the Fourier transform of the product of the ith (Noll's ordering [54]) Zernike polynomial and the aperture weighting function, $Z_i(\vec{\rho})W(\vec{\rho})$, as a function of the radial and azimuthal components of $\vec{k}$, designated k and θ, respectively:

$$\begin{aligned} Q_i(f,\theta) &= \sqrt{n_i+1}(-1)^{(n_i-m_i)/2}\sqrt{-1}^{m_i}\sqrt{2}^{1-\delta_{m_i0}} \\ &\quad \times \frac{J_{n_i+1}(2\pi f)}{\pi f}\cos\left\{m_i\theta + \frac{\pi}{4}(1-\delta_{m_i0})[(-1)^i - 1]\right\}, \end{aligned} \tag{212}$$

where n_i and m_i are the radial and azimuthal orders of the ith Zernike polynomial, $J_\kappa(\cdot)$ is the Bessel function of the first kind of order κ, and δ is the Kronecker delta. The expression for $Q_i(k,\theta)$ in Eq. (212) differs from its conventional form, but is mathematically equivalent to the multi-case expression given by Noll [54].

Since θ_{s_l} is defined as the angle between the vector $\vec{s}_l$ and the unit vector $\hat{x}$, and if $\vec{k}$ is taken to be a vector whose angle with respect to $\hat{x}$ is θ, then it may be said that:

$$\vec{k}\cdot\vec{s}_l = ks_l\cos(\theta-\theta_{s_l}). \tag{213}$$

Hence Eq. (146) may be written as:

$$\begin{aligned} &B_{a_{u1i}a_{v2j}}(\vec{r}_{su},\vec{r}_{a1},\vec{r}_{sv},\vec{r}_{a2}) \\ &= \sum_l \int_0^\infty \mathrm{d}k\, k\, W_\phi(k,z_l) \int_{\theta_{s_l}}^{\theta_{s_l}+2\pi} \mathrm{d}\theta\, \exp[-j2\pi k s_l\cos(\theta-\theta_{s_l})] \\ &\quad \times Q_i\left[R(1-A_{u1l})k,\theta\right] Q_j^*\left[R(1-A_{v2l})k,\theta\right]. \end{aligned} \tag{214}$$

Substituting the expression of Eq. (212) for Q_i and Q_j^* into Eq. (214) yields the following expression:

$$
\begin{aligned}
&B_{a_{u1i}a_{v2j}}(\vec{r}_{su},\vec{r}_{a1},\vec{r}_{sv},\vec{r}_{a2}) \\
&= \sum_l [\pi^2 R^2(1-A_{u1l})(1-A_{v2l})]^{-1}[(n_i+1)(n_j+1)]^{\frac{1}{2}} \\
&\quad \times(-1)^{\frac{1}{2}(n_i+n_j)}2^{[1-\frac{1}{2}(\delta_{m_i0}+\delta_{m_j0})]}(-1)^{m_j} \\
&\quad \times \int_0^\infty \mathrm{d}k\, k^{-1}\, W_\phi(k,z_l)\, J_{n_i+1}\left[2\pi R(1-A_{u1l})k\right] J_{n_j+1}\left[2\pi R(1-A_{v2l})k\right] \\
&\quad \times \int_{\theta_{s_l}}^{\theta_{s_l}+2\pi} \mathrm{d}\theta\, \exp[-j2\pi k s_l\cos(\theta-\theta_{s_l})]\, \cos\left\{m_i\theta+\frac{\pi}{4}(1-\delta_{m_i0})[(-1)^i-1]\right\} \\
&\qquad\qquad \times \cos\left\{m_j\theta+\frac{\pi}{4}(1-\delta_{m_j0})[(-1)^j-1]\right\}. \qquad (215)
\end{aligned}
$$

The product of cosine factors in Eq. (215) can be expanded as follows:

$$
\begin{aligned}
&\cos\left\{m_i\theta+\frac{\pi}{4}(1-\delta_{m_i0})[(-1)^i-1]\right\}\cos\left\{m_j\theta+\frac{\pi}{4}(1-\delta_{m_j0})[(-1)^j-1]\right\} \\
&= \frac{1}{2}\cos\left[(m_i+m_j)\theta+g\right]+\frac{1}{2}\cos\left[(m_i-m_j)\theta+h\right], \qquad (216)
\end{aligned}
$$

where g and h are defined as follows:

$$
\begin{aligned}
g &\equiv \frac{\pi}{4}\left\{(1-\delta_{m_i0})[(-1)^i-1]+(1-\delta_{m_j0})[(-1)^j-1]\right\}, \qquad (217)\\
h &\equiv \frac{\pi}{4}\left\{(1-\delta_{m_i0})[(-1)^i-1]-(1-\delta_{m_j0})[(-1)^j-1]\right\}. \qquad (218)
\end{aligned}
$$

If we now make the substitution $\phi=\theta-\theta_{s_l}$, then the right hand side of Eq. (216) may then be expanded as follows:

$$
\begin{aligned}
&\frac{1}{2}\cos\left[(m_i+m_j)\theta+g\right]+\frac{1}{2}\cos\left[(m_i-m_j)\theta+h\right] \\
&= \begin{cases}
\frac{1}{2}\cos\left[(m_i+m_j)\phi\right]\cos\left[(m_i+m_j)\theta_{s_l}+g\right] \\
-\frac{1}{2}\sin\left[(m_i+m_j)\phi\right]\sin\left[(m_i+m_j)\theta_{s_l}+g\right] \\
+\frac{1}{2}\cos\left[(m_i-m_j)\phi\right]\cos\left[(m_i-m_j)\theta_{s_l}+h\right] \\
-\frac{1}{2}\sin\left[(m_i-m_j)\phi\right]\sin\left[(m_i-m_j)\theta_{s_l}+h\right].
\end{cases} \qquad (219)
\end{aligned}
$$

When this expansion of the cosine terms is substituted into Eq. (215), the integration with respect to θ, designated here as I_θ becomes (using $\phi = \theta - \theta_{s_l}$):

$$I_\theta = \int_0^{2\pi} \mathrm{d}\phi \, \exp[-j2\pi k s_l \cos\phi] \times \begin{cases} \frac{1}{2}\cos\left[(m_i+m_j)\phi\right]\cos\left[(m_i+m_j)\theta_{s_l}+g\right] \\ -\frac{1}{2}\sin\left[(m_i+m_j)\phi\right]\sin\left[(m_i+m_j)\theta_{s_l}+g\right] \\ +\frac{1}{2}\cos\left[(m_i-m_j)\phi\right]\cos\left[(m_i-m_j)\theta_{s_l}+h\right] \\ -\frac{1}{2}\sin\left[(m_i-m_j)\phi\right]\sin\left[(m_i-m_j)\theta_{s_l}+h\right]. \end{cases} \tag{220}$$

Now, using the following definition for the Bessel function of the first kind of order κ [1]:

$$J_\kappa(z) = \frac{1}{\sqrt{-1}^{\kappa}\pi}\int_0^{\pi} \mathrm{d}\phi \, \exp(jz\cos\phi)\cos(\kappa\phi), \tag{221}$$

it can be shown that:

$$\int_0^{2\pi} \mathrm{d}\phi \, \exp(-jz\cos\phi)\cos(\kappa\phi) = 2\pi(-1)^{\frac{3}{2}\kappa}J_\kappa(z), \tag{222}$$

$$\int_0^{2\pi} \mathrm{d}\phi \, \exp(-jz\cos\phi)\sin(\kappa\phi) = 0. \tag{223}$$

Hence, I_θ in Eq. (220) is evaluated as:

$$I_\theta = -\pi \begin{cases} (-1)^{\frac{3}{2}(m_i+m_j)}J_{(m_i+m_j)}(2\pi k s_l)\cos[(m_i+m_j)\theta_{s_l}+g] \\ +(-1)^{\frac{3}{2}|m_i-m_j|}J_{|m_i-m_j|}(2\pi k s_l)\cos[(m_i-m_j)\theta_{s_l}+h]. \end{cases} \tag{224}$$

Substituting Eq. (224) in for the integral over θ in Eq. (215), as well as the definitions of the quantities g and h defined in Eq. (217) and Eq. (218), we obtain the following expression for $B_{a_{u1i}a_{v2j}}$:

$$
\begin{aligned}
&B_{a_{u1i}a_{v2j}}(\vec{r}_{su},\vec{r}_{a1},\vec{r}_{sv},\vec{r}_{a2}) \\
&= \frac{1}{\pi}R^{-2}F\sum_{l}[(1-A_{u1l})(1-A_{v2l})]^{-1} \\
&\times\left\{\begin{array}{l}
G\int_0^\infty \frac{dk}{k}W_\phi\left(\frac{x}{\pi D},z_l\right)J_{(m_i+m_j)}[2\pi k s_l] \\
\qquad\times J_{(n_i+1)}[R(1-A_{u1l})2\pi k]J_{(n_j+1)}[R(1-A_{v2l})2\pi k] \\
+H\int_0^\infty \frac{dk}{k}W_\phi\left(\frac{x}{\pi D},z_l\right)J_{|m_i-m_j|}[2\pi k s_l] \\
\qquad\times J_{(n_i+1)}[R(1-A_{u1l})2\pi k]J_{(n_j+1)}[R(1-A_{v2l})2\pi k],
\end{array}\right.
\end{aligned}
\tag{225}
$$

where the functions F, G, and H are defined as:

$$
F \equiv [(n_i+1)(n_j+1)]^{\frac{1}{2}}(-1)^{\frac{1}{2}(n_i+n_j)}2^{[1-\frac{1}{2}(\delta_{m_i0}+\delta_{m_j0})]}(-1)^{m_j} \tag{226}
$$

$$
\begin{aligned}
G \equiv\ & (-1)^{\frac{3}{2}(m_i+m_j)}\cos\left[(m_i+m_j)\theta_{s_l}\right. \\
& \left.+\pi/4\left\{(1-\delta_{m_i0})[(-1)^i-1]+(1-\delta_{m_j0})[(-1)^j-1]\right\}\right],
\end{aligned}
\tag{227}
$$

$$
\begin{aligned}
H \equiv\ & (-1)^{\frac{3}{2}|m_i-m_j|}\cos\left[(m_i-m_j)\theta_{s_l}\right. \\
& \left.+\pi/4\left\{(1-\delta_{m_i0})[(-1)^i-1]-(1-\delta_{m_j0})[(-1)^j-1]\right\}\right].
\end{aligned}
\tag{228}
$$

By defining $x \equiv \pi D k$, where $D = 2R$, Eq. (225) may be rewritten as:

$$
\begin{aligned}
&B_{a_{u1i}a_{v2j}}(\vec{r}_{su},\vec{r}_{a1},\vec{r}_{sv},\vec{r}_{a2}) \\
&= \frac{4}{\pi}D^{-2}F\sum_{l}[(1-A_{u1l})(1-A_{v2l})]^{-1} \\
&\times\left\{\begin{array}{l}
G\int_0^\infty \frac{dx}{x}W_\phi\left(\frac{x}{\pi D},z_l\right)J_{(m_i+m_j)}\left[\frac{2s_l}{D}x\right] \\
\qquad\times J_{(n_i+1)}[(1-A_{u1l})x]J_{(n_j+1)}[(1-A_{v2l})x] \\
+H\int_0^\infty \frac{dx}{x}W_\phi\left(\frac{x}{\pi D},z_l\right)J_{|m_i-m_j|}\left[\frac{2s_l}{D}x\right] \\
\qquad\times J_{(n_i+1)}[(1-A_{u1l})x]J_{(n_j+1)}[(1-A_{v2l})x],
\end{array}\right.
\end{aligned}
\tag{229}
$$

which is the cross-correlation expression given in Eq. (147).

Appendix C. Spatial cross-correlation of Zernike coefficients for apertures of different diameter

The development presented in Chapter III for the spatial cross-correlation of Zernike coefficients assumed that the two apertures in the analysis geometry of Figure 12 were of equal radius R. This analysis may be modified to yield a more-general expression for the spatial cross-correlation in different-sized apertures. If aperture 1 has radius R_1, and aperture 2 has radius R_2, then the Zernike coefficients a_{u1i} and a_{v2j} are given by:

$$a_{u1i} = \int d\vec{\rho}_1 \, \phi_{u1}(R_1\vec{\rho}_1) Z_i(\vec{\rho}_1) W(\vec{\rho}_1) \tag{230}$$

$$a_{v2j} = \int d\vec{\rho}_2 \, \phi_{v2}(R_2\vec{\rho}_2) Z_j(\vec{\rho}_2) W(\vec{\rho}_2). \tag{231}$$

The projected aperture vectors $\vec{q}_{u1l}$ and $\vec{q}_{v2l}$ are modified accordingly:

$$\vec{q}_{u1l} = (1 - A_{u1l}) R_1 \vec{\rho}_1 \tag{232}$$

$$\vec{q}_{v2l} = (1 - A_{v2l}) R_2 \vec{\rho}_2, \tag{233}$$

where the layer scaling factors A_{u1l} and A_{v2l} remain unchanged from the definitions given in Eq. (118) and Eq. (119), respectively. If Eq. (232) and Eq. (233) are employed throughout the development in Chapter III and Appendix A-B, the steps in the development are the same, with the quantity $R(1 - A_{u1l})$ replaced by $R_1(1 - A_{u1l})$ and $R(1 - A_{v2l})$ replaced by $R_2(1 - A_{v2l})$. When the spectral variable is transformed from k to x in Appendix B, the appropriate transformation is $x \equiv \pi D_1 k$, where the diameter of aperture 1 is $D_1 = 2R_1$. Thus, grouping D_1 with r_0, and accounting for the variable transformation, the expression for $B_{a_{u1i}a_{v2j}}$ in the case of different-sized apertures corresponding to Eq. (152) is given by:

$$
\begin{aligned}
&B_{a_{u1i}a_{v2j}}(\vec{r}_{su},\vec{r}_{a1},\vec{r}_{sv},\vec{r}_{a2}) \\
&= \left(\frac{D_1}{r_0}\right)^{5/3} \sqrt{3}\,\Gamma(8/3)\,2^{-5/3}\frac{6.88}{2.91}\left(\frac{D_2}{D_1}\right) F \sum_l w_l \left[(1-A_{u1l})(1-A_{v2l})\right]^{-1} \\
&\times \left\{ \begin{array}{l} G\int_0^\infty \frac{dx}{x}(x^2+x_0^2)^{-11/6} J_{(m_i+m_j)}\left[\frac{2s_l}{D_1}x\right] \\ \qquad \times J_{(n_i+1)}[(1-A_{u1l})x] J_{(n_j+1)}\left[\frac{D_2}{D_1}(1-A_{v2l})x\right] \\ +H\int_0^\infty \frac{dx}{x}(x^2+x_0^2)^{-11/6} J_{|m_i-m_j|}\left[\frac{2s_l}{D_1}x\right] \\ \qquad \times J_{(n_i+1)}[(1-A_{u1l})x] J_{(n_j+1)}\left[\frac{D_2}{D_1}(1-A_{v2l})x\right], \end{array} \right.
\end{aligned}
\tag{234}
$$

where $D_2 = 2R_2$. Thus, the cross-correlation is normalized for the size of aperture 1 relative to the atmospheric coherence diameter, D_1/r_0, and depends upon diametric-disparity parameter, D_2/D_1.

Bibliography

1. Abramowitz, Milton and Irene Stegun. *Handbook of Mathematical Functions With Formulas, Graphs, and Mathematical Tables*. Washington D.C.: Department of Commerce, 1964.
2. Avila, Remy, et al. "Theoretical spatiotemporal analysis of angle of arrival induced by atmospheric turbulence as observed with a grating scale monitor experiment," *J. Opt. Soc. Am. A*, *14*(11):3070–3082 (November 1997).
3. Babcock, H. W. "The possibility of compensating astronomical seeing," *Publ. Astron. Soc. Pac.*, *65*:229–236 (1953).
4. Babcock, H. W. "Adaptive optics revisited," *Science*, *249*:253–257 (July 1990).
5. Belen'kii, M. S. "Fundamental limitation in adaptive optics: How to eliminate it? A full aperture tilt measurement technique with a laser guide star." *Proc. SPIE: Adaptive Optics in Astromony2201*, edited by Mark A. Ealey and Fritz Merkle. 321–323. 1994.
6. Belen'kii, M. S. "Full aperture tilt measurement technique with a laser guide star." *Proc. SPIE: Atmospheric Propagations and Remote Sensing IV2471*, edited by J. C. Dainty. 289–300. 1995.
7. Belen'kii, M. S. "Tilt angular correlation and tilt sensing techniques with a laser guide star." *Proc. SPIE: Optics in atmospheric propagation, adaptive systems, and lidar techniques for remote sensing2956*, edited by Adam D. Devir, et al. 206–217. 1996.
8. Belen'kii, M. S. "Multiple aperture averaging technique for measuring full aperture tilt with a laser guide star." *Proc. SPIE: Adaptive optics and applications3126*, edited by Robert K. Tyson and Robert Q. Fugate. 101–112. 1997.
9. Born, Max and Emil Wolf. *Principles of Optics* (Sixth Edition). Oxford: Pergamon Press, 1980.
10. Butts, R. R. and D. C. Washburn. "Power spectral density of atmospheric jitter and track loop performance for the ABL." *Airborne Laser System and Component Analysis I*, edited by W. P. Latham and P. H. Merritt, Kirtland AFB, NM: Phillips Laboratory, 1994.
11. Chapman, Suzann. "The Airborne Laser," *Air Force Magazine*, *79*(1):54–55 (January 1996).
12. Colavita, M. M. "Design considerations for very long baseline fringe-tracking interferometers." *Proc. SPIE: Amplitude and Intensity Spatial Interferometry1237*, edited by J. B. Breckinridge. 289–300. 1990.
13. Colavita, M. M. "Interferomery at Keck Telescopes creates powerful array," *OE Reports*, (171):1–8 (March 1998).
14. Dai, Guangming. "Modal compensation of atmospheric turbulence with the use of Zernike polynomials and Karhunen-Loeve functions," *J. Opt. Soc. Am. A*, *12*(10):2182–2193 (October 1995).

15. Dessenne, Caroline, et al. "Optimization of a predictive controller for closed-loop adaptive optics," *Applied Optics*, *37*(21):4623–4633 (July 1998).

16. Ellerbroek, Brent L. "First-order performance evaluation of adaptive-optics systems for atmospheric turbulence compensation in extended-field-of-view astronomical telescopes," *J. Opt. Soc. Am. A*, *11*(2):783–805 (February 1994).

17. Esposito, S., et al. "Focus anisoplanatism effects on tip-tilt compensation for adaptive optics with use of a sodium laser beacon as a tracking reference," *J. Opt. Soc. Am. A*, *13*(9):1916–1923 (September 1996).

18. Foy, R. and A. Labeyrie. "Feasibility of adaptive telescopes with laser probe," *Astr. Astophys.*, *152*:129–131 (1985).

19. Fried, David L. "Statistics of a geometric representation of wavefront distortion," *J. Opt. Soc. Am.*, *55*(11):1427–1435 (November 1965).

20. Fried, David L. "Optical resolution through a randomly inhomogeneous medium for very long and very short exposures," *J. Opt. Soc. Am.*, *56*(10):1372–1379 (October 1966).

21. Fried, David L. "Varieties of isoplanatism." *Proc. SPIE: Imaging through the Atmosphere 75*, edited by James C. Wyant. 20–29. 1976.

22. Fried, David L. "Anisoplanatism in adaptive optics," *J. Opt. Soc. Am.*, *72*(1):52–61 (January 1982).

23. Fried, David L. and John F. Belsher. "Analysis of fundamental limits to artificial-guide-star adaptive-optics-system performance for astronomical imaging," *J. Opt. Soc. Am. A*, *11*(1):277–287 (January 1994).

24. Fugate, Robert Q. "Laser beacon adaptive optics," *Opt. Phot. News*, *9*(6):14–19 (June 1993).

25. Fugate, Robert Q., et al. "Measurement of atmospheric wavefront distortion using scattered light from a laser guide star," *Nature*, *353*:144–146 (September 1991).

26. Fulghum, David A. "USAF sees new roles for Airborne Laser," *Aviation Week and Space Technology*, *145*(15):26–27 (October 1996).

27. Gardner, Chester S., et al. "Design and performance analysis of adaptive optical telescopes using laser guide stars," *Proceedings of the IEEE*, *78*(11):1721–1743 (November 1990).

28. Gardner, Patrick J., et al. "Comparison of measured and computed Strehl ratios for light propagated through a channel flow of a He/N_2 mixing layer at high Reynolds numbers," *Applied Optics*, *36*(12):2559–2567 (April 1997).

29. Gardner, Patrick J., et al. "Statistical anisotropy in free turbulence for mixing layers at high Reynolds numbers," *Applied Optics*, *35*(24):4879–4889 (August 1996).

30. Gaskill, Jack. *Linear Systems, Fourier Transforms, and Optics*. New York: John Wiley and Sons, 1978.

31. Goodman, Josesph W. *Introduction to Fourier Optics*. New York: McGraw-Hill, 1968.

32. Goodman, Josesph W. *Statistical Optics*. New York: Wiley, 1985.

33. Greenwood, D. P. "Bandwidth specifications for adaptive optics systems," *J. Opt. Soc. Am.*, *67*(3):390–393 (March 1977).

34. Hardy, J. W. "Active optics: A new technology for the control of light," *Proc. IEEE*, *66*:651–687 (1978).

35. Hecht, Eugene. *Optics* (Second Edition). Reading: Addison-Wesley, 1987.

36. Hogg, Robert V. and Allen T. Craig. *Introduction to Mathematical Statistics* (Fifth Edition). New York: Macmillan, 1995.

37. Hogge, C. Barry and R. Russell Butts. "Frequency spectra for the geometric representation of wavefront distortions due to atmospheric turbulence," *J. Opt. Soc. Am.*, *66*(3):207–211 (March 1976).

38. Hu, P. H., et al. "Application of Zernike polynomials to atmospheric propagation problems," *J. Opt. Soc. Am. A*, *6*(10):1595–1608 (October 1989).

39. Hufnagel, R. E. "Variations of atmospheric turbulence." *Topical Meeting on Optical Propagation through Turbulence* Washington, D.C.: Optical Society of America, 1974.

40. Hufnagel, R. E. and N. R. Stanley. "Modulation transfer function associated with image transmission through turbulent media," *J. Opt. Soc. Am.*, *54*(1):52–61 (January 1964).

41. Huygens, Christiaan. "Treatise on Light." *Great Books of the Western World 34*, edited by Robert Maynard Hutchins, Chicago: Encyclopedia Brittanica, 1952.

42. Johnston, D. C and B. M. Welsh. "Analysis of multiconjugate adaptive optics," *J. Opt. Soc. Am. A*, *11*(1):394–408 (January 1994).

43. Kay, Steven M. *Fundamentals of Statistical Signal Processing: Estimation Theory*. Upper Saddle River, NJ: Prentice-Hall, 1993.

44. Kolmogorov, A. N. "The local stucture of turbulence in incompressible viscous fluid for very large Reynolds' numbers." *Turbulence, Classic Papers on Statistical Theory* edited by S. K. Friedlander and L. Topper, 151–155, New York: Wiley-Interscience, 1961.

45. Korff, D., et al. "Isoplanicity: The translation invariance of the atmopheric Green's function," *J. Opt. Soc. Am.*, *65*(11):1321–1330 (November 1975).

46. Lawson, Peter R. "Group-delay tracking in optical stellar interferometry with the fast Fourier transform," *J. Opt. Soc. Am. A*, *12*(2):366–374 (February 1995).

47. Lee, R. W. and Harp J. C. "Weak scattering in random media, with applications to remote probing," *Proc. IEEE*, *57*(4):375–406 (April 1969).

48. Loos, G. C. "Using adaptive optics to enhance Michelson interferometry," *Appl. Opt.*, *31*(31):6632–6636 (November 1992).

49. Lukin, Vladamir P. *Atmospheric Adaptive Optics (English translation)*. Bellingham: SPIE Press, 1996.

50. Lukin, Vladimir P. "Monostatic and bistatic schemes and an optimal algorithm for tilt correction in ground-based adaptive telescopes," *Applied Optics*, *37*(21):4634–4644 (July 1998).

51. Molodij, Guillaume and Gerard Rousset. "Angular correlation of Zernike Polynomials for a laser guide star in adaptive optics," *J. Opt. Soc. Am. A*, *14*(8):1949–1966 (August 1997).

52. Mourard, D., et al. "The GI2T interferometer on Plateau de Calern," *Astron. Astrophys.*, *283*:705–713 (1994).

53. Newton, Isaac. *Optiks or A Treatise of the Reflections, Refractions, Inflections and Colours of Light*. New York: Dover, 1979.

54. Noll, Robert J. "Zernike polynomials and atmospheric turbulence," *J. Opt. Soc. Am.*, *66*(3):207–211 (March 1976).

55. Pilkington, J. D. H. "Artificial guide stars for adaptive imaging," *Nature*, *330*:116 (November 1987).

56. Primmerman, Charles A., et al. "Compensation of atmospheric optical distortion using a synthetic beacon," *Nature*, *353*:141–143 (September 1991).

57. Ragazzoni, Roberto. "Absolute tip-tilt determination with laser beacons," *Astron. Astrophys.*, *305*:L13–L16 (1996).

58. Ragazzoni, Roberto, et al. "Auxilary telescopes for the absolute tip-tilt determination of a laser guide star," *Mon. Not. R. Astron. Soc.*, *276*:L76–L78 (1995).

59. Ragazzoni, Roberto, et al. "Minimum diameter of a laser projector for some perspective-based laser guide-star retrieval schemes," *Applied Optics*, *37*(21):4645–4648 (July 1998).

60. Readhead, A. C. S., et al. "Diffraction-limited imaging with ground-based optical telescopes," *Astron. J.*, *95*(4):1278–1296 (April 1988).

61. Roddier, F. "The effects of atmospheric turbulence in optical astronomy." *Progress in Optics XIX*, edited by Emil Wolf, New York: North Holland, 1981.

62. Roddier, F., et al. "One-dimensional spectra of turbulence-induced Zernike aberrations: time delay and isoplanicity error in partial adaptive compensation," *J. Opt. Soc. Am. A*, *10*(5):957–965 (May 1993).

63. Roddier, Nicolas. "Atmospheric wavefront simulation using Zernike polynomials," *Opt. Eng.*, *29*(10):1174–1180 (October 1990).

64. Roggemann, Michael C. "Limited degree-of-freedom adaptive optics and image reconstruction," *Applied Optics*, *30*(29):4227–4233 (October 1991).

65. Roggemann, Michael C. "Optical performance of fully and partially compensated adaptive optics systems using least-squares and minimum variance phase reconstructors," *Comp. Elect. Engng.*, *18*(6):451–466 (June 1992).

66. Roggemann, Michael C. "Photon-noise limits to the detection of the closure phase in optical interferometry," *Appl. Opt.*, *35*:1809–1815 (1996).

67. Roggemann, Michael C., et al. "Sensing three-dimensional index-of-refraction variations by means of optical wavefront sensor measurements and tomographic reconstruction," *Opt. Eng.*, *34*(5):1374–1384 (May 1995).

68. Roggemann, Michael C. and Byron Welsh. *Imaging Through Turbulence*. Boca Raton: CRC Press, 1996.

69. Roggemann, Michael. C., et al. "Improving the resolution of ground-based telescopes," *Rev. Mod. Phys.*, *69*(2):437–505 (April 1997).

70. Sandler, D. G., et al. "Adaptive optics for diffraction-limited infrared imaging with 8-m telescopes," *J. Opt. Soc. Am. A*, *11*(2):925–945 (February 1994).

71. Sasiela, Richard J. *Electromagnetic Wave Propagation in Turbulence*. Berlin: Springer-Verlag, 1994.

72. Sasiela, Richard J. "Wave-front correction by one or more synthetic beacons," *J. Opt. Soc. Am. A*, *11*(1):379–393 (January 1994).

73. Shao, M., et al. "The Mark III stellar interferometer," *Astron. Astrophys.*, *193*:357–371 (1988).

74. Stone, J., et al. "Anisoplanatic effects in finite-aperture optical systems," *J. Opt. Soc. Am. A*, *11*(1):347–357 (January 1994).

75. Swenson, G. W. "Radio-astronomy precedent for optical interferometer imaging," *J. Opt. Soc. Am. A*, *3*(8):1311–1319 (August 1986).

76. Takato, Naruhisa and Ichirou Yamaguchi. "Spatial correlation of Zernike phase-expansion coefficients for atmospheric turbulence with finite outer scale," *J. Opt. Soc. Am. A*, *12*(5):958–963 (May 1995).

77. Tango, William J. and R. Q. Twiss. "Michelson stellar interferometry." *Progress in Optics XVII*, edited by Emil Wolf, 239–277, New York: North Holland, 1980.

78. Tatarski, V. I. *Wave Propagation in a Turbulent Medium*. New York: Dover, 1961.

79. Tatarski, V. I. *The Effects of the Turbulent Atmosphere on Wave Propagation*. U.S. Department of Commerce, 1971.

80. Thompson, Laird A. and Chester S. Gardner. "Experiments on laser guide stars at Mauna Kea Observatory for adaptive imaging in astronomy," *Nature*, *328*:229–231 (July 1987).

81. Troxel, Steven E. *A Diffraction-Based Model of Anisoplanatism Effects in Adaptive Optic Systems*. PhD dissertation, Air Force Institute of Technology, Wright-Patterson Air Force Base, Ohio, 1994.

82. Troxel, Steven E., et al. "Off-axis optical transfer function calculations in an adaptive-optics system by means of a diffraction calculation for weak index fluctuations," *J. Opt. Soc. Am. A*, *11*(7):2100–2111 (July 1994).

83. Troxel, Steven E., et al. "Anisoplanatism effects on signal-to-noise ratio performance of adaptive optical systems," *Journal of the Optical Society of America A*, *12*(3):570–577 (March 1995).

84. Tyler, Glenn A. "Turbulence-induced adaptive-optics performance degradation: evaluation in the time domain," *J. Opt. Soc. Am. A*, *1*(3):251–262 (March 1984).

85. Tyler, Glenn A. "Bandwidth considerations for tracking through turbulence," *J. Opt. Soc. Am. A*, *11*(1):358–367 (January 1994).

86. Tyler, Glenn A. "Merging: a new method for tomography through random media," *J. Opt. Soc. Am. A*, *11*(1):409–424 (January 1994).

87. Tyler, Glenn A. "Wave-front compensation for imaging with off-axis guide stars," *J. Opt. Soc. Am. A*, *11*(1):339–346 (January 1994).

88. Valley, George C. and Stephen M. Wandzura. "Spatial correlation of phase-expansion coefficients for propagation through atmospheric turbulence," *J. Opt. Soc. Am.*, *69*(5):712–717 (May 1979).

89. Voitsekhovich, V. V. "Outer scale of turbulence: comparison of different models," *J. Opt. Soc. Am. A*, *12*(6):1346–1353 (June 1995).

90. Von Bokern, Mark A., et al. "Modal control for and adaptive optics system using LQG compensation," *Computers Elect. Engng.*, *18*(6):421–433 (June 1992).

91. Wallner, Edward P. "Optimal wave-front correction using slope measurements," *J. Opt. Soc. Am.*, *73*(12):1771–1776 (December 1983).

92. Wang, J. Y. and J. K. Markey. "Modal compensation of atmospheric turbulence phase distortion," *J. Opt. Soc. Am.*, *68*(1):78–87 (January 1978).

93. Welsh, Byron M. and Chester S. Gardner. "Effects of turbulence-induced anisoplanatism on the imaging performance of adaptive-astronomical telescopes using laser guide stars," *J. Opt. Soc. Am. A*, *8*(1):69–80 (January 1991).

94. Whiteley, Matthew R., et al. "Temporal properties of the Zernike expansion coefficients of turbulence-induced phase aberrations for aperture and source motion," *J. Opt. Soc. Am. A*, *15*(4):993–1005 (April 1998).

95. Whiteley, Matthew R., et al. "Effect of modal atmospheric compensation on angular anisoplanatism in optical interferometric imaging." *Proc. SPIE: Adaptive Optical System Technologies3353*, edited by Robert K. Tyson and Domenico Bonaccini. in press. 1998.

96. Whiteley, Matthew R., et al. "Optimal modal wave-front compensation for anisoplanatism in adaptive optics," *J. Opt. Soc. Am. A*, *15*(8):2097–2106 (August 1998).

97. Wild, Walter J. "Predictive optimal estimators for adaptive-optics systems," *Optics Letters*, *21*(18):1433–1435 (1996).

98. Winker, D. M. "Effect of a finite outer scale on the Zernike decomposition of atmospheric optical turbulence," *J. Opt. Soc. Am. A*, *8*(10):1568–1573 (October 1991).

Vita

Captain Matthew R. Whiteley was born 25 May 1969 in Marietta, Ohio. He graduated from Fort Frye High School as Valedictorian in 1987. Whiteley then attended Carnegie Mellon University in Pittsburgh, Pennsylvania where he received a B.S. in Physics with University Honors. Upon graduation, he accepted a commission as a Second Lieutenant in the United States Air Force. In September 1991, Whiteley was assigned to the Advanced Guidance Division, Wright Laboratory Armament Directorate, Eglin Air Force Base, Florida. In May 1994, he was assigned to the Air Force Institute of Technology, Wright-Patterson Air Force Base, where he graduated from the Graduate Applied Physics program in September 1995. Whiteley was named a Distinguished Graduate of the Masters program at AFIT, and was presented the Commandant's Award for his thesis research. While in the doctoral program at AFIT, Whiteley attended Squadron Officers' School and was elected a member of Tau Beta Pi, serving as the Ohio Eta chapter president during 1997. Whiteley will continue his research in adaptive optics at the Air Force Research Laboratory Directed Energy Directorate, Kirtland Air Force Base, New Mexico.

Permanent address: P.O. Box 6
Whipple, Ohio 45788

REPORT DOCUMENTATION PAGE			Form Approved OMB No. 0704-0188

1. AGENCY USE ONLY *(Leave blank)*	2. REPORT DATE	3. REPORT TYPE AND DATES COVERED
	1 Sep 98	Dissertation

4. TITLE AND SUBTITLE
Optimal Atmospheric Compensation for Anisoplanatism in Adaptive-Optical Systems

5. FUNDING NUMBERS

6. AUTHOR(S)
Capt Matthew R. Whiteley

7. PERFORMING ORGANIZATION NAME(S) AND ADDRESS(ES)
Air Force Institute of Technology, Department of Engineering Physics
AFIT/ENP
2950 P Street, Building 640
Wright-Patterson AFB, OH 45433-7765

8. PERFORMING ORGANIZATION REPORT NUMBER
AFIT/DS/ENP/98-01

9. SPONSORING/MONITORING AGENCY NAME(S) AND ADDRESS(ES)
Maj Todd D. Steiner
Air Force Research Laboratory, Airborne Laser Technology Branch, AFRL/DEBA
3550 Aberdeen Ave SE
Kirtland AFB, NM 87117-5776

10. SPONSORING/MONITORING AGENCY REPORT NUMBER

11. SUPPLEMENTARY NOTES

12a. DISTRIBUTION AVAILABILITY STATEMENT
Approved for public release; distribution unlimited

12b. DISTRIBUTION CODE

13. ABSTRACT *(Maximum 200 words)*

Anisoplanatism in adaptive optics (AO) systems is a performance-degrading effect that arises whenever light from the wave-front sensor beacon and light from the object of interest sample different volumes of optical turbulence. This effect occurs if there is either a spatial separation between the object and the beacon, or a spatial separation between the wave-front sensor and phase-compensation aperture, or if both types of separation are present in the AO system. In this dissertation, anisoplanatism is characterized by the correlation of Zernike coefficients of object and beacon turbulence-induced phase. It is shown through theoretical calculations validated with experimental data, that while most Zernike modes are uncorrelated in the absence of anisoplanatism, moderate amounts of anisoplanatism result in an enhanced cross-correlation of the phase coefficients. This fact, along with a theoretical description of the performance-degradation process motivates the application of optimal estimation theory to AO compensation. In imaging systems, optimal compensation reduces the effect of anisoplanatism, increasing beacon separation limits by up to three times, and enabling estimation of wave-front tilt from a laser beacon, which cannot be measured conventionally. For beam-projection systems such as Airborne Laser, optimal compensation can decrease the AO update rate by over 70%. In interferometric systems, a fringe visibility increase of 25% is realized by applying optimal compensation, resulting in enhanced image reconstruction at large baseline separations.

14. SUBJECT TERMS	15. NUMBER OF PAGES
adaptive optics, atmospheric optics, turbulence compensation, anisoplanatism, optimal estimation	180
	16. PRICE CODE

17. SECURITY CLASSIFICATION OF REPORT	18. SECURITY CLASSIFICATION OF THIS PAGE	19. SECURITY CLASSIFICATION OF ABSTRACT	20. LIMITATION OF ABSTRACT
UNCLASSIFIED	UNCLASSIFIED	UNCLASSIFIED	UL

Standard Form 298 (Rev. 2-89) (EG)
Prescribed by ANSI Std. 239.18
Designed using Perform Pro, WHS/DIOR, Oct 94